Transactions of the ASME®

Transactions of the ASME, Journal of Engineering for Gas Turbines and Power (ISSN 0022-0825) is published quarterly (Jan., Apr., July, Oct.) for $85 per year by The American Society of Mechanical Engineers, 345 East 47th Street, New York, NY 10017. Second class postage paid at New York, NY and additional mailing offices. POSTMASTER: Send address change to The Journal of Engineering for Gas Turbines and Power, c/o The AMERICAN SOCIETY OF MECHANICAL ENGINEERS, 22 Law Drive, Box 2300, Fairfield, NJ 07007-2300.

CHANGES OF ADDRESS must be received at Society headquarters seven weeks before they are to be effective. Please send old label and new address.

PRICES: To members, $24.00, annually; to nonmembers, $85.00.
Add $6.00 for postage to countries outside the United States and Canada.

INDEXED by Engineering Information

Journal of Engineering for Gas Turbines and Power

Published Quarterly by The American Society of Mechanical Engineers
VOLUME 109 • NUMBER 3 • JULY 1987

TECHNICAL PAPERS

DISCUSSION

ANNOUNCEMENTS

Simultaneous Heat and Mass Transfer in a Catenary Cooling Tower

Yun-Yu Liu
Kaohsiung Refinery,
Lin Yuan, Koahsiung Hsien,
Republic of China

H. E. Hesketh
Department of Mechanical Engineering,
Southern Illinois University,
Carbondale, IL 62901
Mem. ASME

A 6-in. i.d. catenary contactor was used to evaluate the performance of this device as a new type of cooling tower. A fractional factorial statistical study facilitated the incorporation of all 21 independent variables applicable to this system. Regression models showed that the catenary behavior is analogous to and can be predicted by traditional cooling tower theory. These models also showed that an improved available coefficient based on mass transfer more accurately predicts catenary cooling tower performance. In comparison with conventional cooling towers and within the range of these data it appears that a catenary is more stable with changes in liquid-to-gas ratio, L/G, and that it can handle nearly twice the liquid and gas loadings. Catenary contactors could have a promising future in that they should also conserve space and be economical to purchase.

Introduction

The catenary cooling tower is also known as a catenary contactor and a catenary grid scrubber (patented; this name is a registered trademark). This device has only recently been developed and it is an extremely simple and effective mass and heat transfer system. It functions as a countercurrent gas–liquid contacting system. In operation, a two-phase gas–liquid zone is created above the patented catenary grid screen as shown in Fig 1. Because of its appearance, this zone is likened to a "fluidized" mixture. The hydrodynamic properties of this contactor have been studied and reported by Hesketh et al. [1]. Normal rising air speed is about 18 ft/s but flow from 12 to over 30 ft/s can be used. These units have no difficulty handling suspended and/or dissolved solids.

Liquid for mass and/or heat transfer can be introduced either above, at, or below the grid pair section. Single or multiple grid pairs can be used to achieve specialized staging effects, which makes this device extremely versatile. Units larger than 6 ft in diameter are in commercial operation and no size scale-up limitations have been experienced. The open internal nature of the unit and the turbulent action on the grid screens keeps it free from internal buildup and plugging and also results in nearly instantaneous transfer of heat.

A laboratory investigation was conducted in 1985-1986 to study the performance of this type of device as a cooling tower. This paper presents the findings of the simultaneous heat and mass transfer investigations in a catenary contactor.

Traditional Cooling Towers

Cooling towers are widely used in industries to cool hot water from process cooling systems. The various types and designs are usually classified on the basis of draft:

- natural draft (natural convection)
- mechanical draft (forced convection)
- mixed draft (natural and forced convection)

Mechanical draft is the most popular.

A breakdown by type according to Cheremisinoff [2] is given in Fig. 2. Each of these attempts to maximize air–water interfacial contact area at minimum gas phase pressure drop. The greater this interfacial contact area, the greater the rate of heat exchange.

Cooling Tower Theory

The characteristics of cooling towers are generally presented in the form of an empirical correlation. This can be expressed as a power law relation

$$K_a V/L \propto (L/G)^b \tag{1}$$

where

$K_a V/L$ = cooling tower "available coefficient"
K = mass transfer coefficient, lb moles/(ft^2 hr) per mole fraction
a = specific interfacial area, ft^2/ft^3
V = volume of cooling tower per cross-sectional area, ft^3/ft^2
L = liquid flow rate, lb/hr
G = gas flow rate, lb/hr

The exponent b ranges from -0.35 to -1.1 with values from -0.55 to -0.65 being most common. This equation shows the relationship between the available coefficient, $K_a V/L$, and liquid-to-gas ratio, L/G, for a constant gas flow rate.

The traditional cooling tower available coefficient was derived by Merkel in 1925 and is given by Sutherland [3]. Its derivation is based on two assumptions:

Contributed by the Environmental Control Division for publication in the JOURNAL OF ENGINEERING FOR GAS TURBINES AND POWER. Manuscript received by the Environmental Control Division August 14, 1985.

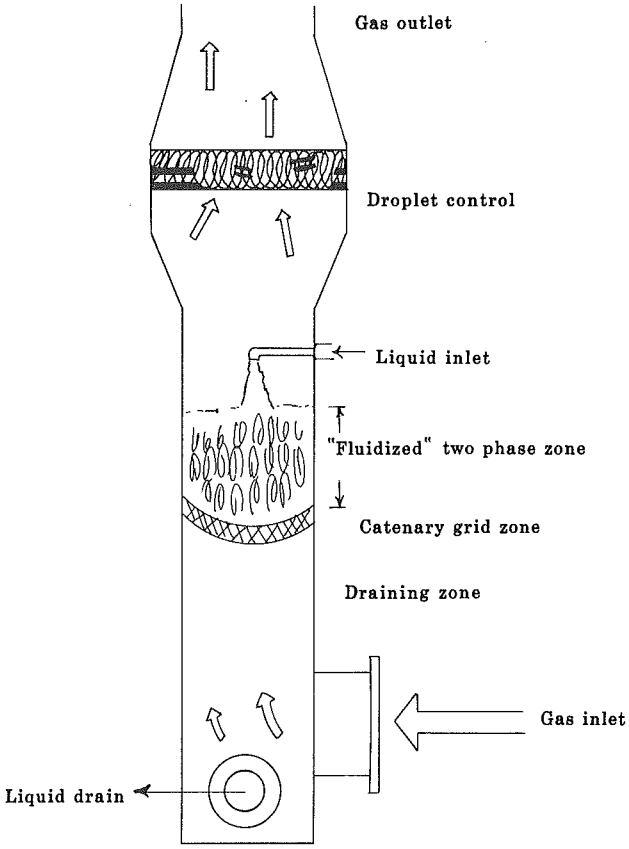

Fig. 1 Schematic drawing of catenary contactor

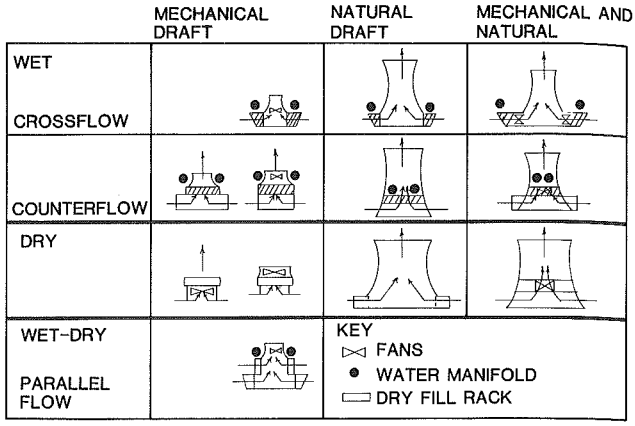

Fig. 2 Classification of cooling towers

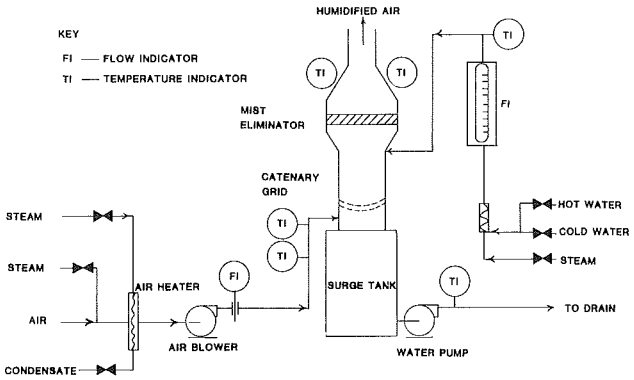

Fig. 3 Schematic flow diagram of catenary contactor cooling tower

(*i*) The water loss by evaporation is negligible. That is, the water flow rate in any position of the contacting device is constant.

(*ii*) The Lewis number for an air/water vapor system is unity.

Based on these asssumptions and a heat balance the following equation is obtained

$$K_a V/L = \int dT_1/(h_s - h) \qquad (2)$$

where

$K_a V/L$ = traditional available coefficient
T_1 = inlet water temperature, °F
h_s = enthalpy of saturated humidified air, Btu/lb dry air
h = enthalpy of humidified air, Btu/lb dry air

Detailed integrating procedures to obtain the traditional available coefficient are given in the works of Cheremisinoff [2] and Sutherland [3]. Note that the Lewis number is Le = h_c/KC where h_c is convection heat transfer coefficient of humidified air and C is specific heat of air.

Experimental Apparatus

The apparatus used in this study consists of:

- humidified air supply system
- hot water supply system
- catenary contactor

A schematic diagram of the whole assembly is shown in Fig. 3.

A blower with a finned radiator at the inlet is used to heat the air to the required operating temperature. Steam injection nozzles installed before the radiator are used to adjust the inlet air humidity to the required level. Air flow is measured by a modified-calibrated venturi meter. The thermocouples, as shown in Fig. 3, are used for dry-bulb and wet-bulb temperatures of the inlet and outlet humidified air and for the inlet-outlet water.

The cantenary contactor used is a 6-in i.d. glass column with a single grid pair installed near the bottom of the glass column. The top grid is four by four mesh stainless wire and the

Nomenclature

a = specific interfacial area, ft^2/ft^3
C_p = specific heat of air
G = air flow rate, lb/hr
h = enthalpy of humidified air, Btu/lb dry air
h_s = enthalpy of saturated humidified air, Btu/lb dry air
K = mass transfer coefficient, lb moles/(ft^2 hr) per mole fraction
$K_a V/G$ = improved available coefficient
$K_a V/L$ = cooling tower available coefficient
L = liquid flow rate, lb/hr
L/G = liquid-to-gas ratio
T_a = inlet humidified air temperature, °F
T_1 = inlet water temperature, °F
V = volume of cooling tower per cross-sectional area, ft^3/ft^2
w = humidity of humidified air, lb water/lb dry air
w_s = saturated humidity of humidified air, lb water/lb dry air

bottom is a two by two mesh wire with the wire direction 90 deg to the wire of the top. Hot water is fed in from the top and humidified air is introduced from the bottom of the contactor.

Statistical Study Design

A mass transport phenomenon occurs in cooling towers so the traditional cooling tower theory was used as the reference mechanism to simulate the performance of this catenary cooling tower. It was desired to obtain an empirical model for this simultaneous transport phenomenon which includes all the main effects and lower order interactions. This leads to the adoption of a three-level five-factor fractional factorial experiment. In this study the levels for each factor are arranged as Table 1. The results of this study are valid within these ranges.

By way of definition: factor = the independent variable in an experiment which will cast certain influence on the outcome; level = the possible form or value of a factor; treatment = a particular combination of one level from each factor; fractional factorial experiment = a study that examines the effect of several factors simultaneously but not all treatment combinations possible are included.

For a three-level five-factor experiment a complete design requires 243 observations. As mentioned, in this study only the main effects and lower order interactions are of concern; hence the number of required observations is reduced to 81. A partial list of the experimental treatments is shown in Table 2.

Procedures

Numerical values of the traditional available coefficient can be obtained by integration of equation (2). However, for the catenary cooling tower the experimental data collected here do not correlate well to this coefficient, so an "improved available coefficient" is derived directly from the mass transfer equation without the need to use the simplifying assumptions noted for traditional cooling towers. This procedure uses the mass differential balance of water

$$dL = Gdw \tag{3}$$

where

Table 1 Level arrangement of each main effect

Factor	Level 0	Level 1	Level 2
Inlet air temperature, °F	100	110	120
Inlet air humidity, lb H_2O/lb dry air	0.0045	0.0067	0.0090
Inlet air volume flow, acfm	180	195	210
Inlet water flow, gpm	1.0	1.5	2.0
Inlet water temperature, °F	100	110	120

L = mass flow rate of water, lb/hr
G = mass flow rate of dry air, lb/hr
w = humidity of humidified air, lb water/lb dry air

The mass transfer equation is

$$Gdw = K_a dV(w_s - w) \tag{4}$$

The accurate form is then obtained

$$K_a V/G = dw/(w_s - w) \tag{5}$$

where

$K_a V/G$ = improved available coefficient for catenary contactor
w_s = saturated humidity of humidified air, lb water/lb dry air

Results

Two different dependent variables can be compared for the catenary cooling tower using the procedures described. They are (1) the traditional cooling tower available coefficient and (2) the improved available coefficient. Using the data of Liu [4] given in Table 3, both of these coefficients are obtained by numerical integration.

There are 21 unknown parameters in the statistical model used for this study. It is not practical to include all of these in the final equation used to express catenary cooling tower performance. In order to reduce the number of variables in the model, only the most significant subsets of variables are used. These are the ones that yield the highest R-square value and the lowest C_p value (C_p is an auxiliary criterion in the selection of variables). In this study, C_p should be numerically small and close to the number of parameters used. The "all-possible-model search" method was used to screen all of the possible combinations of significant parameters. The following two equations are selected as best fitting the data of this study.

The traditional available coefficient for predicting catenary contactor behavior as a cooling tower is

$$\log(K_a V/L) = -4.425 - 0.12\log(T_1) + 1.6\log(G) - 0.36\log(L/G) \tag{6}$$

(R-square = 0.87)

The improved available coefficient for the catenary contactor is:

Table 2 Partial list of experimental treatments

Code	Inlet air flow, acfm	Inlet air temperature, °F	Inlet air humidity	Inlet H_2O flow, gpm	Inlet H_2O temperature, °F
00000	180.0	100.0	0.0045	1.0	100.0
00012	180.0	100.0	0.0045	1.5	120.0
00021	180.0	100.0	0.0045	2.0	110.0
00102	180.0	100.0	0.0067	1.0	120.0
00111	180.0	100.0	0.0067	1.5	110.0
00120	180.0	100.0	0.0067	2.0	100.0
00201	180.0	100.0	0.0090	1.0	110.0
00210	180.0	100.0	0.0090	1.5	100.0
00222	180.0	100.0	0.0090	2.0	120.0
01002	180.0	110.0	0.0045	1.0	120.0
01011	180.0	110.0	0.0045	1.5	110.0
01020	180.0	110.0	0.0045	2.0	100.0
01101	180.0	110.0	0.0067	1.0	110.0
01110	180.0	110.0	0.0067	1.5	100.0
01122	180.0	110.0	0.0067	2.0	120.0
01200	180.0	110.0	0.0090	1.0	100.0
01212	180.0	110.0	0.0090	1.5	120.0
01221	180.0	110.0	0.0090	2.0	110.0

Table 3 Observed data and derived coefficients [4]

Code	Outlet air temperature dry, °F	Outlet air temperature wet, °F	Outlet H_2O temperature, °F	K_aV/L	K_aV/G
00000	84.0	81.0	80.0	1.0482	1.3217
00012	94.0	93.0	90.0	0.8165	2.6133
00021	92.0	91.0	88.0	0.8033	2.4663
00102	92.0	90.0	87.0	0.9907	1.8936
00111	92.0	90.0	88.0	0.8259	1.8936
00120	89.0	87.0	85.0	0.8231	1.7195
00201	90.0	88.0	85.0	1.0742	1.6703
00210	88.0	86.0	84.0	0.9569	1.5496
00222	99.0	98.0	94.0	0.7437	2.9078
01002	92.0	90.0	87.0	0.9867	1.6152
01011	91.0	89.0	88.0	0.8051	1.5738
01020	89.0	87.0	85.0	0.8189	1.4936
01101	90.0	88.0	85.0	1.0687	1.4393

$$\log(K_aV/G) = 0.156 - 2.94\log(T_a) + 0.76\log(T_1)\log(L) - 1.58\log(L) + 2.14\log(G) + 0.58\log(L/G) \quad (7)$$

(R-square = 0.95)

where

T_a = inlet humidified air temperature, °F
T_1 = inlet water temperature, °F
L = water mass flow rate, lb/hr
G = air mass flow rate, lb/hr
L/G = water-to-air mass ratio

These data show good correlation of both the traditional and the improved available coefficients for the catenary contactor. However, from the R-square values of the two equations above, it is apparent that the assumption of Lewis number equal to one does not predict performance of the catenary cooling tower as accurately as the direct derivation method.

Specific values of independent variables can be used in equations (6) and (7) to compare further the catenary with conventional cooling tower behavior. Values within the range of this study, for example, are: T_a = 100°F; T_1 = 120°F; and G = 893.3 lb/hr. For equations (6) and (7), respectively, this gives

$$\log(K_aV/L) = 0.0466 - 0.36\log(L/G) \quad (8)$$

$$\log(K_aV/G) = 0.591 + 0.58\log(L/G) \quad (9)$$

Both equations are now in the form of the power law relationship, which is the form that the traditional cooling tower coefficient usually takes. This confirms the analogies between the conventional cooling tower and the catenary contactor. Comparing traditional cooling tower available coefficients from equation (1) with catenary contactor available coefficients from equation (8) yields, respectively

$$K_aV/L = k(L/G)^{-0.55\text{ to }-0.65} \quad \text{(cooling tower)} \quad (10)$$

$$K_aV/L = 0.0466\ (L/G)^{-0.36} \quad \text{(catenary contactor)} \quad (11)$$

Conclusions and Summary

The catenary is an extremely effective cooling tower in comparison to conventional towers. Figure 4 is a plot of equations (10) and (11). The shallower slope of the catenary curve shows that it is more stable with changes in the L/G ratio.

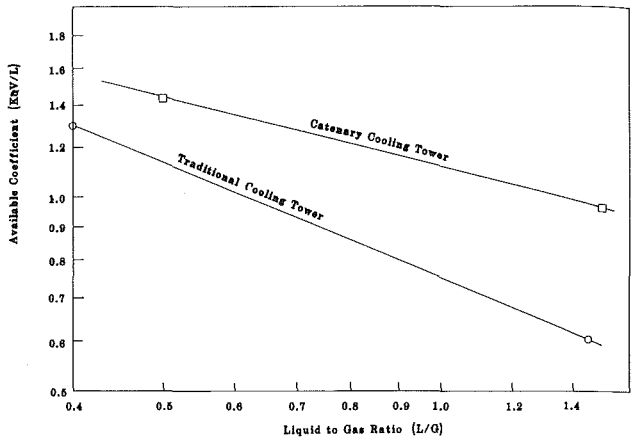

Fig. 4 A comparison between cooling tower and catenary contactor coefficients

It is interesting to compare the operating ranges of the catenary contactor and cooling tower. Cheremisinoff [2] indicates that traditional cooling towers have two critical points of water load. The lower critical point is about 500 lb/(sq ft)(hr). If the water load goes below this the water is unable to spread sufficiently and evenly to cover the entire available fill surface. The upper critical point is about 3000 lb/(sq ft)(hr). Above this the tower fails due to flooding. Thus the average design falls somewhere between these two extremes. In contrast, the water load in a catenary contactor is much higher than that of a traditional cooling tower. For example, the lowest water load in this study is 2525 lb/(sq ft)(hr), and the highest is 5047 lb/(sq ft)(hr). This upper rate is 70 percent higher than the flooding load of the traditional cooling tower. The lower operating rate of typical catenaries is at the average operating rate for the traditional towers.

In sizing a traditional cooling tower, another upper limit is the air load which is 1600 lb/(sq ft)(hr). The operating air load in this research varied from 3726 to 4502 lb/(sq ft)(hr). The larger rate is 180 percent higher than the conventional cooling tower load.

In summary, it can be concluded that:

- Traditional cooling tower theory does predict operational behavior of catenary contactors.
- The assumption that Lewis number equals 1 is not as accurate as the direct application of mass transfer relationships for predicting behavior of the catenary contactor as a cooling tower.
- Catenary contactors are less sensitive to changes in liquid-to-gas ratio, L/G, than conventional cooling towers.
- Catenary contactors can handle nearly twice as much liquid and/or gas mass rate per unit area as traditional cooling towers.

References

1 Hesketh H. E., Schifftner, K. C.,. Hesketh, R. P., and Powell, B., "Describing and Defining the Catenary Grid-Fluidized Bed Mass Transfer Separator," *Atmospheric Environmental*, Vol. 19, 1985, pp. 1565-1572.

2 Cheremisinoff, N . P., and Cheremisinoff, P. N., "Cooling Tower Selection, Design, and Practice," *Ann Arbor Science*, MI, 1981.

3 Sutherland, J. W., "Analysis of Mechanical-Drought Counterflow Air/Water Cooling Tower," ASME *Journal of Heat Transfer*, Vol. 105, 1983, pp. 576-583.

4 Liu, Y. Y., "Simultaneous Heat and Mass Transfer in a Catenary Cooling Tower," Master's Thesis, Mechanical Engineering, College of Engineering and Technology, Southern Illinois University, Carbondale, IL, 1986.

Experimental Investigation of Gas Turbine Recuperator Fouling

T. L. Bowen
Senior Project Engineer.
Assoc. Mem. ASME

D. P. Guimond
Mechanical Engineer.

R. K. Muench
Senior Project Engineer.
Mem. ASME

Engines Branch,
David Taylor Naval Ship Research and Development Center,
Bethesda, MD 20084-5000

This paper discusses an experimental investigation of recuperator fouling currently underway at the David Taylor Naval Ship Research and Development Center. The overall approach involves testing different heat exchangers in the exhaust gas stream of a gas turbine. The two heat exchangers initially tested were the plate-fin type and differed in the gas-side heat transfer surface geometry. Primary surface heat exchangers are being considered for future tests also. Test conditions are defined such that the critical part of full-scale recuperators (i.e., the colder end of the gas passages) is simulated in the small test heat exchangers. The composition of the gas stream is measured to determine amounts of gaseous, particulate, and condensible hydrocarbon emissions. Fuel samples taken during each test are analyzed. The test heat exchangers are specially constructed to allow inspection and measurement of the fouling film inside the unit following each test. The temperature distribution inside the test exchanger is measured, as well as air and gas inlet and exit temperatures. Measurements of fouling film thickness are made using an optical microscope and photographs of fouling deposits were taken. The early results obtained from fouling tests conducted with the first heat exchanger are discussed. Tests were also conducted to demonstrate a fouling removal technique.

Introduction

Development of a recuperated marine gas turbine offers several advantages over the current simple-cycle gas turbine used by the U.S. Navy. Future gas-turbine-powered ships could consume 30 percent less mission fuel, travel 25 percent farther with the same fuel load, have a lower stack temperature, and therefore be less detectable. Previous publications [1, 2] have described in detail the technical aspects of the proposed engine that make it attractive, and have also cited recuperator fouling as a potential problem. Incorporating a recuperator into the design of a large gas turbine increases both weight and volume. Unfortunately, the susceptibility of small gas-side passages to coating and eventually plugging by constituents in the exhaust gas of the turbine limits the compactness or the heat transfer area per unit volume of the recuperator. Since present knowledge of the mechanisms of fouling and particle deposition on low-temperature surfaces is very limited, the allowable compactness of the gas-side heat transfer surface has to be determined experimentally under the operating conditions expected in the recuperated gas turbine. This paper discusses an experimental investigation which is currently underway at the David Taylor Naval Ship Research and Development Center (DTNSRDC) in support of the U.S. Navy's development program for an advanced intercooled and regenerated (ICR) gas turbine. The objective of the investigation is to obtain recuperator fouling data for use in specifying the design and operation of an advanced gas turbine yet to be developed.

Recuperator gas-side fouling may or may not be a problem in a particular engine application depending upon: (1) the emissions characteristics of the gas turbine, which are related to the combustor design and fuel utilized; and (2) the gas side characteristics of the recuperator, including the compactness of the heat transfer surface and the temperature drop. Figure 1 is a plot of recuperator gas inlet and exit temperature as a function of percent rated power. Based on performance data from engine concept feasibility studies done in 1983, the recuperator gas temperatures in the advanced marine engine are expected to fall inside the shaded region of the graph. When compared to gas temperatures experienced in recuperators on three current industrial and vehicular gas turbines, similar ranges in operating temperature are observed. The higher exit gas temperature characteristic of the AVCO AGT-1500 is due to a higher cycle pressure ratio and lower recuperator effectiveness. The three recuperators differ significantly in geometry, but all have a gas-side compactness greater than 1500 m^2/m^3 (450 ft^2/ft^3). Despite the small gas passages in these recuperators, problems caused by fouling have not been experienced, according to the manufacturers. Currently most large industrial recuperated gas turbines are fueled with natural gas and operate at rated power; hence gas-side fouling is not encountered. Past experience using liquid fuels in marine and industrial applications, albeit somewhat dated, still causes concern about gas-side fouling as a potential problem. Unfortunately, few if any data were documented during these related applications, which could be used today to assess quantitatively the fouling problem in a future ap-

Contributed by the Gas Turbine Division of THE AMERICAN SOCIETY OF MECHANICAL ENGINEERS and presented at the 32nd International Gas Turbine Conference and Exhibit, Anaheim, California, May 31–June 4, 1987. Manuscript received at ASME Headquarters February 6, 1987. Paper No. 87-GT-97.

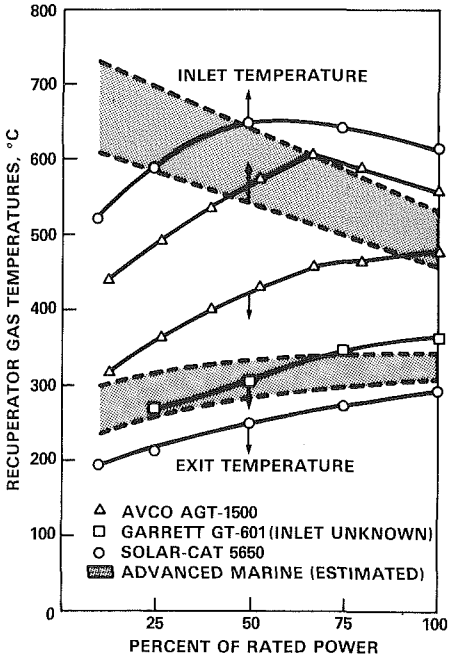

Fig. 1 Recuperator gas temperatures versus power

plication. As mentioned earlier, past and present-day performance is related to the quality of the fuel burned. The quality of readily available liquid fuels to the fleet is expected to worsen in the future. As the aromatic content of future fuels increases, so does the amount of soot and unburned hydrocarbons produced by a given combustor and carried over to the recuperator. A better understanding of the relationship between fuel quality, engine emissions, and fouling deposition is needed to factor recuperator fouling into the design and operation of the advanced marine gas turbine.

Background

Fouling of heat exchangers in combustion gas streams has not been as thoroughly researched as fouling in heat exchangers that reject heat to fresh water or seawater. It is presently known that the lower the heat exchanger surface temperature and the higher the exhaust particulate concentration, the more severe the fouling. Therefore, to overcome the fouling problem, high heat exchanger wall temperatures are maintained with system efficiency being sacrificed or large gas passages are selected and soot blowers used for cleaning.

In a previous investigation of recuperator fouling, Miller [3] obtained data on how the heat transfer coefficient and pressure drop of a heat exchanger deteriorated with time. He performed his experiments with a state-of-the-art gas turbine that had an unknown but high particulate emission rate. The most noteworthy contribution by Miller was his basic explanation of the fouling mechanism which stated that hydrocarbons from the exhaust gas stream diffuse to the heat exchanger surface and condense, allowing carbon particles to adhere to the wall and to each other. Thus, at temperatures in excess of the hydrocarbon condensation temperature, no fouling will form or previously formed fouling will be eliminated. The relationship between heat exchanger fouling and the particulate concentration or composition of the combustion gas is still not understood. In fact, some investigators have failed to quantify the particulate emission rate in their tests. Interpretation of fouling test results should take into account the emissions of the gas turbine, especially the particulate emission and the associated hydrocarbon fraction.

Figure 1 shows that the minimum exhaust gas temperature of the ICR gas turbine recuperator is 230°C (446°F). The minimum wall temperature lies somewhere between the gas exit and air inlet temperature. Table 1 shows that the minimum wall temperature for the recuperator is 150°C (300°F) at low power and low ambient temperature. This temperature is still 15°C (25°F) above the maximum sulfuric acid dew point temperature one would expect for this type of engine burning diesel fuel containing 1 percent sulfur. Other recuperator parameters of interest in this fouling investigation are summarized in Table 1. Typical values for both full-power and low-power operation are shown.

Table 1 Range of recuperator operating conditions in an ICR gas turbine

Parameter	Full-power hot ambient	Low-power cold ambient
Temperatures, °C(°F)		
Air inlet	260–310 (500–590)	100–190 (210–370)
Gas inlet	470–570 (870–1060)	490–700 (920–1300)
Gas exit	330–350 (620–660)	200–240 (400–460)
Wall, gas exit	290–330 (560–620)	150–210 (300–410)
Gas flowrate/area, kg/m^2s (lb/ft^2s)	11.1–11.9 (2.28–2.44)	3.22–4.00 (0.66–0.82)
Gas velocity, m/s (ft/s)	19–21 (62–68)	4–6 (14–19)

The concept feasibility studies have enabled us to estimate the operating conditions of the ICR gas turbine. Unfortunately, the emissions of the ICR engine are not known. It is hoped that they will be as good as or better than today's simple-cycle gas turbines. Typical particulate emissions from engines such as the General Electric LM 2500 or Rolls-Royce Marine Spey range from 1.5 mg/m^3 to less than 0.5 mg/m^3. However, no information on the hydrocarbon fraction is available. Another unknown is the impact of future fuels on recuperator fouling. Once this type of gas turbine is used on a class of combatants, it will see at least 30 years of service. During this time a significant degradation in diesel fuel quality will most likely occur. The soot production potentials of various constituents of future fuels have been investigated [4, 5] and are well understood. The unknown is what quality of fuel the Navy will be buying for its ships in the year 2000 and beyond.

Experimental Approach

This approach tries to (1) account for the major factors which seem to influence the buildup of a fouling film on the heat transfer surfaces of a gas turbine recuperator, and (2) conduct tests which are representative of future applications, despite some unavoidable constraints. The investigation involves testing different heat exchangers in the exhaust stream of a gas turbine. The first heat exchanger to be tested, HX-1, was of the plate-fin variety, and has the same gas-side fin geometry as that found in commercially available flue gas and industrial gas turbine recuperators. The fins are the offset type and the configuration has a compactness of 620 m^2/m^3 (190 ft^2/ft^3). Although this matrix is too heavy and voluminous for a naval ship application, testing of the HX-1 was done primarily to gain experience with test procedures and establish a familiar baseline for comparison with later results. The second heat exchanger, HX-2, is another plate-fin recuperator constructed with plain fins on the gas side. These fins have the same geometry proposed for use in the marine engine having a much higher gas-side compactness, 1380 m^2/m^3 (420 ft^2/ft^3), than HX-1. Figure 2 illustrates the differences between gas-side fins in the HX-1 and HX-2 test modules. A primary surface recuperator is also being proposed in one preliminary design of the marine engine. Consequently, the U.S. Navy is interested in conducting fouling tests using primary surface

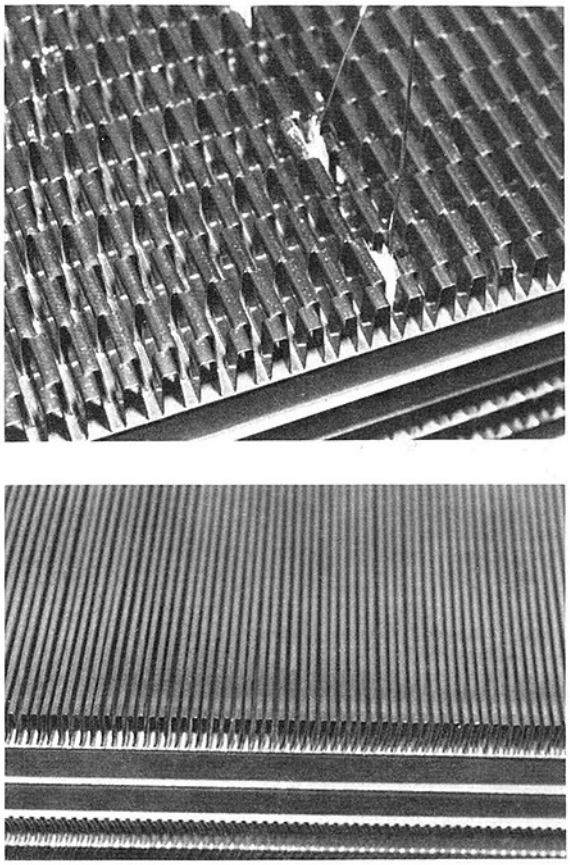

Fig. 2 Gas-side fin surface in HX-1 (upper photo) and HX-2 (lower photo)

heat exchangers as well. As of the writing of this paper, however, such a unit had not been obtained.

The heat exchangers used in the fouling tests are specially constructed to allow inspection of the fouling film inside the unit following each test. Each unit is constructed in two halves held together by a supporting frame as shown in Fig. 3. The gas temperature distribution in the central gas passage of the test unit is measured, as well as air and gas inlet and exit temperatures. Fouling films are inspected using an optical microscope and photographs of fouling deposits are taken. The heat exchangers measure approximately 23 cm (9 in.) wide by 43 cm (17 in.) long and 51 cm (20 in.) high. The volume of the test unit represents a small fraction of the volume of the full-scale recuperator in the marine engine. Therefore, the critical part of the full-scale recuperator, i.e., the colder end of the gas passages, is simulated in the small heat exchangers. Performance data from the 1983 engine concept feasibility studies included recuperator air and gas-side inlet conditions for several engine configurations assuming a recuperator effectiveness of 86 percent. Using these conditions as input to a computer program for plate-fin heat exchanger design, the dimensions and gas-side conditions of full-scale recuperators were established using the industrial and marine fins. Pertinent gas-side conditions calculated at the inlet and exit of the counterflow section include mass flow per unit of free flow area, Reynolds number and velocity, and gas temperature and metal surface temperature over a wide range of engine operating conditions. Test conditions are defined with the aid of another computer program which predicts performance of the specific geometry of either HX-1 or HX-2. In the analysis the gas flow per unit of free flow area in the test recuperator is set equal to that in the full-scale recuperator. Gas inlet temperature, and air side temperature and flowrate are

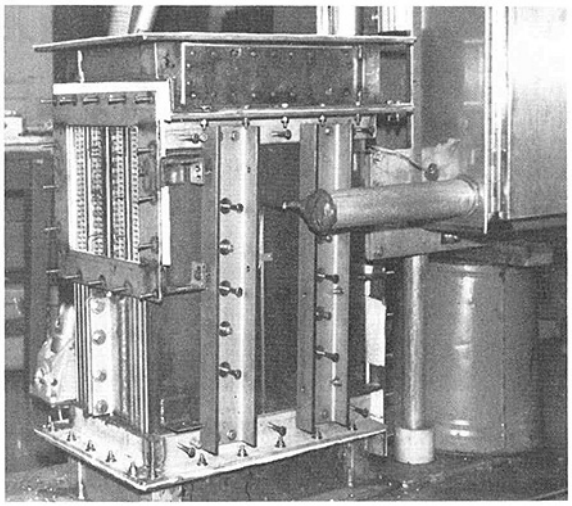

Fig. 3 Assembled HX-2 with supporting frame

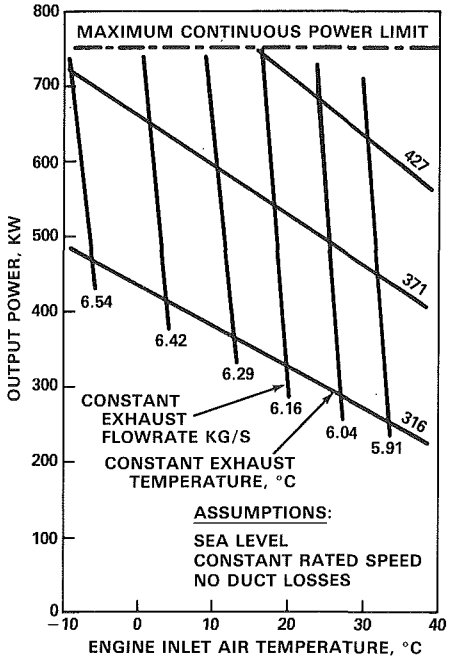

Fig. 4 Gas turbine performance characteristics

iterated upon until the gas side exit conditions cited above are duplicated as nearly as possible. The gas inlet temperature, air inlet temperature, and air inlet flowrate are constrained within the limits of the test rig capabilities.

A 750-kW gas turbine emergency generator set located at DTNSRDC's Annapolis Laboratory provided a readily available source of exhaust gas. Pertinent performance characteristics of the gas turbine are presented in Fig. 4. At the maximum continuous power rating, the peak engine exhaust gas temperature varies from about 380°C (720°F) on a cold day to 460°C (860°F) on a hot day. The temperature of the gas delivered to the inlet of the test recuperator is typically 44°C (80°F) lower than the engine's exhaust temperature due to heat loss through the ducting. Comparing these temperatures to the recuperator gas exit temperatures shown previously in Fig. 1 indicates that an adequate temperature capability exists, particularly when simulating recuperator conditions in the marine engine operating at low power levels. The gas inlet temperature to the test recuperator will correspond to the temperature of the gas in the full-scale recuperator after the

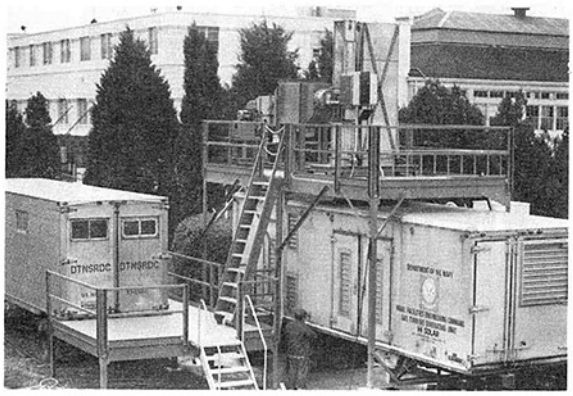

Fig. 5 Recuperator fouling test site

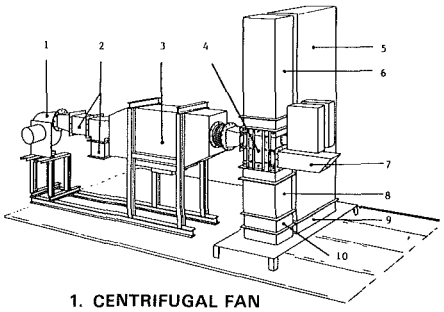

1. CENTRIFUGAL FAN
2. CONTROL DAMPERS
3. ELECTRIC HEATER
4. RECUPERATOR ASSEMBLY
5. GAS BYPASS DUCT
6. RECUPERATOR GAS EXIT DUCT
7. AIR EXIT DUCT
8. GAS SAMPLING DUCT
9. ADJUSTABLE LOUVERS
10. FLOW STRAIGHTENER

Fig. 6 Fouling test equipment layout

gas has traveled some distance through the recuperator where the gas is cooler and fouling is more likely to occur. It is apparent from Fig. 4 that output power must vary significantly with even small differences in the required inlet gas temperature to the test recuperator. Since the emissions of the gas turbine vary with output power, the composition of the gas stream, including amounts of gaseous, particulate, and condensible hydrocarbons, is measured. Fuel samples are taken during each fouling test and analyzed.

Test Facility Description

The recuperator fouling test hardware is assembled atop the gas turbine generator trailer as seen in Fig. 5. A second trailer that houses instrumentation for measuring emissions and a computerized data acquisition system is located next to the gas turbine trailer. Figure 6 shows the layout of the test equipment located on the platform above the turbine. An air flowrate in the range of 0.1 to 0.6 kg/s (0.2–1.2 lb/s) can be supplied to the recuperator using a constant-speed centrifugal fan with two control dampers located in the downstream air ducting. Prior to entering the recuperator, the air passes through an electric, resistance-element, duct heater where the temperature of the air can be raised to as high as 180°C (350°F). The heated air flows into a crossflow, air inlet header at the top of the recuperator assembly. The air stream is turned 90 deg as it enters the counterflow core section. At the end of the core section, the air stream is turned another 90 deg and leaves the recuperator through the crossflow air exit header and air exit duct.

Figure 4 shows that the exhaust flowrate from the single-shaft gas turbine operating at constant speed is essentially independent of output power, but is slightly affected by ambient temperature. Approximately 6 kg/s (13 lb/s) of gas exits the trailer's rooftop exhaust duct and enters a transition duct where the flow is divided into two streams. Less than 0.5 kg/s (1.0 lb/s) of gas is required to flow through the recuperator, while the remainder discharges to the atmosphere through the large gas bypass duct. The exhaust gas flowrate through the recuperator is regulated by a set of adjustable louvers located at the bottom of the gas bypass duct. As these louvers are gradually closed, inlet area to the bypass duct is decreased and the flowrate of gas through the recuperator increases. When the adjustable louvers are set in the full-open position a minimum gas flowrate of approximately 0.3 kg/s (0.6 lb/s) is obtained in the recuperator. To obtain the lower gas flowrates required in some tests, area at the top of the recuperator gas exit duct is also restricted. The stack containing the recuperator incorporates a section containing wire mesh screens for flow straightening and another section where exhaust sampling is performed to obtain gaseous and soot emissions data and smoke number prior to the exhaust gas entering the recuperator.

The recuperator is instrumented with thermocouples to obtain average fluid temperature at the inlet and exit on both sides. Wall temperatures within the center gas passage are estimated from measurements of air and gas temperature on opposite sides of a centrally located plate in the recuperator. The computerized data acquisition system logs test data at specified intervals, and continuously updates and displays test information to the operator during a fouling test.

Table 2 Results of fuel sample analysis

Fuel characteristic	ASTM[a] test method	Mean value
Hydrogen, weight percent	D1018	12.82
Carbon, weight percent	[b]	86.89
Sulfur, weight percent	D129	0.13
Aromatics, volume percent	D1319	30.16
Saturates, volume percent	D1319	68.35
HHV,[c] J/kg	D240	45.2×10^6
(Btu/lb)		(19,432)
Flash point, °C (°F)	D93	63 (145)
Specific gravity	D1298	0.845
Viscosity,[d] m^2/s	D445	2.68×10^{-6}
(centistokes)		(2.68)
Distillation, °C (°F):	D86	
Initial boiling point		176 (348)
10 percent recovery		208 (407)
20 percent recovery		224 (435)
30 percent recovery		237 (458)
40 percent recovery		248 (479)
50 percent recovery		260 (500)
60 percent recovery		271 (520)
70 percent recovery		283 (542)
80 percent recovery		298 (568)
90 percent recovery		317 (603)
End point		342 (647)

[a] American Society for Testing and Materials.
[b] Based on a combustion test.
[c] Higher Heating Value.
[d] Kinematic viscosity at 38°C (100°F).

Analyses of Fuel Samples

Fuel samples were collected during all tests and later analyzed to determine several common fuel characteristics. The arithmetic average or mean value for the fuel characteristics based on results obtained from twelve fuel samples is shown in Table 2. Of the five measurements pertaining to the chemical composition of the fuel, the hydrogen and carbon content were the most consistent between fuel samples (one sigma = 2.0 and 0.2 percent, respectively). The 12.82 percent by weight hydrogen is typical of a No. 2 distillate fuel as well [6]. Sulfur content varied significantly (one sigma = 23.1 per-

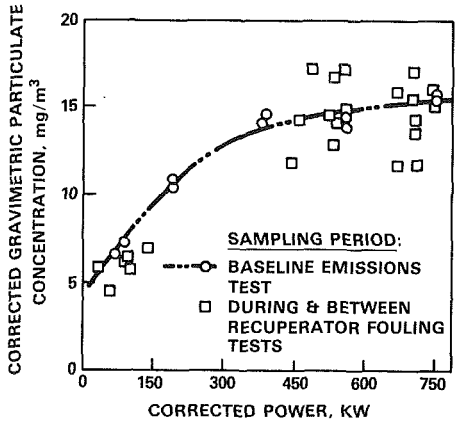

Fig. 7 Correlation of gravimetric particulate concentration with power

cent) among the fuel samples, but all had a relatively low amount of sulfur compared to the 1 percent by weight allowed in the applicable military specification [7] for Diesel Fuel Marine (DFM). With such a low sulfur content, the likelihood of any sulfuric acid attack occurring on the gas-side metal surfaces is very low. By comparison a sample of DFM collected from the USS Hancock (DD 981) while anchored in Annapolis contained 0.49 percent by weight sulfur. Not all the fuel characteristics listed in Table 2 are covered by the military specification. The aromatic content of the fuel is an example of one characteristic of DFM that is not governed by the specification. Yet the aromatic content of the fuel strongly affects the production of soot in the combustor. Although the aromatic content in the twelve fuel samples also varied (one sigma = 14.4 percent), the mean value of 30.16 percent by volume is comparable to that of the DFM sample from the Hancock which was 32.8 percent by volume aromatics. This is a higher aromatic content than the 25 percent maximum allowed in specifications for JP-4 and JP-5 aircraft fuels. A sample of JP-5 collected from the USS Hancock was determined to have 21.7 percent by volume aromatics. A survey of worldwide commercial marine fuels by Burnett et al. [8] found the aromatic content of 20 Marine Gas Oil (MGO) samples to range from 28.4 to 46.7 percent by volume with a mean of 38.2 percent. All of the MGO samples were 100 percent distillate products, and were analyzed using ASTM Test Method D2007. Heating value of the fuel, a combustion property, was very consistent (one sigma = 0.3 percent) between fuel samples. The Lower Heating Value (LHV) used to calculate gas turbine performance is determined from the HHV by the formula:

$$\text{LHV} = \text{HHV} - [91.23 \times \text{percent hydrogen by weight in sample}]$$

The remaining characteristics in Table 2 are physical properties. The values of flash point, specific gravity, and viscosity are typical of a No. 2 distillate fuel according to Lefebvre [6]. The repeatability of the physical property data for the twelve fuel samples was good (one sigma < 2.2 percent for all values except viscosity, which was 3.7 percent). Physical properties governed by the DFM specification include flash point, viscosity, and the 90 percent recovery and end points of the distillation curve. The fuel used during the fouling tests met the specification's requirements in these areas. In summary, the fuel is typical of that being used today aboard gas-turbine-powered combatants. However, broadening fuel specifications to make fuel more available to ships especially in foreign ports will mean higher aromatic content in future fuels, and possibly a higher risk of recuperator fouling.

Gas Turbine Emissions

In a baseline emissions test and at various times during the testing of HX-1, gaseous and particulate emissions of the gas turbine were measured. These data were obtained to ensure that the gas turbine and its combustion system performance were reasonable and constant; to establish and monitor the gaseous and particulate emission level of the gas turbine; and to establish the condensible (hydrocarbon) fraction of the particulate mass for future correlation of heat exchanger fouling. Sampling probes were located in the gas ducting upstream of the recuperator, in line with the plane separating the two halves of the recuperator. Since the gas turbine operates with a high level of excess air, the carbon monoxide emissions are very low and were not monitored, nor were oxides of sulfur and nitrogen.

Oxygen was monitored with a stack gas oxygen analyzer (stabilized zirconium oxide cell) and the carbon dioxide with an analyzer utilizing an infrared sensor. The gaseous emissions data were converted to air-fuel ratio and correlated with the manufacturer's specifications. In general, the air-fuel ratio correlated with the specification.

The particulate emissions of the gas turbine were measured both directly with a modified Environmental Protection Agency (EPA) Method 5 and indirectly with a smoke meter in accordance with the method specified by the Society of Automotive Engineers (SAE) [9]. In the direct method combustion gas, after being cooled to 150°C (300°F) by dilution with nitrogen, was passed through a Whatman or Gelman filter paper. The change in weight of the filter paper was divided by the exhaust gas volume after correcting for the dilution gas to obtain the particle concentration in milligrams per cubic meter (mg/m^3) of dry combustion gas at standard conditions. The smoke meter collects a smudge or spot (dispersed layer of particles) from the exhaust gas on a Whatman filter. The SAE smoke number is obtained from the reflectivity of this layer of particles compared to the reflectivity of the original filter paper. Correlations of data between the two methods are available, but variations of as much as 100 percent can be expected. The smoke meter is not as sensitive to large particles as the gravimetric method. Nevertheless, the smoke meter is much simpler to use, allowing consistent and periodic monitoring of the gas turbine particulate emissions. Figure 7 summarizes the gravimetric particulate concentration as a function of the gas turbine power level. Except for the scatter, the data obtained during the fouling tests are consistent with the initial baseline emissions measurements. Some of the data scatter can be attributed to the dilution process. The additional step of measuring the dilution gas and subtracting it from the total gas flow through the filter will add to the measurement inaccuracy.

In the present investigation the particulate matter has not only been collected to obtain the concentration (gravimetric), but sufficient samples at a known temperature have been collected to analyze for condensible hydrocarbons. The nominal collection temperature was selected as 150°C (300°F). As was mentioned earlier, 150°C is the lowest wall temperature the ICR engine is expected to encounter. The exhaust gas was therefore diluted with nitrogen to yield the desired gas temperature just after the filter. For the investigation of fouling behavior it is the total amount of condensible hydrocarbons that is of interest, and not necessarily the detailed composition.

Thermogravimetric analysis (TGA) was selected for analysis of condensible hydrocarbons. During a period of three months, 15 samples were analyzed. The data showed a definite but small weight loss. Unfortunately the weight loss data had significant scatter. It was then decided to obtain a larger number of samples as a set and analyze these consistently. It appeared that the data scatter had not been significantly

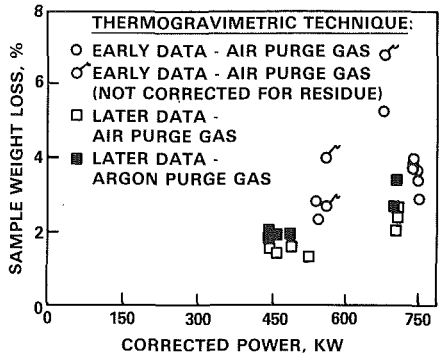

Fig. 8 Correlation of particulate sample weight loss with corrected power

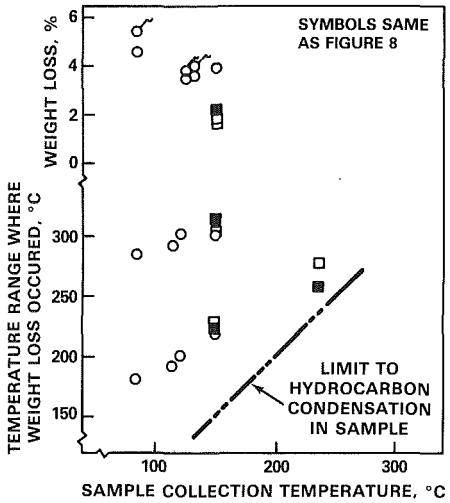

Fig. 9 Correlation of particulate sample weight loss with collection temperature

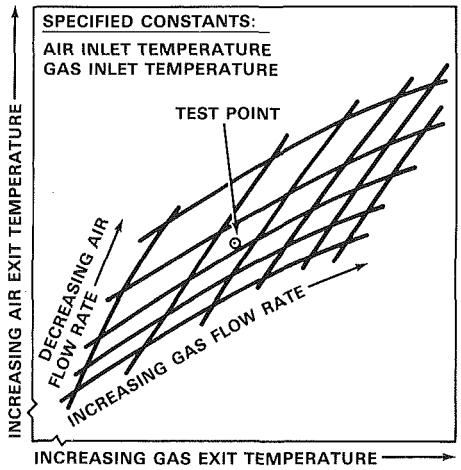

Fig. 10 Typical recuperator performance map for establishing test conditions

reduced. It will be shown that once the dependency on power level is included, the data scatter improves.

When the soot sample is heated in the TGA equipment with an air purge, it exhibits the typical burn-up above 600°C (1110°F). Above 750°C (1380°F) there is a small but finite amount of residue which may consist of sulfur compounds formed during combustion or other contaminants from the filter paper, fuel, and lubricating oil. Between 200 and 300°C (390–570°F) there is a small but finite loss in weight of the sample which corresponds with the temperature range where fouling on the recuperator is observed. Thus the weight loss or volatilization of the sample is associated with condensation of hydrocarbons, which is speculated to contribute to the fouling phenomenon. Above 300°C (570°F) there is an additional small loss of weight which may be associated with the beginning of carbon particle burn-up. The temperature range over which the weight loss takes place exhibits very little scatter. The temperature at which the weight loss starts is 222°C (432°F) [one sigma = 9.1°C (48°F)] and the end point is 304°C (579°F) [one sigma = 17.8°C (64°F)]. On the other hand, the weight loss data scatter significantly. When the weight loss data are plotted against corrected power (Fig. 8), it appears that there is dependency on power. To be absolutely certain of this dependency on power, some additional data at the lower power levels are required.

Limited particulate samples were also collected at temperatures other than 150°C (300°F). Figure 9 plots these data against collection temperature. As expected the weight loss decreases with increasing collection temperatures; less hydrocarbon is adsorbed by the carbon particles or condenses on the filter at higher collection temperatures. The temperature range over which the weight loss occurs moves up with increasing collection temperature. At the highest collection temperature, 235°C (450°F), neither the weight loss nor the end point of weight loss could be determined. It appears that the weight loss (the volatile fraction) is too small to be determined with the present approach. It should be noted that similar particulate sampling and TGA were performed on the exhaust of a diesel engine. The volatile fraction was on the order of 20 percent. These data are consistent with extensive diesel exhaust sampling performed by MacDonald [10].

In summary, the TGA is a relatively simple method for analyzing the small soot samples which are obtained from the filter element. The volatile fraction obtained with this method appears to be reasonable, but additional information is needed to assure correct interpretation of the data and improve the accuracy. Using a flame ionization detector in conjunction with the TGA will assure that only hydrocarbons will be included in the volatile fraction. It may also make it possible to improve the data scatter. Gas chromatography to obtain the boiling point curve of the volatile components is also being investigated.

Fouling Tests

As mentioned earlier, the heat exchanger operating conditions for these tests are chosen so that the small test recuperator's gas-side exit conditions, i.e., gas temperature, metal temperature, and Reynolds number, duplicate as closely as possible the predicted exit conditions in the full-size recuperator of an ICR marine gas turbine operating at a given power level. The operating point of the recuperator in the test rig is set with the aid of a heat exchanger performance map, an example of which is shown in Fig. 10. The map is produced using a computer program that simulates the performance of the HX-1 recuperator. This program is used in pretest analysis to determine the inlet air and gas temperatures and air massflow along with the resultant exit temperatures needed to duplicate full-size recuperator exit conditions in the end of the counterflow section of the test recuperator. This establishes a set of six parameters (2 massflows and 4 temperatures) that define the test point. To generate the performance map, the computer program was run with the inlet air and gas temperatures fixed at the desired value while the massflows were varied.

When running a test, the inlet air and exhaust gas temperatures are set to the predetermined values. Then the air control dampers and gas louvers are used to adjust the

Table 3 Average test conditions

Test	Air-flow, kg/s (lb/s)	Inlet air temperature, °C (°F)	Gas-flow, kg/s (lb/s)	Inlet gas temperature, °C (°F)	Wall temperature core in, °C (°F)	Wall temperature core out °C (°F)
D2-1 8 hr	0.33 (0.73)	147 (297)	0.29 (0.65)	361 (682)	301 (573)	217 (423)
D2-2 8 hr	0.33 (0.73)	146 (294)	0.32 (0.71)	357 (674)	303 (578)	222 (432)
D1-2 8 hr	0.21 (0.47)	118 (245)	0.15 (0.32)	309 (588)	237 (459)	144 (292)
D1-3 8 hr	0.21 (0.47)	118 (245)	0.15 (0.32)	308 (587)	241 (466)	152 (305)

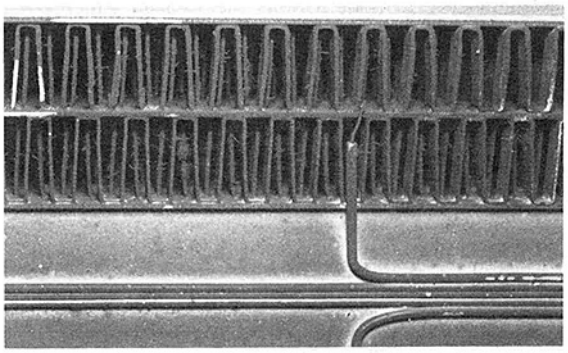

Fig. 11 Typical fouling deposits at recuperator gas inlet

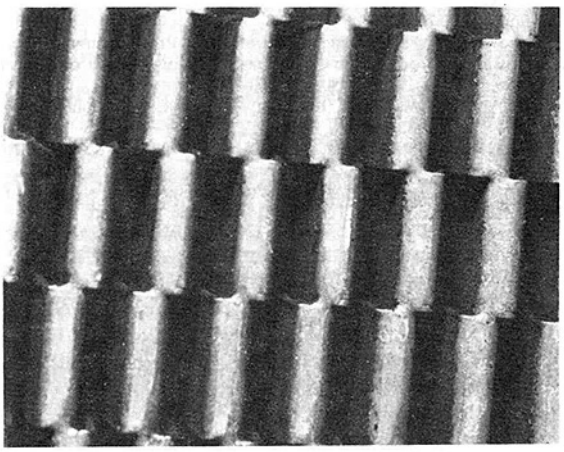

Fig. 12 Typical fouling deposits on interior gas fin surfaces

massflow rates, using the performance map as a guide, until the predicted air and gas exit temperatures are achieved. This procedure allows the correct air and gas massflow rates to be set without actual measurements since there is only one unique combination of air and gas flow that will result in the correct exit temperatures if the inlet temperatures are fixed.

It was originally intended to measure the air and gas massflow rates through the recuperator, but the low flowrates [0.15–0.30 kg/s (0.33–0.67 lb/s)] necessary to duplicate full-size operating conditions in the small test module have made accurate measurements difficult. Several attempts were made to obtain measurements with differential pressure and heat transfer type massflow instrumentation but these were unsuccessful. The low velocities associated with these flowrates produce differential pressures on the order of 0.0005 kg/cm (0.007 psi). When using the heat transfer type instrumentation, problems were encountered with response time and temperature compensation.

The results from four fouling tests using HX-1 are presented

Table 4 Summary of fouling thickness and related parameters

Test	D2-1	D1-2
Wall temperature, °C (°F)	188–238 (370–460)	138–157 (280–315)
Gas temperature, °C (°F)	250–277 (480–530)	171–185 (340–365)
ΔT, °C (°F)	24–38 (75–100)	4–15 (40–60)
Velocity, m/s (ft/s)	10.6 (34.8)	5.0 (16.3)
Fouling thickness, mm (in.)	0.05–0.10 (0.002–0.004)	0.08–0.20 (0.003–0.008)
SAE smoke No.	39	35

in this paper as typical examples. The tests were each 8 hr in duration and can be grouped into two pairs of tests. In each pair the second test is a repeat of the first but with a 10 min "cleaning" performed at the end of the test run. The cleaning technique consists of shutting off the air supply to the test recuperator and then bringing the gas turbine up to full power, allowing the high temperature [400°C (750°F)] exhaust gas to volatilize any condensed hydrocarbon fraction which holds the particulate matter to the recuperator walls, and essentially "bake off" the accumulated fouling deposits. Table 3 is a summary of the average recuperator operating conditions for each test. The D2 tests are representative of the recuperator conditions expected in an ICR marine gas turbine operating at 50 percent power, while the D1 tests with lower temperatures and flowrates simulate 10 percent power operation.

The thickness of the fouling deposits at various locations along the inlet and exit of the counterflow section was estimated using an optical microscope. The post-test inspections of the internal fin surfaces indicated a pattern of temperature-dependent fouling along with deposition on the leading edges of nearly all the offset fins. Figure 11 shows typical fouling buildup at the gas side inlet to the test recuperator, while Fig. 12 illustrates fouling deposits on interior gas fin surfaces and the accumulation of fouling on the leading edges of the offset fins. Preliminary analysis of the effect of the fouling deposits on the performance of the recuperator indicates a drop in effectiveness equal to 3 percent of the starting value over the 8-hr tests and a reduction in the exhaust gas massflow through the recuperator due to the increased pressure drop amounting to 6 and 11 percent of the initial values, respectively, for the simulated 10 and 50 percent power cases. Table 4 summarizes the results of the fouling thickness measurements and some associated parameters. The ranges of values listed in Table 4 encompass the measurements taken at four different points along the interface of the counterflow and the header sections at the gas exit end of the test recuperator. The conditions at each of the four points were different due to the variation of the flowpath lengths in

the air inlet header. This difference in lengths results in the air in the longer flowpaths being heated to higher temperatures before entering the counterflow section of the recuperator. Thus the capacity of the incoming air to cool the exhaust gas varies depending on the flowpath taken.

Inspections of the recuperator following the tests that included "cleaning" (D2-2 and D1-3) revealed a reduced amount of fouling deposition with fouling film thicknesses ranging from trace quantities to 0.02 mm (0.001 in.). These data are encouraging as they indicate a reduction in the fouling film thickness of approximately 90 percent as a result of this simple cleaning technique.

Concluding Remarks

The fuel used in these fouling tests is typical of fuel being used today aboard gas-turbine-powered combatants, while future fuels are likely to have a higher aromatic content and produce more soot in a given combustor. Although fouling tests using a blended DFM-aromatic hydrocarbon mixture are feasible, they may not be necessary because the particulate emission rate experienced is already much higher than today's marine propulsion gas turbines.

Unfortunately, direct measurements of particulate emission rates from modern gas turbines are not readily available, but can be roughly estimated from limited smoke number data. A particulate concentration of 15 mg/m^3 measured during the fouling tests is comparatively high. If fouling of recuperators in future marine engines is to be fully understood, a better knowledge of particulate emission rates and their relationship with fuel quality and combustor design is needed.

The fraction of condensible hydrocarbons in the soot from the gas turbine is believed to be a significant factor in the fouling mechanisms. Analysis of soot samples from the engine utilized in these tests has demonstrated a distinct trend in the volatility of the condensible hydrocarbons, as well as the relative amount of condensible hydrocarbons in the soot. Unfortunately, little is known yet about the composition of the hydrocarbon fraction or how these characteristics of soot may vary from one engine to another. A greater variety of soot samples needs to be collected and analyzed using more sensitive and accurate measuring techniques.

The anticipated effect of recuperator fouling is of course a loss in performance. The fouling tests conducted thus far have shown that sufficient fouling does accumulate during an 8-hr test to cause a slight decrease in relative recuperator effectiveness ($E/E^* = 0.97$). An increase in pressure drop due to the fouling was apparent also.

Understanding the fouling mechanism is a worthwhile goal; however, a practical means of removing fouling deposits when performance degradation reaches an unacceptable level is ultimately required. Based on a limited number of tests conducted thus far, a cleaning technique which involves bypassing flow on the recuperator air side appears to be a very effective method for removing the fouling deposits. This seems to confirm the belief that condensible hydrocarbons play a significant role in the fouling deposition process.

The results presented here are from initial tests. Other tests are planned during 1987 and 1988 using different plate-fin and primary surface recuperator matrices. It would be premature to define a model of the fouling mechanism which correlates with the various operating parameters given the limited amount of data currently in hand. However, such an effort is being undertaken as an integral part of this investigation.

References

1 Bowen, T. L., and Groghan, D. A., "Advanced-Cycle Gas Turbines for Naval Ship Propulsion," *Naval Engineering Journal*, Vol. 96, No. 3, May 1984, pp. 262–271.

2 Bowen, T. L., and Ness, J. C., "Regenerated Marine Gas Turbines, Part I: Cycle Selection and Performance Estimation," ASME Paper No. 82-GT-306, Apr. 1982.

3 Miller, J. A., "Mechanisms of Gas Turbine Regenerator Fouling," ASME Paper No. 67-GT-26, Mar. 1967.

4 Blazowski, W. S., "Dependence of Soot Production on Fuel Structure in Backmixed Combustion," *Combustion Science and Technology*, Vol. 21, 1980, pp. 87–96.

5 Blazowski, W. S., "Dependence of Soot Production on Fuel Blend Characteristics and Combustion Conditions," ASME JOURNAL OF ENGINEERING FOR POWER, Vol. 102, Apr. 1980, pp. 403–408.

6 Lefebvre, A. W., *Gas Turbine Combustion*, Hemisphere Publishing Corp., New York, 1983, p. 350.

7 Military Specification MIL-F-16884H, "Fuel, Naval Distillate (NATO-F-76)."

8 Burnett, M. W., et al., "Worldwide Characterization of Marine Fuels," *Marine Fuels*, ASTM Special Technical Publication 876, Dec. 1983.

9 "Aircraft Gas Turbine Engine Exhaust Smoke Measurement," SAE Aerospace Recommended Practice (ARP) 1179A, June 15, 1980.

10 MacDonald, J. S., et al., "Experimental Measurements of the Independent Effects of Dilution Ratio and Filter Temperature on Diesel Particulate Sampling," SAE Paper No. 800185, 1980.

J. B. Burnham
Chief Controls Engineer,
Energy Services, Inc.,
Farmington, CT

M. H. Giuliani
Manager, LM5000 Program,
General Electric Company,
Cincinnati, OH

D. J. Moeller
V.P., Engineering,
Simpson Paper Co.,
Anderson, CA

Development, Installation, and Operating Results of a Steam Injection System (STIG™) in a General Electric LM5000 Gas Generator

This paper describes the first full-scale field test of a steam injection system for a natural-gas-fired G.E. LM5000 gas generator for the purpose of: (a) decreased exhaust emissions, (b) increased power output, and (c) improved efficiency. It discusses the steam supply system, engine features, test results, and plant economics for steam injection into the combustor and compressor discharge sections of the LM5000 at rates up to 65,000 lb/hr (29,510 kg/hr).

Introduction

An LM5000 steam injection gas generator (STIG™) system was successfully tested at a cogeneration plant of Simpson Paper Company in August 1985. This test was the result of a cooperative effort among five companies: Pacific Gas & Electric Company (PG&E), Simpson Paper Company, Ishikawajima-Harima Heavy Industries (IHI), Energy Services Incorporated, and General Electric Company. Initially, PG&E identified a need in their system for a 50-MW, steam-injected power plant, then acted as the catalyst for beginning the design work. Later, PG&E facilitated contract negotiations for the demonstration installation. Simpson Paper Company, the owner and operator of the IM5000 gas turbine system, recognized that their variable seasonal steam demand was ideally suited for a STIG™ system and became an aggressive and cooperative partner. IHI, who supplied the IM5000 power generating package incorporating the LM5000 gas generator, was an active participant. Energy Services Inc. designed the off-engine hardware and control system installed by Simpson Paper Company, and the General Electric Company designed and incorporated the necessary engine features for steam injection.

Initial study work directed at estimating the performance characteristics of a standard LM5000 and a modified LM5000 with steam injection was begun in September of 1983. Results of this study indicated that a 50-MW power plant with a thermal efficiency of 43 percent would result if both high pressure [600 psig (4140 kPa)] and low pressure [200 psig (1380 kPa)] steam could be injected and if the high-pressure turbine flow function, i.e., the effective flow area, were increased 6.4 percent. Hardware design activity for this configuration began in late 1984 and the first production engines incorporating these features will be available in late 1986.

The demonstration site for this project was the cogeneration plant at the Shasta Mill of Simpson Paper Company, located at Anderson/Redding in northern California. This plant has been in operation since May 1983, and is described in a previous ASME paper [1]. The plant was base load rated at 33,000 kW of electrical power and 110,000 lb/hr (49,940 kg/hr) of process steam from a three-pressure waste heat boiler. With supplementary duct firing, the boiler is capable of 220,000 lb/hr (99,880 kg/hr) of combined steam flow.

The steam injection system tested at Simpson Paper Company incorporated only the high-pressure steam injection features without an increase in the high-pressure turbine flow function. It is essentially a standard LM5000 with steam injection provisions.

Final project authorization for the installation at the Shasta Mill of Simpson Paper Company was received in March of 1985. Off-engine piping fabrication began in late May, and the basic installation was completed in early July. Initial testing with steam injection began on July 14.

This paper presents a description of the on-engine and off-engine equipment, the test results including both emissions and performance characteristics, and the economic considerations which led Simpson Paper Company to proceed with the installation.

Off-Engine System Description

For this steam injection project, a steam delivery system was designed to provide up to 65,000 lb/hr (29,510 kg/hr) of high-pressure [600 psig (4140 kPa), nominal] superheated [600°F (316°C)] steam from the existing waste heat boiler (WHB) to

Contributed by the Gas Turbine Division of THE AMERICAN SOCIETY OF MECHANICAL ENGINEERS and presented at the 31st International Gas Turbine Conference and Exhibit, Düsseldorf, Federal Republic of Germany, June 8–12, 1986. Manuscript received at ASME Headquarters February 14, 1986. Paper No. 86-GT-231.

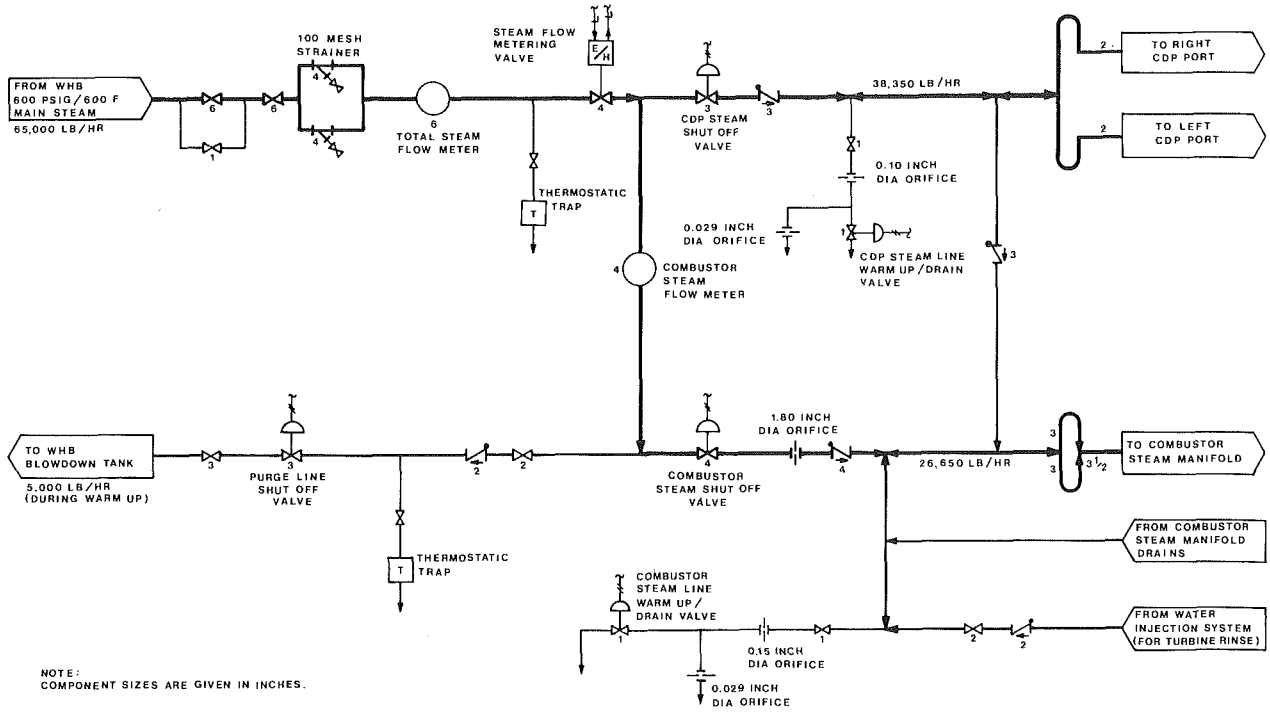

Fig. 1 Steam injection delivery system schematic

the modified LM5000. The steam delivery system is shown schematically in Fig. 1.

The piping for the steam injection delivery system was designed and constructed according to the ANSI B31.1 Piping Code with welding procedures following Section IX of the ASME Boiler and Pressure Vessel Code. Maximum design conditions are 750 psig (5175 kPa) and 1000°F (538°C), although these do not occur simultaneously in the same section.

The system consists of a 6 in. (152 mm) carbon steel steam supply line from the waste heat boiler to duplex steam strainers with 100 mesh elements. Beyond the strainers, the piping is mainly fabricated from A-312 type 316 stainless steel to maintain cleanliness in the system.

Special design considerations were given to the following: prevention of water induction into the gas turbine proper; control of the piping movements due to large thermal expansion of the piping and high steam velocities after the metering valve; meeting the requirement of low allowable reactions at the flanged turbine connections, while providing adequate piping flexibility for thermal expansion as well as appreciable movement of the turbine connections from cold to hot operation; and providing purge air flow to the combustor steam manifold under conditions of no steam flow.

Prevention of Water Induction. Steam is taken from the waste heat boiler downstream of the superheater. The risk of accidental water ingestion by the gas turbine in case of a failure in the mill steam header temperature control system determined the location of this tap upstream of the desuperheater. A drain connection with a high-pressure thermostatic steam trap is provided upstream of the metering valve for warmup of the long 6 in. (152 mm) steam supply line.

The piping downstream of the metering valve splits into a 4 in. (102 mm) header supplying the combustors and a 3 in. (76 mm) header supplying the high-pressure compressor discharge ports (CDP). Each header is provided with an automatic shutoff valve and a check valve. The piping between the metering valve and the shutoff valves has a 2 in. (51 mm) purge line connection at its low point with an automatic shutoff valve discharging into an atmospheric blowdown tank. Upstream of this purge line shutoff valve, a high-pressure thermostatic steam trap discharges to the floor sump.

Immediately downstream of each steam line shutoff valve and check valve, additional drain connections are provided with automatic valves discharging to the floor sump. These valves are used to preheat the supply lines to the turbine to at least 50°F (10°C) above the saturation temperature of the injection steam before it is admitted to the turbine. This is accomplished by bleeding hot air [up to 1000°F (538°C)] from the high-pressure compressor discharge to atmosphere through appropriately sized orifices. When steam is flowing to the engine, a 0.029 in. (0.74 mm) diameter orifice in parallel with each automatic drain valve will pass sufficient steam to prevent condensation in these drain lines.

Control of Piping Movements. Three-way limit stops rather than anchors are used near the steam strainers and the metering valve to preserve flexibility while limiting pipe stress and undue pipe movements during transient conditions. The only anchors in the system are on the roof of the engine enclosure. This location is as close as feasible to the flanges where the steam injection delivery system connects to the gas turbine casing. The anchors are the dividing line between 316SS schedule 40 and 321SS schedule 10 piping.

Control of Flange Reaction Forces. The piping between the anchors and the gas turbine connections is schedule 10 to keep end reactions to a minimum. Type 321 stainless steel was used to minimize intergranular carbide precipitation. Bending stresses are highest in this section of piping. A cold spring of about 80 percent was used here to meet the low allowable reactions at the gas turbine connections at operating conditions. The anchors are bolted to the very rigid top of the enclosure with provision for adjustment to allow for material creep.

Purge Air Flow. To provide purge air flow, a 3 in. (76 mm) crossover pipe with check valve is installed between the CDP steam line and the combustor steam line just upstream of the anchor points on the roof of the gas turbine enclosure. This ensures a flow of more than 1.5 lb/s (0.7 kg/s) of high-pressure compressor discharge air into the combustor steam

manifold during any period when the gas turbine is operating without steam injection. The air which preheats the 4 in. (102 mm) combustor steam line during startup also flows through this crossover pipe.

Turbine Water Wash. Provision was made to permit rinsing the engine turbine section, following a detergent wash of the engine compressors, by injecting demineralized water from the existing NO_x water system. Gravity drain lines from the combustor steam manifold low points ensure that no water remains at the steam injection nozzles when the gas turbine is started following a water wash.

Control System. Components of the control system include: two industrial programmable logic controllers (PLC), an electrohydraulic actuator operating a steam flow metering valve, five pneumatically operated shutoff and warmup/drain valves, a vortex-shedder type total steam flow meter, and pressure and temperature sensors. One PLC, with 64 total discrete (ON/OFF) inputs and outputs (I/O), functions as a sequencer. This PLC controls the shutoff and warmup/drain valves, automatically enables steam flow control when prerequisite conditions are satisfied, and protects the gas turbine by shutting down steam injection when safe limits are exceeded. The other PLC, with 4 analog inputs, 1 analog output, and 32 discrete I/O, functions as a governor operating closed loop on total steam flow. When enabled, it maintains total steam flow to the LM5000 within a deadband [±200 lb/hr (91 kg/hr)] of a setpoint which is adjustable between maximum and minimum adjustable flow limits. The maximum steam flow is a straight line function of compressor discharge pressure (PS3) which limits combustor steam-to-fuel weight ratio to less than 1.8:1. The minimum flow limit is a constant value, initially 12,000 lb/hr (5448 kg/hr), which ensures acceptable NO_x emissions at maximum gas turbine output. The total steam flow setpoint is raised and lowered, either automatically based on 600 psig (4140 kPa) steam header pressure (i.e., the availability of excess steam from the waste heat boiler), or manually by the cogeneration plant operator.

A flowmeter measuring steam flow to the combustors only was included for engineering purposes to determine the exact split of total steam flow into CDP steam flow and combustor steam flow. The desired split (41 percent combustor; 59 percent CDP) is based on emissions data.

Operation

Startup Sequence. During any gas turbine shutdown, the warmup/drain valves are maintained open to allow for condensate drainage. The metering valve and the combustor and CDP steam line shutoff valves are closed. After a gas turbine start is initiated, high compressor discharge air flows through the CDP drain line orifice [0.10 in. (2.5 mm) diameter] and the combustor drain line orifice [0.15 in. (3.8 mm) diameter] to atmosphere for warmup of the CDP and combustor steam lines, respectively. When gas turbine compressor discharge pressure, PS3, reaches 269 psig (1856 kPa), at about 18 MW, the purge line shutoff valve is opened and the metering valve is moved to a fixed position (10 percent open) to begin warmup of the main 6 in. (152 mm) steam supply line.

When the temperature and pressure at the total steam flowmeter, just upstream of the metering valve, have reached 540°F (282°C) and 540 psig (3726 kPa), typically at the same time that the WHB begins to supply steam to the mill, the injection steam supply line is sufficiently superheated to permit safe steam injection. When the CDP and combustor pipe temperature sensors, located just downstream of the shutoff valves, have also reached 500°F (260°C), typically within 15 min after the gas turbine is at full load, gas turbine steam injection is permitted.

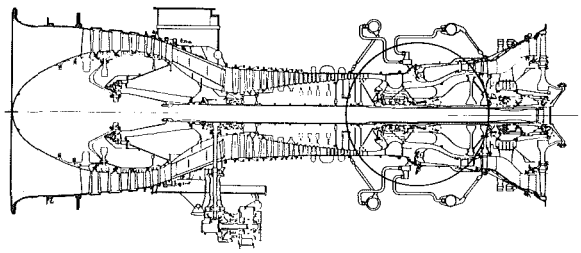

Fig. 2 LM5000 gas generator

At this time, the purge line shutoff valve will close, the combustor steam line warmup/drain valve will close, the combustor steam shutoff valve will open, and the steam injection governor will be enabled to control steam flow to the gas turbine combustor nozzles at the minimum flow rate.

In the automatic control mode, the steam injection flow rate setpoint will increase at a programmed rate, presently 2500 lb/hr/min (1135 kg/hr/min), whenever the mill header pressure exceeds 600 psig (4140 kPa).

When the total steam injection flow reaches 28,000 lb/hr (12,712 kg/hr), the CDP steam line warmup/drain valve will close, the CDP steam shutoff valve will open, and steam flow to the CDP ports will begin. The total steam flow will now split: 41 percent combustor; 59 percent CDP.

If mill conditions permit, the flow rate setpoint will continue to increase until a maximum steam flow limit is reached. This limit is presently 65,567 lb/hr (29,767 kg/hr) of total steam flow at a PS3 value of 390 psig (2691 kPa).

As mill steam demand increases, the steam injection flow rate setpoint will decrease automatically. When total steam flow decreases to 27,000 lb/hr (12,258 kg/hr), the CDP steam shutoff valve will close and the CDP steam line warmup/drain valve will open to maintain the CDP steam line well above superheated steam temperature.

If steam temperature or pressure at the total steam flowmeter falls below 535°F (279°C) or 535 psig (3691 kPa), or if the gas turbine compressor discharge pressure falls below 261 psig (1801 kPa), the steam injection system will be shut down automatically.

On-Engine Description

Gas Generator. The LM5000 gas generator (Fig. 2) is a dual spool design. The low-pressure spool consists of a five-stage compressor (LPC) driven by a single-stage turbine (LPT). At base-rated condition the LPC pressure ratio is 2.5:1, the airflow is 270 lb/s (123 kg/s) and the rotor speed is 3575 rpm. The high-pressure spool consists of a 14-stage compressor (HPC) and a two-stage air-cooled high-pressure turbine (HPT). At base-rated condition, the high-pressure spool has an HPC pressure ratio of 12:1, an HPC discharge temperature of 972°F (522°C), an HPT inlet temperature of 2112°F (1155°C), and a rotor speed of 10,075 rpm. The combustor is annular with 30 fuel nozzles. ISO-rated performance when coupled to the IHI three-stage power turbine, with water injection for NO_x control, after three years of operation at the Shasta Mill, is approximately 33 MW with an average thermal efficiency of 36 percent.

STIG™ Modification. Modifications for the Simpson Paper Company STIG™ configuration are highlighted in Figs. 3 and 4. These consist of adding steam delivery systems for injecting steam into the primary combustion zone of the combustor and into the flow annulus formed by the combustor inner skirt and the inner combustion casing. A baffle is also added to the combustor rear frame to assure good distribution of steam flow in this inner annulus. Steam is injected into the primary combustion zone via fuel nozzles of concentric tube design. The inner delivery passage supplies

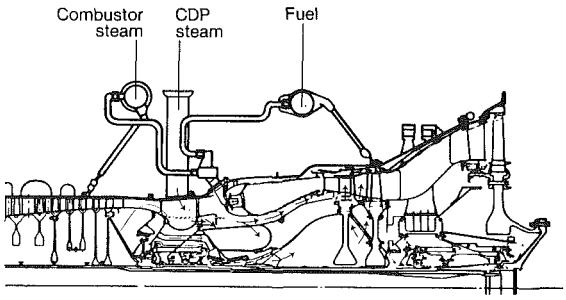

Fig. 3 LM5000 modifications for steam injection

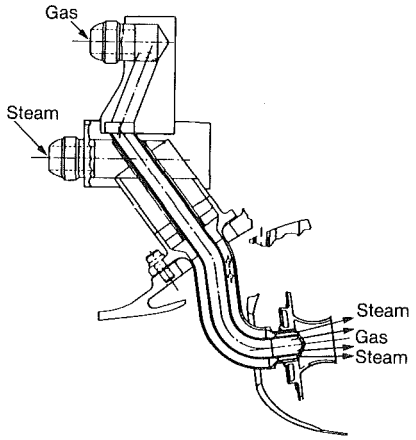

Fig. 4 LM5000 gas/steam fuel nozzle design

fuel while the outer annulus supplies steam to the primary combustion zone. This combustor dome steam is effective in suppression of NO_x emission as well as in providing power augmentation. The steam injected into the annulus between the combustor inner skirt and inner combustion casing mixes with the high pressure turbine cooling air improving its effectiveness. This steam re-enters the primary stream via the turbine cooling circuit and combustion liner dilution holes.

Performance Testing and Results

Performance testing was directed at two primary objectives:

1 test demonstration of the effect of steam on engine power and heat rate;

2 measurement of emissions.

Testing began with steam injection into the annulus between the combustor inner casing and the combustor inner skirt (Compressor Discharge Pressure steam, called CDP steam). This was followed by testing with combustor steam injection and lastly by testing with various mixtures of CDP and combustor steam.

Output Power Enhancement. Gas turbine performance data were taken at full load on LP turbine inlet temperature (T_{44}) control with zero steam flow. When normalized to 66°F (19°C) inlet temperature, sea level pressure, and 1335°F (724°C) T_{44} control temperature, the base value of output power, is 29.9 MW. The highest output power observed was 40.0 MW with 65,200 lb/hr (29,601 kg/hr) of total steam flow. When normalized to the same conditions as the base value of output power, the maximum output power is 41.9 MW. This is a 40.1 percent increase in output power.

Gas turbine output with steam injection at constant firing temperature [$T_{44} = 1335$°F (724°C)] is shown in Fig. 5. In order to evaluate the merits of steam injection for power augmentation at the Shasta Mill, Fig. 5 also shows the total projected cogeneration plant output if the excess waste heat steam available for injection, up to 60,000 lb/hr (27,240 kg/hr), were supplied instead to a typical 5000 kW condensing steam turbine. For direct comparison with the steam turbine, which requires no additional fuel, the gas turbine output with steam injection at constant fuel flow [283×10^6 Btu/hr (299×10^6 kJ/hr)] is also shown.

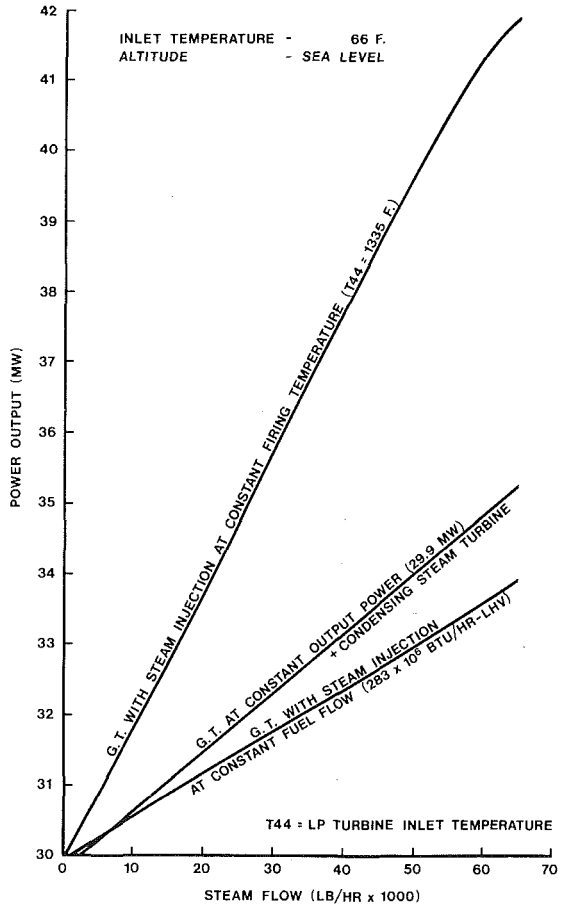

Fig. 5 Gas turbine generator output with steam injection

It is not likely that an actual gas turbine cogeneration plant with varying steam load on the WHB would be able to operate throughout the year at maximum gas turbine firing temperature and maximum steam injection flow. During periods with cold ambient temperatures, when gas turbine operation without steam injection is at or near the engine mechanical limits, or when the electric generator is at or near maximum output, any steam available for injection would primarily have the effect of improving heat rate rather than power augmentation.

Heat Rate Improvement. The IM5000 gas turbine demonstrated a thermal efficiency of 36.0 percent, i.e., a heat rate of 9478 Btu/kWh-lhv (9999 kJ/kWh), at 29.9 MW with no steam flow. With combined CDP and combustor steam flow of 65,200 lb/hr (29,601 kg/hr), the thermal efficiency was 41.8 percent, i.e., a heat rate of 8175 Btu/kWh-lhv (8624 kJ/kWh), at 41.9 MW. This is a 13.8 percent improvement in heat rate.

The demonstrated improvement in heat rate is presented in Fig. 6. The improvement at constant output power reflects the impact of the steam addition while maintaining 29.9 MW. The improvement at the T_{44} control temperature limit represents the effect of steam addition as well as the increased thermal efficiency due to operating at the higher power levels. For comparison, the heat rate improvement with steam injection at constant fuel flow [283×10^6 Btu/hr (299×10^6 kJ/hr)] is also shown in Fig. 6.

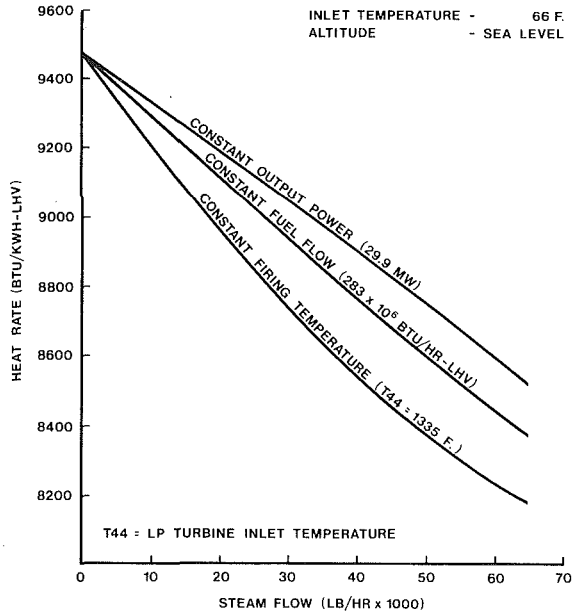

Fig. 6 Gas turbine thermal efficiency with steam injection

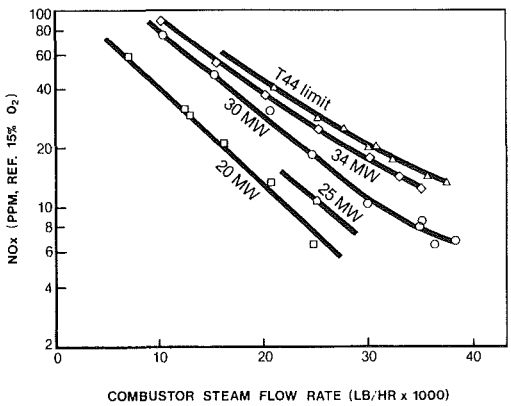

Fig. 7 Effect of steam injection on NO_x emissions

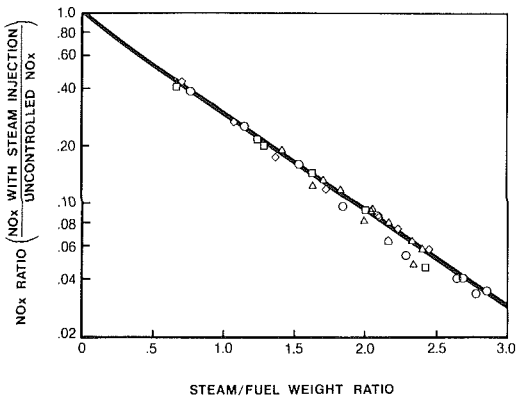

Fig. 8 NO_x reduction ratio with steam injection

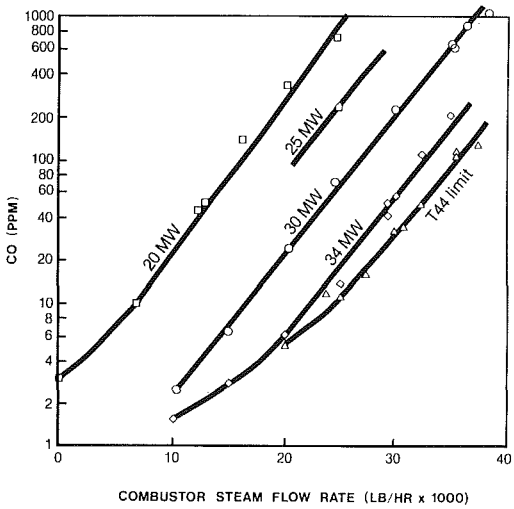

Fig. 9 Effect of steam injection on CO emissions

Emissions. Emissions were measured using a probe inserted into an existing sampling post near the top of the WHB exhaust stack. The continuously flowing sample extracted from the stack was analyzed for carbon monoxide (CO), carbon dioxide (CO_2), total hydrocarbons (HC), oxides of nitrogen (NO_x), and oxygen (O_2). Emissions were measured at several power levels and over a range of steam flow rates. A total of 35 test points were obtained with only combustor dome steam injection. For all steam injection tests reported here, the evaporative cooler on the engine inlet was operational, resulting in inlet temperatures in the range 60–65°F (15–18°C) and a relative humidity of 90–95 percent.

Figure 7 shows the variation in NO_x with combustor steam flow at various power levels. The NO_x is expressed as parts per million (ppm) by volume, dry, referenced to 15 percent O_2, and the units of combustor steam flow are "lb/hr." The NO_x is plotted on a logarithmic scale because its variation is approximately exponential with steam flow. This permits accurate display of the NO_x quantity down to the lowest values measured. The data were taken at constant electric generator output in MW except for the highest power level, at which the data were taken at the maximum low pressure turbine inlet temperature. At this T_{44} limit condition, power output ranges from 34 MW to 37 MW, increasing with increasing combustor steam injection.

Note in Fig. 7 that excellent suppression of NO_x emissions with combustor steam injection occurs even to the maximum injection rate investigated here, which was about 37,000 lb/hr (16,798 kg/hr). This is equivalent to a combustor steam-to-fuel weight ratio of about 2.8:1 at the 30 MW power level. The lowest NO_x values measured were less than 7 ppm at 20 MW and 30 MW. At the maximum power and highest steam flow condition, the measured NO_x was 13.2 ppm at 37 MW and 37,000 lb/hr (16,798 kg/hr) combustor steam flow.

In Fig. 8, the NO_x reduction ratio (NO_x with steam injection divided by uncontrolled NO_x) is plotted against steam-to-fuel weight ratio. As has been previously determined for the LM5000 engine, the NO_x reduction ratio is very nearly an exponential function of steam-to-fuel weight ratio, independent of power level, at least at these higher power levels. This curve is quite useful in predicting NO_x levels for conditions other than those for which these tests were run. It should be noted that the uncontrolled NO_x level is defined as the NO_x that would be measured at the same combustor conditions (temperature, pressure, fuel/air ratio) but with no steam injection. These "dry NO_x" levels are obtained from an analysis of previous test data obtained at the Simpson Paper Company installation. The NO_x reduction curve of Fig. 8 is in excellent agreement with LM5000 combustor component test data which have been previously reported [2].

In contrast to NO_x, CO levels tend to increase rapidly with increasing combustor steam injection rates, as shown in Fig. 9. In this figure, CO in ppm by volume, dry, is very low (several ppm) for zero steam injection but, beyond the "knee" in the curve, increases exponentially with combustor steam injection. As in the NO_x data, these are data points with no CDP

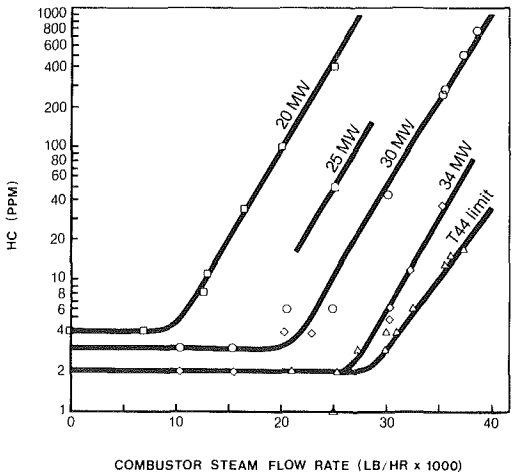

Fig. 10 Effect of steam injection on HC emissions

steam injection. For points with the lowest NO_x, at 20 MW and 30 MW, CO levels between 700 and 1100 ppm were obtained.

The variation of HC emissions is similar to the CO but at a somewhat lower level. Figure 10 shows HC as equivalent carbon in ppm by volume (dry sample) plotted against combustor steam injection rate. The HC level is a few ppm with zero steam injection, but increases exponentially beyond the knee in the curve. The highest HC value measured was 760 ppm.

From these emission measurements we conclude that:

1 For the LM5000 gas turbine engine firing natural gas fuel, NO_x can be suppressed with combustor steam injection to levels below 25 ppm NO_x (ref. 15 percent O_2). At the highest power level (37 MW), and a combustor steam injection rate of 37,300 lb/hr (16,934 kg/hr), a NO_x level of 13.2 ppm (ref. 15 percent O_2) was measured.

2 Very low CO levels (less than 2 ppm) can be obtained at the highest power levels and with no steam injection. However, CO increases exponentially with steam injection rate at fixed power output. At the highest power level (37 MW), and a combustor steam injection rate of 37,300 lb/hr (16,934 kg/hr), a CO level of 130 ppm was measured.

3 As a result of the opposite trends of CO and NO_x with steam injection rates, very low values of CO and NO_x cannot be simultaneously obtained. However, the level of CO and NO_x that can be simultaneously obtained decreases with increasing power level. At the highest power level (37 MW) with 29,000 lb/hr (13,166 kg/hr) of combustor steam injection, less than 25 ppm NO_x (ref. 15 percent O_2) and less than 25 ppm CO were measured, demonstrating that very acceptable levels of NO_x and CO are simultaneously achievable.

Economics

Capital Cost. The costs of equipment, material, and labor to add steam injection capability to the Shasta Mill cogeneration plant were in many respects unique, and would not reflect steam injection system costs for other installations. Shasta costs were increased because the project was a retrofit, developmental, and was executed on an expedited basis to take advantage of the "free" steam available during the summer months of 1985. On the other hand, project costs were not as high as they might have otherwise been because the electric generator, HV distribution system, plant cooling systems, boiler feedwater makeup demineralizer, and gas compressors had adequate margins to accommodate the increased power at the site summertime ambient temperatures, and because of the development contributions made by the sponsors of the project.

However, the estimated capital costs for production engine hardware and plant system costs to accommodate high-pressure steam injection for a new installation are approximately $1,000,000.

Operating Revenue. Waste heat from the gas turbine at the Shasta Mill had been vented to the atmosphere whenever mill steam demand was less than the available steam generating capacity of the waste heat boiler. Past operating experience shows that, due to decreased steam demand during the summer months, an average of 20,000 lb/hr (9080 kg/hr) of steam is available during five months of the year. In addition, when either one of the two paper machines is out of service for maintenance, about 1000 hr per year, an average of 45,000 lb/hr (20,430 kg/hr) of steam is also available. Thus, approximately 120×10^6 lb/yr (54×10^6 kg/yr) of free steam is available for steam injection.

If at least 1 MW is generated by each 6000 lb/hr (2724 kg/hr) of injected steam at maximum gas turbine firing temperature, as shown in Fig. 5, the potential exists for generating an additional 20,000 MWh/yr. At an electric revenue rate of $55/MWh, energy credit only, this represents a maximum annual gross revenue of $1,100,000. The average simple-cycle incremental heat rate for injected steam at maximum gas turbine firing temperature, derived from the data represented in Fig. 6, is approximately 5000 Btu/kWh-lhv (5275 kJ/kWh-lhv). At a gas fuel cost of $4.40/$10^6$ Btu-lhv ($4.17/$10^6$ kJ-lhv), the additional fuel required to produce 20,000 MWh would cost $440,000. However, because injection steam is supplied by the waste heat boiler, at least 20 percent of the additional fuel energy is recovered. The maximum annual net revenue, at constant T_{44} control temperature limit, is then $748,000.

As discussed above, free steam is likely to be available at times when the gas turbine generator is operating at or near its limits. At those times, injected steam has the effect of reducing fuel cost at constant output power. From the data represented in Fig. 6, we may calculate that 1 lb (0.45 kg) of injected steam at 30 MW is equivalent to 437 Btu-lhv (461 kJ-lhv) of displaced gas fuel. If all of the 120×10^6 lb/yr (54×10^6 kg/yr) of free steam were used only to improve heat rate, the minimum annual savings would be $230,000.

Actual revenue is expected to lie between these extremes. If only half of the free steam is used for power generation and half is used to lower fuel costs, the annual net revenue from steam injection, excluding any allowance for increased maintenance, would be $489,000.

During as much as 4000 hr per year, steam required for NO_x control at the Shasta Mill must be produced by supplementary duct firing. Analysis shows that the fuel cost to produce this steam is approximately offset by revenue from the additional power generated.

Conclusions

The testing accomplished at the Shasta Mill of Simpson Paper Company has demonstrated that steam injection in the LM5000 engine is a practical and effective way to achieve significant performance enhancement and NO_x reduction. Pretest predictions on performance, and emissions reduction were verified. With steam injection, output power of the IM5000 gas turbine increased from 29.9 MW to 41.9 MW and thermal efficiency increased from 36.0 percent to 41.8 percent. Ability to suppress NO_x emission to levels less than 25 ppm was demonstrated.

References

1 Moeller, D. J., and Kolp, D. A., "Simpson Paper Co.: First 35MW IM5000 in Cogeneration Plant," ASME Paper No. 84-GT-55, 1984.

2 Bahr, D. W., and Lyon, T. F., "NO_x Abatement Via Water Injection in Aircraft-Derivative Turbine Engines," ASME Paper No. 84-GT-103, 1984.

NDE Reliability and Process Control for Structural Ceramics

G. Y. Baaklini
NASA Lewis Research Center,
Cleveland, OH 44135

The reliability of microfocus x-radiography and scanning laser acoustic microscopy for detecting microvoids in silicon nitride and silicon carbide was statistically evaluated. Materials and process-related parameters that influenced the statistical findings in research samples are discussed. The use of conventional x-radiography in controlling and optimizing the processing and sintering of an Si_3N_4–SiO_2–Y_2O_3 composition designated NASA 6Y is described. Radiographic evaluation and guidance helped develop uniform high-density Si_3N_4 modulus-of-rupture bars with improved four-point flexural strength (857, 544, and 462 MPa at room temperature, 1200°C, and 1370°C, respectively) and reduced strength scatter.

Introduction

Advanced nondestructive evaluation (NDE) techniques to detect critical flaws reliably are needed if fracture mechanics principles are to be applied effectively in the design of ceramic heat engine components [1, 2]. These techniques are also needed to monitor and control the fabrication process in the materials development program to make stronger and more reliable ceramics [2]. Reliable ceramics require fabrication process control to reduce the incidence of various flaws and to ensure that any flaws that occur are noncritical. The dominant critical flaw type in monolithic ceramics is a pore [3–5], which can cause wide strength variations and unacceptably low strength. Recent studies at NASA Lewis Research Center [6, 7] have established the reliability of microfocus x-radiography and scanning laser acoustic microscopy for detecting seeded internal voids in Si_3N_4 and SiC test specimens. Preliminary radiographic characterization of sintered Si_3N_4 specimens [2] revealed the presence of high-density gradients (a high-density case with a low-density core structure), which were believed to be detrimental to strength properties. Therefore a program was undertaken at NASA Lewis [3] to incorporate conventional x-radiographic techniques in an extensive investigation of one Si_3N_4–SiO_2–Y_2O_3 composition in order to monitor its fabrication process.

This paper describes the materials and process-related factors that affected the reliability of microfocus x-radiography and scanning laser acoustic microscopy for detecting internal voids in Si_3N_4 and SiC. The capability of the conventional x-radiographic technique in guiding powder processing and sintering parameter changes to improve the bulk density of sintered Si_3N_4 and to eliminate detrimental density variations is emphasized. Improvements in flexural strengths and reductions in strength scatter are also described.

Materials and Procedures

The preparation of SiC and Si_3N_4 specimens needed for the NDE reliability determinations is shown in Fig. 1. The Si_3N_4 powder had the Si_3N_4–SiO_2–Y_2O_3 composition. The SiC powder contained sintering aids and binder materials of boron and carbonaceous resins. Styrene divinyl benzene microspheres of various sizes (50, 80, 115, 220, and 528 μm dia) were seeded in green specimens and later burned out to create voids within the green and sintered specimens. The seeded test bars had the same densities, compositions, and shapes as typical modulus-of-rupture (MOR) bars of the same materials. Details on specimen fabrication, void characterization, dimensions of specimens and voids, and density determination are given in [6]. Microfocus radiography and scanning laser acoustic microscopy were used to detect the seeded voids (20 to 477 μm in diameter) in the fabricated ceramic samples. References [6, 7] describe in detail the radiography and SLAM systems, respectively.

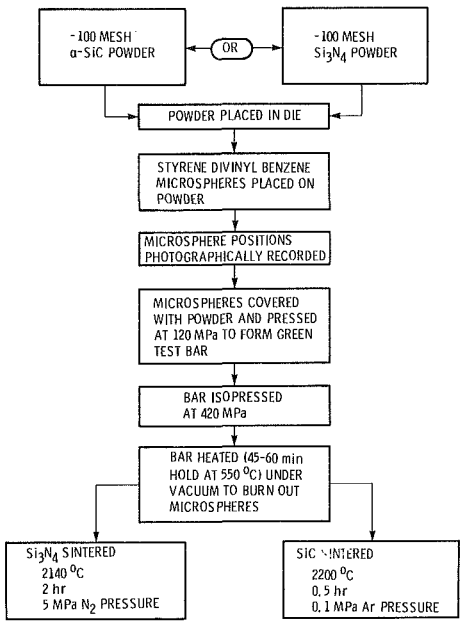

Fig. 1 Fabrication of silicon nitride and silicon carbide test specimens with seeded internal voids

Contributed by the Gas Turbine Division of THE AMERICAN SOCIETY OF MECHANICAL ENGINEERS and presented at the 32nd International Gas Turbine Conference and Exhibit, Anaheim, California, May 31–June 4, 1987. Manuscript received at ASME Headquarters January 30, 1987. Paper No. 87-GT-8.

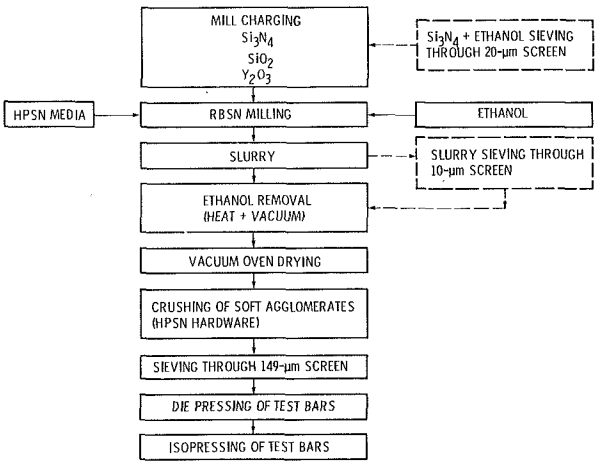

Fig. 2 Powder processing of Si_3N_4-SiO_2-Y_2O_3 composition NASA 6Y

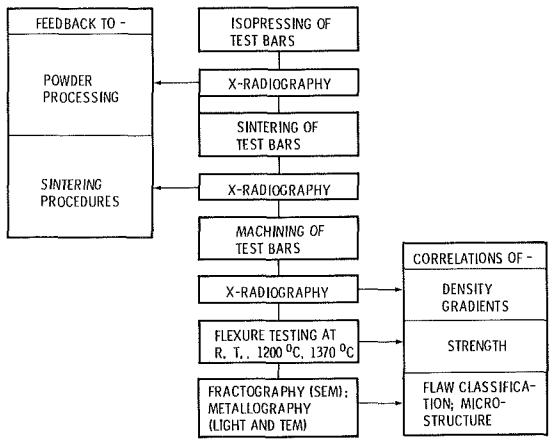

Fig. 3 Characterization, testing, and evaluation of NASA 6Y Si_3N_4

The powder-processing steps of the NASA 6Y Si_3N_4 composition, containing 6 wt percent each of Y_2O_3 and SiO_2, are shown in Fig. 2. Powders were milled (grinding time, t_g, 24, 100, or 300 hr), die pressed into bars at 21 MPa, and then isopressed at 414 MPa. A total of 690 bars (23 batches) were sintered 15 at a time at 2140°C in a tungsten cup. High-purity BN disks separated the bars from one another and from contact with the tungsten cup. Sintering times t_s were 1, 1.25, 1.5, and 2 hr. Nitrogen overpressures P_N of 2.5, 3.5, and 5.0 MPa were employed. All batches were radiographically evaluated at all stages of fabrication as described in Fig. 3. The conventional x-ray system used to characterize the bars was operated at voltages of 25 to 75 kV and beam currents of 5 to 8 mA with a tungsten target and a 700-μm focal spot. The exposure varied from 5 to 12 min, depending on other exposure parameters, to produce an acceptable film density of 1.5 to 2.5. Test bars positioned in direct contact with the x-ray film were radiographed (Fig. 4) in two modes: the (W, L) mode, where x-rays are transmitted through the thickness of the bar; and the (T, L) mode, where x-rays are transmitted through the width of the bar. Radiographic feedback on the density uniformity of the bars was used to adjust the powder-processing and sintering parameters. Four-point flexural strength tests were conducted in air at room and elevated temperatures (1200 and 1370°C) with inner and outer spans of 9.53 and 19.05 mm, respectively. The number of tests conducted were 21, 9, and 13 for room temperature, 1200°C, and 1370°C, respectively. Strength data and radiographic density data were used to further modify processing and sintering variables.

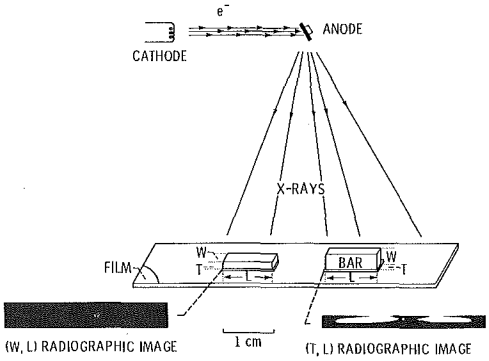

Fig. 4 Schematic configuration of conventional radiography employed for characterization of NASA 6Y Si_3N_4 test bars ($L = 3.0$ cm, $W = 0.56$ cm, $T = 0.28$ cm).

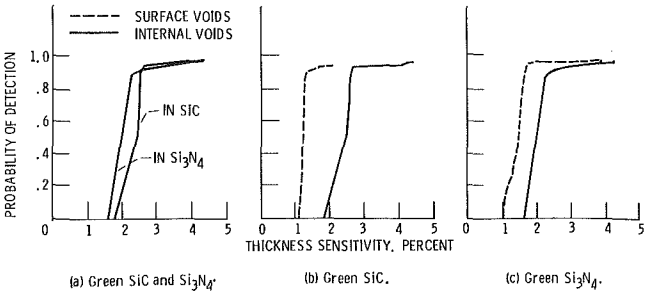

Fig. 5 Lower bound probability of detecting surface and internal voids in green isopressed SiC and Si_3N_4 bars by microfocus x-ray. Thickness sensitivity in percent equals 100 (void dimension in x-ray beam direction)/(thickness of specimen in same direction). Probability of detection calculated at 0.95 confidence level.

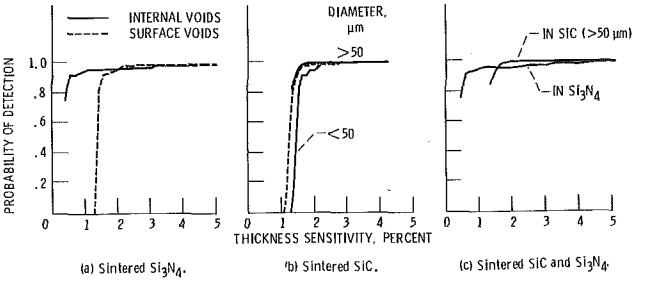

Fig. 6 Lower bound probability of detecting surface and internal voids in sintered SiC and Si_3N_4 bars by microfocus x-ray. Thickness sensitivity in percent equals 100 (void dimension in x-ray beam direction)/(thickness of specimen in same direction). Probability of detection calculated at 0.95 confidence level.

NDE Reliability

Reliability assessment of microfocus x-radiography and scanning laser acoustic microscopy is probabilistic because of the combined uncertainties associated with the equipment, the operator, the flaw characteristics, etc. Therefore a statistical approach must be used to determine the detection reliability. This examination of the seeded specimens was based on either detecting or not detecting known existing voids. Since only two outcomes from this examination were possible, the probability of detection (POD) can be described by a binomial distribution. Detection data were grouped into size intervals and further rearranged by the optimized probability method [8] to calculate the POD values at 0.95 confidence level.

Microfocus X-Radiography. NDE reliability data are presented in Figs. 5 and 6 in the form of plots of POD versus

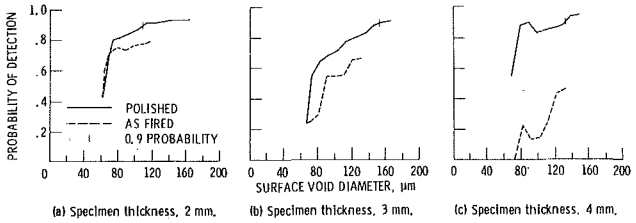

Fig. 7 Effect of specimen thickness and surface condition on probability of detecting voids in sintered silicon nitride by SLAM. Effect of thickness is evident only for specimens with as-fired surfaces. Probability of detection calculated at 0.95 confidence level.

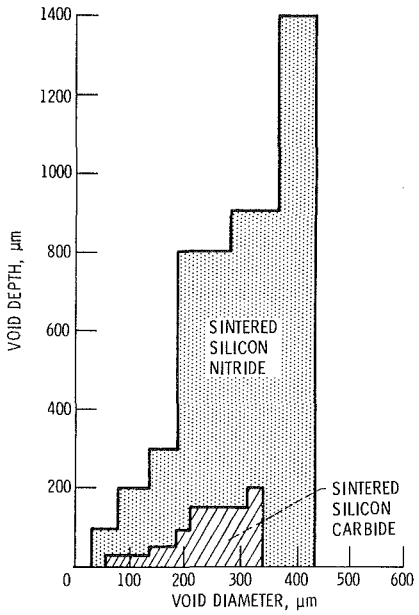

Fig. 8 Effect of void diameter, void depth, and matrix material on probability of detecting internal voids by scanning laser acoustic microscopy. Probability of detection 0.9 at 0.95 confidence limit.

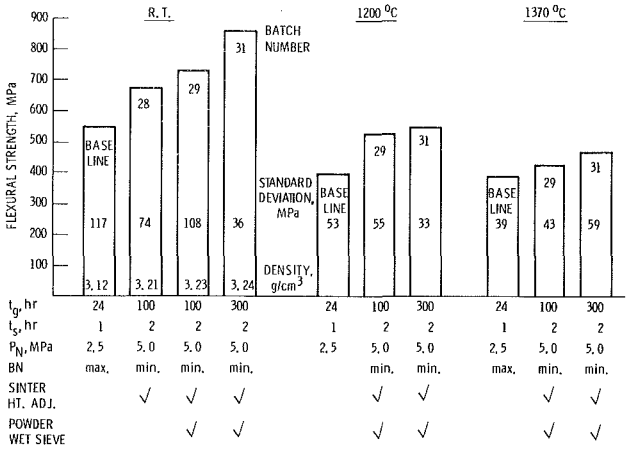

Fig. 9 Effect of modified processing/sintering procedures on flexural strength of NASA 6Y Si_3N_4 sintered at 2140°C

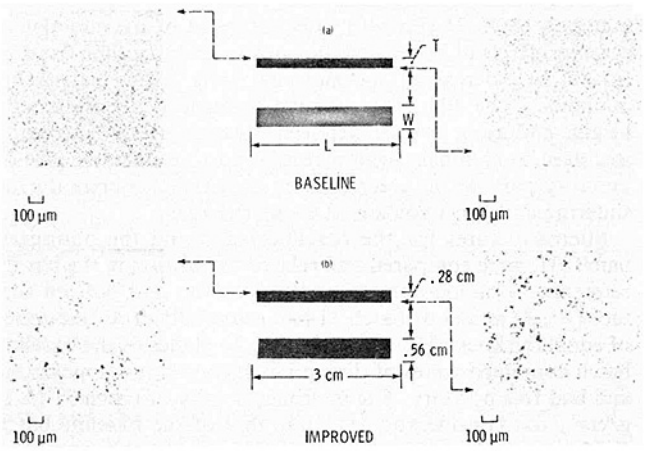

Fig. 10 NASA 6Y Si_3N_4 radiographs and microstructural comparisons of (*a*) baseline material versus (*b*) optimized material (batch 31), illustrating improved structure

void size, expressed as a percent of total specimen thickness. For green materials the POD curves in Fig. 5(*a*) indicate that the detection sensitivity of internal voids in SiC is about the same as in Si_3N_4 (i.e., 2.5 percent of thickness at a POD of 0.9). However, surface voids were easier to detect than internal voids in both materials (Figs. 5(*b*) and (*c*)). This was due to the internal voids being partially filled with powder, which reduced the contrast on the x-ray film. Even though internal voids of this type would simulate an interconnected porosity structure in similar materials, it is difficult to establish reliability statistics for naturally occurring internal voids. Hence only the POD data for surface voids presented herein would apply to naturally occurring internal voids in green dry-pressed, injection-molded, or slip-cast materials. For sintered materials (Fig. 6) the detection sensitivity was about 1.5 percent of thickness for surface and internal voids in SiC, 1.5 percent of thickness for surface voids in Si_3N_4, and better than 1.5 percent of thickness for internal voids in Si_3N_4 at a POD of 0.9. This high sensitivity to internal voids in sintered Si_3N_4 was due to void morphologies that enhanced the x-ray attenuation depending on the density, chemical composition, and thickness of the shell surrounding the voids. Thus the image contrast of some voids was improved. A dense shell formation could occur for materials where high-atomic-number additives are used to promote the sintering process. When local chemical or density variations are not present, as is the case in sintered SiC, the detection reliability for internal voids can be inferred from POD curves for surface voids (Fig. 6(*b*)).

Scanning Laser Acoustic Microscopy. Figure 7 shows how specimen thickness and surface condition affected the POD (at 0.95 confidence level) of surface-connected voids in sintered Si_3N_4 [9]. For as-fired 2, 3, and 4-mm-thick specimens with surface roughness of 8 μm, peak to valley, the 0.9 POD was not attained. After the same specimens were polished to a surface roughness of 2 μm, 0.9 POD was achieved for all thicknesses. This acoustic opacity of the as-fired specimens was attributed to the surface roughness. However, near-surface pore distribution might have scattered the sound wave and resulted in poor void detectability. Figure 8 shows how void size, void depth below the laser-scanned surface, and matrix material affected the POD of internal voids in sintered specimens having diamond-ground surfaces [7]. The boundaries of the bar graphs indicate the smallest void sizes and the maximum depths at which 0.9 POD (0.95 confidence level) was achieved. The detection sensitivity was greater for Si_3N_4 than it was for SiC. This can be attributed to the coarser grain structure and greater porosity of SiC. These microstructural differences might have increased the ultrasonic scatter and resulted in more ultrasonic attenuation in SiC.

NDE Process Control

Processing and sintering conditions were modified on the basis of feedback from radiography to obtain uniform high-density MOR bars associated with improved strength and reduced strength scatter. Figure 9 shows how these modified

procedures affected the flexural strength of NASA 6Y Si_3N_4 sintered at 2140°C. The sensitivity of radiography to the within-bar porosity distribution in the baseline and improved materials is shown in Fig. 10. Efforts were made to eliminate the case-core structure (Figs. 4 and 10) and thereby strengthen the material and reduce its strength scatter.

The case-core structure was examined as a function of powder fineness and the sintering variables grinding time, sinter cup height, nitrogen overpressure, and degree of BN contact. Radiography showed that increasing the powder fineness (by using 100 and 300-hr milling times) resulted in thinner and less distinct cases and thus improved both sinterability and uniformity. Minimizing the BN setter contact resulted in more uniform densification as a consequence of more uniform heating. However, increasing nitrogen overpressure from 2.5 to 3.5 to 5.0 MPa had no effect on the case-core structure. When using 100-hr milling time, smaller BN disks, and a nitrogen overpressure of 5.0 MPa, increasing sintering time from 1 to 2 hr and raising the sinter cup into a more uniform temperature zone were very effective in greatly reducing density gradients in sintered bars. The most uniform material, batch 31 (Fig. 10), was the result of the cumulative positive effects of increasing the powder grinding time from 24 to 300 hr, increasing the sintering time from 1 to 2 hr, minimizing the BN setter contact, adjusting the sinter cup height, and using powder wet-sieving procedures. Wet sieving was used to eliminate agglomerates and to reduce the size of impurity particles in green-pressed bars that vaporize during sintering and leave voids in the sintered bars.

Microstructures for the baseline batch and the optimized batch (31) were compared and related to position in the bar by reference to radiographs (Fig. 10). The top and bottom surface (W, L) planes of batch 31 had essentially pore-free zones of equal thickness. However, the (W, L) planes of the baseline batch contained zones of dissimilar thickness and appearance and had fine porosity. The internal porosity of batch 31 (3.24 g/cm^3) was considerably less than that of the baseline batch (3.12 g/cm^3).

The individual and combined effects of powder fineness and each of the sintering variables on the flexural strength of NASA 6Y at room temperature, 1200°C, and 1370°C are explained in detail in [3]. Only the cumulative positive effects of all the variables on flexural strength are shown in Fig. 9. In processing from batch to batch (baseline to 28 to 29 to 31) the room-temperature strength continually increased, with an overall improvement of 56 percent and more than a threefold reduction in the standard deviation. Strength improved 38 and 21 percent for 1200 and 1370°C, respectively. All successive improvements in the mechanical properties of sintered Si_3N_4 were guided by x-radiographic characterization. For the most improved material the previously dominant failure-causing voids were replaced by large columnar grains, which are less detrimental to strength properties.

Conclusion

The reliability of microfocus x-radiography for nondestructively evaluating sintered ceramics was affected by the seeded void morphologies, which enhanced the x-ray attenuation depending on the density, chemical composition, and thickness of the shell surrounding the voids. The reliability of scanning laser acoustic microscopy was affected by the specimen surface roughness and microstructural characteristics. Rough surfaces, large grains, and high porosity reduced the detection capability.

The successful use of conventional x-radiography in guiding the fabrication process resulted in denser and more uniform Si_3N_4 over the baseline material. The improved material reached four-point average flexural strength/standard deviation values of 857/36, 544/33, and 462/59 MPa at room temperature, 1200°C, and 1370°C, respectively. These strengths represented improvements of 56, 38, and 21 percent over the baseline properties at the three test temperatures. Further, previously dominant failure-causing voids were replaced by large grains, which are less detrimental to strength properties.

References

1 Evans, A. G., et al., "Failure Prediction in Structural Ceramics," *Materials Evaluation*, Vol. 35, No. 4, Apr. 1977, pp. 85–96.

2 Klima, S. J., "NDE of Advanced Ceramics," *Materials Evaluation*, Vol. 44, No. 5, Apr. 1986, pp. 571–576.

3 Sanders, W. A., and Baaklini, G. Y., "Correlation of Processing and Sintering Variables With the Strength and Radiography of Silicon Nitride," NASA TM-87251, 1986.

4 Nishida, K., "Silicon Nitride," *The Development of Structural Fine Ceramics in Japan*, The Japan Industrial and Technological Bulletin, Japan External Trade Organization, Tokyo, 1983, pp. 21–24.

5 Rice, W. R., et al., "Fractography of Si_3N_4 and SiC," *Ceramics for High Performance Applications II*, Burke et al., eds., Brook Hill Publishing Co., Chestnut Hill, MA, 1977, pp. 669–687.

6 Baaklini, G. Y., and Roth, D. J., "Probability of Detection of Internal Voids in Structural Ceramics Using Microfocus Radiography," *Journal of Materials Research*, Vol. 1, No. 3, May–June 1986, pp. 457–467.

7 Roth, D. J., and Baaklini, G. Y., "Reliability of Scanning Laser Acoustic Microscopy for Detecting Internal Voids in Structural Ceramics," *Advanced Ceramic Materials*, Vol. 1, No. 3, July 1986, pp. 252–258.

8 Packman, P. F., et al., "Reliability of Flaw Detection by Nondestructive Inspection," *Metals Handbook*, Vol. 11, 8th ed., American Society for Metals, Metals Park, OH, 1976, pp. 414–424.

9 Roth, D. J., et al., "Reliability of Void Detection in Structural Ceramics by Use of Scanning Laser Acoustic Microscopy," *Materials Evaluation*, Vol. 44, No. 6, May 1986, pp. 761–769.

Tensile Behavior of Glass/Ceramic Composite Materials at Elevated Temperatures

J. F. Mandell

D. H. Grande

J. Jacobs

Department of Materials Science and Engineering, Massachusetts Institute of Technology, Cambridge, MA 02139

This paper describes the tensile behavior of high-temperature composite materials containing continuous Nicalon ceramic fiber reinforcement and glass and glass/ceramic matrices. The longitudinal properties of these materials can approach theoretical expectations for brittle matrix composites, failing at a strength and ultimate strain level consistent with those of the fibers. The brittle, high-modulus matrices result in a nonlinear stress–strain curve due to the onset of stable matrix cracking at 10 to 30 percent of the fiber strain to failure, and at strains below this range in off-axis plies. Current fibers and matrices can provide attractive properties well above 1000°C, but composites experience embrittlement in oxidizing atmospheres at 800 to 1000°C due to oxidation of a carbon interface reaction layer. The oxidation effect greatly increases the interface bond strength, causing composite embrittlement.

Introduction

Fiber-reinforced glass and glass/ceramic matrix composites are an emerging class of materials possessing high strength and toughness, low density, and high temperature resistance potentially attractive for gas turbine engine applications. Several of these materials have now reached a stage of development where they can be produced in sufficient quantity and quality for evaluation as structural materials, although some with higher temperature capability are still at an experimental stage. In pioneering efforts at United Technologies Research Center (Prewo, 1984) a variety of fiber and matrix combinations has been produced using a process involving unidirectional tapes which are arranged into laminates and then hot pressed; a wide variety of other processes has also been demonstrated. While early efforts used glass matrices with limited temperature capability, higher temperature resistance was obtained by UTRC and Corning Glass Works through matrices which are processed as a glass, then crystallized to form a glass/ceramic. While many other fiber composite systems with ceramic as well as glass and glass/ceramic matrices are currently being pursued by a variety of investigators, this paper describes the behavior of the glass and glass/ceramic matrices reinforced with Nicalon ceramic fibers.

During most of the early development of these materials the mechanical properties were evaluated using flexural tests, which are conveniently run at elevated temperatures. However, flexural test data are particularly difficult to interpret for fiber composites as recognized in the efforts of a number of investigators to develop adequate tensile, compression, and shear test methods (Prewo, 1983; Mandell et al., 1985; Larsen et al., 1985). Typical longitudinal flexural strength values are about twice as high as the tensile strength. While emphasis in this paper is on behavior under tension, flexural results tend to be qualitatively similar as to trends and damage development if the failure under flexural loading is tension dominated (Marshall and Evans, 1985).

Tensile Test Methods

Tests using bonded tab load introduction are well established for polymer matrix composites, and have worked well for ceramic composites at low temperatures in the various studies cited previously. However, adequate adhesive bonding materials are not available for high-temperature use. Test specimens with dumbbell shapes perform adequately for multidirectional laminates, but the very low transverse and shear strengths and small sample sizes result in extreme width reduction requirements for unidirectional composites (Prewo, 1983; Larsen et al., 1985).

The test specimen used to obtain most of the results given here is shown in Fig. 1 (Mandell et al., 1985). The specimen is wet ground with a diamond wheel in two stages to a dumbbell shape in the thickness direction, while the sides remain straight. The 5 deg tapered specimen shoulders are fit to inserts in a gripping apparatus so that a compressive normal stress constrains shear cracking at the shoulder. Strains are measured at elevated temperatures with an external extensometer which contacts the specimen with quartz rods at small surface indentations. Gage-section tensile failures have been obtained in most cases with this specimen at temperatures up to 1000°C, the maximum investigated. This test geometry has also been used for multidirectional laminates, where sacrificial surface plies are ground away, leaving the desired symmetrical laminate in the gage section. However, due to the waviness of

Contributed by the Gas Turbine Division of THE AMERICAN SOCIETY OF MECHANICAL ENGINEERS and presented at the 32nd International Gas Turbine Conference and Exhibit, Anaheim, California, May 31–June 4, 1987. Manuscript received at ASME Headquarters February 5, 1987. Paper No. 87-GT-75.

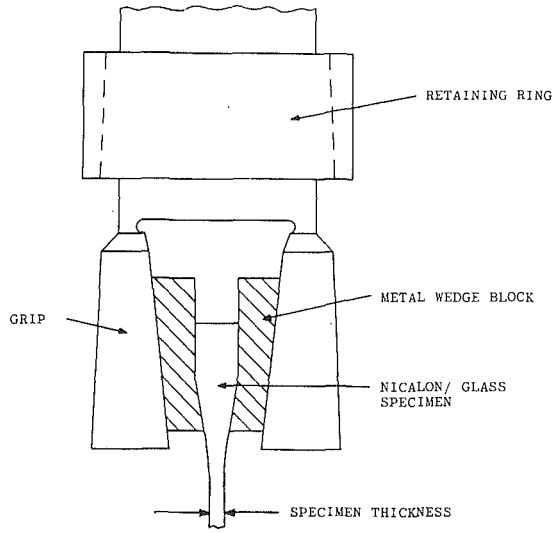

Fig. 1(a) Tensile test specimen in grip (Mandell et al., 1985)

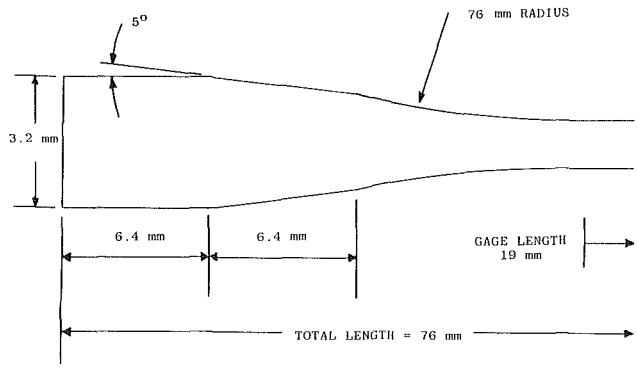

Fig. 1(b) Tensile test specimen geometry

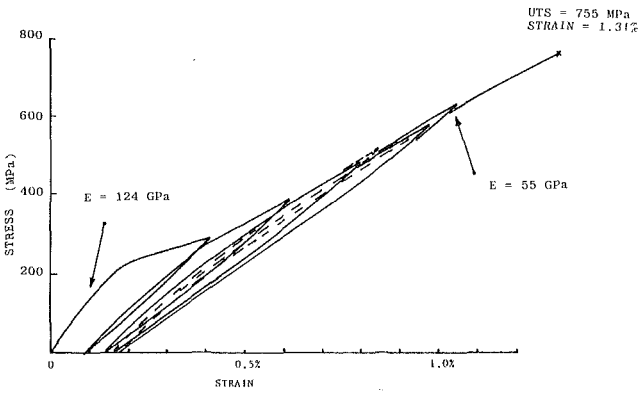

Fig. 2 Tensile stress-strain curve (with cycles) longitudinal Nicalon/1723 tested at 20°C (Mandell et al., 1985)

typical plies, it is more practical to use a width-tapered dumbbell shape with as-molded surfaces for multidirectional laminates wherever possible (Mandell et al., 1986b).

Materials

The materials used in this study were supplied by Corning Glass Works, as were the properties and information given in Table 1. The BMAS glass/ceramic matrix system was an early experimental batch which gave properties well below those which have since been achieved, as discussed later. Both

Table 1 Typical fiber and bulk matrix 20°C properties

	Nicalon® fiber	1723 glass matrix	BMAS III glass-ceramic matrix
Fiber diameter, μm	10–15	–	–
Density, g/cm^3	2.55[b]	2.64	2.77
Coefficient of thermal expansion, (10^{-7}/°C)	31[c]	45.8	17 (25–300°C)
Young's modulus, GPa	193[b]	86	106
Tensile strength, GPa	2.07[b]	–	–
Failure strain, percent	1.0–1.3	–	–
Poisson ratio	–	0.24	–
Apparent maximum use temperature, °C	1100–1300[c]	600–700	1200–1250
Composition	Silicon oxycarbide[d]	Alumino-silicate Corning code 1723	(BaO, MgO, Al_2O_3, SiO_2)

[a]Most data supplied by K. Chyung, Corning Glass Works, except as noted.
[b]Prewo, 1984.
[c]Nippon Carbon.
[d]Taylor, 1986.

materials are composed of unidirectional plies of continuous fibers with a fiber content of 35 to 40 percent by volume, and with little or no porosity. At this fiber content the distribution of fibers is often very uneven, as shown in later micrographs.

An important aspect of this class of brittle, high-modulus matrix composites is that efficient reinforcement by the fibers requires a fiber/matrix interface which will debond as matrix cracks form and propagate. This allows the full fiber strength and failure strain to be realized in the composite even though the matrix may crack at strains in the vicinity of 10–20 percent of the fiber failure strain. As will be shown later, a very strong bond between fibers and matrix results in brittle behavior, with matrix cracks propagating through the fibers. Thus, to be successful, glass and glass/ceramic composites must be fabricated so as to prevent very high interface strengths. Recent studies (Cooper and Chyung, 1986; Taylor, 1986) have shown that under proper processing conditions the materials in Table 1 (and similar materials) form a carbon layer at the interface as a result of favorable diffusion and chemical reactions between the Nicalon fibers and the matrix.

Typical Composite Behavior: Nicalon/1723 Glass

The Nicalon/1723 glass composite shows behavior which is typical of optimized materials in this class, although many details vary from system to system. Figure 2 (Mandell et al., 1985) shows a longitudinal tensile stress-strain curve which includes several unloading cycles. Below 0.1 percent strain the

Table 2 Typical unidirectional composite properties (20°C, $V_f = 0.35 - 40$)

	Nicalon®/1723	Nicalon®/BMAS
Longitudinal tensile modulus, GPa	128	144
Transverse tensile modulus, GPa	101	–
Poisson ratio, LT	0.24	0.20
Longitudinal tensile strength, MPa	734	225
Longitudinal stress at first matrix cracking, MPa	210	190
Transverse tensile strength, MPa	27*	–*
Longitudinal tensile failure strain, percent	1.2	0.37
Transverse tensile failure strain, percent	0.035*	–*
Fiber/matrix interfacial shear strength, MPa	236	60
Sliding friction of debonded fiber, MPa	86	2.8
Short beam interlaminar shear strength, MPa	73	31

*A number of apparently flawed specimens with strength less than 5 MPa are not included.

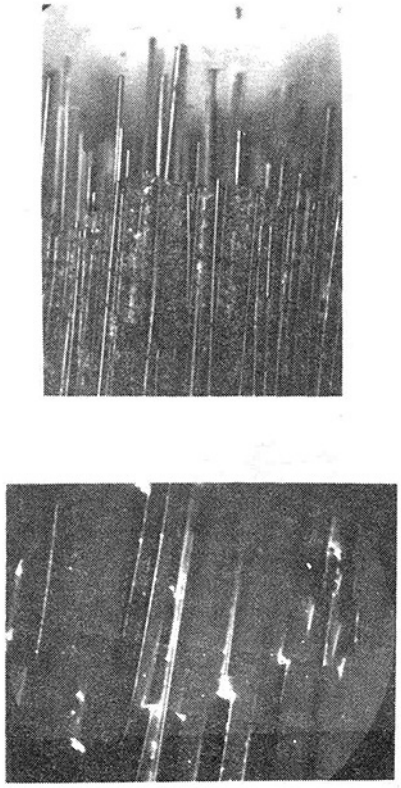

Fig. 3 Fracture profile and matrix cracking for longitudinal Nicalon/1723 tested at 20°C (Mandell et al., 1985)

behavior is linear elastic, with a Young's modulus of 124 GPa, close to the simple rule of mixtures prediction from the matrix and fiber properties. The curve becomes strongly nonlinear beginning around 0.1 to 0.2 percent strain, then becomes nearly linear again above 0.4 to 0.5 percent. Failure occurs close to the average fiber failure strain, and at a tensile ultimate strength close to the fiber strength multiplied by the fiber volume fraction V_f. [Fibers extracted after fabrication usually show a lower strength than in Table 1 (Prewo, 1986). The term "strength" refers to the ultimate strength throughout this paper.] The elastic modulus at high strains also approaches that of the fibers multiplied by V_f, ignoring the matrix. The mechanical properties for this and the BMAS matrix system are listed in Table 2. Systems with very extensive fiber pullout may also show a tail on the stress–strain curve after the maximum stress (Marshall and Evans, 1985).

The longitudinal stress–strain behavior in Fig. 2 is very close to that of a model brittle matrix system as described by Aveston et al. (1971). The nonlinearity at 0.1 to 0.2 percent strain corresponds to the onset of matrix cracking, which reaches a saturation density by 0.4 to 0.5 percent strain; the saturation matrix crack density is on the order of a 0.1 mm spacing, as indicated in Fig. 3 (the magnification of all micrographs is evident from the 10–15 μm fiber diameter). Figure 3 also shows the fracture surface in profile, with typical fiber pullout lengths of about 10 to 20 fiber diameters. The nonlinearity in Fig. 2 is much greater than for polymer matrix composites because of the much higher ratio of matrix to fiber modulus and the relatively low fiber content.

It is evident that most of the behavior in Fig. 2 is optimum for the given fiber and matrix properties, so that little improvement in the composite could be achieved at this fiber content without improving the fibers or matrix. However, theoretical treatment and some experimental evidence (Aveston et al., 1971; Prewo, 1986; Marshall and Evans, 1985) suggest that the stress and strain at which matrix cracking develops may be varied. Fracture mechanics treatment of a matrix crack propagating past fibers indicates that the resistance to opening of the matrix crack along the debonded fibers will determine whether matrix cracks can propagate. The resistance to matrix cracking will increase with an increase in debonding or sliding resistance at the interface, an increase in fiber content (more fibers), or a decrease in fiber diameter (more interface area for the same V_f). Table 2 lists the interfacial bond shear strength for the fiber/matrix interface determined by the microdebonding test method illustrated in Fig. 4 (Mandell et al., 1986c). Also listed are tentative data for the frictional sliding resistance of the debonded interface determined in the microdebonding apparatus by compressing the fiber into the matrix at higher forces, following the technique and analysis of Marshall (1984). These interface properties and measurement techniques will be described in detail by Mandell et al. (1987). Of the composite systems which have been tested in this manner to date, the bond strength and interface frictional resistance are relatively high for the Nicalon/1723 system, and so improvement in matrix crack resistance from a higher bond strength or friction may not be practical without risking composite embrittlement. However, neither the limits nor the interpretation of bond strength for

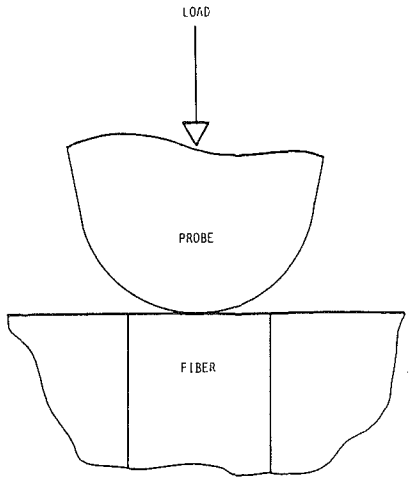

Fig. 4 Schematic of single fiber loading in microdebonding test method (Mandell et al., 1986c)

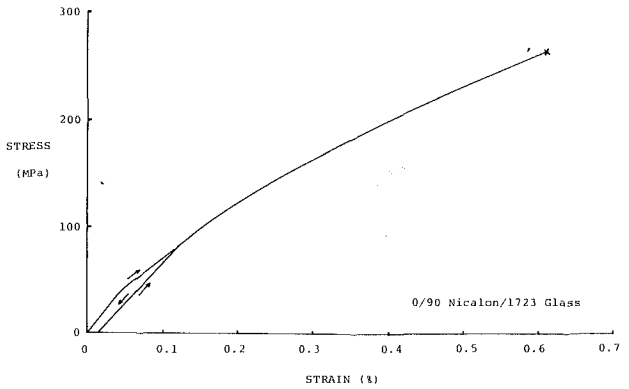

Fig. 5 Tensile stress-strain curve for 0/90 Nicalon/1723 tested at 20°C

these materials is well established. The high interface properties for this material may also reflect thermal residual stresses, as the 1723 glass has a higher coefficient of thermal expansion than does the fiber. The higher bond properties are also evidenced in the fiber pullout length on the fracture surface, which is considerably shorter than reported for systems with a similar failure strain but lower matrix coefficient of expansion, such as Nicalon/LAS (Prewo and Layden, 1984; Marshall and Evans, 1985).

The relatively high interface properties should help the composite mechanical properties in off-axis directions. However, the transverse tensile properties given in Table 2 are still very low, and most specimens failed in handling; similar data are reported for other systems (Prewo, 1984; Sbaizero and Evans, 1986). The transverse strain to failure in the range of 0.03 to 0.04 percent is of particular concern, as it is well below the matrix cracking strain in longitudinal specimens. In fact, most transverse unidirectional specimens either fail during handling or else show negligible strength due to the presence of flaws. The low transverse strain to failure must be expected for materials in this class due to the effects of fibers creating stress concentrations and of flaws oriented in the fiber direction. A low fiber/matrix bond strength would be expected to exacerbate this problem, and the high interface properties for the Nicalon/1723 should be helpful. However, the measured interface properties are shear strengths with a compressive normal component, and their applicability to transverse tension needs further study.

Practical composite materials are usually constructed with plies oriented in several directions, so that some are off-axis relative to an applied uniaxial stress. The low off-axis properties should then produce cracking at low strains in these plies, and the stress-strain curve should become nonlinear at an even lower strain. This effect is evident in Fig. 5 for a 0/90 ply configuration of the Nicalon/1723. The strain to failure in this batch was below that in Fig. 2, possibly due to differing processing conditions as well as the ply configuration. Other studies have shown little difference in failure strains between 0 and 0/90 materials (Prewo, 1984). If composites of this type are to function in practical situations, it may be necessary to tolerate some off-axis ply stable cracking, particularly in areas of stress concentration. If this is the case, then the interface and fibers must be able to withstand exposure to the environment at such crack sites. As indicated in the next section, current materials which depend on a carbon layer at the interface have a problem in this area at elevated temperatures in oxidizing environments.

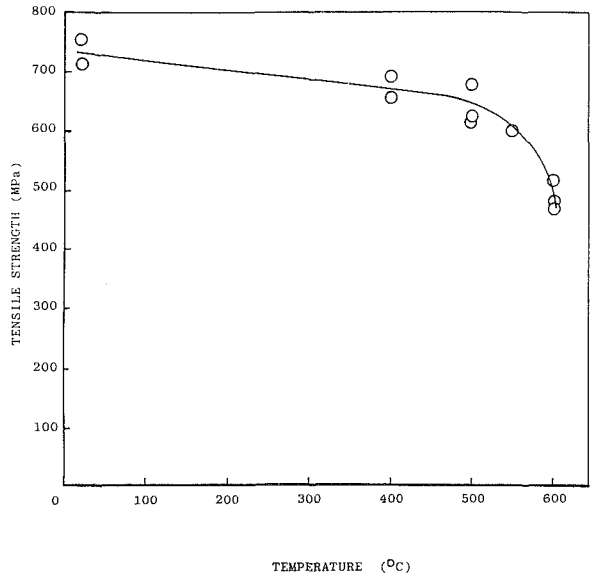

Fig. 6 Longitudinal tensile strength of Nicalon/1723 versus test temperature (Mandell et al., 1985)

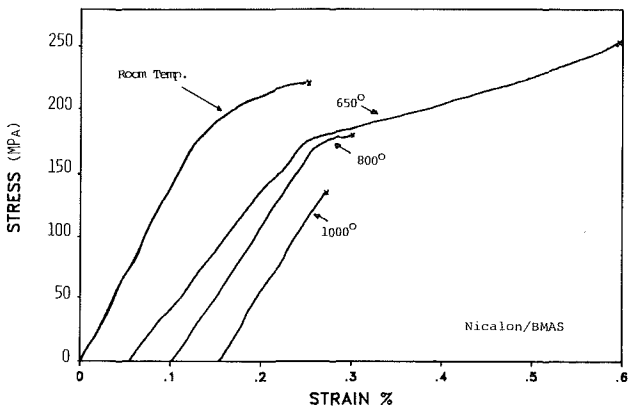

Fig. 7 Longitudinal tensile stress-strain curves for Nicalon/BMAS tested at various temperatures

Figure 6 shows the effects of temperature (in air) on the Nicalon/1723 longitudinal tensile strength (Mandell et al., 1985). The general stress-strain behavior was not significantly affected by temperature up to 500°C, above which the strength decreased. The drop in properties was expected around 600°C based on a softening trend in the matrix modulus. At 600°C some specimens showed a significant increase in fiber pullout on the fracture surface, possibly as a result of release of the residual compression stress at the interface.

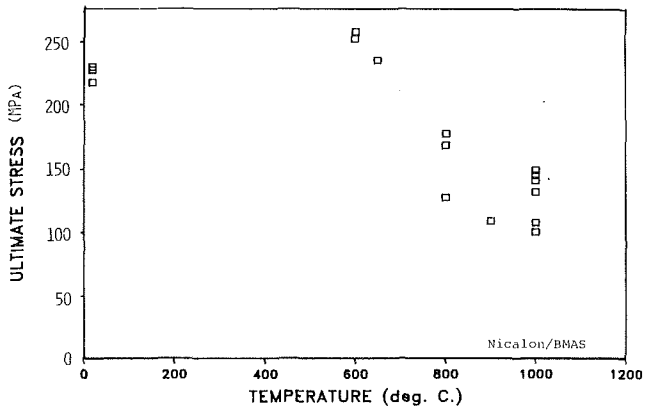

Fig. 8 Longitudinal tensile strength of Nicalon/BMAS versus test temperature

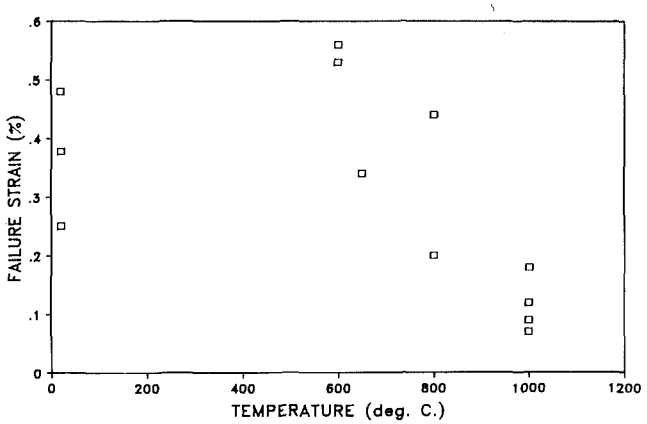

Fig. 9 Longitudinal failure strain of Nicalon/BMAS versus test temperature

Nicalon/BMAS Glass-Ceramic

As noted earlier, the batch of Nicalon/BMAS used in this study did not have the best properties achievable with this system. As shown in Fig. 7, longitudinal stress–strain curves generally did not get past the nonlinear matrix cracking regime evident for an optimized material in Fig. 2, and the failure strain did not approach that of the Nicalon fibers. Comparison of four-point flexural strength data from these batches with other batches at Corning showed about half of the flexural strength of the best batches (flexural failures were tension dominated). The origin of this problem does not appear to be in the carbon layer at the interface, as the bond strength values in Table 2 are in the expected low range; the frictional sliding resistance is on the same order as that reported for Nicalon/LAS glass-ceramic by Marshall (1984). Further tests will be run on other batches to clarify the origin of the problem.

Despite the deficiencies of this batch of material, it still allows study of an interesting aspect of behavior found in other high-temperature glass-ceramic matrix systems (Prewo, 1986). As the test temperature is increased in the air atmosphere used in all cases, the strength and strain to failure initially increase up to about 650°C, as typical specimens withstand higher levels of matrix cracking without failure. By 800°C the properties have decreased significantly, and a further decrease occurs up to the maximum test temperature of 1000°C. Figure 8 shows the change in longitudinal tensile strength with temperature, while Fig. 9 gives the corresponding failure strain data. It should be noted that the heatup time for the high-temperature tests is about 2 hr, with about 30 min

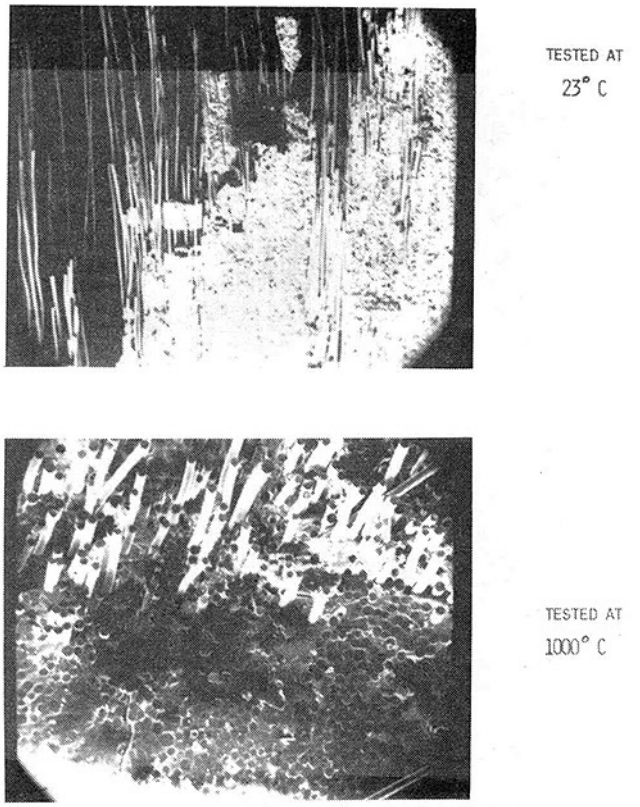

Fig. 10 Nicalon/BMAS tensile failure at 20°C and 1000°C (near edge)

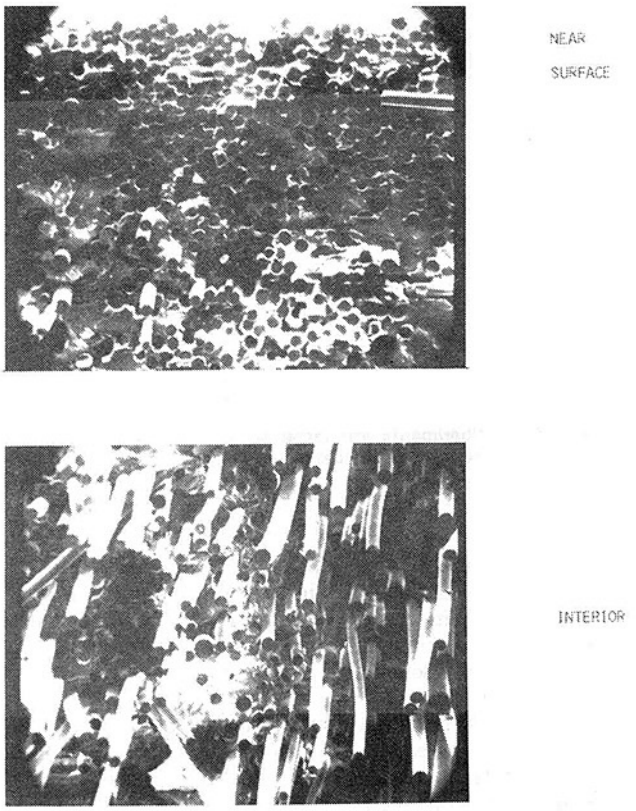

Fig. 11 Fracture surfaces of Nicalon/BMAS tensile failure tested at 1000°C showing embrittled zone at surface and pullout on interior

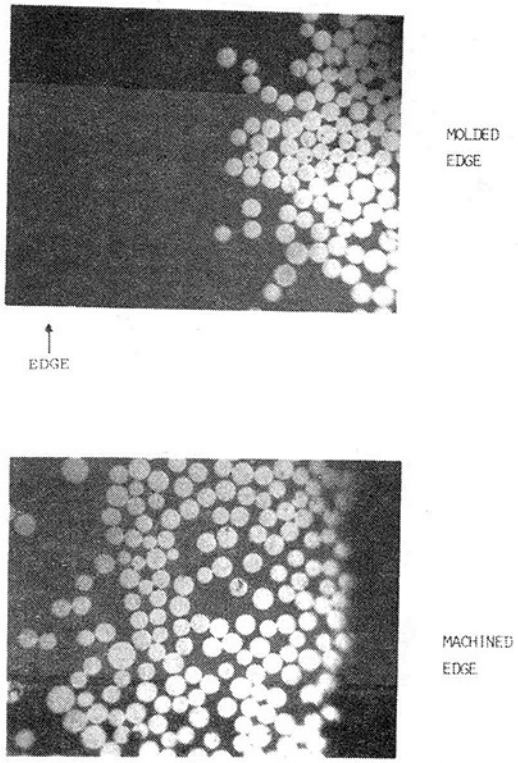

Fig. 12 Polished cross section of Nicalon/BMAS block exposed at 1000°C in air, showing the molded and ground edge regions

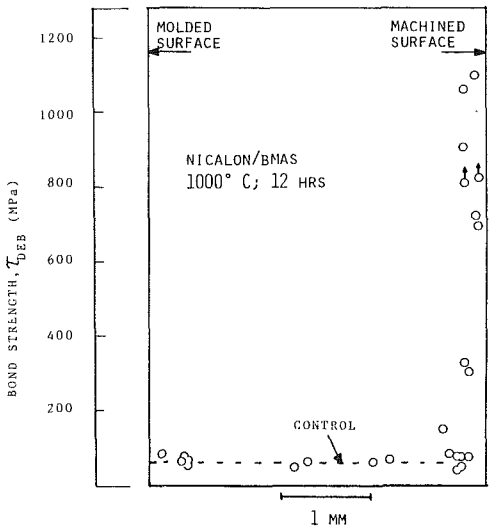

Fig. 13 In-situ fiber/matrix interfacial shear strength from microdebonding test plotted across the cross section in Fig. 12

at test temperature prior to loading. The loading rate of the test is such that failure occurs in several minutes.

The sharp drop in strength and strain to failure in the 800 to 1000°C range is accompanied by a change in the fracture surface appearance. Below this temperature the usual fiber pullout is found over the entire fracture surface (Fig. 10). However, at 1000°C a region of flat, brittle fracture is evident around the exposed edges of the fracture surface, as reported for other similar materials (Prewo, 1986). Figures 10 and 11 show micrographs of the flat fracture region and the interior.

The surface embrittlement effect in similar systems has generally been blamed on oxidation of the interface carbon layer, with subsequent reactions producing a strong bond. To explore this question in the present case, a series of experiments has been run with the microdebonding test in Fig. 4. One such case is given in Figs. 12 and 13. A block of the Nicalon/BMAS with one ground surface and one as-molded surface was conditioned at 1000°C in an air atmosphere with no mechanical load for 12 hr. The specimen was then sectioned and polished as shown in Fig. 12; the as-molded surface contained a layer of pure matrix outside of the first fibers, so that the fiber/matrix interfaces were not exposed. Figure 13 gives the fiber/matrix interfacial shear strength across the cross section shown in Fig. 12. The interface strength is low from the first fibers at the as-molded surface through the thickness, to within about 0.5 mm of the ground surface. The data are close to the value of 46 MPa listed for control material in Table 2. However, as the ground surface is approached in different locations, the bond strength is observed to increase rapidly, with many values exceeding ten times those on the interior. A similar trend has been reported by Luh and Evans (1986) for interface sliding friction. The data in Fig. 13 are a summary of results from all locations, while the bond strength rise approaching the ground surface at particular locations occurred at different depths in from the surface, apparently reflecting the local fiber arrangement.

The results in Fig. 13 show that the interface does increase greatly in strength when exposed in air at 1000°C at a ground surface, or when there is an apparent path for oxidation to penetrate along various interfaces into the interior. Near the exposed end of blocks where fibers were cut, high bond strengths were observed all across the cross section, as oxidation tunnelled in from the fiber ends. The tensile specimens used in this study were ground on all surfaces, and further interface exposure is to be expected as matrix cracks form near the knee in the stress–strain curve. It is apparent that the drop in tensile properties at high temperatures was caused by an increase in fiber/matrix bond strength and consequent embrittlement. While matrix layers may protect specimens with as-molded surfaces in the absence of matrix cracking, the carbon layer at the interface in current materials is a major detriment to their application in high-temperature oxidizing environments. The embrittlement effect is not observed in similar materials in nonoxidizing atmospheres, and the properties are maintained to well above 1000°C (Prewo, 1984).

Conclusions

Fiber composites with ceramic fibers and glass or glass/ceramic matrices show high longitudinal tensile properties, low density, and high temperature resistance. Matrix cracking occurs at relatively low strains, particularly in off-axis directions. The performance at temperatures of 800°C or above in oxidizing environments is diminished by oxidation at exposed interfaces which increases interface strength, leading to embrittlement of the composite.

Acknowledgments

This work was supported by NASA-Lewis Research Center, and materials were supplied by Corning Glass Works. Their support and helpful discussions are greatly appreciated.

References

Aveston, J., Cooper, G. A., and Kelly, A., 1971, "Single and Multiple Fracture," in: *Properties of Fibre Composites; Conference Proceedings, National Physical Laboratory*, I. P. C. Service and Technology Press, Guildford, pp. 15–26.

Cooper, R. F., and Chyung, K., 1986, "Structure and Chemistry of Fiber-Matrix Interfaces in Nicalon Fiber-Reinforced Glass-Ceramic Composites," presented at American Ceramics Society 88th Annual Meeting, Chicago.

Larsen, D. C., Stuchly, S. L., Bortz, S. A., and Ruh, R., 1985, "Test Methodology for Ceramic Fiber Composites: Results for Si/LAS, SiC/SiC, and C/SiC Composites," in: *Metal Matrix, Carbon, and Ceramic Matrix Com-*

posites 1985, NASA Conf. Pub. 2406, J. D. Buckley, ed., NASA Scientific and Technical Branch, pp. 313–334.

Luh, E. Y., and Evans, A. G., 1986, "High Temperature Mechanical Behavior of a Fiber-Reinforced Ceramic Matrix Composite," presented at American Ceramics Society 88th Annual Meeting, Chicago.

Mandell, J. F., Grande, D. H., and Edwards, B., 1985, "Test Method Development for Structural Characterization of Fiber Composites at High Temperatures," *Ceramic Engineering and Science Proc.*, Vol. 6, pp. 524–535.

Mandell, J. F., Grande, D. H., and Jacobs, J., 1986a, "Elevated Temperature Tensile Behavior of Glass-Ceramic Matrix Composites," presented at American Ceramics Society 88th Annual Meeting, Chicago.

Mandell, J. F., Grande, D. H., and Dannemann, K. A., 1986b, "High Temperature Testing of Glass/Ceramic Matrix Composites," presented at ASTM Symposium Test Methods and Design Allowables for Fibrous Composites, Phoenix.

Mandell, J. F., Grande, D. H., Tsiang, T.-H., and McGarry, F. J., 1986c, "Modified Microdebonding Test for Direct In-Situ Fiber/Matrix Bond Strength Determination in Fiber Composites," in: *Composite Materials: Testing and Design (Seventh Conference), STP 893*, J. M. Whitney, ed., ASTM, Philadelphia, pp. 87–108.

Mandell, J. F., Grande, D. H., and Hong, K. C. C., 1987, "Interfacial Shear Strength and Sliding Resistance in Metal and Glass/Ceramic Matrix Composites," presented at 11th Annual Conf. on Composites and Advanced Ceramic Materials, American Ceramics Society, Coco Beach, FL.

Marshall, D. B., 1984, "An Indentation Method for Measuring Matrix-Fiber Frictional Stresses in Ceramic Composites," *Comm. Am. Ceram. Soc.*, Vol. 67, pp. C259–C260.

Marshall, D. B., and Evans, A. G., 1985, "Failure Mechanisms in Ceramic-Fiber/Ceramic Matrix Composites," *J. Am. Ceram. Soc.*, Vol. 68, pp. 225–231.

Prewo, K. M., 1983, "Advanced Characterization of SiC Fiber Reinforced Glass-Ceramic Matrix Composites," ONR Contract N00014-81-C-0571, Report R83-915939-1, United Technologies Research Center, East Hartford, CT.

Prewo, K. M., 1984, "Ceramic and Carbon Fiber Reinforced Glasses," *Proc. of the Metal and Ceramic Matrix Composite Processing Conf.*, Battelle Columbus Labs, Columbus, OH.

Prewo, K. M., and Layden, G. K., 1984, "Advanced Fabrication and Characterization of SiC Fiber Reinforced Glass-Ceramic Matrix Composites," ONR Contract N00014-81-C-0571, Report R84-916175, United Technologies Research Center, East Hartford, CT.

Prewo, K. M., 1986, "Fiber Reinforced Glasses and Glass Ceramics," presented at American Ceramics Society 88th Annual Meeting, Chicago.

Sbaizero, O., and Evans, A. G., 1986, "Tensile and Shear Properties of Laminated Ceramic Matrix Composites," *J. Am. Ceram. Soc.*, Vol. 69, pp. 481–486.

Taylor, M., 1986, "Interface Characteristics of Polymer-Derived Fibers in Glass-Ceramic Matrices," presented at American Ceramics Society 88th Annual Meeting, Chicago.

Surface Flaw Reliability Analysis of Ceramic Components With the SCARE Finite Element Postprocessor Program

J. P. Gyekenyesi
NASA Lewis Research Center,
Cleveland, OH 44135

N. N. Nemeth
WLT Corporation,
Cleveland, OH 44142

The SCARE (Structural Ceramics Analysis and Reliability Evaluation) computer program on statistical fast fracture reliability analysis with quadratic elements for volume-distributed imperfections is enhanced to include the use of linear finite elements and the capability of designing against concurrent surface flaw-induced ceramic component failure. The SCARE code is presently coupled as a postprocessor to the MSC/NASTRAN general purpose, finite element analysis program. The improved version now includes the Weibull and Batdorf statistical failure theories for both surface and volume flaw-based reliability analysis. The program uses the two-parameter Weibull fracture strength cumulative failure probability distribution model with the principle of independent action for polyaxial stress states, and Batdorf's shear-sensitive as well as shear-insensitive statistical theories. The shear-sensitive surface crack configurations include the Griffith crack and Griffith notch geometries, using the total critical coplanar strain energy release rate criterion to predict mixed-mode fracture. Weibull material parameters based on both surface and volume flaw-induced fracture can also be calculated from modulus of rupture bar tests, using the least-squares method with known specimen geometry and grouped fracture data. The surface flaw reliability prediction uses MSC/NASTRAN stress, temperature, and external boundary area output, obtained from the use of linear or quadratic shell and three-dimensional isoparametric finite elements. The statistical fast fracture theories for surface flaw-induced failure, along with selected input and output formats and options, are summarized. A sample problem to demonstrate various features of the program is included.

Introduction

Brittle structures characteristically exhibit a large variation in fracture stress, which must be taken into account in design. This variation in observed strength of nominally identical components is due to the presence of invisible material imperfections. These imperfections are assumed to have a distribution in strength and the structure is assumed to fail when the strength of the weakest flaw or link is exceeded. Structural ceramics are known to contain at least two concurrent types of material imperfections or flaw populations. One type of unavoidable flaws arises from material processing, and is usually restricted to the interior of the structure and referred to as volume or intrinsic flaws. Another flaw population with distinctly different structural response exists on the surface of a ceramic component. These external surface or extrinsic flaws can arise from grinding or other finishing operations, or may be the result of environmental factors or of the intrinsic porosity intersecting the external surface. Statistical fast fracture models, based on the weakest link theories (WLT) of Weibull, have been previously developed for both types of flaw populations (Weibull, 1939; Rufin et al., 1984; Wertz and Heitman, 1980; Batdorf, 1978; Johnson, 1983). Recently, a public domain general purpose reliability code called SCARE has been generated (Gyekenyesi, 1986) to predict the fast fracture response of ceramic structures due to volume distributed flaws. It is the purpose of this paper to describe enhancements to the SCARE program which will allow reliability analysis with linear or quadratic elements of ceramic components due to the presence of a concurrent surface distributed flaw population. Consequently, fracture caused by either internal or external flaws can then be accounted for in the design process.

The first probabilistic method used to account for the scatter in fracture strength of brittle materials was introduced by Weibull (1939). His model was based on the weakest link theory and required certain statistical parameters to describe the failure response of a material phenomenologically. These statistical parameters were usually determined from uniaxially

Contributed by the Gas Turbine Division of THE AMERICAN SOCIETY OF MECHANICAL ENGINEERS and presented at the 32nd International Gas Turbine Conference and Exhibit, Anaheim, California, May 31–June 4, 1987. Manuscript received at ASME Headquarters February 5, 1987. Paper No. 87-GT-69.

loaded, simple geometry specimens. To predict material behavior in other stress states using statistical parameters from uniaxial tests, Weibull proposed calculating the risk of rupture by averaging the tensile normal stress in all directions. Since this approach is arbitrary and requires numerical modeling, other approaches were subsequently introduced. The most widely used of these is the principle of independent action (PIA) model, which is based on the assumption that the principal stresses act independently. The PIA fracture theory is the statistical version of the maximum stress failure theory, which was widely used in early metallic structure design. Most ceramic components in the government sponsored advanced gas turbine (AGT) programs used either or both of the above described polyaxial statistical failure models. Both of these fracture theories, however, can lead to unsafe estimates of failure (Gyekenyesi, 1986) since they both neglect the shear force, and in the case of the PIA hypothesis, the effects of combined principal stresses.

In order to introduce a mechanistic fracture criterion into a statistically based analysis model to more accurately predict the onset of catastrophic crack propagation, Batdorf developed a new theory which also applies to brittle materials in which the cracks are confined to the surface (Batdorf, 1973; Batdorf and Heinisch, 1978). He assumed that the cracks are randomly oriented, that they are perpendicular to the boundary, and that they do not interact. The sizes of the cracks are not explicitly treated and fracture occurs when the remote macroscopic stress normal to the crack plane exceeds some critical stress σ_{cr} characterizing that particular crack. Since the cracks are assumed normal to the surface, crack orientation is given by a single angular measure rather than two, as in the case of volume-distributed flaws. This simplification is not always invoked (Shetty et al., 1984), although there is strong experimental evidence that it is justified (Batdorf, 1973).

In adding the influence of shear loading on the crack face, the external flaws are currently modeled as Griffith cracks and Griffith notches. Unlike with internal flaw analysis in SCARE, only the total critical coplanar strain energy release rate criterion G_c is used to predict mixed-mode fracture (Samos, 1982), and the maximum tensile stress criterion, as described by Batdorf and Heinisch (1978), is not implemented for surface cracks in the program. It has also been concluded (Batdorf and Heinisch, 1978) that the Griffith crack is not an appropriate model of a typical surface imperfection, and is included here mainly for historical and academic reasons.

Surface flaw-based reliability analysis has been implemented in both the SCARE1 and SCARE2 versions of the postprocessor program (Gyekenyesi, 1986). SCARE1 uses only elemental centroidal principal stresses to calculate reliability. In the SCARE2 version of the code, all linear or quadratic QUAD8 shell elements are further discretized into nine subelements, which are then used with interpolated principal stresses to perform all analysis. In order to identify external boundaries, calculate their surface areas, and obtain corresponding surface stress states, appropriate MSC/NASTRAN shell elements of negligible stiffness are used, together with the previously selected three-dimensional HEXA and PENTA elements. The selective use of shell elements permits the identification of only those external areas which contain potentially failure-causing flaws, and it can ignore boundaries from which fracture is not likely, such as finite element model symmetry planes or compressively loaded external surfaces.

Program Capability and Description

The architecture and basic computational elements of the postprocessor program are described by Gyekenyesi (1986). Figure 1 shows the flowchart for the new surface flaw

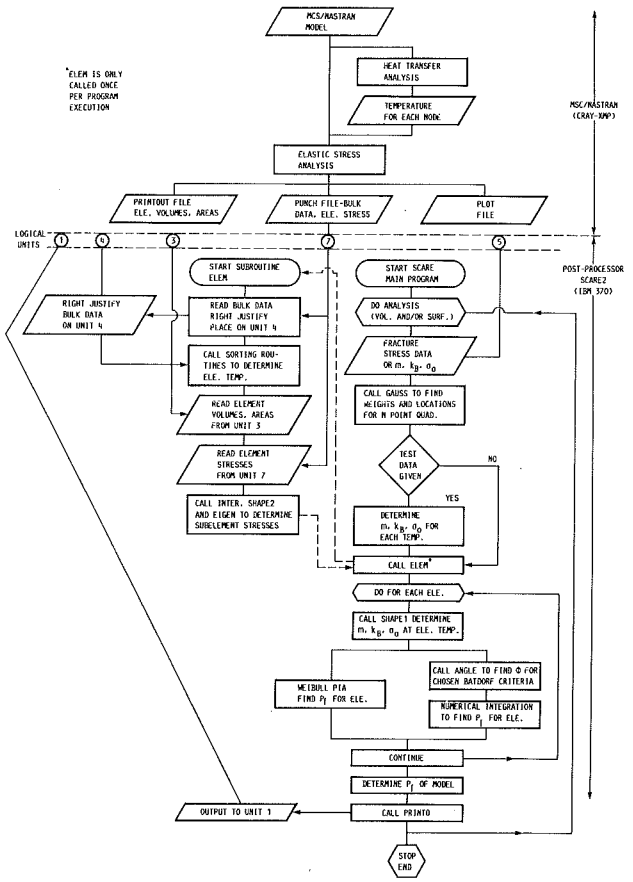

Fig. 1 Computational elements of the SCARE2 reliability analysis program

SCARE2 reliability analysis code, which is designed to be identical in its sequence of calculations to the previously developed volume flaw analysis. For computational efficiency, all experimental fracture stresses as well as all elemental principal stresses are normalized. When using the Weibull scale parameter σ_0 as the normalizing factor, it is important to note that different values of σ_0 are generally used in the volume and surface flaw calculations. For efficient transfer of MSC/NASTRAN output data to SCARE, FORTRAN logical units 3, 4, and 7 are used. Input to SCARE is handled through logical units 3, 5, and 7 while the output is stored on unit 1.

Presently, the program permits use of several fracture criteria, crack configurations, and temperature-dependent statistical material parameters. Uniaxial, surface flaw-induced, fracture data along with specimen geometry from four-point bend tests can be used to calculate Weibull parameters and the Batdorf flaw density coefficient. Figure 2 contains the available options in fracture criteria and flaw configurations used to model surface imperfections. Note that two of the failure criteria are for shear-insensitive cracks, even in multidimensional stress states. The other two are used for the shear-sensitive models, where the mechanistic G_c fracture criterion is employed to predict component reliability. Among the available criteria and crack configurations shown in Fig. 2, the Griffith notch with the G_c criterion has the highest shear sensitivity and hence, the highest failure probability for a given structure, while the PIA approach yields consistently the lowest failure estimate. It should also be noted that the Batdorf shear-insensitive fracture model is conceptually identical to the originally proposed Weibull normal stress averaging method, although it has been recognized early that, when using this method, an amplification factor is required to accentuate the materials sensitivity to surface defects (Paluszny and

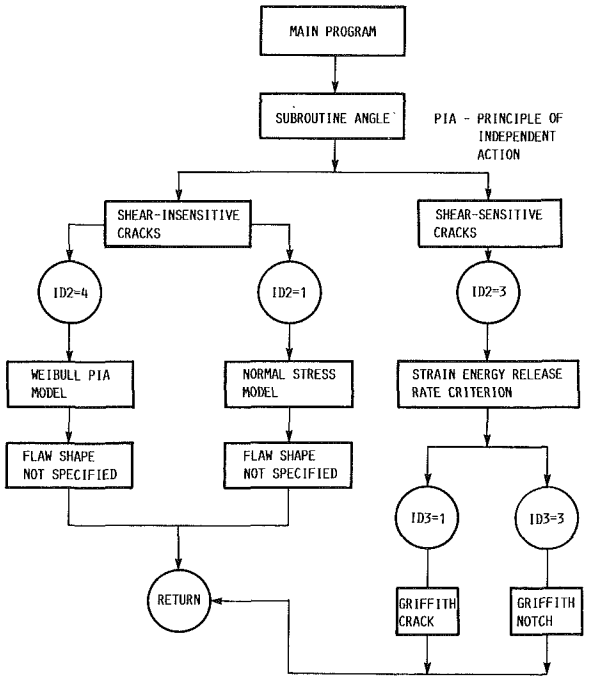

Fig. 2 Flowchart for subroutine ANGLE based on surface flaw fracture analysis

COLUMNS	VARIABLE	ENTRY AND DESCRIPTION
1-5	ID1	CONTROL INDEX FOR EXPERIMENTAL DATA 2: 4-PT. BENDING TEST DATA 3: ALL THE MATERIAL PARAMETERS m_s, σ_{os}, $\bar{k}_{Bs}$ ARE KNOWN AS INPUT
6-10	ID2	CONTROL INDEX FOR FRACTURE CRITERIA 1: SHEAR-INSENSITIVE, NORMAL STRESS CRITERION 3: TOTAL ENERGY RELEASE RATE CRITERION 4: WEIBULL PIA SHEAR-INSENSITIVE MODEL
11-15	ID3	CONTROL INDEX FOR CRACK SHAPES 1: GRIFFITH TYPE CRACK 3: GRIFFITH NOTCH TYPE CRACK
16-20	ID4	CONTROL INDEX FOR TYPE OF ANALYSIS 1: VOLUME FLAW BASED FRACTURE ANALYSIS 2: SURFACE FLAW BASED FRACTURE ANALYSIS 3: BOTH VOLUME AND SURFACE FLAW BASED FRACTURE ANALYSIS
21-25	IPRINT	CONTROL INDEX FOR PRINTING STRESSES 1: DO NOT PRINT ELEMENT STRESSES 0: PRINT ELEMENT STRESSES
END OF FIRST CARD OR STATEMENT NUMBER ONE		
BEGINNING OF SECOND CARD OR STATEMENT NUMBER TWO		
1-5	NE	NUMBER OF TOTAL HEXA AND PENTA ELEMENTS
6-10	NH	NUMBER OF HEXA ELEMENTS USED
11-15	NP	NUMBER IF PENTA ELEMENTS USED
16-20	NES	NUMBER OF TOTAL QUAD8 AND TRIA6 ELEMENTS
21-25	NSQ	NUMBER OF QUAD8 ELEMENTS USED
26-30	NST	NUMBER OF TRIA6 ELEMENTS USED
31-35	NA	NUMBER OF TRIAX6 ELEMENTS USED IN THE MODEL (VOLUME FLAW ANALYSIS ONLY)
36-40	NT	THE NUMBER OF TEST SPECIMENS AT A GIVEN TEMPERATURE
41-45	NGP	NUMBER OF GAUSSIAN QUADRATURE POINTS
46-50	NS	NUMBER OF SEGMENTS REQUIRED TO FORM THE ENTIRE STRUCTURE
51-55	JT	NUMBER OF TEST TEMPERATURES AT WHICH MATERIAL DATA IS SPECIFIED
56-60	LONL	CONTROL INDEX FOR SELECTING USE OF LINEAR OR NONLINEAR (QUADRATIC) ELEMENTS 0: ONLY LINEAR ELEMENTS ARE USED IN THE MODEL 1: ONLY QUADRATIC ELEMENTS ARE USED IN THE MODEL

Fig. 3 SCARE surface flaw-based analysis master control deck data requirements

Wu, 1977). No such factors, however, are used in the current version of the SCARE code.

In selecting thin shell elements to determine surface stress states, the existence of only two surface principal stresses is intrinsic to the analysis. In order to use WLT, any compressive elemental principal stress is not permitted to exceed three times the tensile principal stress in absolute value. Otherwise, compressive stress state predominates and the corresponding reliability is set equal to unity. Just like in uniaxial compressive loading, when using the PIA model with Weibull statistics, fracture due to compression is inadmissible.

Input Information

The SCARE computer program requires output from MSC/NASTRAN elastostatic analysis to determine component fast fracture reliability. Gyekenyesi (1986) discusses some of the available rigid format solution sequence options and also how the NASTRAN and SCARE programs interface on the Lewis laboratory computer system. The surface flaw analysis capability uses only HEXA, PENTA, QUAD8, and TRIA6 MSC/NASTRAN library elements, and modeling with axisymmetric elements is not permitted for external flaw reliability predictions. This restriction is due to NASTRAN finite element properties which rule out mixing of axisymmetric elements with any other element type in a given mesh. Only the HEXA and PENTA isoparametric elements should contribute to structural stiffness and the planar shell elements should have negligible thickness t, specified in NASTRAN ($t = 10^{-6}$ in. for the rotating disk example in this paper). In addition to the previously listed reasons for using shell elements, modeling a ceramic structure with them will also avoid the need for elemental stress transformations when calculating required surface principal stresses. For available stress recovery options, users should consult the appropriate analysis code manuals. With today's automatic mesh generation programs, little difficulty will be encountered in adding the required external elements. A solid element face is identified as an external surface when its nodes are shared by a shell element. The midside nodes may or may not be present, but current capability requires that either they are all there consistently, or they are all absent. Mixing of linear or quadratic elements in a given finite element mesh is not permitted. When using shell elements, only the membrane properties should be invoked and the uncoupled bending stiffness should not be included in the model.

SCARE input requirements for external flaw analysis are almost identical to the input data for internal flaw analysis, which has been previously summarized (Gyekenyesi, 1986). The postprocessor program is capable of doing the volume and surface flaw analysis in one execution. However, only the surface-distributed crack capability will be described in this paper. As before, program input can be grouped into three categories. The first category, shown in Fig. 3, is called the master control deck, which includes organization of control indices for fracture criteria, finite element model requirements, and material parameter format. Note that for calculating statistical parameters, data only from four-point bend tests can currently be used. In addition, two-lines or cards of data entry are now required rather than one as in the previous volume flaw analysis. The fracture criteria and flaw shapes for representing volume and surface imperfections can be independently specified, and users can select to perform analysis for volume flaw-based fracture only, for surface flaw-based fracture only, or for both simultaneously in one execution. Details on included options and limitations can be found in the program user's manual.

The second category, called the specimen deck, uses fracture specimen data required in calculating statistical fracture parameters, or direct input of material properties including Poisson's ratio. These material parameters are generally temperature dependent. Therefore, provision is made for input of multiple flaw populations at different temperatures. Unless material parameters are directly read, this section re-

quires four-point bend bar geometry and surface flaw-based failure stresses of the sample population. These extreme fiber failure stresses must be arranged in ascending order and currently up to 200 specimens can be used for a given temperature. The specimen deck also requires test temperatures, arranged in ascending order for multiple temperatures, since calculated material parameters are interpolated within SCARE. At a specified temperature, fracture stresses must be unique and multiple values of identical magnitudes are not permitted. The number of available fracture readings for all temperature tests must be the same. Additional explanation of the required input, including size limitations, can be found in the user's manual.

The last SCARE input category, called the structures deck, contains results of the finite element structural analysis required for failure probability predictions. These include solid element volumes, shell element areas, nodal temperatures (MSC/NASTRAN does not permit access to element temperatures), elemental principal stresses and corresponding element identification numbers. In the present version of SCARE, which relies on MSC/NASTRAN output files, all of these data are internally manipulated through subroutine ELEM, and the structures deck requires no specific input by the user.

Output Information

Grid point temperatures in the finite element mesh of a selected component can be obtained at transient or steady-state conditions from performing MSC/NASTRAN thermal analysis. Combining the resulting thermal loads with additional mechanical loads, the displacement and elastic stress fields can then be calculated. For surface flaw-based fracture analysis, shell element stresses, areas and temperatures are the required output from the analysis code. For available output options, users should consult the appropriate program manuals. The shell element stresses as well as the nodal temperatures from MSC/NASTRAN are stored in specified punch files, while surface element areas are listed in the program output file. Consequently, NASTRAN's punch option must be invoked to store the required stress and temperature data with the program's parameter call feature needed to calculate the required elemental areas.

The first part of all SCARE output data contains an echo of important NASTRAN finite element analysis results. Identifying labels, element type, and number of elements in the model are noted. Since in a large finite element mesh the stress output could be excessive, printed element stress tables in the new version of SCARE are optional as shown in Fig. 3. In addition, two new element cross-reference tables are printed. The first table lists the shell element number and gives the corresponding solid element with which its grid points are shared. The second table lists the solid element identification number and gives up to six associated shell elements (a HEXA element could have all of its six faces as an external surface). Element areas and temperatures (nodal averaged) are summarized in the following table. Next the selected fracture model is identified and the room temperature statistical fracture parameters are shown. Additionally, a table of discrete input temperatures with corresponding material parameters, which were either internally calculated or directly supplied, is printed. For the shear-sensitive fracture models, the crack shape is identified along with a more specific description of the fracture criterion. The last table in the SCARE output file contains an element results summary, listing the shell element number, corresponding element survival and failure probabilities, and interpolated (based on temperature) element material parameters. Finally, the overall component probability of failure as well as the component probability of survival are printed.

Theory

The most widely used mathematical models describing the statistical nature of fracture in brittle materials have been previously summarized by Gyekenyesi (1986). It is generally recognized that the weakest link hypothesis and the two-parameter Weibull cumulative strength distribution are appropriate to modeling surface flaw-induced failure in ceramic structures. Consequently, the uniaxial fracture data are approximated by

$$P_{fs} = 1 - \exp\left[-\int_A \left(\frac{\sigma_s}{\sigma_{0s}}\right)^{m_s} dA\right] \tag{1}$$

where the subscript s denotes parameters associated with the surface, P_{fs} is the cumulative failure probability, σ_{0s} is the scale parameter with dimensions of stress x (area)$^{1/m_s}$, m_s is the Weibull modulus which measures the degree of variability, σ_s is the applied surface tensile stress, and A the stressed area. The scale parameter is often called the unit area characteristic strength, and as m_s increases it approaches the material's ultimate strength. The selectively used Weibull threshold stress parameter σ_{us} is taken to be zero in equation (1) and is not shown therein.

In the analysis of failure of brittle materials subject to multiaxial stress states, the Weibull model, when combined with the PIA hypothesis, yields

$$P_{fs} = 1 - \exp\left\{-\int_A \left[\left(\frac{\sigma_{1s}}{\sigma_{0s}}\right)^{m_s} + \left(\frac{\sigma_{2s}}{\sigma_{0s}}\right)^{m_s}\right] dA\right\} \tag{2}$$

where σ_{1s} and σ_{2s} are the principal in-plane stresses acting on the surface of the structure. Equation (2) has been widely used in the past to estimate failure probabilities of ceramic components (Wertz and Heitman, 1980). The failure probability using the normal stress-averaging method, as extended to surface distributed flaw problems, can be calculated from

$$P_{fs} = 1 - \exp\left\{-\int_A \left[k_{wps}\int_C \sigma_{ns}^{m_s}\, dC\right] dA\right\} \tag{3}$$

where k_{wps} is the polyaxial Weibull crack density coefficient for surface flaws. This constant can be obtained by making the result of integrating equation (3), using the normal stress σ_{ns} distribution on an arbitrary plane, obtained from the reduced, plane-stress Cauchy infinitesimal tetrahedron in principal stress space as shown in Fig. 4, for uniaxial stress cases, agree with the results obtained from the uniaxial, two-parameter Weibull equation. Unlike for volume flaw-based analysis where closed-form integration is possible, the polyaxial Weibull surface crack density coefficient must be evaluated numerically. The contour integration is performed on the circumference of the unit circle C where the normal stress is tensile and neglecting regions where the normal stress is compressive. The cracklike flaws can then be regarded as located in these arbitrary planes which are tangent to the unit circle and are acted upon by σ_{ns} which is induced by the principal

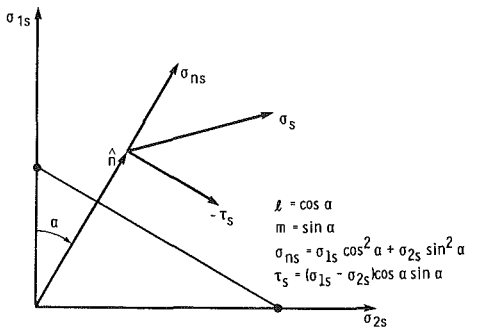

Fig. 4 Stresses on the reduced plane-stress Cauchy infinitesimal tetrahedron in principal stress space

stresses σ_{1s} and σ_{2s}. Since equation (3) is just the shear-insensitive case of the more general Batdorf polyaxial stress fracture model, its SCARE implementation follows a somewhat different format. The polyaxial Weibull equation has also been selectively used in the past (Paluszny and Wu, 1977), but since it neglects the effects of shear loads, it also underestimates failure for the more general loading condition. These unconservative predictions have been recognized early in ceramic structures and the use of amplification factors was proposed to better correlate predictions with measurements.

In the previously described two multidimensional stress fracture models, no mechanistic fracture criterion was needed to predict impending failure. In prior work by Batdorf (1973), Batdorf and Heinisch (1978), Shetty et al. (1984), and Samos (1982), attention is focused on cracks and their failure under stress. Since there is yet no consensus regarding how to treat mixed-mode fracture, even in metallic structures, the SCARE program includes several fracture criteria and flaw shapes. These criteria and flaw configurations include those traditionally treated, although recent research in ceramic fracture emphasizes more advanced fracture criteria and better modeling of flaw shapes (Petrovic, 1985).

Consider now a small uniformly stressed material element of area ΔA. The probability of failure under an applied state of stress can be written as

$$P_{fs} = P_{1s}\, P_{2s} \tag{4}$$

where P_{1s} is the probability of existence in ΔA of a crack having a critical stress in the range of σ_{cr} to $\sigma_{cr} + d\sigma_{cr}$, and P_{2s} denotes the probability that a crack of critical stress σ_{cr} will be oriented in a direction such that an effective stress σ_{es} equals or exceeds σ_{cr}. σ_{cr} is defined as the remote, uniaxial, normal fracture stress of a given crack. Failure will occur when the effective stress (a function of chosen crack configuration and fracture criterion) exceeds σ_{cr} for a particular crack. P_{1s} has the form

$$P_{1s} = \Delta A\, \frac{dN_s}{d\sigma_{cr}}\, d\sigma_{cr} \tag{5}$$

and

$$P_{2s} = \frac{\omega}{\pi} \tag{6}$$

where $N_s(\sigma_{cr})$ is the surface crack density function (the density of cracks having a critical stress $\leq \sigma_{cr}$) and ω is the angle in principal stress space containing all the crack orientations for which $\sigma_{es} \geq \sigma_{cr}$. Using the weakest link theory, the overall failure probability can be calculated from (Samos, 1982)

$$P_{fs} = 1 - \exp\left[-\int_A dA \int_0^{\sigma_{1s}} \left(\frac{\omega}{\pi}\right) \frac{dN_s}{d\sigma_{cr}}\, d\sigma_{cr}\right] \tag{7}$$

The surface crack density function $N_s(\sigma_{cr})$ is a material property which is expected to be of Weibull form since it is directly the cause of the observed Weibull strength distribution. However, for values of $m_s >> 1.0$, and assuming that large number of cracks are sampled, that is $\sigma_{cr} << \sigma_{0s} A^{-1/m_s}$, the Weibull distribution can be approximated by a power function, leading to

$$N_s\left(\sigma_{cr}\right) = k_{Bs}\sigma_{cr}^{m_s} \tag{8}$$

The surface flaw distribution parameters k_{Bs} and m_s can be evaluated from experimental data using uniaxial specimens and an appropriate fracture criterion. Since cracks in a real material are assumed to have an equal likelihood of orientation, and it is believed that there are so many cracks present that there is always one crack with the least-favorable orientation and that crack growth from this flaw causes failure, mode I fracture is intrinsic to uniaxial loading and the critical normal stress fracture criterion is always used to determine k_{Bs} from these tests. However, finishing operations such as grinding and environmental damage from erosion or oxidation may lead to anisotropic surface conditions, which then must be carefully accounted for in material characterization.

It is important to note that the use of various mixed-mode fracture criteria to evaluate k_{Bs} from uniaxially loaded specimens will result in different corresponding values of this flaw density parameter, from which it follows that the component reliability predictions will also change (Shetty et al., 1984). In fact the use of an identical mixed-mode fracture criterion to evaluate k_{Bs} from MOR bars first, and then subsequently calculate multiaxially loaded component reliability with it will result in contradictory trends, where with increased shear sensitivity, component failure rate predictions will decrease. In the present version of SCARE, failure rate predictions increase with increasing shear sensitivity, which follows from always assuming mode I fracture in uniaxial tests. Limited experimental data with monolithic ceramics (Samos, 1982) tend to validate the present approach, and the need for more pessimistic failure predictions than those obtained from the early phenomenological models is evident from component test records.

The statistical analysis of fracture is greatly simplified by assuming that cracks are shear insensitive. For this case fracture occurs when $\sigma_{es} = \sigma_{ns} \geq \sigma_{cr}$ and there is no need to specify the crack shape or the material's Poisson ratio. The effective stress just equals the normal stress acting on the crack plane.

When cracks are shear sensitive, equations for σ_{es} using various fracture criteria can be derived by equating selected parameters, induced by a uniaxial normal stress acting on a specified crack shape, to the selected parameters calculated for the mixed-mode or multiaxially loaded identical crack configuration. Some of the most widely used parameters to predict impending failure include the total coplanar strain energy release rate or crack extension force G_c, the maximum strain energy release rate $G_{\max}$, the minimum strain energy density S_c, the normal stress σ_{ns}, and the maximum tangential or hoop stress $\sigma_{\theta\theta}$. The $G_{\max}$, S_c, and $\sigma_{\theta\theta}$ fracture parameters predict out-of-plane crack extension, and consequently, are believed to be the most accurate for mixed-mode crack propagation. In any event, for polyaxial stress states, the effective stress σ_{es} is a function of both σ_{ns} and τ_s where τ_s is the shear stress in the crack plane. Both σ_{ns} and τ_s, acting on a plane whose normal and the maximum principal stress direction form an angle α, can be calculated from considering the equilibrium of forces in Fig. 4. Summing forces in the normal and tangential directions gives, respectively

$$\begin{aligned} \sigma_{ns} &= \sigma_{1s}\cos^2\alpha + \sigma_{2s}\sin^2\alpha \\ \tau_s &= \left(\sigma_{1s} - \sigma_{2s}\right)\cos\alpha\sin\alpha \end{aligned} \tag{9}$$

Using the G_c criterion and the two selected crack configurations, the effective stress equations obtained are (Samos, 1982)

$$\begin{aligned} \sigma_{es} &= \sqrt{\sigma_{ns}^2 + \tau_s^2} \qquad \text{(Griffith crack)} \\ \sigma_{es} &= \sqrt{\sigma_{ns}^2 + \frac{1}{1-\nu}\left(\frac{S_s}{1.1215}\right)^2} \qquad \text{(Griffith notch)} \end{aligned} \tag{10}$$

where ν is the Poisson ratio and S_s is the out-of-plane shear stress since τ_s does not cause crack growth in a Griffith notch. In general, the total coplanar strain energy release rate can be expressed in terms of stress intensity factors, summing damage in all appropriate crack growth modes. From equality of cross-shears, $S_s = \tau_s$ and equation (9) can be used to evaluate σ_{es} for both cracks.

The angle ω depends on the fracture criterion selected, the assumed crack configuration, and the applied stress state.

Closed-form expressions for ω can be derived for some fracture criteria in uniaxial and equibiaxial stress states (Samos, 1982). Assuming a uniaxial stress $\sigma_{1s} = \sigma_s$, and the normal stress (shear-insensitive) fracture criterion, we obtain from equation (9) at $\sigma_{ns} = \sigma_{cr}$, $\alpha = \alpha_{cr}$, and $\omega = 2\alpha_{cr}$ that

$$\frac{\omega}{\pi} = \frac{2}{\pi} \cos^{-1} \sqrt{\frac{\sigma_{cr}}{\sigma_s}} \tag{11}$$

Note that when a shear-sensitive fracture criterion is used, the crack shape must also be specified. In general, for two-dimensional stress states, ω must be determined numerically. Using the shear-insensitive case as an example, we obtain at fracture

$$\sigma_{es} = \sigma_{ns} = \sigma_{cr} = \sigma_{1s} \cos^2\alpha_{cr} + \sigma_{2s} \sin^2\alpha_{cr} \tag{12}$$

If we define $K = \sigma_{2s}/\sigma_{1s}$ and we note that $\alpha_{cr} = \omega/2$, equation (12) yields

$$P_{2s} = \frac{\omega}{\pi} = \frac{2}{\pi} \cos^{-1} \left[\frac{\left(\frac{\sigma_{cr}}{\sigma_{1s}}\right) - K}{1 - K} \right]^{1/2} \tag{13}$$

In order to avoid singular conditions ($\sigma_{1s} = \sigma_{2s}$) in equation (13), the following constraints must be imposed in calculating P_{2s}:

if $(\sigma_{cr}/\sigma_{1s} - K)/(1-K) < 0.0$ then $\omega = \pi$

if $(\sigma_{cr}/\sigma_{1s} - K)/(1-K) > 1.0$ then $\omega = 0$

$$\text{if } K = 1.0 \text{ then} \begin{cases} \omega = \pi \text{ if } \sigma_{1s} \geq \sigma_{cr} \\ \omega = 0 \text{ if } \sigma_{1s} < \sigma_{cr} \end{cases}$$

A similar procedure can be followed for the shear-sensitive Griffith crack using both of equation (9) in equation (10). However, for the Griffith notch it is computationally convenient to define $\phi = \cos^2\alpha_{cr}$, so that the fracture condition $\sigma_{es} \geq \sigma_{cr}$ can be written as (Samos, 1982)

$$c_1\phi^2 + c_2\phi + c_3 = 0 \tag{14}$$

Solving for ϕ gives

$$\phi = \cos^2\alpha_{cr} = \frac{-c_2 \pm \sqrt{c_2^2 - 4c_1c_3}}{2c_1} \tag{15}$$

where

$$\begin{aligned} c_1 &= (1-K)^2 \left(1 - \frac{0.795}{1-\nu}\right) \\ c_2 &= (1-K) \left[2K + (1-K) \frac{0.795}{1-\nu}\right] \\ c_3 &= K^2 - \left(\frac{\sigma_{cr}}{\sigma_{1s}}\right)^2 \end{aligned} \tag{16}$$

From equation (15), $\alpha_{cr} = \cos^{-1}\sqrt{\phi}$. Consequently

$$\frac{\omega}{\pi} = \frac{2}{\pi}\alpha_{cr} = \frac{2}{\pi} \cos^{-1} \left[\frac{-c_2 \pm \sqrt{c_2^2 - 4c_1c_3}}{2c_1} \right]^{1/2} \tag{17}$$

Following an analogous procedure to the above in using fracture criteria and flaw shapes, similar expressions for P_{2s} in terms of principal stresses and σ_{cr} can be developed. Results of this analysis are summarized in Table 1 and details are given by Samos (1982). In addition, special stress states, such as the equibiaxial loading case where $K = 1.0$ and when equation (17) becomes singular, are treated.

The equations in Table 1 apply only when σ_{ns} is tensile. When a compressive normal stress state exists, the angle where the normal stress changes from tensile to compressive is calculated. This transition angle divides all possible crack orientations into a tensile normal stress region and a compressive normal stress region, where each region has a different effective stress equation. In the compressive stress region σ_{ns} is set equal to zero, and with friction between crack faces ignored, σ_{es} is a function of only the applied shear load. In each region, the angle at which $\sigma_{es} = \sigma_{cr}$ is calculated. This angle further divides the region into areas where $\sigma_{es} \geq \sigma_{cr}$ and $\sigma_{es} < \sigma_{cr}$. If there is no such angle within the given region, then either there is no contribution to ω from that region or the entire region is included. A calculation comparing σ_{es} to σ_{cr} for a selected angle α identifies which subregion, or whether the whole region, contributes to ω. After determining each ω from the tensile and compressive regions separately, the total angle ω is simply the sum of the two contributions.

Table 1 Forms of P_{2s} for various shear-sensitive fracture criteria and selected surface crack configurations (σ_{ns} is tensile)

Fracture criterion	Crack configuration	P_{2s} where $K = \frac{\sigma_{2s}}{\sigma_{1s}}$
Coplanar strain energy release rate (G_c)	Griffith crack (G.C.)	$\frac{\omega}{\pi} = \frac{2}{\pi}\cos^{-1}\left[\frac{\left(\frac{\sigma_{cr}}{\sigma_{1s}}\right)^2 - K^2}{1-K^2}\right]^{1/2}$ if $\left[\left(\frac{\sigma_{cr}}{\sigma_{1s}}\right)^2 - K^2\right] \Big/ (1-K^2) < 0$, then $\omega = \pi$ if $\left[\left(\frac{\sigma_{cr}}{\sigma_{1s}}\right)^2 - K^2\right] \Big/ (1-K^2) > 1.0$, then $\omega = 0$ if $K = 1.0$ then $\begin{cases} \omega = \pi \text{ if } \sigma_{1s} \geq \sigma_{cr} \\ \omega = 0 \text{ if } \sigma_{1s} < \sigma_{cr} \end{cases}$
	Griffith notch (G.N.)	$\frac{\omega}{\pi} = \frac{2}{\pi}\cos^{-1}\left[\frac{-c_2 \pm \sqrt{c_2^2 - 4c_1c_3}}{2c_1}\right]^{1/2}$ where $c_1 = (1-K)^2\left[1 - \frac{0.795}{1-\nu}\right]$; $c_3 = K^2 - \left(\frac{\sigma_{cr}}{\sigma_{1s}}\right)^2$ $c_2 = (1-K)\left[2K + \frac{0.795}{1-\nu}(1-K)\right]$ and if $c_2^2 - 4c_1c_3 < 0$, then $\begin{cases} \omega = \pi \text{ if } \sigma_{2s} \geq \sigma_{cr} \\ \omega = 0 \text{ if } \sigma_{2s} < \sigma_{cr} \end{cases}$ Let $\phi_1 = \frac{-c_2 - \sqrt{c_2^2 - 4c_1c_3}}{2c_1}$ and $\phi_2 = \frac{-c_2 + \sqrt{c_2^2 - 4c_1c_3}}{2c_1}$ if $\begin{cases} \phi_1 < 0.0 \text{ and } \phi_2 < 0.0 \\ \text{or } \phi_1 < 0.0 \text{ and } \phi_2 > 1.0 \\ \text{or } \phi_1 > 1.0 \text{ and } \phi_2 < 0.0 \\ \text{or } \phi_1 > 1.0 \text{ and } \phi_2 > 1.0 \end{cases}$ then $\begin{cases} \omega = \pi \text{ if } \sigma_{2s} \geq \sigma_{cr} \\ \omega = 0 \text{ if } \sigma_{2s} < \sigma_{cr} \end{cases}$ if $K = 1.0$ then $\begin{cases} \omega = \pi \text{ if } \sigma_{1s} \geq \sigma_{cr} \\ \omega = 0 \text{ if } \sigma_{1s} < \sigma_{cr} \end{cases}$

An alternate approach to calculating P_{2s} has also been previously developed, where the angle α is incremented over the unit circle, and at each discrete point the contribution of σ_{ns} or σ_{es} is summed depending on whether they are equal to or greater than σ_{cr}. Since σ_{cr} is always positive, compressive σ_{ns} or σ_{es} will never contribute to fracture. The same method can also be used in volume flaw-based failure analysis, where two angles must be incremented so that the stresses are checked at all points on the unit sphere. This procedure, when compared to the previous method used to calculate P_{2s}, is computationally much more intensive. Consequently, SCARE employs the more efficient approach and the equations summarized in Table 1 are coded to calculate critical crack orientations.

In the SCARE program the required integration is performed by using Gaussian quadratures. Employing the power function form of $N_s(\sigma_{cr})$ and the appropriate equation for P_{2s} in equation (7), the failure probability using the Batdorf approach for surface flaws can be calculated. Unlike for volume

flaw analysis where a double numerical integration is generally required, surface flaw analysis uses only a single integration for the critical stress. Assuming that the stress state is constant in any given shell element (SCARE1 version) or subelement (SCARE2 version), the area integration over the material surface becomes trivial. For component reliability analysis, the elemental survival probabilities are summed according to established probability axioms, that is, we evaluate the product of all the individual, constant stress state elemental reliabilities. For two mutually exclusive events, such as the calculation of P_{fs} and P_{ss}, it is well known that for a given area increment their sum is always unity, where P_{ss} denotes surface survival probability. Finally, if a component includes two concurrent modes of possible failure, such as due to simultaneous internal or external flaws, its total reliability can be determined from the product of its individual cause reliabilities.

Material Strength Characterization

Uniaxial ceramic strength data are usually obtained from flexure testing of simple geometry specimens, and recording the extreme fiber tensile stress in the most highly loaded area at fracture. The Weibull parameters σ_{0s} and m_s as well as the Batdorf flaw density parameter k_{Bs} are evaluated in SCARE using four-point MOR data with known geometry. Fracture is sometimes assumed to occur always between the symmetrically placed inner loads on the tensile side (Samos, 1982), but in SCARE an effective area is used which permits failure in any tensile loaded areal element of the bar (Govila, 1983). It should be noted that for uniaxial tensile loading the effective area A_e reduces to A, the specimen gauge surface area. In all other types of loading, A_e is a function of specimen geometry and material Weibull modulus. If we express the uniaxial flexure failure probability in terms of the maximum extreme fiber fracture stress σ_f or MOR using Weibull form, that is

$$P_{fs} = 1 - \exp\left[-C_s \sigma_f^{m_s}\right] \tag{18}$$

then after evaluating C_s and m_s by the least-squares method, σ_{0s} and k_{Bs} can be calculated. Using the effective area for a rectangular beam in four-point bending (Govila, 1983)

$$A_e = \left\{ \left[\frac{\left(\frac{L_2}{L_1}\right) m_s + 1}{2(m_s+1)^2} \right] \left(\frac{m_s w}{w+h} + 1 \right) \right\} 2L_1(h+w) \tag{19}$$

where L_1 is the length between the outer loads, L_2 is the length between the inner loads, w is the beam width, and h is the beam height, we can rewrite equation (1) as

$$P_{fs} = 1 - \exp\left[-A_e \left(\frac{\sigma_f}{\sigma_{0s}}\right)^{m_s}\right] \tag{20}$$

Comparing equations (18) and (20) where in both equations the maximum extreme fiber stress is used as the reference value, we conclude that for the same failure probability

$$\sigma_{0s} = \left(\frac{A_e}{C_s}\right)^{1/m_s} \tag{21}$$

In addition to determining σ_{0s} and m_s, the SCARE program requires knowledge of k_{Bs}. Assuming shear-insensitive fracture, equation (11) can be substituted into equation (7) to obtain

$$P_{ss} = \exp\left[-\int dA \int_0^{\sigma_{1s}} \left(\frac{2}{\pi} \cos^{-1} \sqrt{\frac{\sigma_{cr}}{\sigma_{1s}}}\right) \frac{dN}{d\sigma_{cr}} d\sigma_{cr}\right] \tag{22}$$

Taking the natural log of equation (22) and integrating by parts yields

$$\ln P_{ss} = -\frac{A_e}{\pi} \int_0^{\sigma_{1s}} \frac{N_s(\sigma_{cr})}{\sqrt{\sigma_{cr}}\sqrt{\sigma_{1s}-\sigma_{cr}}} d\sigma_{cr} \tag{23}$$

where A_e is given by equation (19) ($A_e \approx wL_2$) for the four-point bend specimen. Equation (23) is an Abel integral equation with the solution (Batdorf and Chang, 1977)

$$A_e N_s(\sigma_{cr}) = -2\sqrt{\sigma_{cr}} \int_0^{\sigma_{cr}} \frac{d^2}{d\sigma_{1s}^2} \cdot [\ln P_{ss}(\sigma_{1s})] \sqrt{\sigma_{cr}-\sigma_{1s}}\, d\sigma_{1s} \tag{24}$$

From equation (18) with $\sigma_{1s} = \sigma_f$ as the reference stress

$$\frac{d^2}{d\sigma_{1s}^2} [\ln P_{ss}(\sigma_{1s})] = m_s(m_s-1)\,[-C_s \sigma_{1s}^{m_s-2}] \tag{25}$$

Introducing a new variable η defined as $\eta = (2\sigma_{1s}/\sigma_{cr}) - 1$ and substituting equation (25) into equation (24), we obtain

$$N_s(\sigma_{cr}) = \frac{2^{3/2-m_s}}{A_e} C_s m_s (m_s-1) \sigma_{cr}^{m_s} \cdot \int_{-1}^{1} (1+\eta)^{m_s-2}(1-\eta)^{1/2}\, d\eta \tag{26}$$

Now from equation (21) $C_s = A_e \sigma_{0s}^{-m_s}$, and consequently C_s and A_e can be eliminated from equation (26) and σ_{0s} used instead. Since $N_s(\sigma_{cr}) = k_{Bs}\, \sigma_{cr}^{m_s}$, k_{Bs} can be evaluated by numerically integrating equation (26) using Gaussian quadratures. Since σ_{0s} is used, the effective area given by equation (19) is inherent in $N_s(\sigma_{cr})$. It is interesting to note that $N_s(\sigma_{cr})$ can be determined more easily from equibiaxial tensile tests since for $\sigma_{1s} = \sigma_{2s} = \sigma_{ns} = \sigma$, $\omega/\pi = 1.0$ and

$$N_s(\sigma_{cr}) = -\frac{1}{A_{eb}} \ln P_{ss} = \frac{C_s}{A_{eb}} \sigma_{cr}^{m_s} = k_{Bs}\, \sigma_{cr}^{m_s} \tag{27}$$

where A_{eb} is the effective equibiaxially loaded tensile area and the equibiaxial failure rate is assumed to also follow equation (18). When using the least squares method with equation (18) to evaluate C_s and m_s, P_{fs} can be determined from ranked fracture stress data using the simple equation

$$P_{fs}\ (\sigma_{js}) = \frac{j}{N+1} \tag{28}$$

where N is the total number of uniaxial or equibiaxial tests and j is the rank of the surface fracture stress σ_{js}.

Example

In order to test the surface crack distributed reliability analysis in SCARE, several sample problems were analyzed from the open literature. In addition, the rotationally loaded, silicon nitride annular disk (Gyekenyesi, 1986) was reanalyzed assuming that fractures in the MOR bars as well as the disks were caused by surface flaws. The Weibull modulus m_s was set equal to $m = 7.65$ as before, but the previously used, volume flaw-based scale parameter σ_0 was readjusted so that $P_f = P_{fs}$ in the MOR bars, when both are loaded in uniform tension. As a result of this requirement, we obtain for the four-point bend specimen that

$$\sigma_{0s} = \left(\frac{A_e}{V_e}\right)^{1/m_s} \sigma_0 = \left[\frac{2(m_s w + w + h)}{wh}\right]^{1/m_s} \sigma_0 \tag{29}$$

From Gyekenyesi (1986), $\sigma_0 = 74.82$ MPa $m^{0.3922}$ (45,800 psi $in.^{0.3922}$) and the "A-size" test bars had dimensions of $w = 0.635$ cm (0.25 in.), $h = 0.3175$ cm (0.125 in.), $L_1 = 1.905$ cm (0.75 in.), and $L_2 = 0.9525$ cm (0.375 in.). A_e is given by equation (19) and V_e is the effective volume in four-point bending, that is

$$V_e = \frac{wh}{2}\left[\frac{L_1 + m_s L_2}{(m_s+1)^2}\right] \tag{30}$$

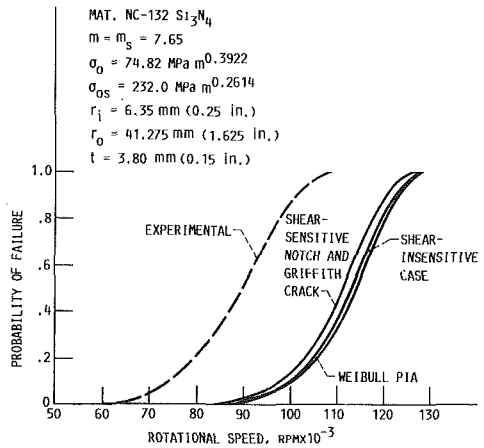

Fig. 5 Example 1 probability of failure versus disk rotational speed for various fracture models (SCARE2 data). Surface flaw-induced failure is assumed in all analysis.

Table 2 Example 1 failure probabilities as a function of rotational speed for various fracture models

$[m_s = 7.65;\ \sigma_{0s} = 232.0$ MPa $(m)^{0.2614};\ k_{Bs}\sigma_{0s}^{m_s} = 4.986;$ NGP = 15]

Angular speed, rpm	SCARE2 (HEXA AND QUAD8 elements)				Experimental (Ford Motor Co.)[a] (Gyekenyesi, 1986)
	Weibull PIA	Batdorf shear-insensitive	Batdorf shear-sensitive G.C. G_c criterion	Batdorf shear-sensitive G.N. G_c criterion	
80 000	0.0031	0.0034	0.0044	0.0045	0.2017
85 000	.0078	.0087	.0113	.0114	.3367
93 000	.0304	.0339	.0438	.0441	.6321
100 000	.0898	.0996	.1276	.1283	.8714
105 000	.1796	.1979	.2496	.2508	.9640
110 000	.3309	.3610	.4418	.4436	.9949
115 000	.5497	.5889	.6857	.6877	.9997
120 000	.7828	.8176	.8908	.8922	1.0000
125 000	.9417	.9579	.9838	.9842	1.0000
130 000	.9945	.9970	1.0000	1.0000	1.0000

G.C. - Griffith crack
G.N. - Griffith notch
[a]Experimental data fitted to a Weibull equation and calculated at the speeds shown.

Using the given data in equation (29), we obtain that $\sigma_{0s} = 232.0$ MPam$^{0.2614}$ (87,891 psi in.$^{0.2614}$). The dimensions of the disk are given in Fig. 5, and the same MSC/NASTRAN analysis was performed as for volume flaws with the exception that shell elements were added to identify external surfaces, to calculate their areas and to identify appropriate surface stress states. Reliability calculations were made at various speeds using several surface crack fracture models. Selected results from these analyses are shown in Fig. 5 and Table 2. For a given speed, failure probabilities are considerably less than those obtained by Gyekenyesi (1986) for all fracture models, indicating that failure was most likely due to volume flaws as originally concluded. Obviously, the main reason for the greatly decreased failure estimates is the much higher equivalent surface Weibull scale parameter σ_{0s}. Results for the shear-sensitive Griffith crack and notch were practically identical, with the notch being slightly more shear sensitive as expected. The importance of post-mortem fractography to identify the nature of the fracture-causing flaws is evident from the two widely different set of answers obtained for the same problem. Furthermore, the difference between predictions from various available surface crack fracture theories for a specified loading is considerably less than the difference found in volume flaw-based failure models.

In addition to comparing surface and volume flaw-based analyses for the same ceramic structure, failure probability was calculated for a transversely loaded circular alumina disk and compared to data obtained by Brockenbrough et al. (1985). These data consisted of calculated failure probabilities obtained from using Batdorf's shear-insensitive fracture theory in conjunction with the finite element analysis code ANSYS. The selected disk had an outside radius $r_o = 25$ mm (0.984 in.), a thickness of $t = 2.5$ mm (0.098 in.), was loaded by a circular line load at $r = 1.5$ mm (0.059 in.) and was simply supported at a radius of 22 mm (0.866 in.). After matching the stress solutions for a given load from the two different finite elements codes (MSC/NASTRAN and ANSYS), the failure probabilities were calculated at various loads. Typically, to obtain a $P_{fs} = 0.50$, SCARE2 predicted a total line load of 1105 N (248.3 lb), while according to Brockenbrough et al. (1985) (corrected version) a line load of approximately 1130 N (253.9 lb) had to be applied, showing good agreement between the two load predictions.

Conclusions

The general purpose, statistical, fast fracture failure probability code SCARE has been enhanced to include the possibility of failure due to two concurrent but not interacting flaw populations. In addition, reliability analysis with linear finite elements is now also possible. The program includes a number of widely used polyaxial fracture models, appropriate extreme value statistics, and the ability to calculate material failure distribution parameters for both volume and surface-distributed flaws. Current work includes the planned addition of more advanced increasingly shear-sensitive failure criteria which permit out-of-plane crack extension for both types of imperfection. In addition, the influence of bimodal flaw populations on individual material parameters, through censored data analysis, needs to be determined. Finally, the problem of a transversely loaded circular plate will be newly studied to resolve some of the contradictory trends reported by Rufin et al. (1984) and Shetty et al. (1984).

References

Batdorf, S. B., 1978, "Fundamentals of the Statistical Theory of Fracture," in: *Fracture Mechanics of Ceramics*, Vol. 3, Flaws and Testing, R. C. Bradt, D. P. H. Hasselman, and F. F. Lange, eds., Plenum Press, pp. 1–30.

Batdorf, S. B., 1973, "Fracture Statistics of Isotropic Brittle Materials With Surface Flaws," Air Force Systems Command, Air Force Rep. No. SAMSO-TR-73-378.

Batdorf, S. B., and Chang, D. J., 1977, "On the Relation Between the Fracture Statistics of Volume Distributed and Surface Distributed Cracks," University of California at Los Angeles, UCLA-ENG-7723.

Batdorf, S. B., and Heinisch, H. L. Jr., 1978, "Fracture Statistics of Brittle Materials With Surface Cracks," *Engineering Fracture Mechanics*, Vol. 10, No. 4, pp. 831–841.

Brockenbrough, J. R., Forsythe, L. E., and Rolf, R. L., 1985, "Reliability of Brittle Materials in Thermal Shock," Alcoa Laboratories, AL Rep. No. 52-85-22.

Govila, R. K., 1983, "Statistical Strength Evaluation of Hot-Pressed Si_3N_4," *American Ceramic Society Bulletin*, Vol. 62, No. 11, pp. 1251–1258.

Gyekenyesi, J. P., 1986, "SCARE: A Postprocessor Program to MSC/NASTRAN for Reliability Analysis of Structural Ceramic Components," ASME JOURNAL OF ENGINEERING FOR GAS TURBINES AND POWER, Vol. 108, No. 3, pp. 540–546.

Johnson, C. A., 1983, "Fracture Statistics of Multiple Flaw Distributions," *Fracture Mechanics of Ceramics*, Vol. 5, Surface Flaws, Statistics, and Microcracking, R. C. Bradt, A. G. Evans, D. P. H. Hasselman, and F. F. Lange, eds., Plenum Press, New York, pp. 365–386.

Paluszny, A., and Wu, W., 1977, "Probabilistic Aspects of Designing With Ceramics," ASME JOURNAL OF ENGINEERING FOR POWER, Vol. 99, No. 4, pp. 617–630.

Petrovic, J. J., 1985, "Mixed-Mode Fracture of Hot-Pressed Si_3N_4, "*Journal of the American Ceramic Society*, Vol. 68, No. 6, pp. 348–355.

Rufin, A. C., Samos, D. R., and Bollard, R. J. H., 1984, "Statistical Failure Prediction Models for Brittle Materials," *AIAA Journal*, Vol. 22, No. 1, pp. 135–140.

Samos, D. R., 1982, "Experimental Investigation and Probability of Failure Analysis of Pressure Loaded Alumina Discs," M.S. Thesis, University of Washington.

Shetty, D. K., Rosenfield, A. R., and Duckworth, W. H., 1984, "Statistical Analysis of Size and Stress State Effects on the Strength of an Alumina Ceramic," *Methods for Assessing the Structural Reliability of Brittle Materials*, ASTM-STP-844, S. W. Freiman and C. M. Hudson, eds., American Society for Testing and Materials, Philadelphia, PA, pp. 57–80.

Weibull, W., 1939, "A Statistical Theory of the Strength of Materials," *Ingeniors Vetenskaps Akademien Handlinger*, No. 151.

Wertz, J. L., and Heitman, P. W., 1980, "Predicting the Reliability of Ceramic Turbine Components," *Advanced Gas Turbine Systems for Automobiles*, SAE-SP-465, Society of Automotive Engineers, pp. 69–77.

Mixed-Mode Fracture Criteria for Reliability Analysis and Design With Structural Ceramics

D. K. Shetty
Department of Materials Science and Engineering,
University of Utah,
Salt Lake City, UT 84112

Increasing use of ceramics in structural applications has led to the development of a probabilistic design methodology that combines three elements: linear elastic fracture mechanics theory that relates strengths of ceramics to size, shape, and orientation of critical flaws, a characteristic flaw size distribution function that accounts for the size effect on strength via the weakest-link concept, and a time-dependent strength caused by subcritical crack growth or other mechanisms. This paper reviews recent research that has been focused on the first of the above three elements, the investigation of fracture criteria for arbitrarily oriented flaws in ceramics, i.e., the mixed-mode fracture problem in linear elastic fracture mechanics theory. Experimental results obtained with two-dimensional through cracks and three-dimensional surface (indentation) cracks are summarized and compared to mixed-mode fracture criteria. The effects of material microstructure and the stress state on mixed-mode fractures are discussed. The application of mixed-mode fracture criteria in reliability analysis is illustrated for several simple stress states in the absence of time-dependent strength degradation.

Introduction

Advanced ceramics such as Si_3N_4 and SiC possess a combination of properties that make them attractive as structural materials, particularly in high-temperature applications. Among these properties are outstanding high-temperature strength and creep resistance, oxidation, corrosion and erosion resistance, and low coefficient of thermal expansion. These properties, coupled with their low densities, ready availability of source raw materials, and potential low cost in large-scale production, have made ceramics attractive substitutes to replace high-temperature alloys in applications such as advanced heat engines (Katz, 1985). The potential for designing advanced heat engines with ceramic components that can operate at high temperatures with significantly reduced cooling and the consequent improved fuel efficiency is a major driving force for using ceramics in heat engines.

With the exception of some high-toughness grades of zirconia ceramics and the newly emerging ceramic-matrix composites, structural ceramics are generally brittle and exhibit little or no plasticity and a low resistance to fracture. The low fracture toughness poses unique challenges in structural design with ceramics. First, failure in ceramics is initiated at small flaws, typically 50 to 200 μm, a size range that is below the detection capability of currently available nondestructive examination techniques. Flaws in this size range are also difficult to avoid or control in ceramic processing, surface finishing, or in in-service damage. As a consequence, fracture stresses of ceramics exhibit considerable scatter and require statistical or probabilistic description. Secondly, failure stress of a ceramic is often determined by the critical stress for the unstable extension of the most severe flaw; in other words, failure stresses of ceramics follow the weakest-link principle. This results in a size dependence of the fracture stress since the severity of the critical flaw increases with increasing size of the ceramic under stress. The scatter and size dependence of ceramic strengths are treated by statistical fracture theories that are based on the weakest-link or extreme-value principles (Weibull, 1939; Batdorf and Crose, 1974). A third characteristic of ceramic strengths that complicates structural design is its variation due to the combined effects of stress, temperature, and environment in service conditions. Strengths of ceramics can degrade in service as a result of subcritical growth of existing flaws or due to generation of new flaws by such mechanisms as creep cavitation, oxidation, corrosion, or erosion.

The design methodology that has evolved over the last decade for structural ceramics incorporates all of the above characteristics of the strengths of ceramics. The major elements of this design methodology are outlined in Fig. 1. There are two distinct stages in the design procedure. First, a fast fracture reliability, i.e., the probability of survival on application of the service load, is assessed for the ceramic component under consideration based on a precise stress analysis of the component, usually by finite element methods, and the intrinsic strength distribution of the ceramic assessed in simple laboratory tests such as the four-point bend tests. The second stage of the design exercise calculates long-term reliability or probability of survival under the design loading conditions

Contributed by the Gas Turbine Division of THE AMERICAN SOCIETY OF MECHANICAL ENGINEERS and presented at the 32nd International Gas Turbine Conference and Exhibit, Anaheim, California, May 31–June 4, 1987. Manuscript received at ASME Headquarters February 5, 1987. Paper No. 87-GT-70.

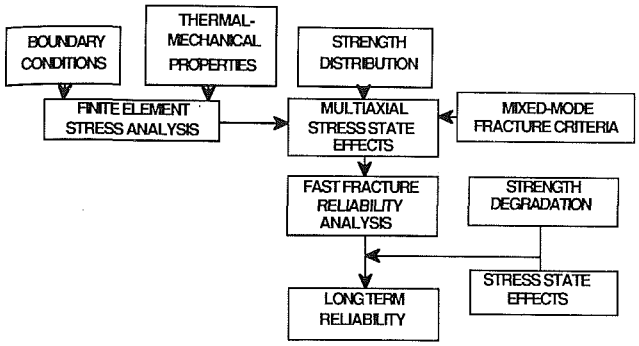

Fig. 1 Major elements of a reliability analysis of design with structural ceramics

based on an input of material parameters that characterize strength degradation in service.

Since structural ceramics such as Si_3N_4 and SiC fail from cracklike flaws, it is reasonable to expect that fracture mechanics theory should play a central role in reliability analysis. However, until very recently brittle material design practice predominantly used the Weibull approach to predict fast fracture reliability of ceramic components using the fast fracture strength distributions assessed in simple uniaxial stress states (Paluszny and Wu, 1977). Fracture mechanics theory has been used only peripherally to account for the time dependence of reliability by incorporating semiempirical models for strength degradation via slow crack growth (Paluszny and Nicholls, 1978).

More recently, NASA has initiated the development of a brittle materials design program that combines a finite element stress and thermal analysis program with a reliability analysis based explictly on the weakest-link and fracture mechanics concepts as outlined by Batdorf (Gyekenyesi, 1986). The Batdorf analysis differs from the Weibull approach in that stress state effects on fracture stresses are accounted for in a physically realistic way by explicitly considering fracture criteria for cracklike flaws arbitrarily oriented with respect to the applied stresses, i.e., mixed-mode fracture criteria in fracture mechanics terms. The purpose of this paper is twofold. First, it presents a summary of the recent investigations that have examined mixed-mode fracture in structural ceramics. Secondly, the paper illustrates how the mixed-mode fracture criteria established for structural ceramics can be used in reliability analysis of simple biaxially loaded test specimens based on uniaxial strength data.

Fast Fracture Reliability Analysis

For a structural ceramic that fails from cracklike flaws the cumulative probability of fracture F, when subjected to a general multiaxial loading, can be written as (Batdorf and Heinisch, 1978a)

$$F = 1 - \exp[-\rho \int\int f(\sigma, \sigma_c)\{dN(\sigma_c)/d\sigma_c\} d\sigma_c dA] \quad (1)$$

where ρ = surface flaw density, i.e., number of cracks per unit area; A = surface area under stress; σ = remote applied stress, i.e., maximum principal stress; $N(\sigma_c)$ = a cumulative flaw size distribution function expressed as the fraction of the flaws that can lead to fracture when the effective stress relative to the crack plane is $< \sigma_c$; $f(\sigma, \sigma_c)$ = fraction of the flaws that can cause fracture in the critical stress range σ_c to $\sigma_c + d\sigma_c$.

Equation (1) assumes that a single population of surface flaws, characterized by the distribution function $N(\sigma_c)$, contributes to the fracture of the ceramic. N is dependent on the surface condition of the ceramic and it can be influenced by the surface finish given to the ceramic. For volume flaws, the size distribution function N is integrated over the stressed volume. The flaw density ρ is usually incorporated in a scale parameter of N, and therefore it is not necessary to determine the absolute density of the flaws. For multiple-flaw populations, for example, surface flaws and volume flaws, two separate distribution functions must be considered in equation (1).

Following Weibull (1939), the distribution function for flaw sizes is usually taken to be a simple power function

$$N(\sigma_c) = (\sigma_c/\sigma_0)^m \quad (2)$$

where m is a shape parameter commonly referred to as the Weibull modulus and σ_0 is a scale parameter. Although the power function form of equation (2) is used here for analytical convenience, the formalism of equation (1) can be used with more general flaw distribution functions (Batdorf and Crose, 1974).

The fraction f is determined by the orientation distribution of the flaws, the mixed-mode fracture criterion applicable to the flaws, and the applied stress state. Thus, f serves as the fracture mechanics link to the weakest-link formalism of the statistical fracture theory. For example, for surface cracks normal to the stressed surface but randomly oriented in the plane, $f = 1$ for an equibiaxial stress state, since cracks of all orientations relative to the principal stresses are subjected to the same normal stress.

For randomly oriented surface cracks subjected to uniaxial tension, the fraction of cracks that can cause fracture at any applied stress can be formulated as

$$f = (2\theta_c/\pi) \quad (3)$$

where θ_c is a critical maximum angle between the normal to a crack plane and the applied stress ($\sigma = \sigma_1$) direction. Only those cracks whose normals lie at angles less than θ_c can cause fracture and contribute to the fracture probability. The functional form of θ_c depends upon the applicable mixed-mode fracture criterion. It should be noted that equation (3) is applicable only for randomly oriented flaws. For nonrandom or preferentially oriented surface flaws or for volume flaws appropriate relations for f can be formulated for specific cases of anisotropically distributed flaws (Batdorf and Heinisch, 1978b).

If it is assumed, for example, that only the remote stress normal to the crack plane causes fracture, it can be shown that θ_c for random surface flaws in uniaxial tension has the functional form

$$\theta_c = \cos^{-1}[(\sigma_c/\sigma)^{1/2}] \quad (4)$$

On the other hand, if the fracture criterion for an arbitrarily oriented surface crack is assumed to be of the form

$$\sigma_e = (\sigma_N^2 + \tau^2)^{1/2} = \sigma_c \quad (5)$$

where σ_e = an effective stress that causes fracture; σ_N = tensile stress normal to the crack plane; and τ = shear stress parallel to the crack plane; i.e., a fracture criterion that combines the effects of both remote tensile and shear stresses, a mixed-mode fracture criterion in fracture mechanics terminology, then θ_c for uniaxial tension and random surface flaws can be shown to be (Batdorf and Heinisch, 1978b)

$$\theta_c = \cos^{-1}[\sigma_c/\sigma] \quad (6)$$

Equations (4) and (6) for the critical angles were derived for particularly simple analytical forms of the fracture criteria. In general, strength-controlling flaws in ceramics do not necessarily obey these simple fracture criteria when they are arbitrarily oriented to the principal stresses. A number of studies in recent years have addressed this issue of mixed-mode fracture of ceramics from the viewpoint of linear elastic fracture mechanics theory. These results should be applicable to reliability analysis provided the behavior of large, well-defined cracks treated by linear elastic fracture mechanics

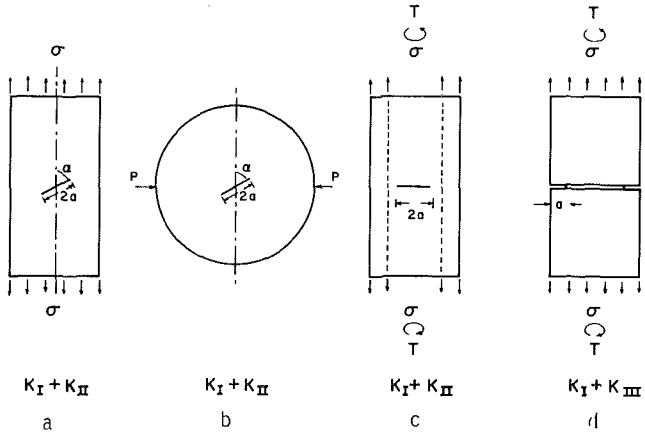

Fig. 2 Test methods used to study mixed-mode fracture in ceramics

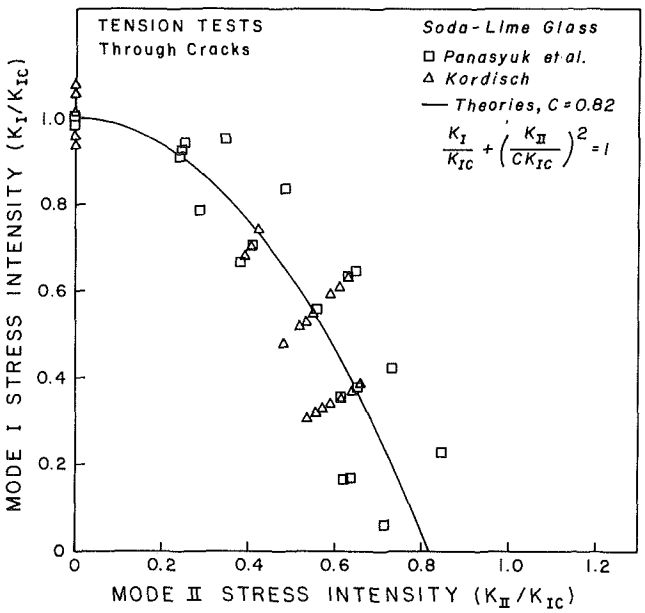

Fig. 3 Combined mode I-mode II fracture toughness of soda-lime glass measured in tension tests with inclined through cracks

theory can simulate the behavior of small, strength-controlling flaws in structural ceramic components.

Mixed-Mode Fracture of Structural Ceramics

Experimental Results – Large Through Cracks. Figure 2 illustrates the different test specimens and large crack geometries that have been used in experimental studies of mixed-mode fracture of brittle materials. The plate specimen with an inclined through crack that is loaded by a uniform remote tension (Fig. 2*a*) is the most common method that has been used to study fracture under combined crack-opening (mode I) and edge-sliding (mode II) modes of crack face displacements. The technique was first used by Erdogan and Sih (1963) in their classic study of mixed-mode fracture in PMMA. It has since been used by a number of investigators for studying mixed-mode fracture of a variety of brittle polymers, but data on ceramic materials are limited to soda-lime glass. The mixed-mode fracture data reported by Panasyuk et al. (1965) and Kordisch et al. (1984) for soda-lime glass are shown in Fig. 3 in terms of mode I and mode II stress-intensity factors normalized with respect to the critical stress-intensity factor for mode I crack extension or mode I fracture toughness, K_{Ic}. It is clear from these data that superposition of longitudinal shear loading significantly reduces the critical value of the mode I stress-intensity factor or fracture toughness. The data show significant scatter, but the following empirical equation gives a reasonably good fit to the data:

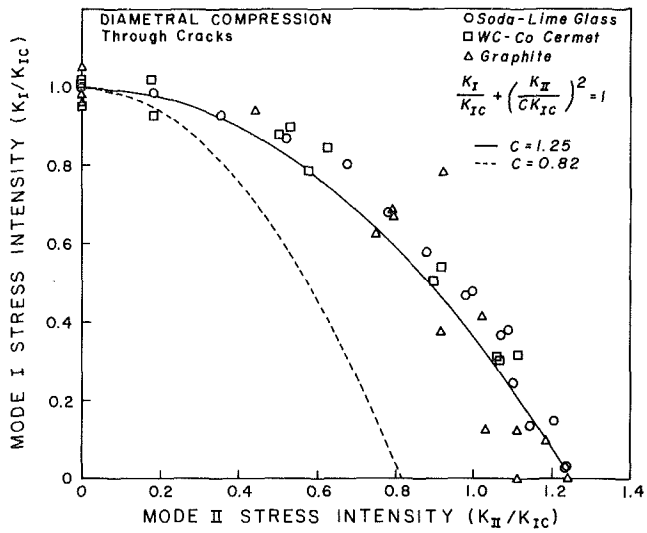

Fig. 4 Combined mode I-mode II fracture toughness of three ceramics measured with through cracks in diametral-compression tests

$$(K_I/K_{Ic}) + (K_{II}/CK_{Ic})^2 = 1 \quad (7)$$

where K_I is the mode I stress-intensity factor, K_{II} is the mode II stress-intensity factor, and C is an empirical constant. A value of $C = 0.82$ was chosen to plot the curve shown in Fig. 3. It should be noted that the value of the empirical constant C is also the ratio of the critical value of K_{II} in pure mode II loading and the mode I fracture toughness K_{Ic}. The rationale for the functional form of equation (7) and the specific value of C will be discussed in a later section.

The disk specimen with an inclined crack that is loaded in compression along a diameter, as shown in Fig. 2(*b*), has been used by a number of investigators to study fracture under combined mode I and mode II loading. This test geometry has the advantage that all stress states ranging from pure mode I to pure mode II can be obtained in the disk specimen with a simple alignment of the crack. This is not the case with the tension test specimen of Fig. 2(*a*) where both mode I and mode II stress intensity factors go to zero as the angle α approaches zero. Secondly, mixed-mode fracture tests can be conducted on disks precracked by using chevron notches instead of using machined notches (Shetty et al., 1985). The fracture toughness of polycrystalline ceramic materials in mode II loading can be quite sensitive to the nature of the crack or the notch used in testing.

Figure 4 shows the results of the disk tests on graphite reported by Awaji and Sato (1978), a sintered cemented carbide studied by Yarema et al. (1984), and soda-lime glass studied by Shetty et al. (1987). The soda-lime glass specimens were precracked, but the graphite and the sintered cemented carbide specimens were tested with machined notches 300 and 80 μm in width, respectively. Despite the differences in the microstructures and the crack/notch geometries the three ceramics show consistent behavior in combined mode I and mode II fracture. However, the results of the disk tests differ significantly from the results of the tension tests shown in Fig. 3. The solid line in Fig. 4 is a fit of equation (7) with an arbitrarily selected value $C = 1.25$. The dashed line in Fig. 4 corresponds to $C = 0.82$, i.e., the curve fitted in Fig. 3. It is clear from the two plots and the data sets for the same material (soda-lime glass) in the two test geometries that there is no unique K_I–K_{II} plot for combined mode fracture. As a conse-

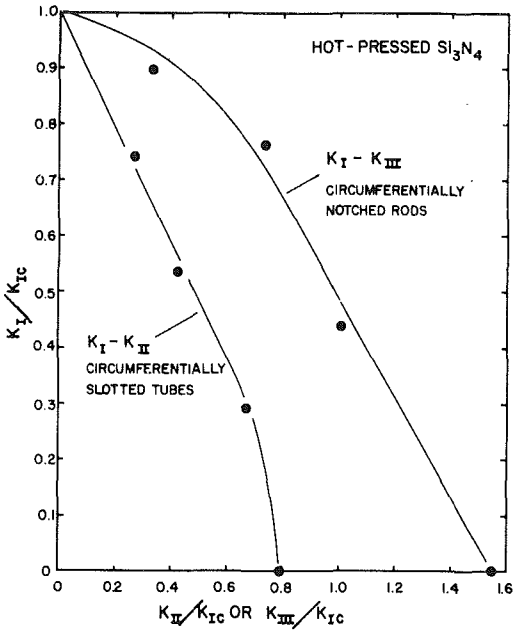

Fig. 5 Combined mode I-mode II and mode I-mode III fracture toughness of hot pressed Si_3N_4 in combined tension-torsion tests

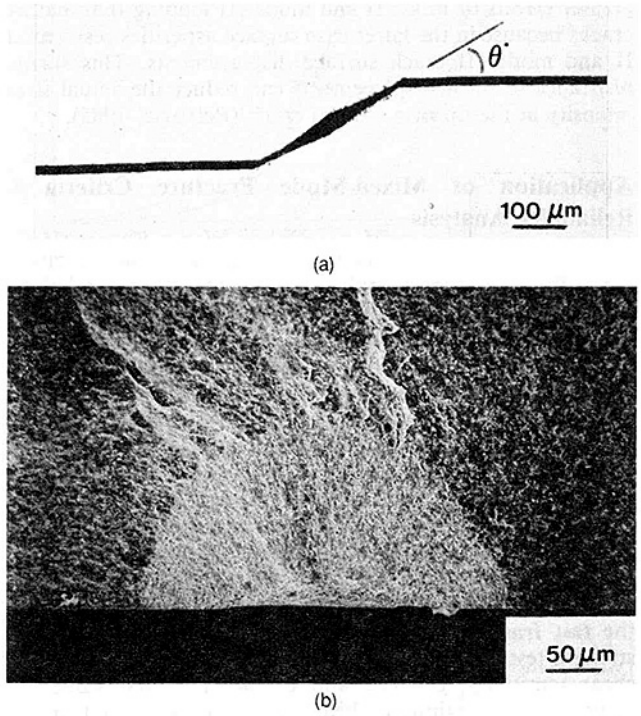

Fig. 6 (a) Mixed-mode fracture morphology of an inclined Knoop surface flaw; (b) semicircular surface crack on the fracture surface

quence, there is no unique fracture toughness for mode II loading, i.e., the critical value of K_{II} for pure mode II loading is not a unique material property.

Figures 2(*c*) and 2(*d*) show tube and rod specimens with circumferential slot and circumferential notch, respectively. Under combined tension and torsion loading these specimen and crack geometries have been used to study fractures in combined mode I–mode II and combined mode I–mode III loading, respectively. Figure 5 shows the K_I–K_{II} and K_I–K_{III} combined fracture toughness data for hot-pressed Si_3N_4 obtained by Petrovic (1985) using the slotted tube and the notched rod specimens, respectively. These data suggest

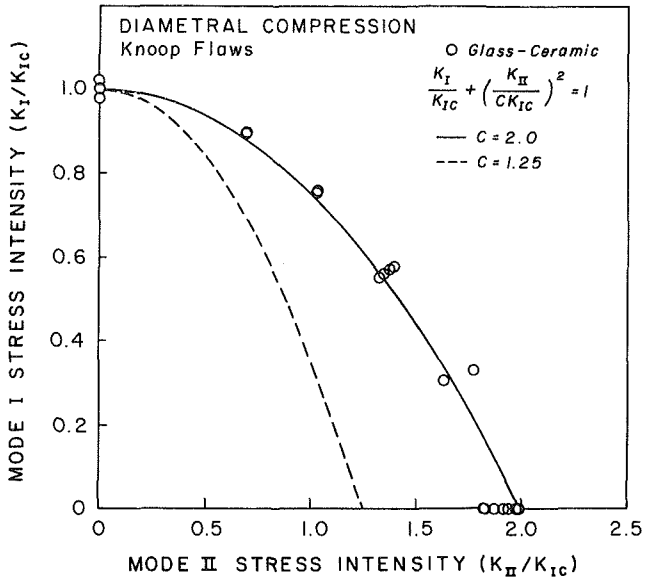

Fig. 7 Combined mode I-mode II fracture toughness of a glass-ceramic tested with surface (indenter) flaws in diametral compression

$K_{II} = 0.8 \cdot K_{Ic}$ for pure mode II loading and $K_{III} = 1.55\ K_{Ic}$ for pure mode III loading. Thus, the results of the combined tension/torsion tests on the slotted tubes (Fig. 2*c*) agree reasonably well with the tension tests on angled cracks (Fig. 2*a*). There are no other reported data on fracture toughness of ceramics in combined mode I and mode III loading. It should be noted that the data shown in Fig. 5 for Si_3N_4 were obtained with machined slots and notches of widths 0.58 and 0.35 mm, respectively.

Experimental Results – Surface (Indenter) Cracks. Mixed-mode fracture of ceramics has also been studied using small inclined surface cracks produced by microhardness indentation at high loads (Petrovic, 1985; Marshall, 1984; Shetty et al., 1986). Figure 6 shows a typical inclined surface flaw in an alumina ceramic that was produced by indenting with a Knoop microhardness indenter at 50 N load and subsequently extended in mixed-mode loading. The indenter flaws have been used quite extensively in fracture research in ceramics in recent years because they are easy to produce and they possess many of the characteristics of the surface flaws in surface-ground ceramics. The mixed-mode fracture data for these surface flaws are not easy to analyze, however, because of the three-dimensional crack geometry and the variation of the mode I, mode II, and mode III stress-intensity factors along the crack front. Secondly, the cracks are also subject to a residual crack-opening force from the central plastic zone. Figure 7 shows some representative data obtained on a glass-ceramic with diametral-compression disk specimens that were annealed following indentation to relieve the residual stress effects. The data are plotted in terms of normalized K_I and K_{II} only and this is based on the assumption that a surface crack extends first from the free surface locations where the crack front is subject to only modes I and II.

The solid line in the figure is again a fit of equation (7) where the constant C now has a value of about 2. This value is significantly greater than the best-fit value, $C = 1.25$, used in Fig. 4 for the through cracks. The dashed line in the figure represents the best-fit line from Fig. 4. It is clear from Fig. 7 that surface cracks produced by microhardness indentation show less sensitivity to mode II loading than the corresponding through cracks. These results suggest that there is no unique value of K_{II} for fracture in pure mode II loading. The reasons for the apparently different mixed-mode fracture behavior of the through cracks in tension (Fig. 3), through

cracks in diametral compression (Fig. 4), and the surface cracks in diametral compression (Fig. 7) will now be addressed in light of the different mixed-mode fracture criteria.

Mixed-Mode Fracture Criteria. In linear elastic fracture mechanics theory three different criteria have been proposed to account for fracture in mixed-mode loading: (*a*) maximum hoop stress theory; (*b*) minimum strain energy density theory; and (*c*) maximum strain energy release rate theory.

The mathematical formulations of these three criteria and their application to the crack geometries shown in Figs. 2(*a*) and 2(*b*) have been discussed by Shetty et al. (1987). In summary, the maximum hoop stress criterion, proposed originally by Erdogan and Sih (1963), postulates that a crack under combined mode loading extends in a direction along which the near crack-tip hoop stress, $\sigma_{\theta\theta}$, is a maximum and crack extension occurs when $\sigma_{\theta\theta} = \sigma_{\theta\theta}^*$, where $\sigma_{\theta\theta}^*$ is the critical value of the hoop stress when fracture occurs in pure mode I loading.

Sih (1974) proposed an alternative criterion according to which a crack subjected to combined mode loading extends in a direction along which the strain energy density ϕ is a minimum and crack extension occurs when $\phi = \phi^*$, where ϕ^* is the critical value of the strain energy density when fracture occurs in pure mode I loading.

The critical conditions for crack extension under mixed-mode loading have also been formulated by global energy balance in the manner of the Griffith analysis. However, these treatments explicitly consider the noncoplanar mode of crack extension by maximizing the strain energy release rate for noncoplanar crack extension (Palaniswamy and Knauss, 1978; Wu, 1978). These are referred to as the noncoplanar strain energy release rate criteria.

Despite their different physical bases the three criteria result in quite similar predictions for both the directions of crack extensions and the critical conditions of loading for mixed-mode fracture, i.e., the combinations of K_I, K_{II}, and K_{III}, that lead to fracture (Swedlow, 1976). These theoretical predictions can also be fitted very closely with the empirical function of equation (7). Palaniswamy and Knauss (1978), for example, have shown that the following empirical equation is a good fit to the predictions of their maximum strain energy release rate analysis for combined mode I and mode II loading:

$$(K_I/K_{Ic}) + 1.5(K_{II}/K_{Ic})^2 = 1 \tag{8}$$

It should be noted that for pure mode II loading equation (8) gives $K_{II} = (2/3)^{1/2} K_{Ic} = 0.82 K_{Ic}$; thus, the experimental results of Fig. 3 for soda-lime glass with inclined cracks in the tension tests agree with the strain energy release rate theory.

Table 1 compares the predictions of (K_{II}/K_{Ic}) and (K_{III}/K_{Ic}), and the respective angles of crack extension θ^* (see Fig. 6*a*), for pure mode II and pure mode III loading for the three fracture criteria with the experimental results for ceramics obtained with the test geometries shown in Fig. 2. The data listed are only for the large through cracks or notches. Data for the surface (indenter flaws) cracks are not included. Examination of Table 1 reveals that the experimental results for soda-lime glass tested in tension (Figs. 2*a* and 3) agree well with the predictions of the maximum hoop stress and the strain energy release rate criteria. Results from the diametral compression tests are consistent for the three materials but (K_{II}/K_{Ic}) values are significantly higher than the hoop stress and the strain energy release rate predictions. Shetty et al. (1987) have suggested that this deviation is due to a second-order effect of the in-plane compressive stress on the near-crack-tip stress field.

It is also interesting to note that the surface crack data of Fig. 7 show the maximum deviation from the theories. This deviation could be due to two reasons. First, the mixed-mode fracture behavior of the surface flaws could be inherently different from the behavior of the large cracks. Secondly, the surface flaw data for the glass-ceramic in Fig. 7 were obtained with natural cracks, while the mixed-mode data for the polycrystalline ceramics in Figs. 4 and 5 were obtained with machined notches. Machined notches are likely to exhibit greater effects of mode II and mode III loading than natural cracks because in the latter case surface asperities resist mode II and mode III crack surface displacements. This surface resistance to shear displacements can reduce the actual stress intensity at the tip of a natural crack (Petrovic, 1985).

Table 1 Comparison of predictions of the mixed-mode fracture criteria and experimental results in ceramics

		Pure Mode II Loading		Pure Mode III Loading	
		(K_{II}/K_{Ic})	θ^*	(K_{III}/K_{Ic})	θ^*
Theories	Maximum Hoop Stress	0.866	- 70.5		
	Strain Energy Density	1.054#	- 79.2#	0.748#	
	Strain Energy Release Rate	0.814	- 77.4		
Experiments	Tension Tests (Figure 2a)				
	Soda-Lime Glass	0.8	- 70.3		
	Diametral Compression Tests (Figure 2b)				
	Soda-Lime Glass	1.23	- 66.5		
	WC-Co Cermet	1.1	- 71		
	Graphite	1.1-1.2			
	Tension/Torsion Tests (Figure 2c)				
	Si_3N_4	0.79	- 60		
	Tension/Torsion Tests (Figure 2d)				
	Si_3N_4			1.55	- 53.5

for ν = 0.22
θ* : Crack Extension Angle (see Figure 6a)

Application of Mixed-Mode Fracture Criteria to Reliability Analysis

The objective of this section is to employ realistic mixed-mode fracture criteria applicable to ceramics in a reliability analysis of ceramic specimens subjected to equibiaxial tension using the strength distribution parameters assessed in uniaxial tests. It is clear from the results and discussion of the above section that there is no unique mixed-mode fracture criterion that can account for all the observed behaviors in ceramics. The shear sensitivity of fracture, as characterized by the empirical parameter C, ranges from about 0.8 to 2 depending on the type of test, the crack or notch geometry, and the material microstructure. Ongoing research on mixed-mode fractures of structural ceramics is directed toward resolving the effects of these test and material variables.

To examine the effect of mixed-mode fracture criteria on the fast fracture reliability analysis of uniaxial and biaxial strength test specimens we will consider two limiting cases of shear sensitivity, $C = 0.82$ and $C = \infty$. The first value corresponds to maximum shear sensitivity observed in experiments and supported by theories, while the second case represents shear-insensitive or normal stress criterion. Natural strength-controlling flaws are expected to exhibit a shear sensitivity between these limiting cases, as seen, for example, in the behavior of the indenter flaws (Fig. 7). The critical orientation angle θ_c for the normal stress criterion applied to the case of surface flaws in uniaxial tension is given by equation (4). For the shear sensitive fracture criterion of equation (8), i.e., $C = 0.82$, it can be shown that θ_c for surface flaws in uniaxial tension is given by the nontrivial positive root of the following equation:

$$\cos^4\theta - [1 + (2\sigma_c/3\sigma)]\cos^2\theta + 2(\sigma_c/\sigma)^2/3 = 0 \tag{9}$$

The critical flaw orientations defined in equations (4) and

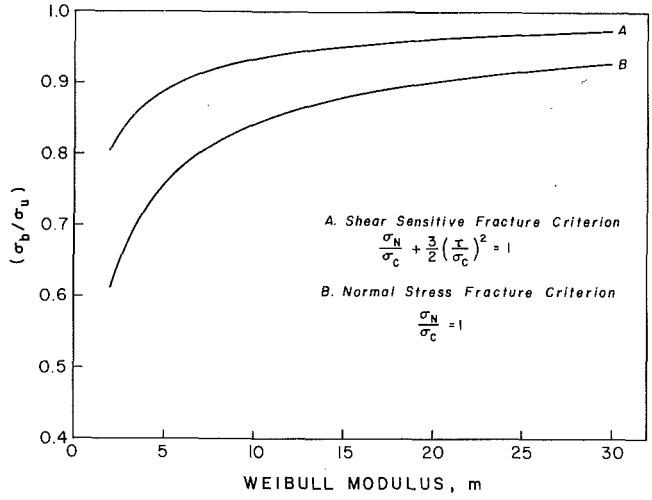

Fig. 8 Relative fracture stresses in equibiaxial tension for shear sensitive and normal stress fracture criteria

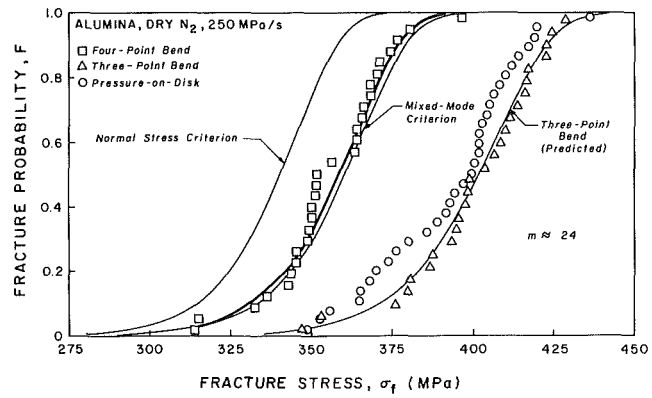

Fig. 9 Weibull plots of fracture stresses of an alumina ceramic tested in three test geometries in an inert environment

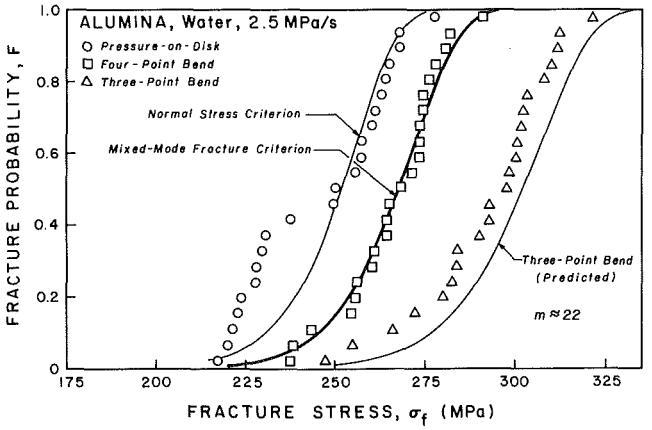

Fig. 10 Weibull plots of fracture stresses of an alumina ceramic tested in three test geometries in water

(9) can now be employed in equation (1) (via equation (3)) along with the flaw size distribution function, equation (2), to assess the intrinsic flaw size distribution parameters m and σ_0 by matching the experimental and theoretical probabilities of failure for uniaxial bend specimens. The parameters so derived are then used to predict probabilities of fracture of specimens subjected to equibiaxial tension specimens to independently compare with experiments. It should be noted that this exercise in fast fracture reliability analysis involves accounting for both the size and stress gradient effects as well as stress state effects in the various test geometries. The stress state effect appears through θ_c and f which take the values $\pi/2$ and 1, respectively, for surface flaws in equibiaxial tension.

It is useful to examine the role of mixed-mode fracture criteria in reliability analysis in two stages. First, we consider only the stress state effects by comparing the relative fracture stresses in equibiaxial and uniaxial stress states at equal fracture probabilities for hypothetical test specimens of unit areas subjected to uniform stresses. Next, we will include the size and stress gradient effects by examining the relation between uniaxial and biaxial fracture strengths of ceramics. Figure 8 shows plots of this ratio for the two limiting mixed-mode fracture criteria as a function of the Weibull modulus m. The equibiaxial to uniaxial stress ratios in Fig. 8 were calculated from equation (1) for uniformly stressed unit areas using the respective values of f for the two stress states. As can be seen in the figure both fracture criteria predict biaxial weakening, i.e., a lower stress in equibiaxial tension produces the same probability of fracture than in uniaxial tension. This biaxial weakening effect is a direct consequence of the larger fraction of flaws that contribute to fracture in biaxial tension than in uniaxial tension ($f = 1$ for surface flaws in equibiaxial tension and $f < 1$ for surface flaws in uniaxial tension). The degree of this "biaxial weakening" is dependent on the specific fracture criterion employed and the Weibull modulus. The shear sensitive fracture criterion predicts less biaxial weakening than the normal stress fracture criterion. This is because the fraction of flaws that contributes to fracture in uniaxial tension is larger for a shear-sensitive fracture criterion than for a normal stress criterion because the superposed shear stress enlarges the critical orientation angle θ_c. Finally, the relative biaxial weakening decreases with increasing Weibull modulus. This is because when the Weibull modulus is large only the flaws oriented nearly normal to the principal stress in uniaxial tension contribute significantly to the cumulative probability of fracture and the influence of the critical fraction f is reduced.

Reliability Analysis of Uniaxial and Equibiaxial Fracture Strengths

A number of investigators have used the reliability analysis outlined in the previous section to examine size and stress state effects on strengths assessed in uniaxial and equibiaxial tension tests. Figures 9 and 10 show fracture stress data obtained by Shetty et al. (1984) on an alumina ceramic using four-point bend, three-point bend, and biaxial disk bend tests in dry N_2 and water environments, respectively. Shetty et al. (1983, 1984) have described the details of these experiments and the analytical procedures for applying the fracture probability analysis of equation (1). In Figs. 9 and 10 the four-point bend data (square points and the heavy line fitted to these data) are used as the reference strength data to establish the strength distribution parameters (m and σ_0). The three-point bend and the biaxial disk fracture stress predictions (light lines) based on these parameters are then independently compared with the experimental data (triangles and circles). In both figures the predicted three-point bend fracture stresses agree with the theoretical predictions. Thus, the size effect on the strength of the alumina ceramic is consistent with the weakest-link hypothesis. It should be noted that this size effect prediction is independent of the fracture criteria.

The biaxial fracture stress predictions show an interesting anomaly in terms of the effect of the test environment. In the

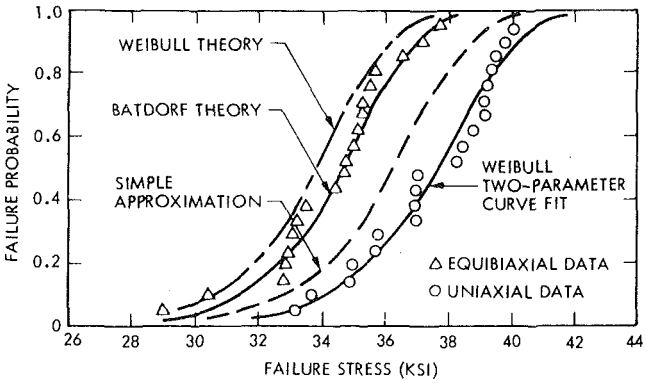

Fig. 11 Correlation of uniaxial and biaxial fracture stresses of an alumina ceramic with a statistical analysis employing different fracture criteria

inert environment (data shown in Fig. 9) the measured biaxial fracture stresses are greater than the theoretical predictions based on either one of the two fracture criteria. In the water environment (data shown in Fig. 10) the biaxial strength data are closer to the predictions based on the normal stress criterion. This apparent influence of the test environment on the relative strengths in uniaxial and biaxial stress states has also been observed for a glass-ceramic (Shetty et al., 1981), but there is no satisfactory explanation for this result. It should be noted that the fracture stresses of the ceramic in the water environment are significantly lower than those measured in the dry N_2 environment. This is due to water-assisted subcritical growth of the strength-controlling cracks that results in environment and stressing-rate-dependent strength degradation. The reliability analysis should strictly take this into account in correlating the uniaxial and the biaxial fracture stresses in water. It is important to note in Figs. 9 and 10 that biaxial fracture stress degrades more severely than uniaxial fracture stresses. Thus, the kinetics of strength degradation appears to be sensitive to the stress state. Strength degradation parameters assessed in uniaxial tension may not give conservative predictions of time-dependent reliability for components subjected to complex loading.

Giovan and Sines (1979), Rufin et al. (1984), and Gyekenyesi (1986) have also employed different mixed-mode fracture criteria to assess fracture probabilities of biaxially loaded test specimens or components of ceramics. The results of Giovan and Sines are shown in Fig. 11. Failure probabilities of disk specimens loaded in a ring-on-ring loading arrangement were calculated from strength distribution parameters assessed in four-point bend tests. Predictions based on the Batdorf theory that used a shear-sensitive fracture criterion gave the best agreement with the experimental results. The traditional Weibull theory gave conservative predictions of the failure probability. An approximate analysis that treats the principal stresses as noninteracting and independent gave clearly nonconservative results.

Rufin et al. (1984) and Gyekenyesi (1986) have followed a different procedure in applying mixed mode fracture criteria in reliability analysis. For volume distributed flaws, they evaluated the strength distribution parameters (σ_0 and m) from uniaxial bend tests using the normal stress fracture criterion. Subsequently, they employed these parameters for biaxial tension with either the normal stress criterion or the mixed-mode fracture criterion. Their procedure leads to a reversal in the relative predictions of the two criteria, i.e., a mixed-mode fracture criterion gives a more conservative prediction than does the normal stress criterion. This difference in the procedure for employing fracture criteria in fast fracture reliability analysis is the focus of current research.

Summary

The present paper has outlined the essential elements of a reliability analysis used in the design of structural ceramics. An important part of this reliability analysis is the use of realistic mixed-mode fracture criteria applicable to structural ceramics. Recent studies devoted to the study of mixed-mode fracture in ceramics have been reviewed. It is clear from this review that no single mixed-mode fracture criterion can adequately account for all the experimental results. Effects of tests and crack/notch geometries and of the ceramic microstructure are noted in the results. Two extreme cases of the fracture criteria were then employed in a reliability analysis to correlate biaxial fracture stresses to uniaxial fracture stresses of an alumina ceramic. Both the criteria were found to be adequately conservative in predicting biaxial fracture stresses in inert conditions, but subcritical crack growth complicates the picture for tests in water.

Acknowledgments

Some of the results reported in this paper were obtained at Battelle's Columbus Laboratories with the support of the U.S. Department of Energy under grant No. DE-FG02-84 ER45073. However, any opinions, findings, conclusions or recommendations expressed herein are those of the author and do not necessarily reflect the views of the Department of Energy.

References

Awaji, H., and Sato, S., 1978, "Combined Mode Fracture Toughness Measurement by the Disk Test," ASME *Journal of Eng. Mater. Technol.*, Vol. 100, No. 4, pp. 175–182.

Batdorf, S. B., and Crose, J. G., 1974, "A Statistical Theory for the Fracture of Brittle Structures Subjected to Nonuniform Polyaxial Stresses," ASME *Journal of App. Mech.*, Vol. 41, pp. 459–464.

Batdorf, S. B., and Heinisch, H. L., Jr., 1978a, "Weakest Link Theory Reformulated for Arbitrary Fracture Criterion," *Journal of Am. Ceram. Soc.*, Vol. 61, No. 7–8, pp. 355–358.

Batdorf, S. B., and Heinisch, H. L., Jr., 1978b, "Fracture Statistics of Brittle Materials With Surface Cracks," *Engineering Fracture Mechanics*, Vol. 10, pp. 831–841.

Erdogan, F., and Sih, G. C., 1963, "On the Crack Extension in Plates Under Plane Loading and Transverse Shear," ASME *Journal of Basic Engineering*, Vol. 85D, pp. 519–527.

Giovan, M. N., and Sines, G., 1979, "Biaxial and Uniaxial Data for Statistical Comparisons of a Ceramic's Strength," *Journal of Am. Ceram. Soc.*, Vol. 62, No. 9–10, pp. 510–515.

Gyekenyesi, J. P., 1986, "SCARE: A Postprocessor Program to MSC/NASTRAN for Reliability Analysis of Structural Ceramic Components," ASME JOURNAL OF ENGINEERING FOR GAS TURBINES AND POWER, Vol. 108, pp. 540–546.

Katz, R. N., 1985, "Applications of High Performance Ceramics in Heat Engine Design," *Materials Science and Engineering*, Vol. 71, pp. 227–249.

Kordisch, H., Riedmuller, J., and Sommer, E., 1984, "The Strain Energy Density Criterion – Investigations for Its Applicability," in: *Proc. of Symposium on Absorbed Specific Energy/Strain Energy Density*, G. C. Sih, E. Czoboly, and F. Gillemot, eds., Akademiai Kiado, Budapest, pp. 33–43.

Marshall, D. B., 1984, "Mechanisms of Failure From Surface Flaws in Mixed-Mode Loading," *Journal of Am. Ceram. Soc.*, Vol. 67, No. 2, pp. 110–116.

Palaniswamy, K., and Knauss, W. G., 1978, "On the Problem of Crack Extension in Brittle Solids Under General Loading," *Mechanics Today*, Vol. 4, pp. 87–148.

Paluszny, A., and Wu, W., 1977, "Probabilistic Aspects of Designing With Ceramics," ASME JOURNAL OF ENGINEERING FOR POWER, Vol. 99, No. 4, pp. 617–630.

Paluszny, A., and Nicholls, P. F., 1978, "Predicting Time Dependent Reliability of Ceramic Rotors," *Ceramics for High-Performance Applications–II*, Proc. of the Fifth Army Materials Technology Conference, Brook Hill Publishing Co., New York, pp. 95–112.

Panasyuk, V. V., Berezhnitskiy, L. T., and Kovchik, S. Ye., 1965, "Propagation of an Arbitrarily Oriented Rectilinear Crack During Extension of a Plate," *Prikladnaya Mekhanika*, Vol. 1, No. 2, pp. 48–55.

Petrovic, J. J., 1985, "Mixed-Mode Fracture of Hot-Pressed Si_3N_4," *Journal of Am. Ceram. Soc.*, Vol. 68, No. 6, pp. 348–355.

Rufin, A. C., Samos, D. R., and Bollard, R. J. H., 1984, "Statistical Failure Prediction Models for Brittle Materials," *AIAA Journal*, Vol. 22, No. 1, pp. 135–140.

Shetty, D. K., Rosenfield, A. R., Bansal, G. K., and Duckworth, W. H., 1981, "Biaxial Fracture Studies of a Glass-Ceramic," *Journal Am. Ceram. Soc.*, Vol. 64, No. 1, pp. 1–4.

Shetty, D. K., Rosenfield, A. R., Duckworth, W. H., and Held, P. R., 1983, "A Biaxial Flexure Test for Evaluating Ceramic Strengths," *Journal Am. Ceram. Soc.*, Vol. 66, No. 1, pp. 36–42.

Shetty, D. K., Rosenfield, A. R., and Duckworth, W. H., 1984, "Statistical Analysis of Size and Stress-State Effects on the Strength of an Alumina Ceramic," *Methods for Assessing the Structural Reliability of Brittle Materials*, ASTM STP 844, American Society for Testing and Materials, Philadelphia, PA, pp. 57–80.

Shetty, D. K., Rosenfield, A. R., and Duckworth, W. H., 1985, "Fracture Toughness of Ceramics Measured by a Chevron-Notch Diametral-Compression Test," *Journal Am. Ceram. Soc.*, Vol. 68, No. 12, pp. C325–327.

Shetty, D. K., Rosenfield, A. R., and Duckworth, W. H., 1986, "Mixed-Mode Fracture of Ceramics in Diametral Compression," *Journal Am. Ceram. Soc.*, Vol. 69, No. 6, pp. 437–443.

Shetty, D. K., Rosenfield, A. R., and Duckworth, W. H., 1987, "Mixed-Mode Fracture in Biaxial Stress State: Application of the Diametral Compression (Brazilian Disk) Test," *Engineering Fracture Mechanics*, in press.

Sih, G. C., 1974, "Strain-Energy-Density Factor Applied to Mixed-Mode Crack Problems," *Int. Journal of Fracture*, Vol. 10, No. 3, pp. 305–320.

Swedlow, J. L., 1976, "Criteria for Growth of the Angled Crack," *Cracks and Fracture*, ASTM STP 601, American Society for Testing and Materials, Philadelphia, PA, pp. 506–521.

Yarema, S. Ya., Ivanitskaya, G. S., Maistrenko, A. L., and Zboromirskii, A. I., 1984, "Crack Development in a Sintered Carbide in Combined Deformation of Types I and II," *Probl. Proch.*, Vol. 16, No. 8, pp. 51–56.

Weibull, W., 1939, "A Statistical Theory of the Strength of Materials," *Ingeniors Vetenskaps Akademiens Handlingar*, Vol. 151, pp. 1–45.

Wu, C. H., 1978, "Maximum Energy Release Rate Criterion Applied to a Tension-Compression Specimen With a Crack," *Journal of Elasticity*, Vol. 8, No. 3, pp. 235–257.

Hot Isostatic Pressing of Sintered Alpha Silicon Carbide Turbine Components

M. O. Ten Eyck

R. W. Ohnsorg

Standard Oil Engineered Materials Company, Niagara Falls, NY 14302

L. E. Groseclose

Allison Gas Turbine Division, General Motors Corporation, Indianapolis, IN 46206

Hot isostatic pressing (HIPing) without encapsulation has been investigated with sintered alpha silicon carbide plates and Modulus of Rupture (MOR) bars made by dry pressing and with MOR bars and gas turbine rotors made by injection molding. Early HIPing trials indicated that substantial density increases up to 99.5 percent of theoretical could be achieved. At least 98 percent densification was consistently attainable on components initially having greater than 95 percent density and less than about 1 percent open porosity. Several HIPing cycles were investigated by varying maximum temperature, maximum pressure, and their respective rates. Analysis of densities, MOR bar strength and Weibull modulus, and microstructures were used to assess the influence of HIPing parameters on material properties. Vacuum spin test results and room temperature flexural strength data on MOR bars cut from HIPed rotors were compared with results from pressureless sintered rotors. Although densities and flexural strength showed improvement, data on rotor spin-test performance were inconclusive. Emphasis is now being placed on optimizing the HIPing cycle for gas turbine rotors.

Introduction

Hot isostatic pressing, or HIPing as it is commonly referred to, is a process in which materials or components are subjected simultaneously to high isotropic pressure and high temperature. It has gained importance as a processing step in the development of high-performance ceramics such as silicon nitride and silicon carbide. While several investigators have reported their findings on HIPing silicon nitride (Larker, 1979, 1980, 1983; Sikora and Yeh, 1976; Yamada et al., 1981) development work on HIPing silicon carbide has been much more limited. Published work on SiC has concentrated on the investigation and characterization of HIPing pressureless sintered components (Watson et al., 1985; Whalen, 1984).

HIPing is being used more routinely and on a commercial basis for alloy and superalloy investment castings of individual turbine blades and integral turbine rotors in the aerospace industry (McFadden, 1983; Price, 1982). It has also been employed in powder metal (P/M) technology (Moll, 1983) for the near net shape fabrication of high-speed tool steels and superalloys and it has been found beneficial for other high-performance applications such as plungers, dies, and wear components made of cemented carbides or computer memory cores and magnetic heads based on ferrites. More recently, the HIPing technology has been applied to the development and fabrication of dual-alloy turbine wheels and large P/M titanium alloy airframe parts as well as high-performance ceramics for wear applications, tool bits, and gas turbine components.

Until recently, structural designers selected mainly superalloys for applications where high strength and stability at elevated temperatures were required. Interest in the use of structural ceramics for these applications has increased with the advent of sintered silicon nitride and sintered silicon carbide since both of these materials have the potential for comparable or better high-temperature characteristics.

One particular program stimulating mechanical property and fabrication development of these high-performance ceramic materials is the Advanced Gas Turbine (AGT) project which is funded by the Department of Energy (DOE) and administered by the National Aeronautics and Space Administration (NASA). The goal of this project is the development of a multifuel, energy efficient turbine engine with low emission for passenger cars while utilizing nonstrategic materials for individual components which can be mass produced at an affordable cost. Turbine inlet temperatures of 2350°F (1288°C) to 2500°F (1371°C) are necessary to meet all the goals of this project.

Not only are the superalloys rendered unsuitable at these temperatures due to softening and creep, they also weigh almost three times more than ceramics, which results in an increased moment of inertia and adversely affects fuel efficiency. In addition, these high-performance ceramics are made up of some of the most abundant elements on earth – silicon, carbon, and nitrogen – and not strategic metals such as titanium, cobalt, or nickel.

Work reported within this paper is based on HIPing without encapsulation of simple geometric shapes such as plates and

Contributed by the Gas Turbine Division of THE AMERICAN SOCIETY OF MECHANICAL ENGINEERS and presented at the 32nd International Gas Turbine Conference and Exhibit, Anaheim, California, May 31–June 4, 1987. Manuscript received at ASME Headquarters February 17, 1987. Paper No. 87-GT-161.

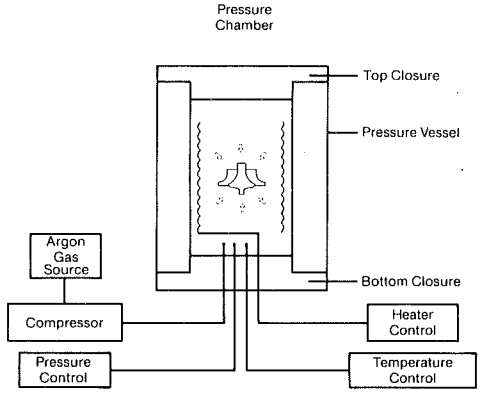

Fig. 1 Hot isostatic pressing system

test bars to establish a set of baseline conditions suitable for increasing density of pressureless sintered alpha silicon carbide components. Further development effort was directed toward the optimization of HIPing conditions for a large and complex component. A portion of this work was carried out under the AGT project and was specifically oriented toward the injection molded gasifier turbine rotor for the AGT-100 (Ohnsorg et al., 1985) where the Allison Gas Turbine Division of the General Motors Corporation is the prime contractor.

Pressureless sintered alpha silicon carbide gasifier turbine rotors made by injection molding have been successfully vacuum spin tested at room temperature up to 120 percent of design speed (86,240 rpm = 100 percent). HIPing without encapsulation was incorporated into the development plan to increase the strength of the pressureless sintered rotor in the hub region ultimately to improve burst speed and decrease the probability of failure.

Several HIPing cycles were investigated varying maximum pressure, temperature, and hold time. Density, test bar flexural stength, Weibull modulus, microstructure, and rotor spin results were used to assess the influence of HIPing parameters on material properties.

Hot Isostatic Pressing

The HIPing process utilizes simultaneously high isotropic pressure and high temperature. Pressures up to 30,000 psi (207 MPa) using an inert gas such as argon or nitrogen at temperatures up to 2200°C have been achieved. A simplified schematic of a hot isostatic pressing system is shown in Fig. 1. Two basic concepts using either a cladding process, where green or partially densified compacts are encapsulated in a glass forming substance, or where dense components with little or virtually no open porosity are placed directly into the chamber of the HIPing furnace, are being used for high-performance ceramics. The encapsulation method appears to be favored by silicon nitride fabricators (Larker et al., 1983) while containerless HIPing appears to be the preferred method for silicon carbide articles (Whalen, 1984).

The ultimate purpose of HIPing is to obtain near net shape components having virtually theoretical density thereby eliminating porosity and critical flaws. It has been shown by S. Amberg et al. (1974) that closed pores of 150 μm could be eliminated in cemented carbides while open porosity near the surface was not affected by the HIPing conditions. Larker (1983) showed that HIPing with encapsulation can efficiently heal defects present in green Si_3N_4 bodies. Hermansson et al. (1986) obtained densification with no exaggerated grain growth on encapsulated SiC using significantly reduced densification temperatures of 1750 to 1900°C.

HIPing is related to two older concepts in powder technology, cold isostatic pressing and hot pressing. The former is often used to make shaped preforms whereby a fluid medium is pressurized applying isostatic pressure to a powder compact in a sealed flexible mold. These preforms are then green machined into the desired configuration prior to densification. The latter is a method for compacting powder at elevated temperatures under uniaxial pressure into strong, dense final products. However, property directionality often occurs, shaping is fairly limited, and expensive final grinding is frequently required. In addition, uniaxial hot pressing is typically restricted to pressures below 5000 psi (34 MPa) because of the strength-limiting characteristics of the graphite molds and plungers.

Table 1 Density and porosity summary

Test	Configuration	Samples	Before HIPing Density (g/cm³)	Before HIPing Open Porosity (%)	After HIPing Density (g/cm³)	After HIPing Open Porosity (%)
1	2" x 2" x 0.29"	10	3.147-3.165	0.1	3.199	<0.1
2	2" x 2" x 0.29"/ ½" x ½" x 2"	5/22	3.107-3.136	0.1	3.162-3.192	<0.1
3	1" x 15" x 0.06"	6	3.122-3.159	1-0.4	3.143-3.163	0.8-0.4
4	1" x 15" x 0.06"	7	2.802-3.159	3.7-0.1	2.981-3.193	0.3-<0.1
5	1" x 1.5" x 0.06"	29	3.124-3.150	0.2-0.1	3.173-3.191	<0.1

Determination of HIPing Parameters

Initial HIPing experiments were carried out on pressureless sintered dry pressed plates and MOR bars made of alpha silicon carbide powder of about 0.8 μm median particle size and 0.5 percent boron and 2 percent carbon as sintering aids. Five individual HIPing experiments were conducted using one furnace run. The specimens in Experiment 1 consisted of ten 2-in.-square plates with a 0.29-in. thickness. These plates were pressureless sintered to densities between 98.0 and 98.6 percent of theoretical (3.21 g/cm³) with about 0.1 percent residual open porosity and then subjected to HIPing to determine if even further densification and reduced open porosity could be realized.

For Experiment 2 five plates with the same dimension as in Experiment 1 having pressureless sintered densities of 96.8 to 97.7 percent of theoretical were each cut into eight to ten test bars. Each set of bars was randomly separated into two groups. One group was used as a control and the second group was subjected to HIPing to determine the influence on density, open porosity, strength, and fracture toughness of individual small test specimens.

Experiments 3 through 5 were carried out on 0.06 in. × 1 in. × 1.5 in. plates. The specimens of Experiment 3 had high pressureless sintered densities (97.3 to 98.4 percent of theoretical) combined with relatively high open porosity (0.4 to 1 percent) and the specimens of Experiment 4 exhibited a wide range of densities and porosities. Finally, Experiment 5 consisted of a large group of plates (29) with high initial sintered densities combined with low open porosity. These three sets of specimens were subjected to HIPing to determine the influence on density and open porosity.

The HIPing trial was conducted at ASEA Pressure Systems in Columbus, OH using their QIH-9 furnace with graphite heaters having a hot zone of 6 in. (152 mm) diameter and 12 in. (305 mm) height. This system is capable of gas pressures of up to 30,000 psi (207 MPa) using an inert atmosphere such as argon or nitrogen and has a maximum temperature capability of 2200°C. The conditions selected were maximum argon pressure and 2200°C. The total run time was approximately 3.5 hr with a 0.5 hr hold at temperature.

A summary of the density and porosity measurements for all five experiments before and after HIPing is given in Table 1. All samples from this HIPing trial showed significant density improvements. However, it was found that sintered densities of about 95 percent (3.05 g/cm³) were necessary to take

Table 2 MOR strength

	# of Samples	Strength (ksi)	Std. Dev. (ksi)	Strength (MPa)	Std. Dev. (MPa)	Weibull m
As sintered	22	54.93	4.53	378.61	31.24	12.7
As HIPed	22	54.63	5.63	376.67	38.84	10.16

Table 3 Indentation fracture toughness

Sample	Density		Toughness (MPa • m$^{1/2}$)	Std. Dev. (MPa • m$^{1/2}$)
As sintered				
A7	3.102		2.859	0.094
B6	3.075		3.221	0.171
C2	3.104		3.091	0.098
D2	3.059		2.936	0.109
E8	3.164		2.974	0.135
		Avg.	3.016	
After HIPing				
A2	3.181		2.775	0.095
B4	3.180		2.819	0.074
C3	3.181		2.805	0.083
D5	3.183		2.875	0.038
E7	3.181		2.846	0.057
		Avg.	2.824	

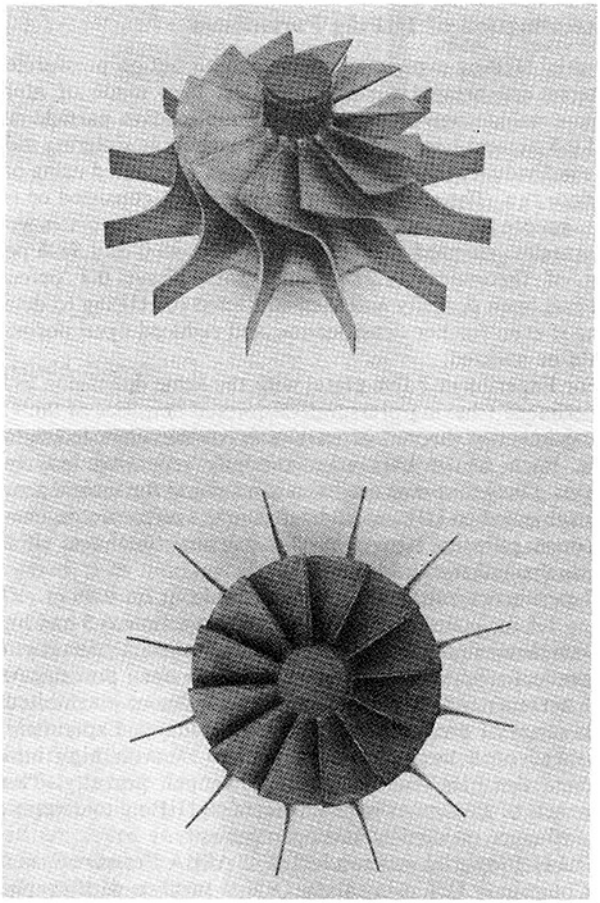

Fig. 2 AGT-100 gas turbine rotor

full advantage of the HIPing process to achieve 98 percent or better densification.

Room temperature flexural strength and indentation fracture toughness data obtained on test specimens from Experiment 2 are summarized in Tables 2 and 3. It was found that even though extremely high densities were obtained using the post-HIPing processing step, no change in the room temperature strength characteristics occurred. Both groups exhibited the same strength with only a small variation in the

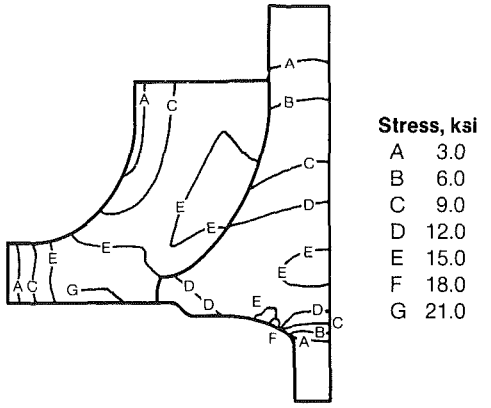

Fig. 3 Stress distribution at design speed (86,240 rpm)

standard deviation, which indicates that the HIPing conditions of this trial did not influence the strength-limiting flaws of these MOR bars.

With respect to the fracture toughness measurements it was found that the control group with the lower density as-sintered MOR bars showed slightly higher fracture toughness with more variation than the HIPed MOR bars.

In summary, the evaluation of these HIPing experiments indicated that this procedure can be applied to sintered alpha silicon carbide components without introducing additional strength-limiting defects. The conditions selected caused a noticeable increase in final density, which is of special importance for components having somewhat lower than desired densities or with density gradients. Further HIPing experiments were then carried out on injection molded gas turbine rotors and MOR bars.

HIPing of Gas Turbine Rotors

Gas turbine rotors fabricated under the AGT-100 program were selected as a suitable large-scale component which could benefit from HIPing. Destructive and nondestructive methods have been used to assess the quality of these rotors and an extensive data base has been collected on pressureless sintered components.

The rotor used for this study as shown in Fig. 2 has a radial flow design and a tip diameter of 120 mm (4.73 in.). It represents the gasifier turbine rotor of the AGT-100 engine which is designed for an inlet temperature of 2350°F (1288°C) and 86,240 rpm. Figure 3 illustrates the stress distribution for cold spin conditions without shaft attachment at design speed. Maximum principal stresses of up to 21.0 ksi (145 MPa) can be observed in the blade backface region. Other high-stress areas are the fillet radius between the backface and the shaft and also the center of the hub.

This HIPing study focuses on improving upon the integrity, density, and ultimately the strength of this third high-stress region. It has been known from density measurements and microstructural evaluations of sintered alpha silicon carbide components that large cross sections are prone to lower densification and increased grain growth. Even after optimization of the sintering parameters it is difficult to obtain a homogeneous microstructure throughout a component as complex as the radial rotor where thin cross sections as in the blade tips coexist with extremely large cross sections as in the hub area (Ohnsorg et al., 1986).

The gas turbine rotors were injection molded as a solid one-piece configuration using a highly filled thermoplastic alpha silicon carbide compound. This method was selected as one of the most promising forming approaches for complex shapes because of the potential for fabricating structurally sound,

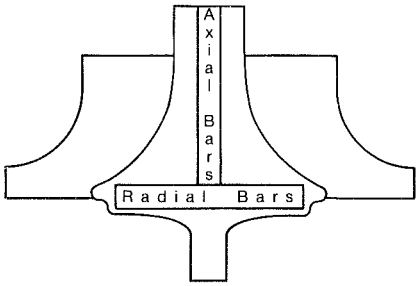

Fig. 4 Rotor test bar orientation

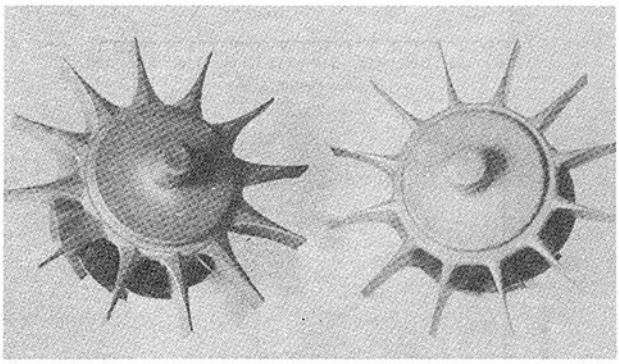

Fig. 5 Rotor design modifications

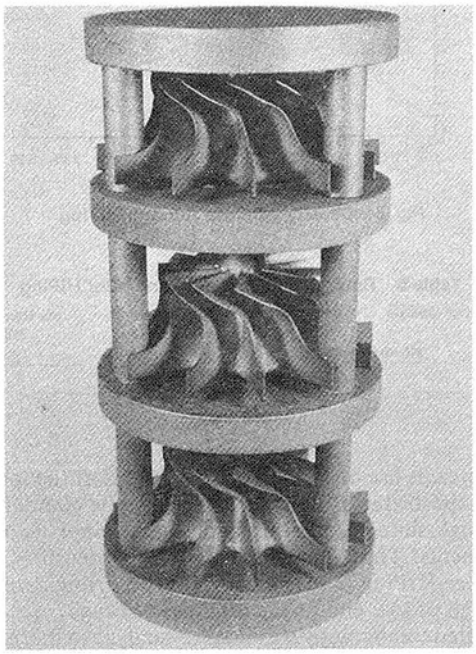

Fig. 6 HIPing fixture

high-quality, near net shape components economically in high volume.

Visual examination with and without a microscope was primarily used to assess molding quality. Sintered components were evaluated using microfocus X-ray, fluorescent penetrant inspection (FPI), visual examination, and density measurements. For further assessment rotors were spin tested and flexure bars were cut from some of the rotors. The orientation of these bars is shown in Fig. 4.

Table 4 summarizes in chronological order rotor performance data obtained for four different groups of rotors. Rotors from Groups A through C are of the same design but were formed using different molding procedures and machine

Table 4 Rotor performance

Group	No. of Rotors	Spin Performance (krpm)	Weibull Modulus	MOR (ksi) Axial	MOR (ksi) Radial
A	10	99.3	6.9	41.6	58.9
B	16	80.5	6.6	49.3	50.4
C	70	99.8	12.0	47.2	53.6
D	26	90.7	16.5	N/A	N/A

parameters. Rotors from Group D are of a modified design where the airfoils are thickened for improved impact resistance against foreign object damage (FOD). Both designs are shown in Fig. 5.

Initial rotors (Group A) exhibited good spin performance even though the flexure strength on test bars cut from rotors from the same lot varied noticeably between radially cut bars from the backface region and axially cut bars from the hub center with a disappointingly low value for the latter.

The following set of rotors (Group B) showed improved flexure values for axial test bars and reduced values for radial test bars resulting in equal values for both. This result indicated that improved packing in the center of the hub and a more homogeneous component were obtained. Fracture analyses determined that the low-spin results were primarily caused by surface defects near the shaft fillet, the second highest stress area on the rotor. Rotors from Group C combined the positive aspects, high-spin speeds, and good test bar strength of the two previous groups of rotors.

The design modification implemented on rotors from Group D caused an increase in stress resulting in an 8.3 percent reduction of the analytically predicted mean failure speed. Actual spin performance (Group C versus Group D) closely duplicated this analysis.

Experimental Procedure

Sintered rotors and similarly fabricated test bars were selected for a series of HIPing runs after completion of microfocus X-ray, fluorescent dye penetrant inspection, and visual examination. The rotors varied in blade design and sintered densities. Also, some of the rotors had been previously proofed in a vacuum spin test to 100 or 110 percent of design speed.

HIPing runs were conducted at the ASEA Pressure Systems facility in Columbus, Ohio. A second set of six experiments was carried out at the National Aeronautics and Space Administration (NASA) Lewis Research Center, Cleveland, Ohio. The major difference between the two systems was maximum pressure capability. The NASA furnace could reach 20,000 psi (138 MPa) whereas the ASEA furnace was capable of 30,000 psi (207 MPa).

Maximum pressure capability was used for each of the respective HIPing experiments. All experiments were designed such that peak pressure was attained at the same time as peak temperature. The rotors and test bars were loaded onto a specially designed tiered graphite fixture as shown in Fig. 6, which provided support for three rotors in the ASEA experiments or two rotors in the NASA experiments. After completion of each of the experiments each component was subjected to a density check per ASTM C20-80a. Photomicrographs were taken on a polished cross section of a rotor HIPed at 2100°C and 30,000 psi (207 MPa).

A few selected rotors were cut into test bars before HIPing and a similar smaller group was selected for flexure testing after HIPing. Bars were cut in the radial direction from the backface region and the axial direction from the central portion of the hub (see Fig. 4).

In addition, thin and thick-bladed rotors were spun to failure after HIPing and results were compared to the performance data of pressureless sintered Group C and Group D rotors presented in Table 4.

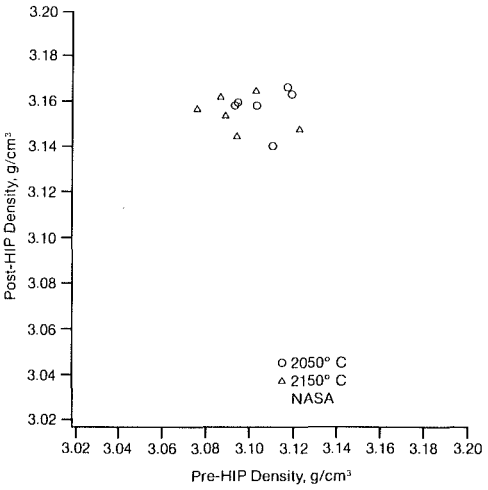

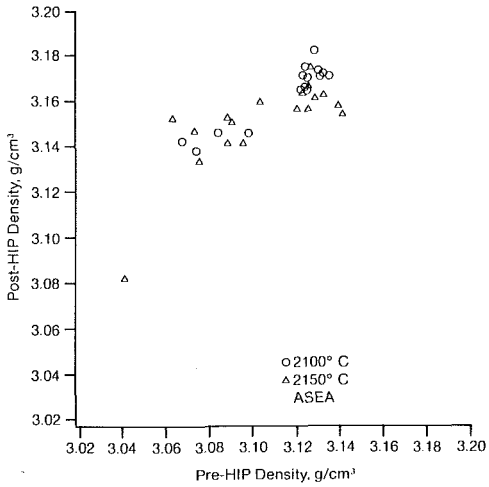

Fig. 7 Densities of rotors before and after HIPing

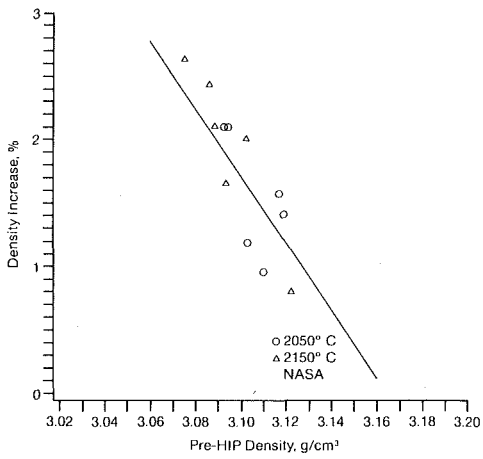

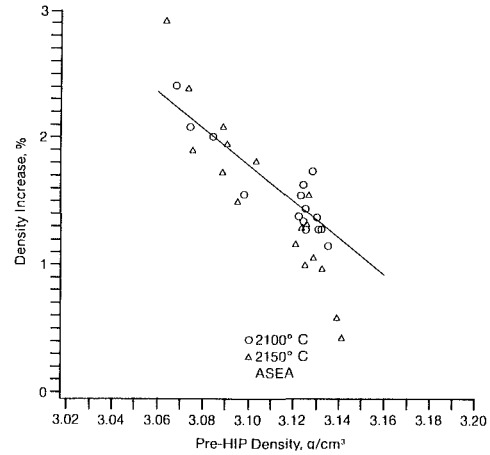

Fig. 8 Density increase through HIPing

Table 5 Rotor densities before and after HIPing

Facility	No. of Rotors	Av. Density Before HIPing (g/cm³)	Av. Density After HIPing (g/cm³)
NASA	12	3.10	3.16
ASEA	30	3.11	3.16

Densification

A total of 45 rotors and 125 test bars were subjected to various HIPing cycles. The densities measured after pressureless sintering ranged from 94.7 to 97.8 percent for rotors and from 92.5 to 98.8 percent of theoretical for test bars. A substantial density increase was realized for each of the components from the 17 HIPing runs. The relationship between sintered and HIPed densities for rotors grouped by maximum HIPing pressure and temperature is graphically shown in Fig. 7. The graphs indicate that all the conditions selected for these experiments promote densification to about 98 percent of theoretical density or higher for articles above about 95 percent (3.05 g/cm^3) starting density. A comparison of the data obtained at both HIP facilities is given in Table 5. It was found that the thirty rotors HIPed at ASEA exhibited an average density of 3.16 g/cm^3 (98.4 percent theoretical) as did the twelve NASA HIPed rotors. Similar to the early HIPing parameter investigation it was also shown during these HIPing experiments that sintered silicon carbide articles with less than 3.05 g/cm^3 do not densify to the desired range of about 98 percent or better.

Figure 8 illustrates the relationship between density increase (percent) and starting density. The two sets of experiments (ASEA, NASA) are analyzed separately and the individual data are described using a least squares regression fit. Maximum increases are observed on components at the lower end of the established starting density range while components of already high sintered densities show only minor incremental improvements. Thus, about the same final densities are obtained after HIPing independently if the starting density was on the high or low end of the established range.

Computed tomography was used to analyze in more detail a pressureless sintered rotor which had a 3.12 g/cm^3 (97.2 percent of theoretical) overall density as measured using the water immersion technique. Figure 9 represents a schematic of the X-ray tomography result which clearly shows a low density center. A significantly higher density can be seen for areas which are closer to the component surface. Thus, the pressureless sintered rotor has a distinct density gradient of about 0.25 g/cm^3.

For comparison, Fig. 10 shows the tomography result of the same rotor with an overall density of 3.17 g/cm^3 (98.8 percent of theoretical) after HIPing at ASEA using 2100°C and 30,000 psi (207 MPa). The lower density center has completely disappeared and only minor variations remain. The area near the backface shows highest densification and a density gradient toward the rotor nose becomes apparent. The overall density gradient, however, is reduced by more than 50 percent. This

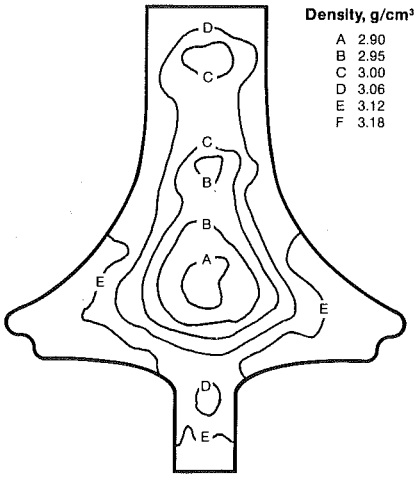

Fig. 9 Computed tomography result for sintered rotor

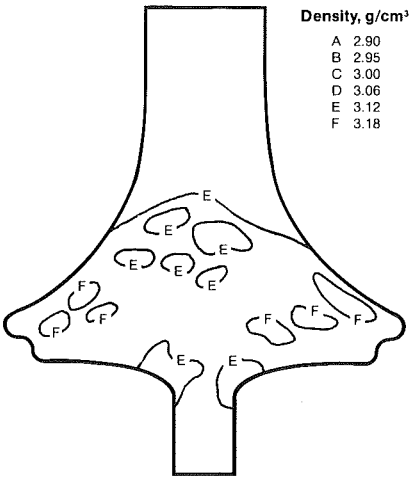

Fig. 10 Computed tomography result for HIPed rotor

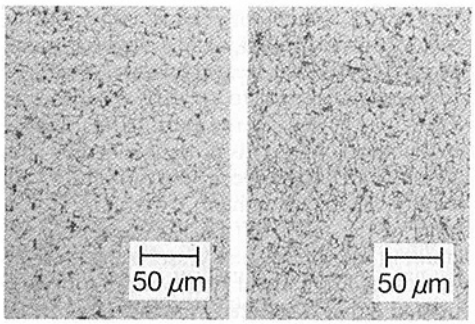

Fig. 11 Blade microstructure before (left) and after (right) HIPing

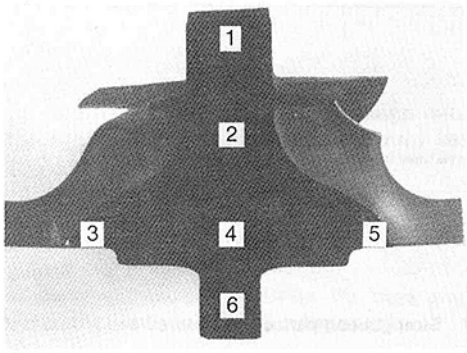

Fig. 12 Polished rotor section

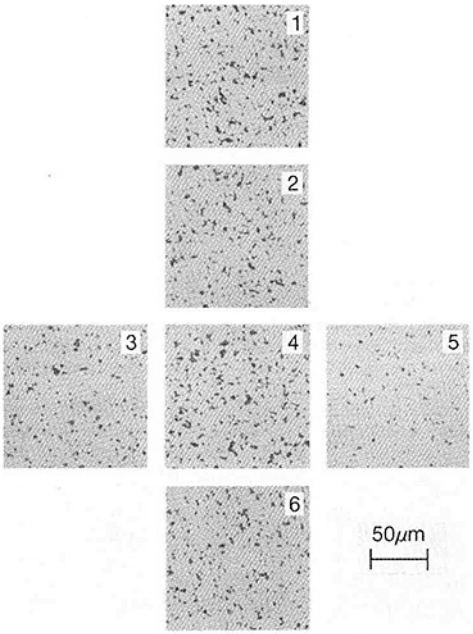

Fig. 13 Photomicrographs of sintered rotor

increase in overall densification manifests itself also in an observable volumetric shrinkage of about 1.2 percent.

Additional work with respect to quantitative density measurements using computed X-ray tomography is in progress. Tests are being conducted to improve upon sensitivity levels and calibration standards and reduce beam hardening effects.

Microstructures

Microstructures before and after HIPing were obtained by breaking off individual blades from selected rotors before HIPing. The blade surfaces were polished and etched photomicrographs were taken to show the grain structure with particular emphasis on the maximum grain size. Figure 11 compares photomicrographs of the same rotor blade before and after HIPing at 2150°C and 207 MPa (30 ksi). Relatively small variations were observed and typical grain sizes were in the range of 7.5 to 15.0 μm.

Similarly, two rotors, one before and one after HIPing (ASEA), having densities of 3.15 g/cm^3 (98.1 percent) and 3.17 g/cm^3 (98.8 percent of theoretical), respectively, were cut in half and polished. Photomicrographs were taken at six zones within the rotors as illustrated in Fig. 12. Figures 13 and 14 show the respective photomicrographs (unetched) of the sintered and HIPed rotors. In Fig. 13 (sintered rotor) zones 3 and 5 located near the outer hub surface show lower porosity than the remaining zones which are located in the central portion along the rotor axis. Microstructures of the HIPed rotor (Fig. 14) show approximately the same characteristics for all six zones. However, the porosity in all zones was significantly reduced and the lower density core section was virtually eliminated by the HIPing process. These findings agreed well with the initial results from the computed X-ray tomography experiment.

Table 6 Strength comparison of sintered and HIPed rotors

Rotors Tested at Allison

Condition	No. of Rotors	Axial Direction MOR (ksi)	Axial Direction No. of Bars	Radial Direction MOR (ksi)	Radial Direction No. of Bars
Sintered	2	47.2	12	53.6	28
HIPed (NASA)	2	59.9	12	56.8	28

Rotors Tested at Standard Oil

Condition	No. of Rotors	Axial Direction MOR (ksi)	Axial Direction No. of Bars	Radial Direction MOR (ksi)	Radial Direction No. of Bars
Sintered	4	43.8	18	45.1	23
HIPed (ASEA)	2	47.9	11	53.6	16

Table 7 Strength comparison of sintered and HIPed test bars

Group No.	After Sintering MOR ± SD (ksi)	m	After HIPing (ASEA) MOR ± SD (ksi)	m
1	61.2 ± 8.4	7.1	71.9 ± 13.8	5.6
2	60.1 ± 8.8	7.1	66.5 ± 6.0	11.9
			64.5 ± 7.4	8.9
			64.9 ± 9.4	6.7
			64.5 ± 9.6	7.0
		Average	65.1 ± 8.3	8.9

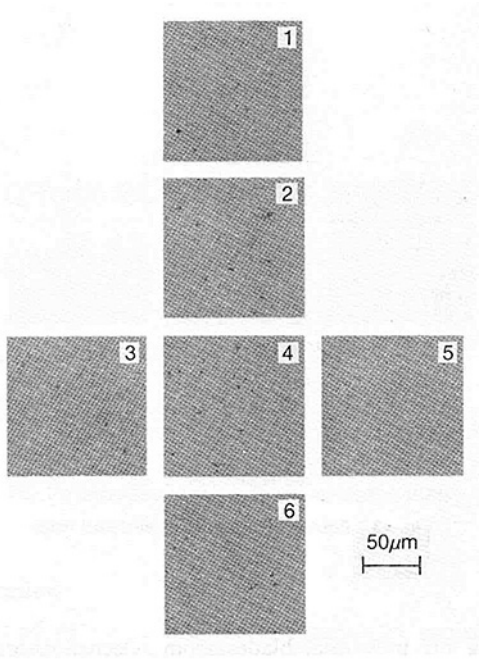

Fig. 14 Photomicrographs of HIPed rotor

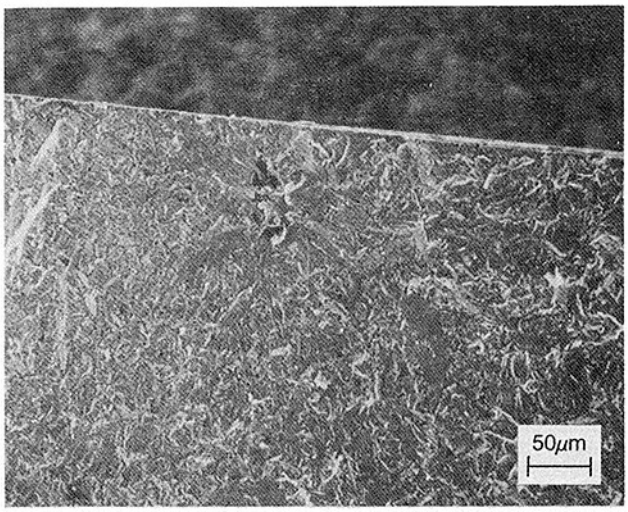

Fig. 15 Fracture origin

Strength Data

Influence of HIPing on material strength was assessed using injection molded test bars and test bars cut from rotors. Each group was compared with control samples which had been fabricated and processed in parallel through pressureless sintering. Flexure strength tests were conducted on 3.2 mm × 6.4 mm × 50.8 mm (1/8 in. × 1/4 in. × 2 in.) specimens at room temperature.

Table 6 shows average flexure strength for test bars cut from rotors and tested by both Allison and Standard Oil. NASA HIPed rotors were tested at Allison while ASEA HIPed rotors were tested at Standard Oil. Table 7 lists the data obtained for individually processed test bars. Each of the flexure strength values in this table represents the average of 25 data points. Both sets of data show some increase in flexure strength after HIPing and the material strength of some of the HIPed rotors closely approaches the strength of pressureless sintered individually processed test bars. Because of the two different test sites no conclusion will be drawn on the influence of HIPing pressures on flexure strength.

The strength data on the individually processed test bars HIPed at ASEA showed an increase for each group tested and about a 10 percent improvement was observed on average. Analysis of the Weibull moduli obtained for the various sets of test bars indicate mixed results. In one case a largely improved Weibull modulus was observed, in the other case a slight decline was determined. Failure analysis work is in progress to determine whether the fracture origins show any significant difference between sintered and HIPed specimens.

Observed failure origins for test bars cut from rotors were generally surface or subsurface porosity on the tension face, probably caused by compound or molding inhomogeneities. Figure 15 shows a subsurface void of a test bar having a strength of 49.7 ksi (343 MPa). The void is surrounded by a characteristic smooth mist region and outward radiating stress lines.

Spin Testing

Proof spin testing has been utilized in the production of aircraft and industrial turbine engines for several decades and until recently was concentrated in the aerospace and related industries. More recently spin testing has been utilized for high-performance ceramic rotors to qualify rotor design and to monitor rotor quality during the fabrication steps. Verification of the structural integrity is accomplished by spinning the rotors to at least the design speed, the minimum value acceptable, in a controlled environment.

Spin testing of the AGT-100 gas turbine rotors was carried out in vacuum in an armor-lined vessel at room temperature. The rotors, attached to a metal shaft, were air driven in a vertical position to either a selected spin speed or to burst. The system used has a maximum capability of 150,000 rpm. Blade tip or hub fracture was determined by recording vibration as a function of speed using a noncontacting probe on the drive shaft to detect balance changes during the test.

Spin test results for a large population of 70 pressureless sintered rotors (Group C) provided an average burst speed of 99.8 krpm (634 m/s). Suspended item analysis was utilized (Groseclose, 1985) in determining average burst speed because only 40 rotors were spun to failure while the remaining thirty were proof-tested to 110 to 120 percent of design speed.

A total of ten HIPed rotors also from Group C was spun to failure. The results are shown in Fig. 16. Eight of these rotors were HIPed under the NASA experiments using 20,000 psi (138 MPa) and the remaining two rotors had been subjected to

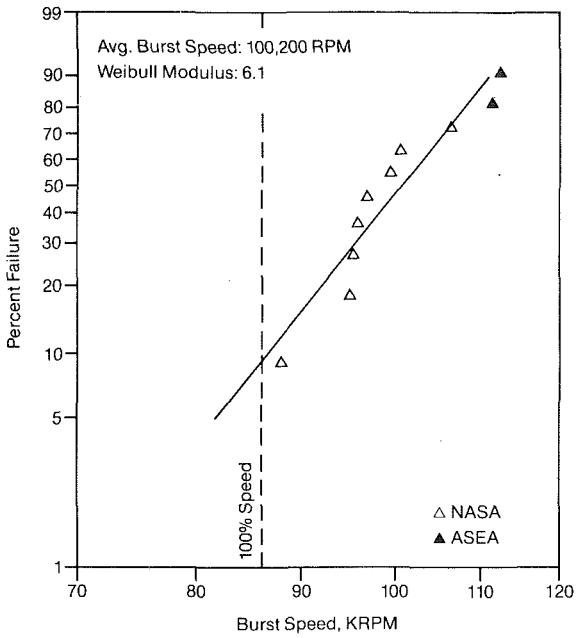

Fig. 16 Spin results of HIPed rotors

30,000 psi (207 MPa) in the ASEA experiments. The average burst speed of these ten HIPed rotors [100.2 krpm (636 m/s)] equals the result obtained for the larger control group. However, at this point it should be noted that the two rotors HIPed at the higher pressure burst at 111.5 (708 m/s) and 112.5 krpm (714 m/s), which would indicate a substantial improvement over pressureless sintered rotors [99.8 krpm (634 m/s)] as well as over rotors HIPed at NASA at the lower pressure [97.3 krpm (618 m/s)]. Additional data are being collected on Group D rotors to further substantiate the influence of select HIPing parameters.

Since both density and strength have increased as a result of HIPing one would also expect an increase in the spin values particularly since the rotor failure characteristics are believed to be largely volume driven. However, spin data obtained so far have not shown any significant improvements with the exception of two data points. Additional work is planned to investigate further the correlation of high HIPing pressures with spin speeds to determine whether the observed spin speeds on the ASEA HIPed rotors can consistently be duplicated.

Summary

It has been shown that complex sintered alpha silicon carbide shapes such as gas turbine rotors can be HIPed at high temperatures and pressures to provide densities in excess of 98 percent of theoretical. It was demonstrated that densification can be accomplished utilizing a range of temperatures and pressures. Density gradients as observed on sintered components were significantly decreased and a more uniform microstructure with smaller pores and no exaggerated grain growth was obtained. In addition, increased room temperature strengths on test bars cut from rotors and on individually fabricated test bars were observed. Average spin test data on HIPed rotors have not shown an improvement over sintered rotors, although the individual data points suggest that rotors HIPed at high pressures may have improved spin test results.

Further experiments regarding the influence of the HIPing parameters, especially of high HIPing pressure, on physical properties such as flexure strength and performance in spin testing are being planned. In addition, failure analyses will be utilized more extensively to assess the type and size of the failure-causing flaws in HIPed components.

Acknowledgments

The U.S. Department of Energy, Office of Conservation and Renewable Energy, Transportation Systems, William Sanders and James D. Kiser, NASA Lewis Research Center, and Ronald Howard, ASEA Pressure Systems, are acknowledged.

References

Amberg, S., Nylander, E. A., and Uhrenius, B., 1974, "The Influence of Hot Isostatic Pressing on the Porosity of Cemented Carbide," *Powd. Metall. Int.*, Vol. 6, pp. 178–180.

Groseclose, L. E., and Johnson, R. A., 1985, "Status on the AGT 100 Advanced Gas Turbine Program," ASME Paper No. 85-GT-205.

Hermansson, L., Mystrom, L., and Adlerborn, J., 1986, "Hot Isostatic Pressing of Silicon Carbide With no Sintering Agents," 2nd International Symposium Ceramic Materials and Components for Engines, Travemunde-Lubeck, Apr.

Larker, H., 1980, "Hot Isostatic Pressing of Shaped Silicon Nitride Parts," in: *High-Pressure Science and Technology*, Vol. 2, Plenum Publishing Corporation, New York, pp. 651–655.

Larker, H. T., 1980, "HIP Silicon Nitride," NTIS AGARD CP-276, Mar. p. 18-1 ff.

Larker H. T., 1983, "On Hot Isostatic Pressing of Shaped Ceramic Parts," Ceramics in Engine Conference, Hakone, Japan, Oct. 17–21.

McFadden, J., 1983, "Hot Isostatic Densification of Castings," Seminar by Thermatech Division, Howmet Turbine Components Corp. at ASEA Pressure Systems, Apr. (unpublished).

Moll, J. H., 1983, "HIP of Powder Metal Structural Materials," Seminar by P/M and Titanium Crucible Research Center at ASEA Pressure Systems, Apr. (unpublished).

Ohnsorg, R., Ten Eyck, M., Zanghi, J., and Sweeting, T., 1985, "Ceramic Component Fabrication," *Proceedings of the Twenty-Third Automotive Technology Development Contractors' Coordination Meeting*, Detroit, pp. 173–181.

Ohnsorg, R., Ten Eyck, M., and Sweeting, T., 1986, "Development of Injection Molded Rotors for Gas Turbine Applications," ASME Paper No. 86-GT-45.

Price, P. E., 1982, "Hot Isostatic Pressing in the Aerospace Industry," *Metal Progress*, pp. 46–47.

Sikora, P. F., and Yeh, H. C., 1976, "Consolidation of Silicon Nitride Without Additives," NASA TM 73693, Am. Ceram. Soc. Fall Meeting, San Francisco, CA, Oct. 31-Nov. 3.

Watson, G. K., Moore, T. J., and Millard, M. L., 1985, "Effect of Hot Isostatic Pressing on the Properties of Sintered Alpha Silicon Carbide," *Am. Cerm. Soc. Bull.*, Vol. 64, pp. 1253–1256.

Whalen, T. J., 1984, "HIPing of SiC," *Ceram. Eng. Sci. Proc.*, Vol. 5, pp. 341–349.

Yamada, T., Shimada, M., and Koizumi, M., 1981, "Fabrication of Si_3N_4 by Hot Isostatic Pressing," *Am. Ceram. Soc. Bull.*, Vol. 60, pp. 1225–1228.

J. S. Anderson

E. L. Carls[1]

P. J. Mainhardt[2]

W. M. Swift[1]

J. M. Wheeldon

NCB (IEA Grimethorpe) Ltd., United Kingdom

S. Brooks

Central Electricity Generating Board, United Kingdom

A. J. Minchener

NCB Coal Research Establishment, United Kingdom

J. Stringer

Electric Power Research Institute, USA

Wastage of In-Bed Heat Transfer Surfaces in the Pressurized Fluidized Bed Combustor at Grimethorpe

The wastage of in-bed heat transfer surfaces has recently emerged as a potentially serious problem for both pressurized and atmospheric fluidized bed combustors. The experimental pressurized fluidized bed combustion facility at Grimethorpe has accumulated a considerable quantity of data covering the wastage of in-bed tubes obtained during a total of just over 3600 h of operation. The combustor operated with different tube banks, with some degree of wastage being experienced with each one. The data are described, evidence for possible solutions is presented, and plans for future tests at Grimethorpe to prove these solutions are outlined.

Introduction

The pressurized fluidized bed combustion (PFBC) of coal offers several advantages over conventional techniques. These include:

- A more compact combustion system because of both the pressurized operation and enhanced heat transfer rates to the steam-raising tubes. This results in a reduction in the capital cost of boilers.
- A reduction in sulfur dioxide emissions through the addition of limestone or dolomite to the bed to capture the sulfur present in the coal as a dry waste product.
- Using the pressurized off gases to drive a gas turbine. The combination of gas and steam turbines offers higher electrical power generation efficiencies than a cycle based solely on a steam turbine.

These potential advantages were recognized by the energy authorities of the governments of the Federal Republic of Germany, the United Kingdom, and the United States of America and led to the founding in 1975 of the Grimethorpe Project under the auspices of the International Energy Agency. The three governments shared equally the costs of designing, building, and operating the Facility from 1976 to July 1984. Since August 1984 further work has been jointly sponsored by the National Coal Board and the Central Electricity Generating Board of the United Kingdom. The results presented in this paper were obtained during the IEA-funded period, during which a variety of performance data were collected [1].

Investigations into the wastage of in-bed tubes were not part of the original experimental program at Grimethorpe. However, wastage occurred that was sufficiently severe to prevent the implementation of the planned program. In the time available it was decided to incorporate measures which would alleviate the wastage sufficiently to allow the planned program of work to be completed, and that thorough investigations of the wastage would be carried out elsewhere.

The paper describes the investigations into the wastage of in-bed tubing which were carried out as part of the Grimethorpe program and indicates the directions which future work should take to overcome the problem.

Brief Description of the Facility

A schematic layout of the combustor is presented in Fig. 1. The fluidized bed is contained within a water-cooled square-sectioned combustor supported within a pressure shell. The pressure shell is refractory lined, has an outer diameter of 4 m, and is 14 m tall. The combustor walls are constructed of

[1]Present address: Argonne National Laboratory, USA.
[2]Present address: Burns & Roe, Inc., USA.

Contributed by the Power Division for publication in the JOURNAL OF ENGINEERING FOR GAS TURBINES AND POWER. Manuscript received by the Power Division January 1986.

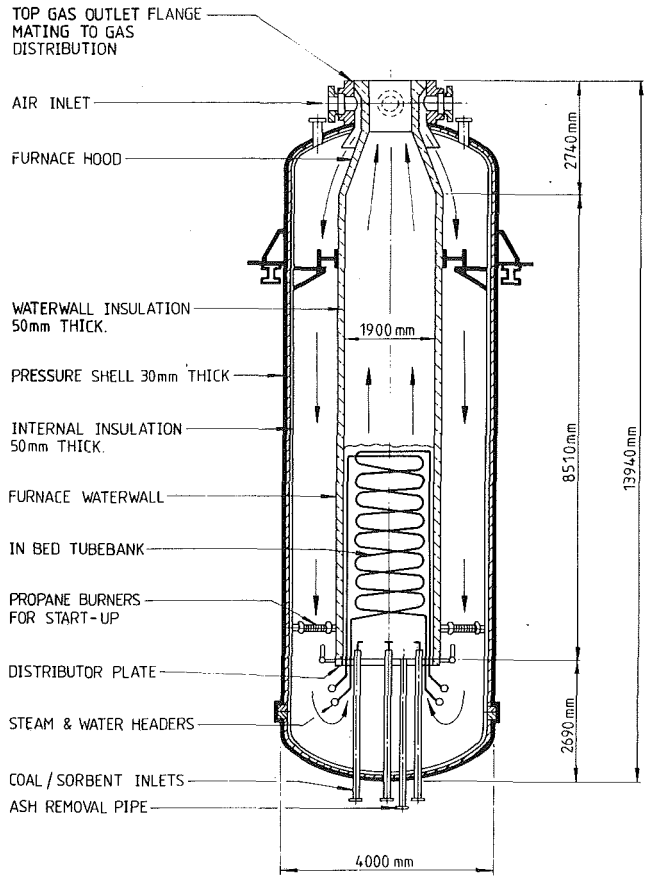

Fig. 1 General arrangement of combustor

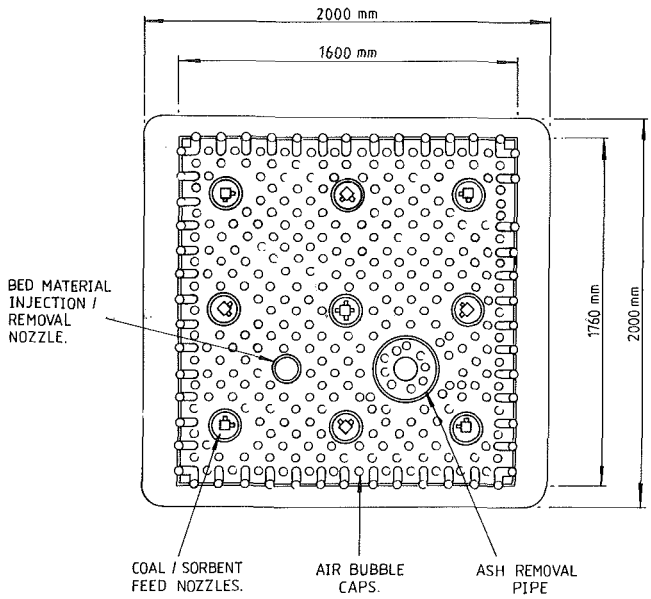

Fig. 2 Distributor plate layout

refractory-lined water-cooled tubing, and the combustor is over 8 m tall with a cross section of 1.9 × 1.9 m. Combustion air enters the top of the pressure shell and flows down its length before entering the combustor through the distributor plate.

Excess heat is removed by the water flowing in the water-cooled walls and by means of an in-bed tube bank which raises superheated steam. Fuel and sorbent, which can be prepared and mixed to specific sizes and mass ratios over a wide range, are injected into the combustor at controlled rates by a maximum of nine rotary valves via a lock-hopper and pneumatic feed system. The bed level is maintained constant by periodically removing excess bed material through a refractory-lined ash transport pipe which passes up through the pressure vessel to the surface of the distributor plate. From the combustor, two high-temperature refractory-lined ducts direct the off gas into a dust removal system, consisting of two primary and two secondary cyclones. The off gases are then cooled in a waste heat boiler before passing to pressure let-down and discharge to atmosphere.

The precise details of the distributor plate layout varied slightly between test series but a typical layout is presented in Fig. 2. Air at approximately 250°C and the required operating pressure passes through the distributor and into the combustor via 325 bubble caps. These are simple cylinders capped at the top and drilled such that the air enters by a series of horizontal holes around the upper vertical portion. The coal and the sorbent are fed as a blend through as many as nine feed nozzles arranged as shown. The temperature of the incoming mixture is around 20°C and the conveying air represents around 10 percent of the total fluidizing air. Even when a feed line is not in use a reduced quantity of air is still passed through to prevent blocking of the pipe.

The bed injector nozzle has a deflector plate over the opening to prevent jets of air and solids impinging directly on the tube bank. As with the conveying lines, air is passed through the nozzle continuously to prevent the line from blocking.

A full description of the Grimethorpe Facility is contained in [2].

Table 1 Datum operating conditions for each of the tube banks used

	Tube bank A	Tube bank C	Tube bank C2
Freeboard pressure, bar abs	10	12	12
Air mass rate, kg/s	31	21	19
Mean bed temperature, °C	850	850	880
Fluidizing velocity, m/s	2.5	1.5	1.4
Bed height, m	3.5	4.5	4.2
In-bed gas residence time, s	1.4	3.0	3.0
Excess air level, percent	20–50	35	35
Coal heat input, MW	80–65	46	40
Tube bank heat load, MW	30	18	22
Mean bed particle size, μm	1190	1170	1110

Tube Bank Metal Wastage Experience

Three different tube banks were used during the IEA Phase, tube banks A, C, and C2. The first two banks consisted of plain tubes and the last one used, tube bank C2, was finned to reduce the rate of metal wastage. The datum operating conditions for each of these banks are presented in Table 1.

Tube Bank A. Tube bank A consisted of 42 parallel flow paths, making a total surface area of 162 m^2. Each of the 42 flow paths was constructed as a vertical serpentine of 19 near horizontal tubes each having an o.d. of 31.8 mm and a wall thickness of 4.5 mm. The lower 12 rows were made from 15Mo3 (approximate U.S. equivalent T11); the 13th row was half 15Mo3 and half 10CrMo910 (approximate U.S. equivalent T22); and the upper six rows were made from 10CrMo910 (see Table 2 for a list of the compositions of the alloys used). Adjacent serpentines were positioned such that the tubes formed a triangular pitch arrangement. The mean pitching is shown, in relation to the other two tube banks used, in Fig. 3. The tube bank was designed to remove 30 MW of heat with a bed temperature of 850°C.

At several positions within the tube bank, tubes were omitted from the matrix to facilitate the insertion of measurement probes (heat transfer probes, corrosion probes, erosion probes, etc.).

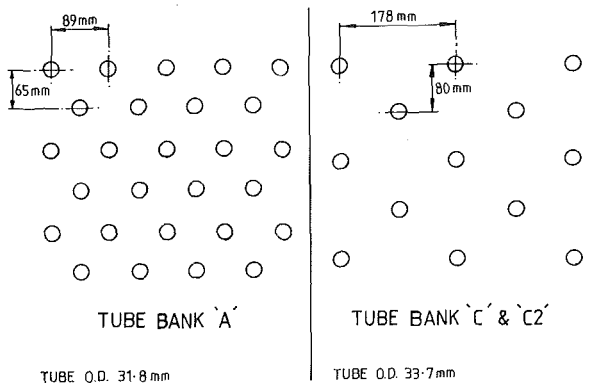

Fig. 3 Comparison of tube layouts for tube banks A and C

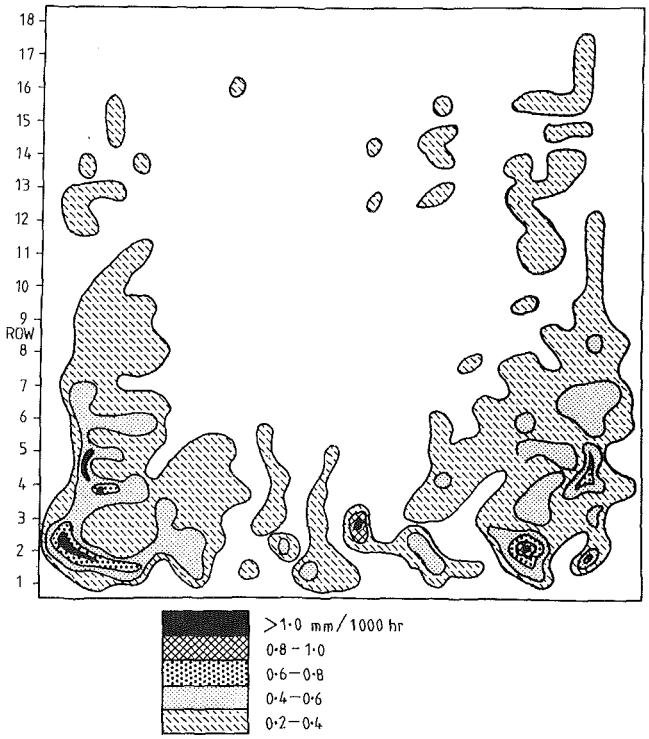

Fig. 4 Distribution of metal wastage on tube bank A after 864 h

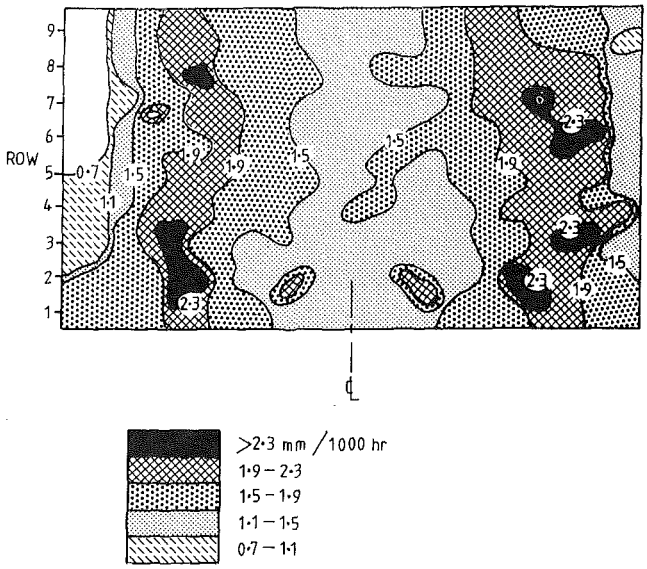

Fig. 5 Distribution of metal wastage on tube bank C after 468 h

After 864 h of coal burning, tube bank A was removed from the combustor and subjected to a detailed visual examination. Although some localized erosion caused by jets formed at badly sealed thermocouple penetrations was found, this examination failed to identify any generalized wastage of tubes. Only later when the more severe wastage was found on tube bank C and measurements of tube diameter were then made on tube bank A did wastage become apparent. The diameter of each tube was determined at five locations along its length in both the vertical and horizontal planes as well as the two 45-deg diagonals.

The measurements were obtained using micrometers and vernier calipers with quoted accuracies of ± 25 μm. It was found that the worst losses had occurred in the vertical diameter; the distribution is shown in Fig. 4.

The most severe losses on tube bank A occurred in the lower rows. Inspection of individual loss measurements at each of the five measurement planes showed that in the region of highest loss wastage rates of up to 1.7 mm/1000 h were recorded. The pattern of wastage is remarkably symmetric about the center line. There are two regions of relatively high wastage which extend well up into the tube bank. A more detailed description of the losses which occurred with tube bank A is given in [3].

Experiments carried out subsequent to the specification of tube bank A had indicated that the high fluidizing velocity would lead to unacceptably low combustion and sulfur-retention efficiencies. In additon it was shown that the close packing and high combustion intensity would lead to a large temperature drop across the tube bank. The first tests at Grimethorpe confirmed that this was indeed the case, the vertical temperature drop being as high as 150°C. Thus the design of a new tube bank, tube bank C, was initiated. The new tube bank would have a more open structure to promote better mixing within the bed and reduce the vertical temperature drop, and would be taller than tube bank A to increase the in-bed gas residence time and so promote better combustion and sulfur-retention efficiencies. The in-bed gas residence time was further increased by reducing the datum fluidizing velocity from 2.5 to 1.5 m/s.

Tube Bank C. Tube bank C consisted of 21 parallel flow paths, making a total of 102 m^2. Each of the 21 flow paths was constructed as a vertical serpentine of 21 near horizontal tubes each having an o.d. of 33.7 mm and a wall thickness of 4.5 mm. The lower 13 rows were made from 15Mo3; row 14 was half 15Mo3 and half 10CrMo910; and the upper seven rows were made from 10CrMo910. Adjacent serpentines were positioned such that the tubes formed a triangular pitch arrangement. The mean pitching is shown in relation to the other two tube banks used, in Fig. 3. The tube bank was designed to remove 18 MW of heat with a bed temperature of 850°C. Tubes were again omitted from the matrix at several positions to facilitate the insertion of measurement probes.

The design of tube bank C was successful in that the vertical temperature drops experienced with tube bank A were reduced to 40°C and the performance of the combustor in terms of combustion efficiency and sulfur retention was improved. However, tube bank C suffered very high rates of generalized metal wastage.

Following 468 h of coal burning a thorough examination of the accessible lower rows of tube bank C was undertaken. The inspection revealed that considerable wastage had occurred on the tubes. It was decided that the losses which had occurred were sufficiently severe to warrant the removal of the lower rows. Only the lowest three rows were accessible for measurement, so having removed the lowest three rows it was possible

Table 2 Alloys used in the tube banks

ALLOY	COMPOSITION (%)									
	Cr	Ni	C	Mo	Mn	Si	V	Cu	S	Fe
15Mo3	–	–	0.12–0.20	0.25–0.35	–	–	–	–	–	Bal.
Incoloy 800H	20.6	31.9	0.04	–	0.75	0.35	–	0.27	0.0007	46.05
13CrMo44	0.7–1.0	–	0.10–0.18	0.4–0.5	0.5	–	–	–	–	Bal.
10CrMo910	2.0–2.5	–	0.15 max.	0.9–1.1	0.5	–	–	–	–	Bal.
X20CrMoV12.1	11.0–12.5	0.3–0.8	0.17–0.23	0.8–1.2	0.3–0.8	0.1–0.5	0.25–0.35	–	–	Bal.
Sicromal 23/20	25	20.5	0.2	–	2.0	2.0	–	–	–	Bal.

Table 3 Rates of metal loss for different tube materials used in row 1

Hours of exposure	Alloy (No. of tubes)	Rate of loss (mm/1000 h)
468	15Mo3 (21)	1.9
205	15Mo3 (5)	1.8
	13CrMo44 (4)	2.3
	10CrMo910 (4)	2.5
	Incoloy 800H (2)	2.8
	X20CrMoV12.1 (4)	3.5

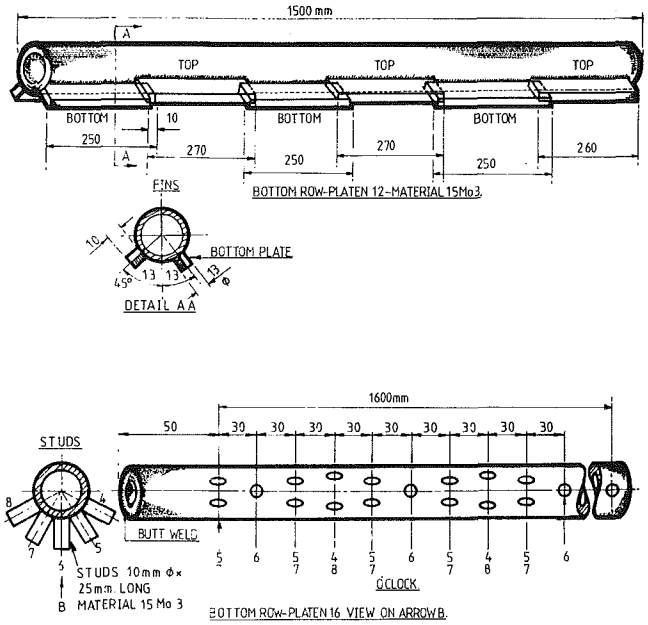

Fig. 6 Attachment of fins and studs to row 1 of tube bank C

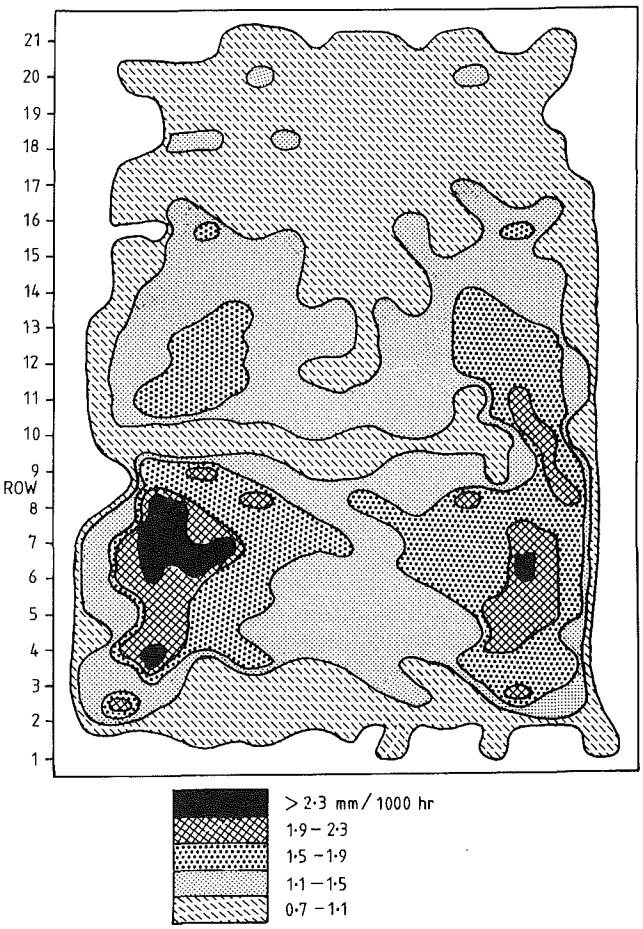

Fig. 7 Distribution of metal wastage on tube bank C after 1223 h

to measure the next three rows, which it was decided would also have to be removed. The distribution of the losses on the vertical diameter is shown in Fig. 5. The symmetry observed with tube bank A is again visible with the same two regions of high wastage extending up into the tube bank. Inspection of individual losses in each of the five measurement planes showed that in the region of highest loss, wastage rates in excess of 3 mm/1000 h were recorded. It was also found that the losses were not decreasing with height, so the removal of tubes was stopped at row 7 and it was decided that the rates of metal loss were such that a new tube bank would be needed to complete the planned tests. In order to be able to continue with testing in the short term, the rows which had been removed were replaced. Rows 2 to 7 were replaced with Incoloy 800H, chosen primarily because of its availability, and row 1 was replaced by tubes made from a variety of boiler tube alloys which were readily available; these are shown in Table 2. Note that the replacement tubes of row 1 of platens 12 and 16 were fitted with fins and studs, respectively, as shown in Fig. 6.

Following these tube replacements the tube bank was operated for a further 205 coal-burning hours. The bottom row was again measured and the results are shown in Table 3 compared with the results for the first 468-h period. These results showed firstly that the wastage of the tubes had continued at the same rate, and perhaps more importantly, that the rate was not dependent upon alloy type. This confirmed what had been suspected from metallographic examination of tubes removed previously from the tube bank, that the mechanism of wastage was an erosion/abrasion process without any contribution from corrosion. It was also found that the fitting of fins and studs to the tubes in platens 12 and 16 reduced the rate of metal loss by approximately a factor of 4, the studs being slightly more effective than the fins.

A number of further modifications were then implemented. Row 1 was replaced with tubes, all of which were fitted with studs, and the distributor plate was raised to reduce the gap between the distributor plate and the bottom of the tube bank from 0.9 to 0.6 m. This latter modification was based on the results of cold model studies which are described later. After a total of 1222 coal-burning hours the entire tube bank was removed from the combustor and subjected to a detailed metrological examination. The most severe wastage was again found to be in the vertical diameter with the average rate of

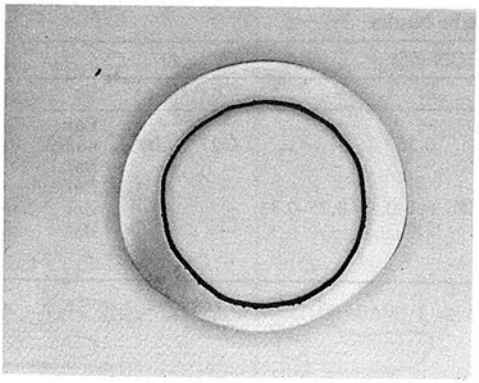

Fig. 8 Badly wasted tube from tube bank C

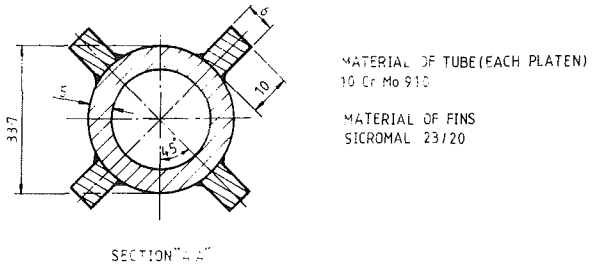

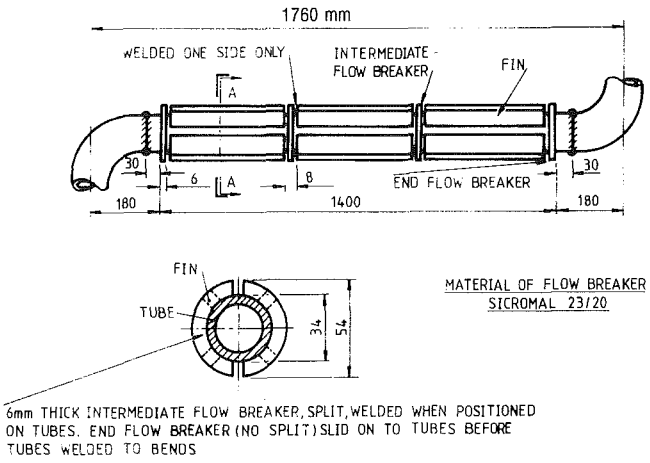

Fig. 9 Finning arrangements for tubes on tube bank C2

loss for the whole tube bank being 1.1 mm/1000 h. The distribution of losses in the vertical diameter is shown in Fig. 7. Unlike earlier measurements made on tube banks A and C, the lowest rows suffered relatively little loss; this was the result of raising the distributor plate. Once again the losses show symmetry about the center line. Inspection of individual losses in the five measurement planes showed that in the region of maximum loss, wastage rates of up to 3 mm/1000 h were recorded. A severely wasted tube from tube bank C is shown in Fig. 8. Further details of the loss measurements can be found in [4, 5].

The design of the new tube bank to replace tube bank C, tube bank C2, incorporated those measures which it was thought would bring about a reduction in wastage rate. These measures were mostly identified by tests carried out in cold model studies.

Cold Model Studies. The cold model studies were carried out at CRE (the NCB Coal Research Establishment, Cheltenham), at CURL (the NCB Coal Utilisation Research Laboratory, Leatherhead) and also at the University of Bradford. The results of some of these investigations are summarized in Table 4.

Table 4 Summary of results from cold model studies

(*a*) Influence of reducing the gap between the distributor plate and the bottom row of the tube bank upon the rate of material loss.

Gap	Fluidizing velocity, m/s	Relative material loss	
		Bottom row	Remainder of rows
0.9	2	100	48
0.45	2	27	47

(*b*) Influence of fluidizing velocity and longitudinal fins upon material loss.

Gap	Fluidizing velocity, m/s	Relative material loss	
		Bottom row	Remainder of rows
0.45	2	100	27
0.45	1	16	2.5

Note: All above tests with the same sized sand, 0.5 to 2.0 mm, with a mean size of 0.75 mm.

The results presented were obtained by weighing aluminum tubes before and after exposure in a fluidized bed of sand. The major findings of this work were:

- reducing the gap between tube bundle and air distributor from 0.9 m to 0.45 m resulted in a reduction in material loss for the lower rows, the reduction for row 1 being by a factor of 4. The material loss for the remainder of the tubes was not affected.
- the addition of four longitudinally mounted fins to the tubes reduced the erosion rate by a factor of 3.7 at 2 m/s and 6.4 at 1 m/s.
- reducing the fluidizing velocity from 2 to 1 m/s resulted in a sixfold reduction in the erosion rate of the plain tubes and elevenfold for the finned tubes.
- four longitudinal fins fitted to tubes were more efficient than studs at reducing erosion.

With the exception of the reduction in fluidizing velocity, all of the above results were taken into account in the design of tube bank C2.

Tube Bank C2. Tube bank C2 was similar in many respects to tube bank C. The overall height and pitching were the same. This was to ensure that the successful aspects of the design of tube bank C were not lost, i.e., low vertical temperature drop and good combustion and sulfur retention efficiencies. The material used for the tubes was 10CrMo910 throughout. The design also incorporated all measures which it was thought would reduce wastage of the tubes. The most important of these was the fitting of four longitudinal fins, made from Sicromal 23/20, to each of the horizontal tubes, as shown in Fig. 9. There was concern that the fitting of these fins could cause enhanced flow along the tubes which might lead to erosion of the walls of the combustor and downcomers. To prevent this, so-called flow-breaker rings were fitted, as shown in Fig. 9. Attachment of the fins brought about an increase in heat transfer per unit length of tube of about 18 percent, and so to maintain the same thermal duty for the tube bank, a number of tubes were omitted from the tube array. As before, tubes were also omitted from the matrix at several positions to allow the insertion of measurement probes.

After a total of 1519 coal-burning hours the IEA test program was completed and tube bank C2 was removed from the combustor for thorough visual and metrological examinations. It was apparent after removal of the tube bank from the combustor that the appearance of tube bank C2 after service was quite different from that of the previous two tube banks. The tubes were covered with a layer of what was later found to

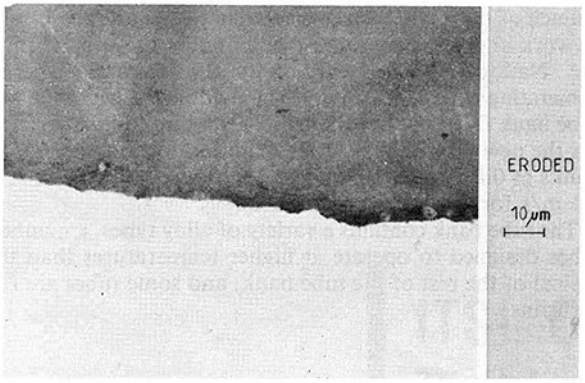

Fig. 10(a) Surface of tube from tube bank C showing result of erosion/abrasion process

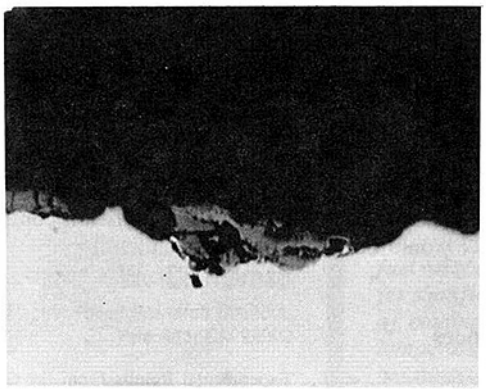

Fig. 10(b) Surface of tube from tube bank C2 showing result of oxidation-erosion/abrasion process

be oxide (magnetite) covered with a mixture of oxide and bed material. This suggests that the mechanism of wastage with tube bank C2 was quite different from that for tube bank C and that rather than erosion/abrasion alone being the cause, a two-stage oxidation–erosion/abrasion process had been occurring. Sections of tubes from both tube bank C and tube bank C2 are shown in Fig. 10 and the difference in the appearance of the tubes is clearly visible. In order to obtain tube loss data which could be compared to those for the previous tube banks the layer was removed by scraping with a metal blade and the tubes were then measured in the usual manner. The losses were very similar for the vertical and the horizontal diameters with the average rate of wastage for the whole tube bank being about 0.22 mm/1000 h. This compares with 1.1 mm/1000 h for the vertical diameter of tube bank C and 0.29 in the horizontal diameter. Thus the apparent effect of adding the fins to the tube bank was similar to that observed in the cold model studies. The distribution of the wastage experienced with tube bank C2 in the vertical diameter is shown in Fig. 11. In the region of highest losses wastage rates of up to 0.5 mm/1000 h were recorded. The symmetry seen with the previous two tube banks is still visible although the considerably lower losses encountered make the pattern less clear. A more detailed account of the losses which occurred with tube bank C2 is given in [6].

Effect of Temperature on Metal Wastage

During operation with tube bank C2 there were two sets of erosion probes installed within the tube bank. One set consisted of five water-cooled probes and the other of three stream-cooled probes. These probes were made from the same material as the tube bank, 10CrMo910; of the same size tubing; and were installed in such a way that they formed part of the triangular pitch arrangement of the tube bank. All of the

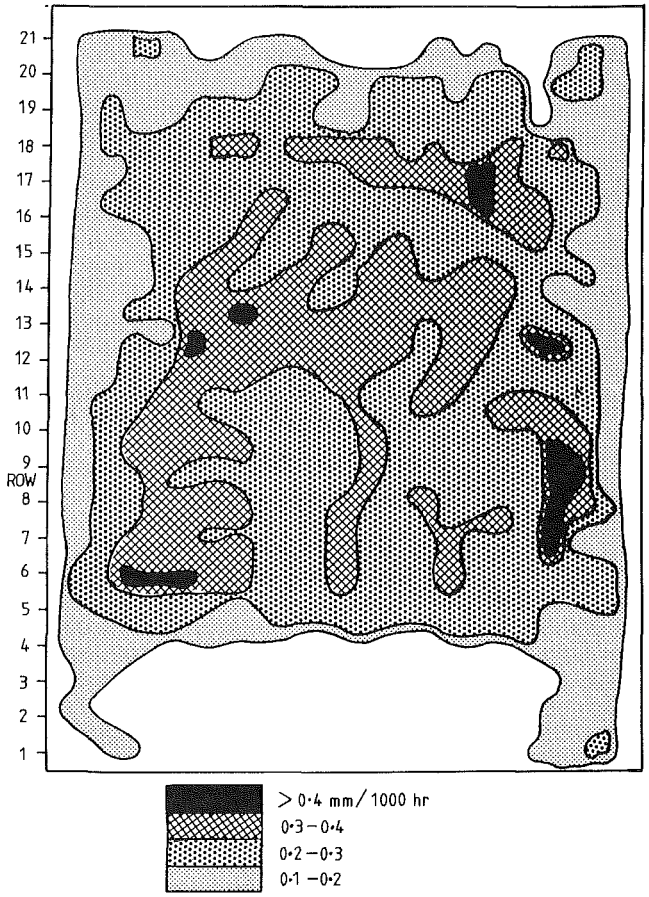

Fig. 11 Distribution of metal wastage on tube bank C2 after 1519 h

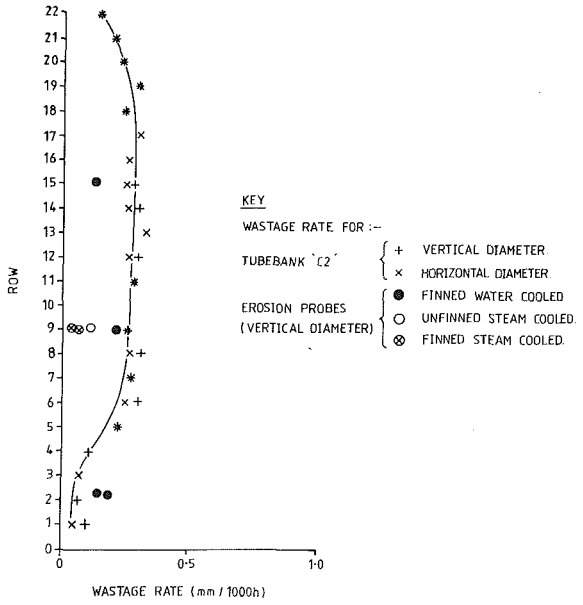

Fig. 12 Average rate of wastage for tube bank C2, all platens (1519 h)

water-cooled probes and two of the three steam-cooled probes were fitted with fins of the same design as those fitted to the tube bank. The third steam-cooled probe was not fitted with fins. These probes produced some most interesting results and are presented in Fig. 12. It was found that the water-cooled probes, as might be expected, wasted at much the same rate as

the tube bank surrounding them, but the steam-cooled probes suffered far less wastage. The only difference between the steam-cooled probes and the other tubes tested is the surface metal temperature. The tube bank operated with metal temperatures in the range 300 to 400°C and the water-cooled probes had metal temperatures in the range 250 to 300°C, whereas the steam-cooled probes operated with metal surface temperatures in the range 450 to 550°C. The considerable importance of this result is that in a commercial PFBC unit the metal temperatures employed would be in the range 450 to 700°C, far higher than those used at Grimethorpe. The results from the erosion probes indicate that the wastage rates which might be expected under these more realistic conditions would be far less than those experienced by the low-temperature Grimethorpe tube banks.

Effect of Alloy Type on Metal Wastage

It has already been shown that with tube bank C a variety of alloys were tested and found to waste at essentially similar rates. This is taken as an indication that the mechanism of wastage was erosion alone. However, with tube bank C2 it seems that the rate of wastage was reduced by the attachment of fins to a point where the mechanism became one of an interactive oxidation/erosion type. Under conditions which allow this oxidation/erosion mechanism to prevail, there might well be benefits to be obtained by the use of higher alloy steels than those generally used for evaporator duty. There is evidence [7] that under conditions which produced similar dual layers of tube oxide and bed material, tubes containing more than a threshold concentration of 9 percent chromium suffered considerably less wastage than tubes with chromium contents below the threshold. This effect is probably the result of the ability of these higher-alloy steels to produce adherent, erosion-resistant oxides.

Conclusions

Although the wastage of in-bed tubes is clearly a serious problem to be overcome before the full potential of AFBC and PFBC can be sought with confidence, there is every reason to be confident that acceptable lifetimes for tubes can be achieved. The results from Grimethorpe and elsewhere indicate that the solution to the problem will probably involve utilizing the beneficial effects of some or all of the following:

- higher surface metal temperatures
- using steels which contain higher concentrations of chromium
- the attachment of fins or studs to tubes
- reductions in fluidizing velocity

Each of these will be investigated in the continuing program of work at the Grimethorpe facility under the sponsorship of the National Coal Board and the Central Electricity Generating Board of the United Kingdom. A new tube bank, tube bank D, has been installed. The datum fluidizing velocity for the new tube bank is lower than that for the previous tube banks at 0.8 m/s (compared to 2.5 m/s for tube bank A and 1.5 m/s for tube banks C and C2).

The tube bank contains a variety of alloy types, a number of tubes designed to operate at higher temperatures than those typical of the rest of the tube bank, and some tubes are fitted with fins.

Acknowledgments

The above work was performed while the authors were associated with NCB (IEA Grimethorpe) Ltd., which carried out the project activities on behalf of the sponsors: the governments of the United Kingdom, the United States, and the Federal Republic of Germany. The views expressed are those of the authors and not necessarily those of NCB (IEA Grimethorpe) Ltd. or the sponsors.

The authors also wish to acknowledge the help of the large number of engineers seconded to the project from the three sponsoring countries, without whose significant contributions the paper would not have been written.

References

1 Wheeldon, J. M., et al., "Experimental Results From the Grimethorpe PFBC Facility," 8th International Conference on PFBC, Houston, TX, Mar. 1985.

2 NCB (IEA Grimethorpe) Ltd., "Design of the Facility as at March 1984," Report No. GEF/U/84/22, Mar. 1985; also published by US National Technical Informance Service (NTIS), US Department of Commerce, Springfield, VA, Report No. DOE/ET/10393-1857.

3 NCB (IEA Grimethorpe) Ltd., "Materials Related Problems and Investigations During Test Series 1," Report No. GEF/U/83/16, June 1984; NTIS Report No. DOE/ET/10393-1658.

4 NCB (IEA Grimethorpe) Ltd., "Tube Bank 'C' Metal Wastage Status Report – November 1982," Report No. GEF/U/82/21, Dec. 1982; NTIS Report No. DOE/METC-83-54.

5 NCB (IEA Grimethorpe) Ltd., "Tube Bank 'C' Metal Wastage Status Report – August 1983," Report No. GEF/U/83/5, May 1984; NTIS Report No. DOE/ET/10393-1623.

6 NCB (IEA Grimethorpe) Ltd., "Materials Related Activities During Test Series 2.2 and 2.3," Report No. GEF/U/84/15, June 1985; NTIS Report No. DOE/ET/10393-1905.

7 Radermakers, P. L. F., Bos, L., Van Wortel, J. C., and Kolster, B. H., "Corrosion/Erosion Tests in a Fluidised Bed Boiler," Institute of Energy Conference "Fluidised Bed Combustion—Is It Achieving Its Promise?" London, Oct. 1984.

ITSL Coal Liquid as a Combustion Turbine Fuel

K. L. Rieke

H. G. Lew

Westinghouse Electric Corporation,
Combustion Turbine Operations,
Concordville, PA 19331

W. C. Rovesti

Electric Power Research Institute,
Palo Alto, CA 94303

The combustion characteristics of low-hydrogen-content distillate fuels produced from coal differ from those of conventional petroleum distillates. The differences include: increased flame emissivity which contributes to higher combustor liner temperature, and increased fuel-bound nitrogen which contributes to higher NO_x emission. This paper presents the results of a laboratory test program to evaluate the emissions and combustor performance characteristics when burning the ITSL heavy distillate coal-derived liquid (CDL), and thus determine its acceptability and suitability as a utility combustion turbine fuel. The chemical and physical properties characterizing the test fuel were determined. The trace metals, such as sodium, potassium, vanadium, etc., are low and within concentrations presently allowable in fuel oil specifications. The burner performance factors on the CDL fuel did not differ significantly from those of the baseline No. 2 fuel. Evaluation and comparison of combustor wall temperatures when burning ITSL showed the increase in wall temperature (above No. 2 fuel) to be consistent with expectations. Emissions were measured over an equivalent load range of 30 to 100 percent engine base load. The increase in the measured NO_x emissions with increasing combustor temperature rise (load) was observed. The usual reduction of NO_x with water injection into the combustor was also observed. Other emissions, such as CO, UHC, O_2, and CO_2 for the ITSL fuel generally followed the usual characteristics with load. The ITSL Heavy distillate was found to be an acceptable coal-derived liquid fuel for combustion turbine applications.

Introduction

This paper reports the results of work performed by the Westinghouse Electric Corporation, Combustion Turbine Engineering Department, Combustion Turbine Operations as an extension of EPRI's overall program to determine the suitability of using coal-derived liquids as utility combustion turbine fuels under Contract RP2112-5, Evaluation of Coal Liquids as Utility Combustion Fuels. The added experimental program included laboratory testing of the Integrated Two-Stage Liquefaction (ITSL) coal-derived liquid (CDL) fuel, and was a logical extension of earlier testing of CDL fuels in a utility gas turbine power plant to assess the effects of burning coal liquids on gas turbine systems [1, 2].

The objective of the laboratory test program was to evaluate the emissions and combustor performance characteristics of a W251AA combustor when burning the ITSL coal-derived liquid fuel, and thus determine the acceptability of the test fuel as an electric utility combustion turbine fuel.

The ITSL fuel is produced in limited quantities in the Wilsonville, AL, Advanced Coal Liquefaction Unit operated by Catalytic, Inc., under contract to Southern Company Services. The Wilsonville coal liquefaction program is sponsored by EPRI, U.S. Department of Energy and Amoco Corporation. The production process incorporates two stages of hydrogenation. The test fuel from the Wilsonville plant was a heavy distillate product with a high distillation range [95 percent at 865°F (463°C)].

Combustion Test System

The ITSL CDL combustion tests were run in the Westinghouse Combustion Turbine Development Center located at Concordville, PA. The test combustor was installed in the facility test rig shown in Fig. 1. The rig is configured to simulate a sector of an engine. Inlet and exit instrumentation are identified on the figure. The combustor pressure rakes are located at the diffuser exit; the air inlet temperature is measured within the rig inlet chamber. Air and fuel flow are metered upstream of the rig. The exit gas temperature and emissions sampling rake locations are shown on the figure.

The W251AA test combustor is shown in Fig. 2. The test combustor and fuel nozzle configuration was the same as that field tested on H-Coal® and EDS coal-derived liquid (CDL) at the Philadelphia Electric Company's (PECO's) Richmond Station at Philadelphia, PA in 1982–1983 [1, 2]. Figure 2 shows the modifications required to fit the combustor within the laboratory test rig. The figure also shows the wall thermocouple locations for the ITSL fuel test program. Rings 0 through 5, inclusive, were instrumented the same as was the PECO field test combustor. The fuel nozzle was an air-assist atomizing nozzle. The air assist was used only during startup.

Contributed by the Gas Turbine Division of THE AMERICAN SOCIETY OF MECHANICAL ENGINEERS and presented at the 32nd International Gas Turbine Conference and Exhibit, Anaheim, California, May 31-June 4, 1987. Manuscript received at ASME Headquarters February 17, 1987. Paper No. 87-GT-157.

Fuel Characterization

The ITSL CDL fuel was fully characterized. The chemical and physical properties of the fuel were obtained using appropriate ASTM Procedures. The resulting data are presented in Table 1. The table includes the properties for H-Coal and EDS CDL liquids, burned in the W251AA engine during field tests [1, 2] for comparison purposes.

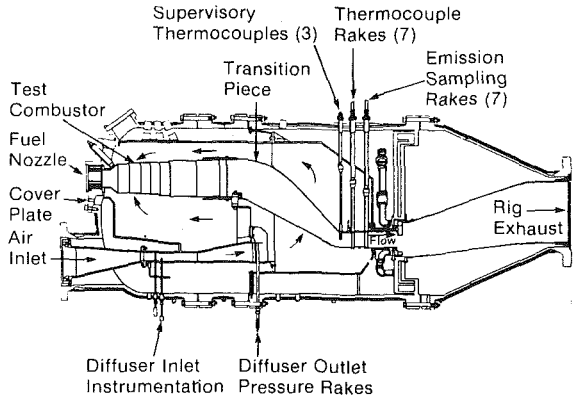

Fig. 1 Combustor test rig

The results of the fuel analyses indicated the fuel to be fully acceptable as a combustion turbine fuel. The trace metals, such as sodium, potassium, vanadium, etc., of concern from the high-temperature corrosion aspect of the turbine vane and blade materials, are within concentrations presently allowable in combustion turbine petroleum fuel oil ASTM specifications. As shown in Fig. 3, the viscosity versus temperature characteristic of the ITSL test fuel was such that the fuel was heated to about 110°F (43°C) at the combustor nozzle to assure proper fuel atomization in the primary combustion zone of the burner.

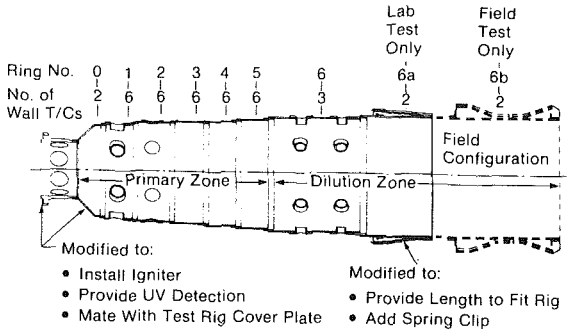

Fig. 2 W251AA test combustor with wall T/C locations

Table 1 Fuel physical/chemical properties

Fuel:	No. 2 distillate typical	ITSL heavy distillate	H-COAL light distillate	EDS full-range distillate
Sample date:		12/10/85	12/13/82	3/17/83
Viscosity:				
SSU/°F	42.0/ 65	163.7/ 60	38.0/ 70	52.5/ 72
	36.5/100	64.9/100	34.5/100	44.0/100
	32.5/150	42.5/150	32.5/125	39.0/120
Specific gravity				
SPG/°F	0.8510/ 65	0.9552/ 60	0.9295/ 60	0.963/ 63
	0.8400/100	0.9405/100	0.9170/100	0.948/100
	0.8270/150	0.9218/150	0.8940/150	0.941/120
	°F	°F	°F	°F
Flash point	195	268	205	230
Fire point	200	291	215	238
HHV, Btu/lb	19113	18682	17647	18273
	%V	%V	%V	%V
Sediment and water	<0.05	0.08	<0.05	0.25
Water	N.D.	0.05	N.D.	N.D.
Composition	wt %	wt %	wt %	wt %
Carbon	86.74	88.17	86.24	87.02
Hydrogen	13.25	10.91	10.48	9.97
Nitrogen	0.02	0.13	0.41	0.17
Oxygen	0.69	<0.5	2.75	1.12
Sulfur	0.027	0.03	0.057	0.035
	ppmw	ppmw	ppmw	ppmw
Ash	<0.5	<100	51	6
Trace Metal				
Sodium	0.020	<0.1	0.044	<0.02
Potassium	N.D.	<0.1	0.024	0.03
Vanadium	0.20	<0.2	1.00	<0.19
Calcium	N.D.	<0.02	0.100	0.06
Lead	0.060	<0.1	0.060	N.D.
Zinc	0.012	0.3	0.060	0.01
Cadmium	N.D.	<0.02	N.D.	N.D.
Nickel	N.D.	0.4	N.D.	N.D.
Iron	0.50	1.64	28.00	3.4
Manganese	0.07	0.04	0.20	N.D.
Magnesium	0.01	<0.02	0.014	0.025
Copper	N.D.	<0.02	0.28	N.D.
Chromium	<0.050	<0.02	<0.050	N.D.

Notes: N.D. = Not Detected.
°C = (°F − 32)/1.8.

Table 2 Fuel distillation characteristics

Method of analysis	Air distillation ASTM D-86	Vacuum distillation ASTM 0-1160		
Fuel:	No. 2 Distillate Typical	ITSL Heavy Distillate 12/10/85	H-COAL Light Distillate Typical	EDS Full Range Distillate Typical
%V	°F	°F	°F	°F
IBP	360	375	320	422
5	–	460	380	–
10	420	480	400	422
20	450	510	410	433
30	480	540	420	449
40	500	565	425	475
50	520	585	435	542
60	540	615	445	549
70	560	640	450	610
80	580	695	470	668
90	610	775	480	745
95	–	865	–	806
FBP	660	890	520	806
Percent recovery		97		
Percent residue	<0.5	2	<0.1	<0.1
Percent loss		1		

Note: °C = (°F − 32)/1.8.

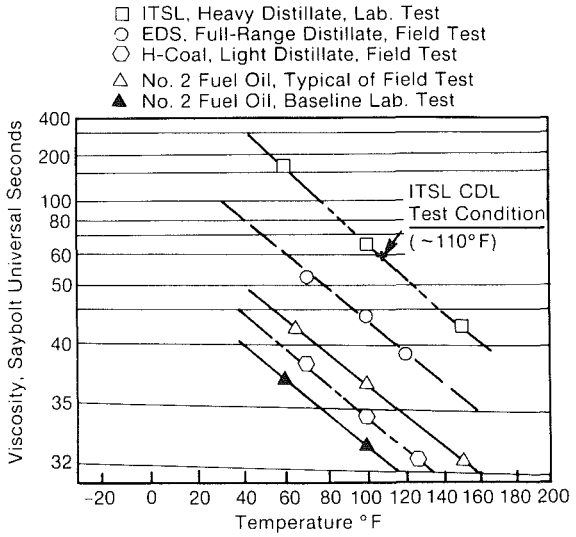

Fig. 3 Viscosity versus temperature characteristics of test fuels

Table 2 shows that the ITSL CDL has a high boiling temperature range when compared with typical No. 2 distillate and H-Coal and EDS CDL fuels. The initial boiling point (IBP) is 375°F (191°C), and is comparable to the IBP of 360°F (182°C), 320°F (160°C), and 422°F (217°C) for No. 2 distillate, H-Coal, and EDS CDLs, respectively. The final boiling point (FBP) of 890°F (477°C) for the ITSL CDL is much higher [84 (47°C) to 370°F (206°C)] than the other fuels. This characteristic is considered to be a unique property of the ITSL (heavy distillate) test fuel when compared with the H-Coal (light distillate) and the EDS (full-range distillate) CDL fuels. The high FBP appeared to cause no difficulty in fuel handling or burning of the test fuel.

The laboratory fuel forwarding systems, the fuel heating system, and the fuel flow control and metering systems operated well on the ITSL CDL fuel. All data indicated that the test fuel could be handled by the combustion turbine fuel forwarding and control systems, with appropriate sealing and gasket material changes, if required. Long term stability and storage problems, if any, with the ITSL CDL fuels were not investigated during this experimental program.

Combustion Test Results and Comparisons With Previous Data

The combustion tests run to evaluate the ITSL CDL fuel are outlined below. The steady-state test conditions were selected to simulate the W251AA engine steady-state conditions where data were taken during field operation at PECO [1, 2].

- Two test series
  - Baseline No. 2 fuel oil
  - ITSL CDL fuel
- Equivalent engine load conditions of test series
  - 100, 75, 50, 30 percent
  - Without and with water injection
  - Water-to-fuel injection ratios from 0 to approximately 1.
- Test conditions simulating engine operating environment
  - Air flow of 36.2 lb/s (16.5 kg/s)
  - Air inlet temperature of 623°F (328°C)
  - Combustor pressure level of 148.4 psia (10.4 kg/cm^2)
- Approximate combustor temperature rise versus percent load

Load percent	Temperature rise	
	°F	°C
100	1180	656
75	990	550
50	800	444
30	715	397

Tests on No. 2 fuel oil were made to establish the baseline combustion characteristics, as was done during the W251AA field testing. These baseline tests were followed by a test series burning the ITSL CDL fuel. In each series, the combustor load condition and the water injection into the combustor (to study reduction in thermal NO_x) were the principal variants. The tests on No. 2 fuel oil and the ITSL CDL were made at the same laboratory operating conditions. The test conditions were chosen to provide data equivalent to those obtained during the field tests on H-Coal and EDS CDL fuels. In this manner the laboratory test data, in conjunction with the field data, would provide the data base to determine the acceptability of the ITSL as a combustion turbine fuel.

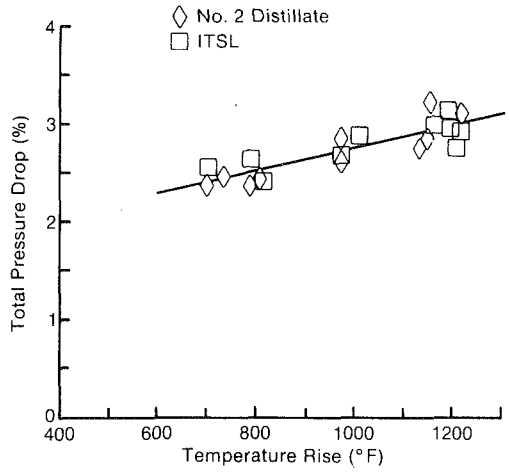

Fig. 4 Total pressrue drop versus combustor temperature rise

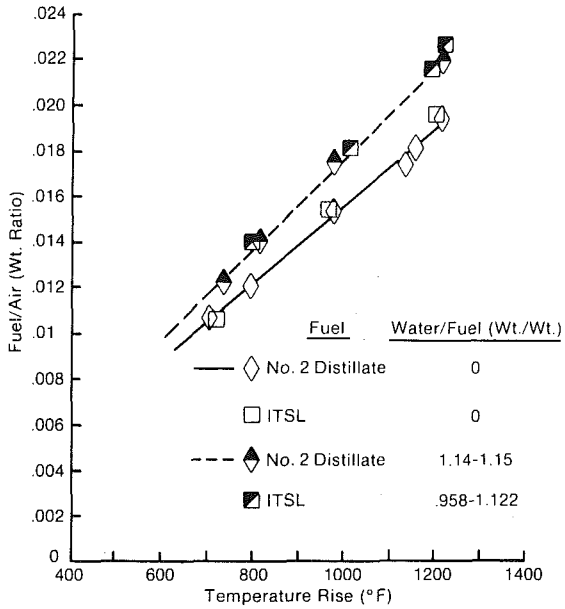

Fig. 5 Fuel/air ratio versus combustor temperature rise

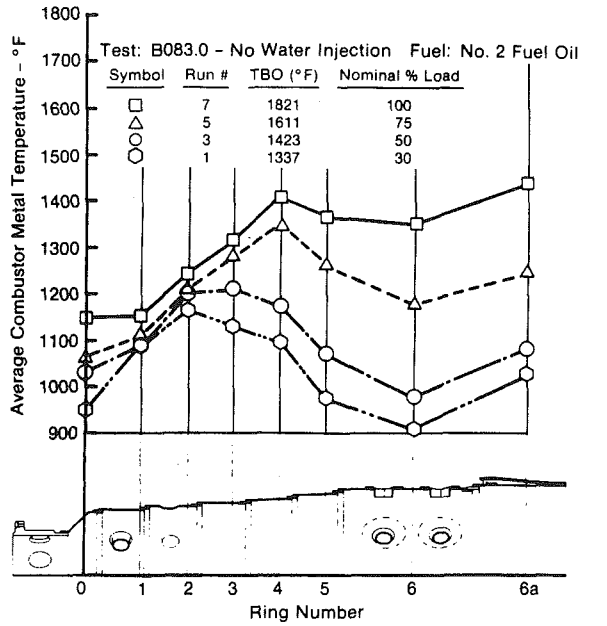

Fig. 6 Average combustor metal temperature versus ring number (ITSL CDL fuel)

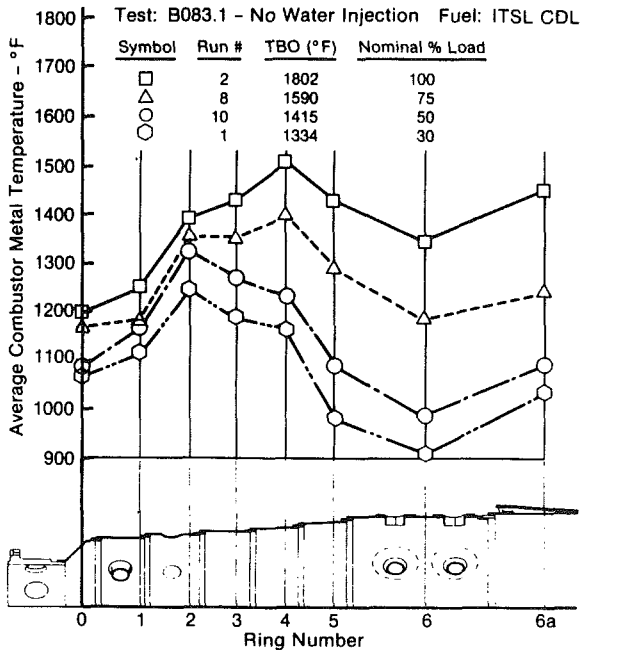

Fig. 7 Average combustor metal temperature versus ring number (baseline No. 2 fuel oil)

Combustion Performance. The combustor performance data, relative to the baseline No. 2 fuel operation, shows the ITSL fuel to be fully acceptable as a utility gas turbine fuel from a combustion performance viewpoint. The burner performance factors on the CDL test fuel did not differ significantly from those of the baseline No. 2 fuel. The efficiencies when burning either fuel were high (99+ percent) from the equivalent of 30 to 100 percent of engine baseload operation without water injection, and from 75 to 100 percent with water injection. The turbine temperature pattern factor parameter values, $(T_{max}-T_{avg})/(T_{avg}-T_{inlet})$, were low, and ranged between 0.067 and 0.131 for both fuels. T_{max} and T_{avg} are the maximum and the average combustor exit gas temperatures, respectively; T_{inlet} is the combustor air inlet temperature. The combustor gas temperature profiles and the combustor percent total pressure loss (less than 3 percent) are also similar for the test and the baseline fuels for comparable operating conditions. The total pressure loss characteristics of the combustor for both fuels are shown in Fig. 4. Figure 5 shows the relationship between the combustor fuel/air ratio and the gas temperature rise (i.e., combustor load) including the effects of water injection.

The combustor operation on the ITSL fuel with water injection was stable and comparable to that on the baseline No. 2 fuel oil at greater than 50 percent load. At 30 percent load and a water-to-fuel ratio of 1, the burner became unstable from the quenching action of the injected water. This observed characteristic would not preclude the ITSL fuel as an acceptable fuel. The combustion turbine in utility operation would seldom, if ever, be dispatched to operate at 30 percent load. If it were to operate at 30 percent, a high water injection rate would not be required to limit the NO_x to acceptable EPA limits.

Combustor Wall Metal Temperature Evaluation. The combustor wall temperatures were recorded at all laboratory test conditions for the baseline No. 2 and the ITSL test fuels. The wall thermocouples used to measure local metal temperatures were located at the same positions as those on

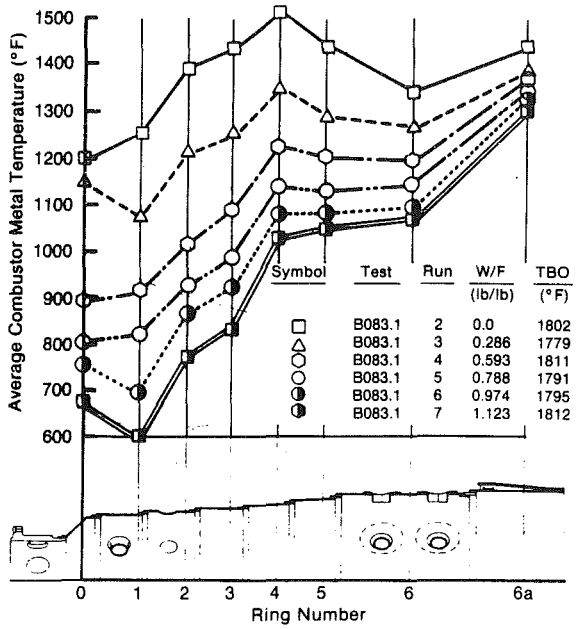

Fig. 8 Effect of water injection on metal temperatures (at 100 percent load and burning ITSL fuel)

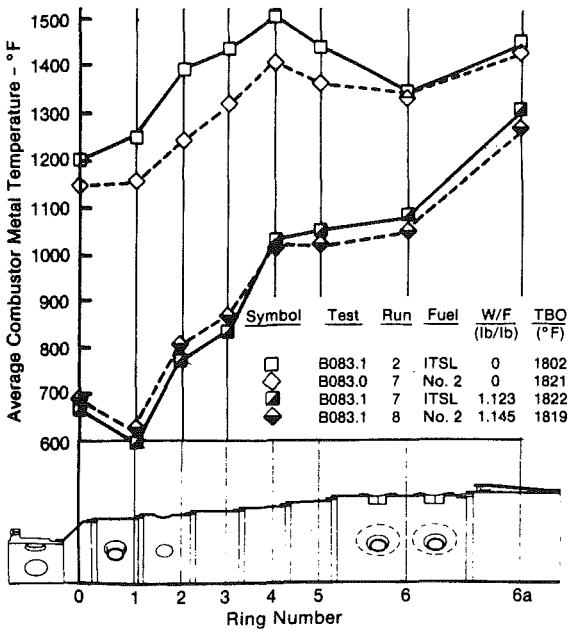

Fig. 9 Comparison of metal temperatures with and without water injection (at 100 percent load)

the W251AA test combustor used during the RP2112-5 engine testing of CDL fuels [1, 2]. The majority of the T/Cs were positioned on the wall of the combustor primary combustion zone (see Fig. 2), as this is the region most affected by the flame characteristics of the fuels. The primary combustion zone contains the highest flame temperatures and the greatest flame luminosity; both factors contribute to higher thermal radiation heat loads on the combustor wall. This increased heat load results in higher wall temperatures.

Evaluation and comparison of the ITSL and baseline No. 2 test data, both with and without water injection, show the increase in wall temperatures to be consistent with expectations. Figures 6 and 7 present the wall temperature test data without water injection. The maximum metal temperature of 1506°F (819°C) on combustor ring 4 when burning ITSL CDL test fuel (Fig. 6) compared with 1402°F (761°C) on No. 2 fuel (Fig. 7) when operating at the equivalent of 100 percent W251AA engine base load. When the measured temperature difference was referred to the No. 2 fuel baseline load operation, a referred temperature increase of 121°F (67°C) was calculated at ring 4 where the maximum wall temperatures occur. The peak of the metal temperature increase from the additional flame radiant heat load, however, occurred upstream of ring 4. The referred temperature increase (above baseline No. 2 fuel oil data) of 163°F (91°C) and 215°F (119°C) occurred at combustor ring 2 at the 100 and 75 percent load conditions, respectively. In the primary combustion zone the wall temperature increase ranged from about 75°F (42°C) to 215°F (119°C) over the test load range. The downstream air dilution zone showed increases in temperature of about 25°F (14°C) or less.

Figures 8 and 9 show the effect of water injection on wall temperatures. The water injection effect overshadows the increased flame radiation effect in the primary zone of the combustor. The net effect of water injection on the combustor wall temperatures was a major reduction in temperature level in the primary combustion zone region. The effect in the downstream air dilution region was much less pronounced as is shown in the figures.

Comparison of the ITSL test data with the prior data base developed during the engine testing of H-Coal and EDS CDL fuels [1, 2], and earlier data from the EPRI RP989-1 test program [3] is presented in Figs. 10–13. The figures present data comparisons in various ways. Figure 10 depicts the temperature increase (above baseline No. 2 fuel oil data) for the CDL fuel operation.

Figure 11 presents the effect of water injection on the rings with highest metal temperatures. Similarity of the ITSL fuel laboratory and the EDS field test data is apparent. Figure 12 presents the maximum wall temperature increase (at maximum burner outlet temperature) for the ITSL fuel plotted on field test data curve reported in [1, 2]. Reasonable agreement is seen.

A correlation of the wall temperature data base was made using a dimensionless temperature parameter $TP(R)$ that referred the CDL wall temperature data to the baseline No. 2 fuel load conditions so that the evaluation of data could be made using a common base for comparison. With the exception of the PECO H-Coal data, the referred temperature parameter $TP(R)$ correlated well as a linear function of the hydrogen content (percent H_2 by weight) (see Fig. 13). TM is metal temperature, TC is combustor air inlet temperature, and the subscripts (X) and (2) refer to CDL and baseline No. 2 test fuels, respectively. The load factor LP is the ratio of the combustor temperature rise on No. 2 fuel oil to temperature rise on CDL test fuel, and is a factor referring the CDL test load environment to the comparable No. 2 fuel test. The H-Coal wall temperatures did not correlate with other data during the analysis of the PECO test data. This deviation from expected was attributed, at that time, to the high iron content (28 ppmw) of the H-Coal [1, 2]. Iron compounds are sometimes used as smoke reduction additives. This would affect the flame radiation characteristics.

The data correlations provide information that can be used by the hardware designer to determine whether low-hydrogen fuels, such as is typical of coal-derived fuels, are acceptable for use with conventionally film-cooled combustors similar to the test combustor used for the fuels evaluation, or whether hardware design changes to improve wall cooling would be necessary.

The ITSL test data complement and extend the CDL data base for evaluation of coal-derived liquid fuels. From the standpoint of comparing and correlating the laboratory wall temperature data with previous test results, the objectives of the experimental program were achieved. The evaluation of

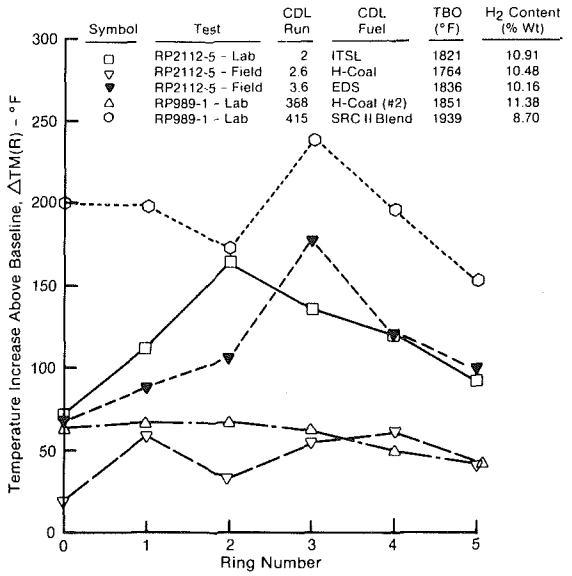

Fig. 10 Combustor metal temperature increase for CDL fuels (field and lab tests at 100 percent load)

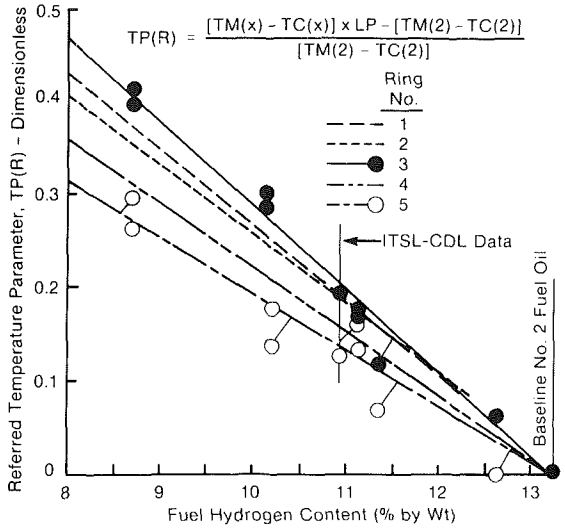

Fig. 13 Referred temperature parameter versus hydrogen content (for 100 percent load test conditions)

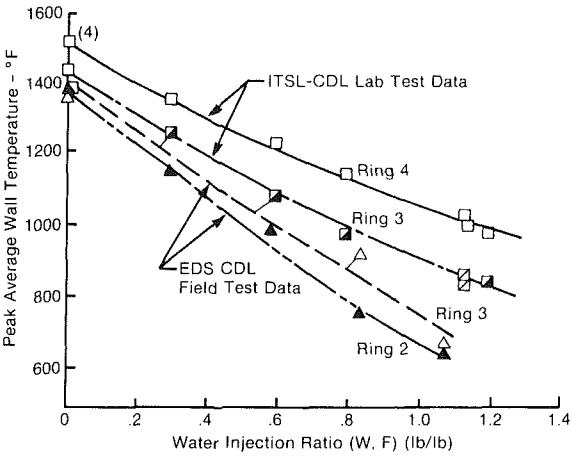

Fig. 11 Water injection effect on average metal temperatures (field and laboratory tests at 100 percent load)

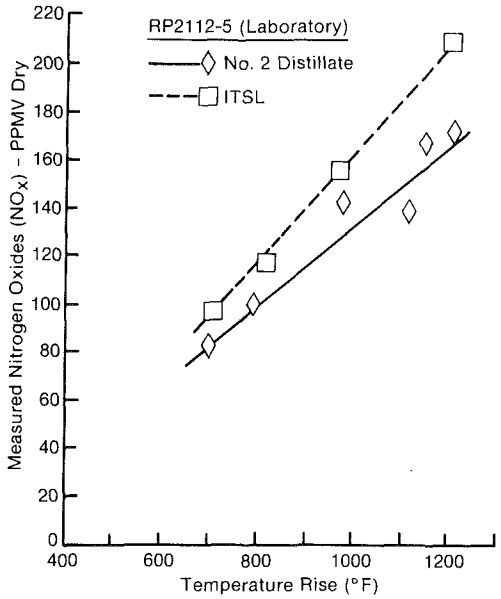

Fig. 14 Measured nitrogen oxides versus temperature rise

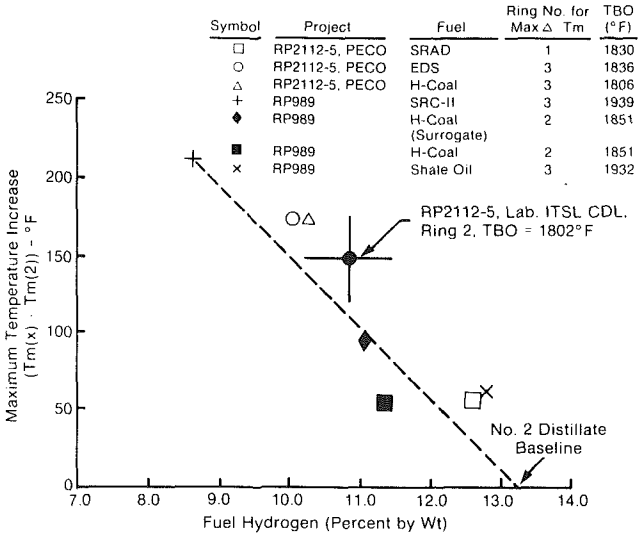

Fig. 12 Comparison of maximum temperature increase versus hydrogen content (field and laboratory tests at maximum burner outlet temperature)

the combustor wall temperature data shows the ITSL fuel acceptable.

However, combustor wall cooling flow must be utilized to maintain acceptable material temperatures needed for long life operation.

Emissions Test Results and Comparison With Prior Data. Emissions were measured for the two combustion test series (ITSL CDL and No. 2 fuels) over an equivalent load range of 30 to 100 percent engine base load. Both test series included the effects of water injection into the burner.

The measured NO_x emissions in the products of combustion at the combustor exit are reported in Fig. 14. The data normalized to EPA ISO-standard conditions of ambient temperature, pressure, and humidity, and corrected to 15 percent oxygen, standard engine heat rate, and allowance for fuel-bound nitrogen were determined, and are shown in Fig. 15.

The expected increase in the measured NO_x emissions with increasing combustor temperature rise (load), or outlet gas temperature, was observed. The ITSL CDL fuel measured

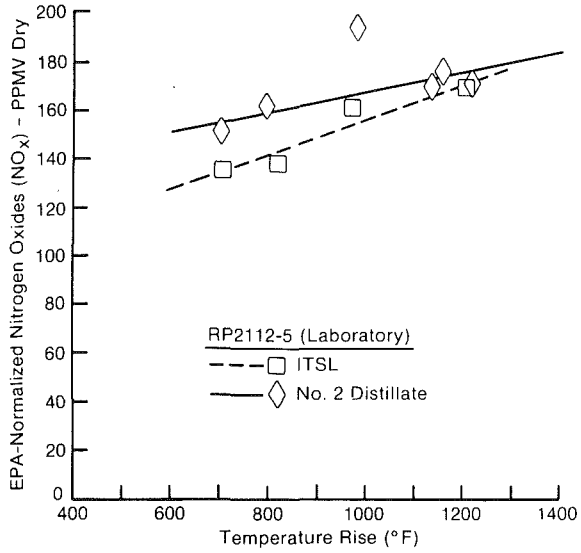

Fig. 15 EPA-normalized nitrogen oxides versus temperature rise

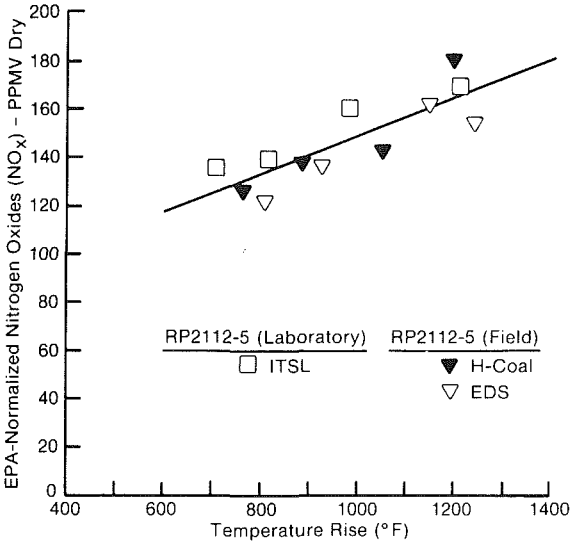

Fig. 16 Comparison of field and laboratory EPA-normalized NO_x

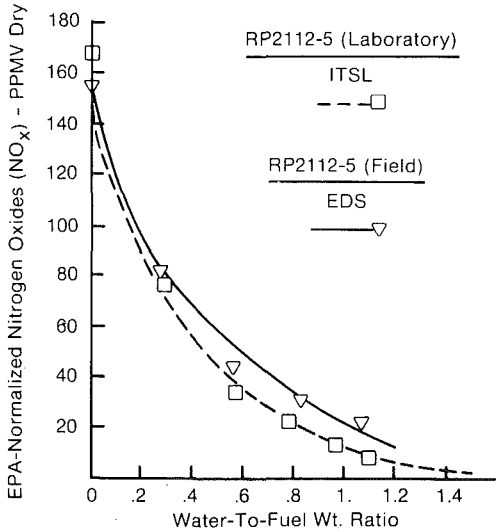

Fig. 17 Comparison of effect of water injection on NO_x (field and laboratory)

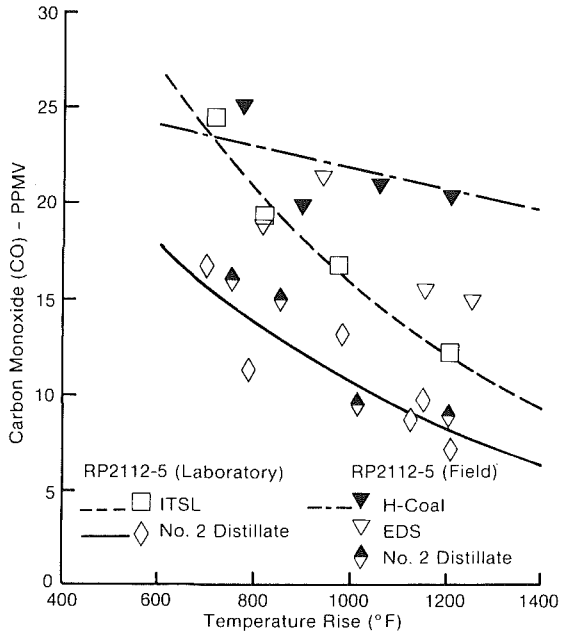

Fig. 18 Comparison of carbon monoxide emissions (field and laboratory)

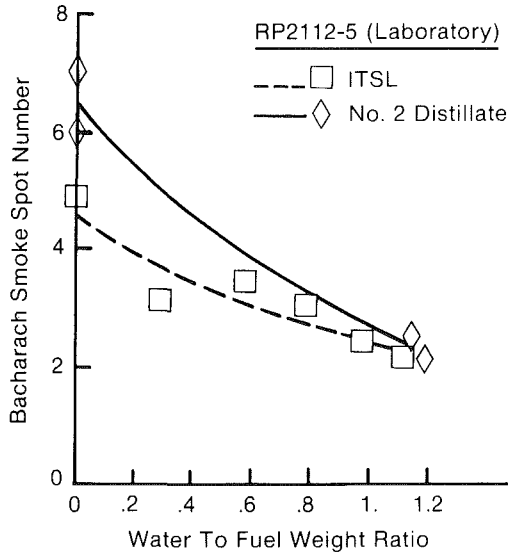

Fig. 19 Effect of water injection on smoke spot number (at 100 percent load)

NO_x values were about 30 ppmv (dry) above the baseline No. 2 fuel NO_x values near 100 percent load [~1180°F (656°C) temperature rise] (see Fig. 15). This difference is attributed primarily to the higher FBN (0.13 percent weight versus <0.01 percent) in the CDL fuel. Both sets of NO_x data show linear variation with increasing load within the range of data.

The EPA normalized ITSL CDL data are compared with the field data in Fig. 16. The EPA data for the CDL fuels can be reasonably fitted with a straight line. All CDL fuels show similar characteristics.

The usual effect of water injection into the combustion chamber reducing the thermal NO_x generation was observed when burning the ITSL CDL and No. 2 fuels. The reduction of NO_x as a function of water-to-fuel ratio (W/F) for the ITSL laboratory test was very similar to that observed for EDS fuel during the field tests as shown in Fig. 17. A water-to-fuel (W/F) ratio of about 0.4 reduces the EPA normalized NO_x to about 75 ppmv (dry). The field and laboratory data show that the W/F ratio required for compliance with the

EPA requirement of 75 ppmv NO_x increases linearly with the fuel-bound nitrogen content at the rate of 1.5 *W/F* ratio per FBN (percent). The EPA NO_x limits can be realized with water injection.

Other emissions, such as CO, UHC, O_2, and CO_2 for the ITSL CDL fuel generally followed the usual characteristics with load and with water injection. Figure 18 presents the ITSL, laboratory, and EDS and H-Coal field test carbon monoxide emissions without water injection as a function of combustor temperature rise. The low CO concentration (30 ppmw or less over the combustor load range of 30 to 100 percent) implies high combustion efficiency.

The No. 2 distillate, and the ITSL and EDS CDL fuels data show good comparison. The field H-Coal data appear somewhat higher than other CDL comparable data. However, the low CO concentrations reflect high combustion efficiencies in all instances.

Figure 19 presents the Bacharach smoke spot number of the combustor exhaust as a function of the injected water/fuel weight ratio respectively when operating at the 100 percent load condition. The reduction in smoke with water injection is typical of the W251AA combustion turbine burner operation. The values are shown for the laboratory test data are of the same order as observed during the field testing [1, 2].

Conclusions

The conclusions reached from the ITSL CDL test program to determine the acceptability as a utility combustion turbine fuel are summarized as follows:

- The ITSL fuel is an acceptable coal-derived liquid fuel for electric utility combustion turbines.
- ITSL fuel was heated to about 110°F to assure good atomization in the combustor. This caused no problem during laboratory testing.
- The concentrations of trace metals (sodium, potassium, vanadium, etc.) that cause high-temperature corrosion of vane and blade materials are low and well within the allowable limits permitted in present combustion turbine liquid petroleum fuel specifications.
- The ITSL fuel system operation using the laboratory fuel storage, forwarding, heating, control, and metering systems was uneventful; no fuel handling difficulty was experienced.
- The combustor performance when operating on ITSL CDL fuel did not differ significantly from the baseline No. 2 fuel oil operation. The effects of water injection were also similar for the two fuels.
- The increased flame luminosity in the primary combustion zone (without water injection) increased the combustor wall temperatures as expected. The ITSL CDL wall temperature test data correlated well with the prior data.
- The emissions (NO_x, CO, UHC, CO_2, and O_2) characteristics of the products of combustion when burning ITSL CDL fuel (with 0.13 wt percent FBN) were consistent with those found during the engine testing of H-Coal and EDS CDL fuels. The laboratory data correlated well with the prior data.

The above conclusions were based on very short periods of operation of the storage, fuels forwarding and flow control systems during both the laboratory and the engine tests. The long-term CDL compatibility and stability problems, if any, with materials currently used in the combustion turbine fuel distribution systems, and in supporting fuel storage and forwarding systems, were not addressed. When the CDL fuels became commercially available and cost competitive for electric utility usage, long-term effects of the CDL on fuel storage and supply systems must be evaluated. Such evaluations could first be done by testing on a laboratory scale, followed by field evaluations.

References

1 Ambrose, M. J., Costello, R. F., and Schrieber, H., "Utility Combustion Turbine Evaluation of Coal Liquid Fuels," ASME Paper No. 84-JPGC-GT-13.

2 *Evaluation of Coal Liquids as Utility Combustion Fuels*, Electric Research Institute, Palo Alto, CA, Dec. 1984, Paper No. AP-3670.

3 *Gas Turbine Combustor Performance on Synthetic Fuels*, Vols. 1 and 2, Electric Power Research Institute, Palo Alto, CA, June 1981, Paper No. AP-1623.

Combustion of Coal/Water Mixtures With Thermal Preconditioning

M. Novack

G. Roffe

G. Miller

General Applied Science Laboratories, Inc.,
Ronkonkoma, NY 11779

Thermal preconditioning is a process in which coal/water mixtures are vaporized to produce coal/steam suspensions, and then superheated to allow the coal to devolatilize producing suspensions of char particles in hydrocarbon gases and steam. This final product of the process can be injected without atomization, and burned directly in a gas turbine combustor. This paper reports on the results of an experimental program in which thermally preconditioned coal/water mixture was successfully burned with a stable flame in a gas turbine combustor test rig. Tests were performed at a mixture flowrate of 300 lb/hr and combustor pressure of 8 atm. The coal/water mixture was thermally preconditioned and injected into the combustor over a temperature range from 350°F to 600°F, and combustion air was supplied at between 600°F to 725°F. Test durations varied between 10 and 20 min. Major results of the combustion testing were that: A stable flame was maintained over a wide equivalence ratio range, between $\phi = 2.2$ (rich) and 0.2 (lean); and combustion efficiency of over 99 percent was achieved when the mixture was preconditioned to 600°F and the combustion air preheated to 725°F. Measurements of ash particulates, captured in the exhaust sampling probe located 20 in. from the injector face, show typical sizes collected to be about 1 μm, with agglomerates of these particulates to be not more than 8 μm. The original mean coal particle size for these tests, prior to preconditioning, was 25 μm. Results of additional tests showed that one third of the sulfur contained in the solids of a coal/water mixture with 3 percent sulfur was evolved in gaseous form (under mild thermolized conditions) mainly as H_2S with the remainder as light mercaptans.

Introduction

The Department of Energy's Coal-Fueled Gas Turbine Technology Development Program seeks innovative alternative injection methods to enhance the application of coal fuels for gas turbine use as well as methods for enhancing the combustion performance of coal-fueled gas turbines. The thermal preconditioning process (TP) is an alternative to conventional atomized injection of coal/water mixtures (CWM). It is also a combustion enhancement technique which can broaden the range of stable operation and reduce the combustor volume required for a given level of carbon conversion.

The use of atomization for the injection of CWM into directly fired gas turbine engines involves a number of important combustion-related problems, among these being possible difficulties with flame stability and efficiency at off-load operating conditions, the need for substantial quantities of high-pressure steam or air to accomplish atomization, and possible difficulties with flame length and carbon burnout in combustion chambers of limited volume. Thermal preconditioning of CWM is a process which offers the potential of reducing or eliminating these problems. The process is one in which the CWM is heated before delivery to the combustor in order to accomplish the water vaporization and if desired, the coal pyrolysis/devolatilization steps prior to injection. Under ideal operating conditions, a thermally preconditioned mixture delivered to the gas turbine combustion chamber would consist of gaseous coal volatiles and steam carrying a suspension of fine pulverized char.

The TP process offers a number of potential advantages relative to direct slurry injection. Among these are the elimination of the atomization process, the removal of the heat-absorbing water vaporization process from the flame stabilization region, the immediate availability of coal volatiles, and decoupling of the slurry vaporization and pyrolysis processes from conditions in the combustion chamber. These properties of the process offer the potential of employing a high solids loading in the slurry without the need to provide an auxiliary gas to assist in the atomization process, the ability to stabilize flames over a wide range of fuel/air ratios, the ability to start the engine using the same slurry fuel which is employed during all other operating conditions, and the ability to provide a compact and intense gas phase combustion region for the earliest possible char burnout and maximum stable turndown capability. In addition, it is possible that a significant portion

Contributed by the Gas Turbine Division of THE AMERICAN SOCIETY OF MECHANICAL ENGINEERS and presented at the 32nd International Gas Turbine Conference and Exhibit, Anaheim, California, May 31-June 4, 1987. Manuscript received at ASME Headquarters February 27, 1987. Paper No. 87-GT-268.

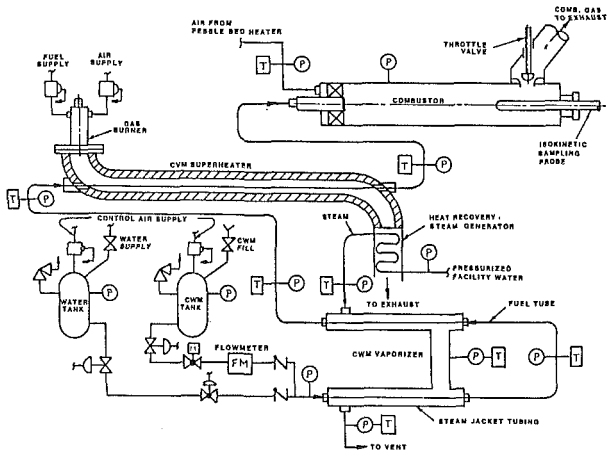

Fig. 1 Layout of test apparatus

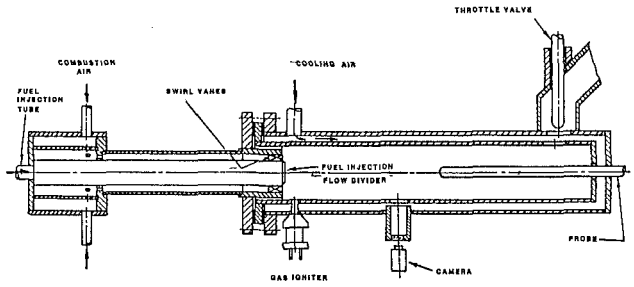

Fig. 2 Pressurized test combustor

of the organic sulfur compounds in the coal can be gasified during the TP process. This offers the additional possibility of using a more economical minimally processed CWM and incorporating a sulfur capture step into the TP process.

This paper reports on the results of an experimental program in which coal/water mixtures were preconditioned and burned in a laboratory gas turbine combustor simulator to assess their combustion characteristics and determine the effects of preconditioning temperatures and residence time on pyrolysis and sulfur evolution.

Description of Test Apparatus

General. The test apparatus was designed to thermally precondition and burn 300 lb/hr of coal/water mixture in a laboratory combustor which duplicates conditions in the primary zone of a gas turbine combustor. Thermal preconditioning consisted of preheating, vaporizing, and superheating the CWM to produce a suspension of coal particles in steam referred to hereafter as a coal/vapor mixture (CVM).

Overall Configuration of the Test Apparatus. The overall configuration of the test apparatus is illustrated in Fig. 1. CWM is stored in a tank which is pressurized using air from GASL's main air supply. The CWM flows through a metering valve and flowmeter into the vaporization section of the preconditioning apparatus where it is heated by a flow of saturated steam which jackets the vaporization tube. The coal/steam suspension then enters a superheater section where it is heated to temperatures up to 1000°F by an external flow of hot gas. The superheated CWM is then injected into the laboratory combustor. Samples of combustion products are withdrawn from the combustor using an isokinetic sampling probe while the mainstream exits through a water-cooled back pressure valve.

Heat for the apparatus is provided by a gas burner which produces 3000°F exhaust products which are ducted through

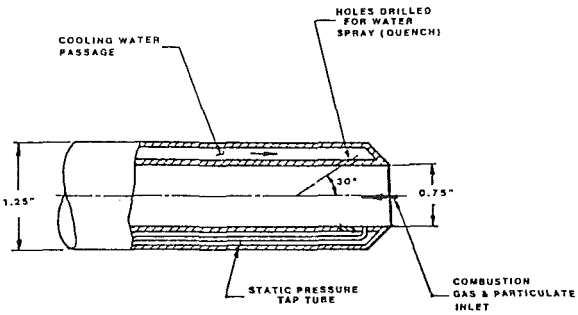

Fig. 3 Water-quench sampling probe

the CWM superheater section and then, slightly cooled, are used in a heat recovery steam generator to provide the steam used by the CWM vaporizer unit.

Pressurized Test Combustor. The pressurized test combustor is illustrated schematically in Fig. 2. The unit employs an outer pressure shell and an inner liner separated by an annular passage through which a flow of cooling air is maintained for realistic liner heat losses during operation. The liner and cooling system are designed for stoichiometric conditions in the flame while the pressure shell is designed for operation at pressures to 300 psia. Combustor pressure is controlled by a water-cooled plug valve. The inside diameter is 5 in. and the length is 44 in.

The combustor is designed with off-axis air entry and exhaust, allowing a fuel injector assembly and a sampling probe to be inserted from opposite directions along the axis of the combustor, facilitating movement of the probe and removal of the injector for inspection and service. The sampling probe can be positioned anywhere from 12 in. to 36 in. from the air inlet plane. The combustor employs a 35 deg swirler to produce a swirl number of 0.6. The entrance expansion ratio is 4.

The combustor is provided with a view port for flame observation which is located 21 in. downstream of the air entry plane. The view port is air cooled and employs a labyrinth seal to prevent the leakage of liner cooling air into the combustor.

The fuel injector receives thermally preconditioned coal/steam suspension through a 1/2 in. inlet duct which divides smoothly into eighteen 0.125 in. diameter holes inclined at an angle of 30 deg to the injector axis. The holes produce a constant velocity dispersion of the suspension of coal in steam.

The fuel injector is centered by three small lugs in a support tube which passes through the center of the air inlet plenum and swirler assembly. A small tube brings pilot gas into the annular space between the injector and the support tube. The pilot gas is supplied by a metering valve and a solenoid connected to a momentary on/off switch.

A small gas igniter penetrates the sidewall of the combustor 1.4 in. from the air inlet plane. The igniter fires radially into the combustor to light either the CVM or the pilot gas.

The sampling probe shown in Fig. 3 employs the direct water quench technique described by Burkinshaw et al. [5]. The probe captures a 0.75-in.-dia streamtube of combustion gas and particulates and quenches it with a spray of water in an amount adequate not only to cool the sample but also to wash the probe with liquid. A gas and particulate sampling train is depicted in Fig. 4, where the mixture of combustion gas, particulate and cooling water leaving the combustor sampling probe passes through a control valve where the flowrate is adjusted to produce isokinetic conditions at the probe entrance and enters a set of separator tanks where the liquid/solids sample settles to the bottom while gaseous species are withdrawn from the top. The gas is filtered and then pumped to the gas analysis instruments. An all-Beckman Instrument train was used here with parallel lines leading to a

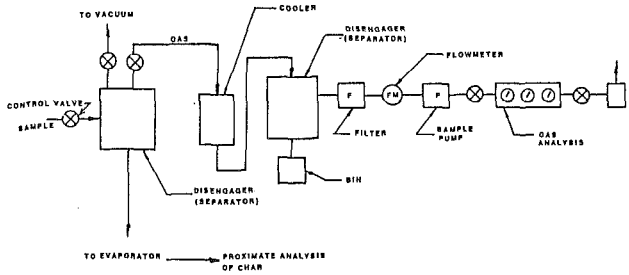

Fig. 4 Gas and particulate sampling train

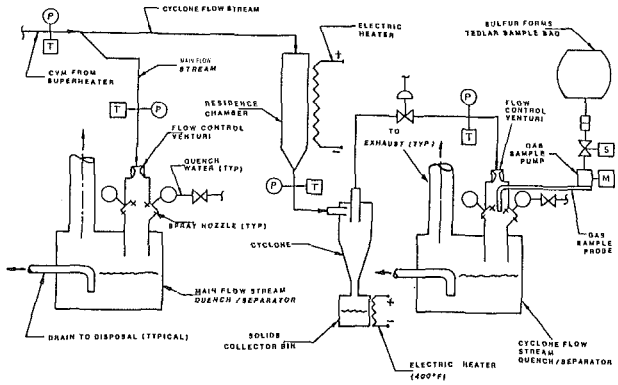

Fig. 5 Sulfur reduction test apparatus

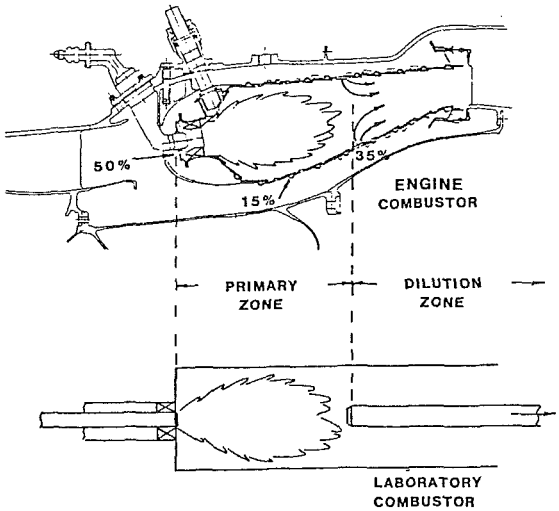

Fig. 6 Burner experiment concept

flame ionization detector for unburned hydrocarbons, a chemiluminescence analyzer for NO_x, and a series arrangement of a dryer and infrared analyzers for CO and CO_2.

Test Apparatus for Sulfur Testing. The apparatus for sulfur reduction and gaseous compound forms testing is shown in Fig. 5. The system consists of mainstream and cyclone stream flow trains. Initially, superheated steam is produced in the superheater and is routed through both streams to preheat the thermally insulated systems up to the required test temperature. The CWM is then routed through the TP system and the main flow stream. When the CVM produced is at its required temperature, approximately 20 percent of the mainstream flow is diverted to the cyclone stream which passes through a residence chamber at elevated temperature where pyrolysis and devolatilization occur. The mixture of steam, char, and volatiles then passes through the cyclone where the thermally processed solids are collected for subsequent proximate and ultimate analysis.

The remaining volatiles and steam are routed to a quench/separator tank where a gas sample is collected in a Tedlar bag for subsequent gaseous sulfur forms analysis, and where the gas pressure and temperature are reduced.

Fuel Specifications. Three coal/water mixture formulations were used in this program: a low-sulfur (1.0 percent) fine grind (10 μm mean), a low-sulfur (1.0 percent) coarse grind (20 μm mean) and a high-sulfur (2.8 percent) fine grind (10 μm mean). These CWM's were supplied by the AMAX Extractive Research and Development Corporation. The slurries were delivered with solids loadings of 54 percent (for high-sulfur formulation) and 60 percent (for the low-sulfur formulations) and contained 0.02 percent Pfizer Flocon as a stabilizer and 1.8 percent dispersant in the form of Diamond Shamrock No. 823. Approximately 80 percent of the sulfur contained in the coal was in organic form, most of the inorganic sulfur having been removed during air washing. The ash content of the parent coals varied between 3 and 4 percent, after washing.

Experimental Program

Test Program Objectives. The test program had as its primary objective the measurement of combustion efficiency and particulate emissions from a gas turbine combustor simulator firing thermally preconditioned CWM. A secondary objective of the program was the determination of the amount of sulfur which is volatilized during preconditioning and the identification of the principal forms in which it is evolved.

Concept of the Combustion Experiment. The concept of the laboratory burner portion of the experimental program can be illustrated with the aid of the burner schematics presented in Fig. 6. Here, a representative gas turbine combustor is illustrated in comparison with the laboratory combustor. The engine combustor consists of a primary burning zone which receives about one third of the engine airflow followed by a secondary or dilution zone which receives about one third of the engine airflow, the remaining air being injected as a film to cool the walls of the combustor can.

For recent engine designs, the need to limit smoke production has resulted in limiting operation of the burner primary zone to stoichiometric and fuel-lean conditions. As a result, perfectly efficient combustion in the primary zone will eliminate the presence of unburned fuels and products of incomplete combustion such as CO before the dilution air enters the combustor. When combustion is less than complete by the end of the primary zone, the addition of dilution air can produce some increase in efficiency by providing additional mixing and reaction time. However, the rapid decrease in temperature which accompanies the introduction of the dilution air minimizes the ability of the secondary zone to significantly improve combustion efficiency beyond the level which is achieved in the primary zone.

Since the primary zone can be (conservatively) assumed to be entirely responsible for the combustion efficiency of the engine, the laboratory simulator need only reproduce conditions in the primary zone of the engine combustor. Combustion efficiencies measured in such a device represent a lower limit. Some small improvement in efficiency may occur when the secondary zone is added, but any improvement would be expected to be of second order importance. Meanwhile, the use of a single-stage laboratory burner allows a sampling probe to be inserted and moved to a variety of positions along the combustor axis, effectively yielding a variable combustor length. It is then possible to use the laboratory burner to determine not only the effects of primary zone stoichiometry but also the effects of primary zone length.

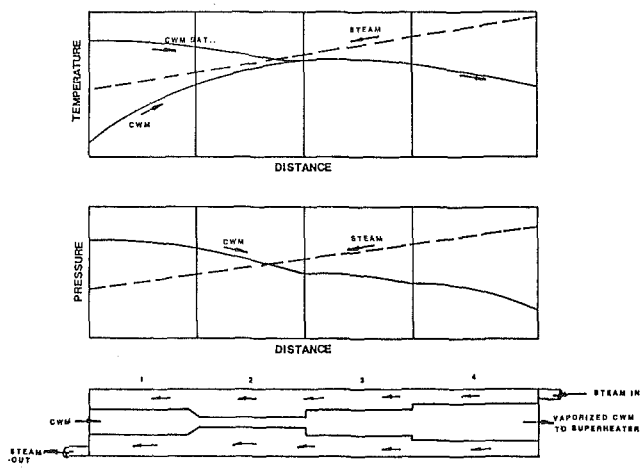

Fig. 7 CWM preheat and vaporization process

In order to present the laboratory burner results in a form consistent with that used for engine combustion, data will be shown as a function of engine turbine inlet temperature. The value of engine turbine inlet temperature is calculated from the measured values of fuel/air ratio and combustor inlet temperature for the typical case represented in Fig. 6 where 50 percent of the engine airflow enters the combustor primary zone.

CWM Vaporizer Development. The steam-jacketed CWM vaporizer described in the section under description of test apparatus was the product of an evolutionary process carried out during the early stages of this program. The final vaporization and superheat process is illustrated functionally in Fig. 7. CWM, which moves counterflow to the steam heating medium, flows through the inside tube of the double-pipe heat exchanger. The CWM enters the first section at a low (ambient) temperature and a pressure which is high enough to raise its saturation temperature to a level higher than the temperature of the heating steam to preclude the possibility of boiling. During preheat and vaporization, the CWM should not be exposed to tube wall temperatures between 500°F and 1000°F, to avoid formation of tars, and subsequent clogging. As the CWM enters the second section, its bulk temperature approaches the steam temperature, as well as its own saturation temperature. Here, the increase in CWM bulk temperature causes a substantial decrease in slurry viscosity. Therefore, the inside diameter of the second heating section is substantially reduced in order to increase velocity and therefore pressure gradient. As the pressure in the CWM tube decreases with distance, the slurry saturation temperature also decreases, eventually dropping below the steam temperature. Vaporization begins at this location. At this point the pressure in the CWM tube is lower than that in the steam jacket (see Fig. 7). The CWM tube diameter is increased in the region downstream of the initial boiling point to compensate for the increasing vapor flow and to avoid excessive pressure drop in the CWM/CVM flow. Note that while the temperature of the CWM/CVM is decreasing due to decreasing pressure, the temperature differential between it and the steam is increasing, accelerating the vaporization process. As the vapor velocity increases still further, the CWM/CVM enters the fourth section. The internal diameter is again increased to control pressure drop. The CVM emerges from this fourth section fully vaporized at its saturated pressure/temperature condition. It is then routed to the superheater where final heating takes place.

Combustion Tests. Combustion testing was carried out at air inlet temperatures of 600°F and 725°F and a fixed combustor pressure level of 115 psia. Fuel flowrate was held constant at 300 lb/hr and air flow was varied to change equivalence ratio. Gas and particulate samples were taken at two stations, 20 in. and 30 in. from the combustor entrance plane. For the range of equivalence ratio for which sampling was carried out, the calculated bulk residence time in the combustor varied from 14 msec to 37 msec. It should be noted, however, that the swirler produces an entrance velocity which is from two to three times higher than the bulk velocity (depending on flame temperature) and the distance over which this velocity diffuses to the bulk velocity is approximately 15 in., leading to an estimated actual combustor residence time of from 7 msec to 10 msec for samples taken at the 20 in. station and 10 msec to 17 msec for samples taken at the 30 in. station, the longer residence times corresponding to the lower fuel/air ratio conditions.

An engine starting simulation was also run in which the inlet temperature and pressure were held at ambient levels with an air entrance velocity of 50 ft/s.

Combustion Test Procedures. Test sequences began with the TP unit processing only water and discharging it as steam in the combustor. Once steady operation of the preconditioning system was achieved with water, the flow of CWM was begun along with airflow to the combustor. A period of 30 s was allowed for the leading edge of the CWM slug to pass through the preconditioning apparatus at which point the side-mounted igniter was turned on and a momentary flow of pilot gas was injected through the annular injection slot. The pilot duration was always less than one second. If ignition did not occur, the process was repeated 5 s later in order to provide additional time for undiluted CWM to reach the injector. The side-mounted igniter was shut off immediately following ignition of the main fuel stream.

The test was terminated by reversing the starting procedure. The flow of CWM was halted and immediately replaced by a flow of water through the preconditioning apparatus in order to flush all slurry from the system before shutting down. The combustor flame would extinguish when the flush water reached the nozzle (as steam) at which point combustor airflow was terminated followed by the shutoff of flush water.

Combustion Test Results. Thermally preconditioned CWM was ignited at a condition corresponding to the startup of a gas turbine engine and at conditions peculiar to the startup of the laboratory burner. The engine startup simulation used ambient air with a velocity of 50 ft/s at the combustor entrance. The side-mounted igniter was used alone; the central gas pilot was not in place. CWM was supplied to the injector at a temperature of 380°F and a flowrate of 100 lb/hr. Ignition of the CWM occurred at relatively low airflow rates, corresponding to an equivalence ratio on the order of 3. The igniter torch was extinguished immediately after ignition and stable combustion continued as the airflow was increased to its normal operating value.

During pressurized test sequences, ignition occurs with full airflow and a fuel flow rate corresponding to an equivalence ratio of 0.6 in the burner. The pressure control valve is positioned to yield (approximately) 115 psia once burning begins. Before ignition, however, the lower gas temperature at the choked exit orifice of the combustor results in a pressure in the burner of approximately 70 psia. Under these conditions, firing the small side-mounted gas igniter flame did not produce ignition of the preconditioned CWM. However, gas delivered to the annular pilot injector was ignited by the side-mounted igniter and the ignition of this pilot gas caused instant ignition of the preconditioned fuel.

The pilot gas for ignition is supplied by closing a momentary switch to power its control valve. The total time of pilot gas flow never exceeds 1 s. This is sufficient, however, for ignition of the main coal flame. After ignition, the pilot and the

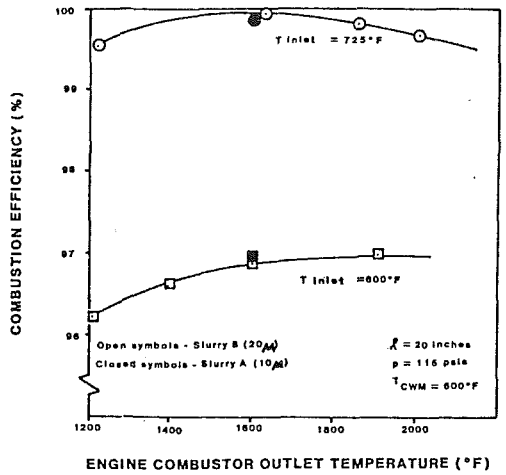

Fig. 8 Effect of combustor inlet and outlet temperature on combustion efficiency

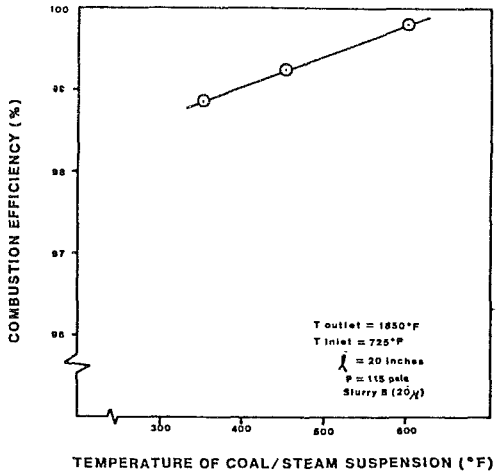

Fig. 10 Effect of preconditioning temperature on combustion efficiency

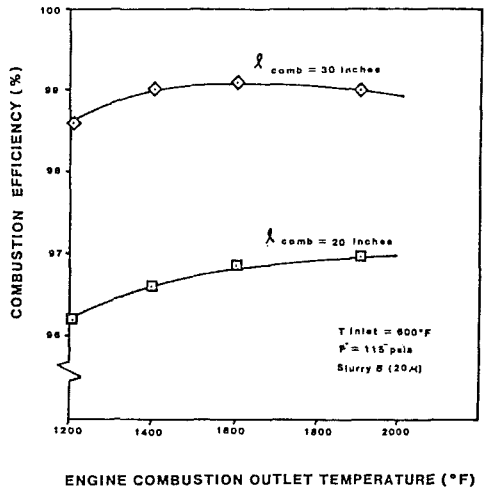

Fig. 9 Effect of combustor length on combustion efficiency

side-mounted igniter are both turned off. Once lit, the main coal flame remains stable without external assistance.

The equivalence ratio of the burner was changed by varying the airflow rate. The laboratory air supply system employs a choked venturi to produce constant airflow. The range over which this airflow could be varied was limited on the high side by air system supply pressure and the low side by the need to maintain a choked venturi flow. For the test arrangement used here, airflow could be varied over a range of 10:1, yielding combustor equivalence ratios from 0.22 to 2.2. The CWM flame remained stable over this range for both air entrance temperature conditions (i.e., 600°F and 725°F).

Figure 8 presents the measured levels of combustion efficiency for a 20-in. primary zone combustor operating at a pressure of 115 psia with preconditioned CWM fuel supplied at a temperature of 600°F. As a general comment, the efficiency of the system does not appear to be strongly influenced by combustor outlet temperature, an indication that the range of fuel/air ratios covered is such that the lean stability limit of the device was not approached and the flame length is not strongly affected by fuel flowrate.

The very high level of combustion efficiency achieved when the inlet air temperature is 725°F is quite gratifying. However, combustion efficiency shows a pronounced sensitivity to inlet air temperature with a decrease to 600°F lowering combustion efficiency by approximately 3 percentage points. The difference between the efficiency level measured using the fine (10 μm mean) CWM and the coarse (20 μm mean) CWM is not distinguishable within the accuracy of this experiment.

Figure 9 illustrates the effect of combustor length on combustion efficiency. Here, for the lower efficiency case of 600°F inlet temperature, increasing combustor length from 20 in. to 30 in. raises efficiency by approximately 2 percentage points. The increase in efficiency is not commensurate with the increase in combustor residence time, implying a mixing rather than a reaction rate limited system.

Figure 10 shows the effect of increasing the temperature of the preconditioning process. The lowest temperature condition (350°F) is one where the temperature of the coal/steam suspension is only 10°F higher than the saturation level at the superheater exit. Given some heat loss in the delivery tube, this is essentially the condition of CWM prevaporization but no superheat. Increasing preheat temperature to 600°F improves combustion efficiency by approximately one percentage point. The mechanism for the improvement is not clearly defined by the data. However, the tests reported in [3, 4] indicated very little devolatilization at 600°F so the improvement is probably not due to improving this aspect of the process. Video pictures of the flame show occasional sparklers in the flame at the 350°F CVM temperature condition which disappear as the CVM delivery temperature increases. It is possible, then, that heat losses in the delivery line result in a small fraction of recondensed CWM being delivered to the injector when the preheat temperature is low. Superheating the CVM very likely reduces and eventually eliminates the effect. The presence of a small amount of liquid in the injected mixture would produce droplet combustion, a slower process, and would reduce the overall efficiency of the system.

Measurements of the larger forms of particulate collected by the sampling probe show the largest agglomerate dimension to be approximately 8 μm, but the nonspherical shape yields a diameter of approximately 6 μm for weight equivalence. In view of the 150 μm top size for coal particles in the raw slurry, this is a sizable reduction. Most of the particles collected are either small (approximately 2 μm) spheroids or chain type agglomerates of particles 1 μm and under in diameter.

It is of interest to note that no difference was found in particulate samples obtained using the finer (10 μm mean, 44 μm top size) and the coarser (20 μm mean, 150 μm top size) coal/water mixture. This raises the interesting possibility that the particle size distribution may be changed by the preconditioning process, perhaps by collision fracturing in the high-speed turbulent coal/steam flow tubes. It also agrees with the limited combustion data taken with the fine slurry which showed no difference in combustion efficiency between coarse and fine coal grinds.

The amount of sulfur evolution data which could be obtained was limited by the performance of the superheater. The heat transfer rate from the inconel superheater tube to the coal/steam suspension was found to be about half that anticipated by the design. The reason for this difference is not evident. Nevertheless, the reduced effectiveness of the CVM as coolant limited the preconditioning temperature to a maximum of 850°F, restricting the amount of devolatization which could be accomplished.

The results of proximate and ultimate analysis of unprocessed CWM and CWM thermally preconditioned at temperatures of 700°F and 850°F indicate increasing preconditioning temperature from 700°F to 850°F increased the degree of devolatilization from 33.2 to 46.2 percent and increased the degree of sulfur evolution from 27.4 to 32.0 percent. The sulfur evolution data agree with those of [3, 4] but the inability to raise the CVM temperature above 850°F leaves the question of the maximum amount of possible sulfur evolution unanswered. It should be noted, however, that the sulfur content of the coal was 80 percent organic, a form which is quite expensive to remove by chemical cleaning of the raw coal. The ability to remove 32 percent of the sulfur from the solids is encouraging. Further testing to determine the effectiveness of preconditioning temperatures above 850°F would be of great interest.

The chemical form of the evolved gaseous sulfur species is also of great interest. Gas samples obtained downstream of the residence tube were analyzed by gas chromatography. The results of the gas analysis performed during the 850°F preconditioning temperature run indicate that approximately 78 percent of the evolved sulfur is in the form of H_2S, the remainder being in the form of light mercaptans. This is an encouraging result as hot gas sulfur cleanup processes capable of capturing H_2S are currently being developed.

Conclusions

1 Coal/water mixtures can be vaporized in a heated flow system to form a suspension of coal particles in steam. The successful operation of a CWM vaporizer requires avoiding wall temperatures between 500°F and 1000°F and maintaining sufficient local pressure gradient to assure stable boiling.

2 Thermally preconditioned CWM burns quickly and efficiently in a gas turbine combustor primary zone. Efficiencies above 99 percent are achievable in residence times on the order of 10–30 ms.

3 Preconditioned CWM can be ignited by a gas pilot. Impulse ignition is possible. It is not necessary to go through a gradual transition from the starting fuel to the CWM.

4 There is no agglomerate of preconditioned CWM either in the preconditioning apparatus or in the combustor. Product of combustion (POC) solids show top sizes on the order of 8 μm starting with coal particle top sizes as large as 150 μm in the fuel slurry. It is possible that this substantial size reduction is caused by fracturing of the coal particles as they are carried through the stream passages of the preconditioning apparatus but there are as yet no data available to test this hypothesis.

5 Increasing preconditioning temperature increases devolatilization and sulfur evolution but has little effect on combustion efficiency.

6 Approximately one third of the sulfur contained in the coal solids (80 percent of which is organic for the coal used in these experiments) is evolved in gaseous form for a preconditioning temperature of 850°F. The evolved sulfur is mainly in the form of H_2S with the remainder as light mercaptans.

Acknowledgments

The authors wish to thank Mr. Floyd Crouse and Ms. Janna Thames of the Morgantown Energy Technology Center for their guidance throughout the course of the program. This work was performed under Contract No. DE-AC21-84MC21390 for the US Department of Energy, Morgantown Energy Technology Center.

References

1 Koncheski, J. L., et al., "Laboratory Scale Gasification of Coal Water Slurries in a Metallic Tube Coil," U.S. Bureau of Mines, R.I. 5704, 1960.

2 Solomon, P. R., and Hamblen, D. G., "Finding Order in Pyrolyses Kinetics," *Prog. Energy Combustion Sci.*, Vol. 9, 1983.

3 Roffe, G., and Miller, G., "Thermal Preconditioning of Coal-Water Mixtures," Final Report under DOE/METC Contract DE-AC21-83MC20463, Oct. 1984.

4 Roffe, G., and Miller, G., "Thermal Preconditioning of Coal-Water Mixtures for Gas Turbine Applications," ASME Paper No. 85-GT-198, 1985.

5 Burkinshaw, J. R., et al., "Analysis of Sulfur and Nitrogen Pollutants in Three-Phase Coal Combustion Effluent Samples," *Ind. Eng. Chem. Fundamentals*, Vol. 22, 1983, pp. 292–298.

S. G. Kimura

C. L. Spiro

C. C. Chen

General Electric Corporate Research and Development, Schenectady, NY 12301

Combustion and Deposition in Coal-Fired Turbines

Combustion and deposition behavior of coal in the form of highly beneficiated coal-water mixtures (CWM) has been investigated. The solids content of the CWM fuels was typically 50 percent, with a mean coal particle size of 4 μm and an ash content of 0.8 percent (dry). Combustion efficiencies in excess of 99.5 percent based on the carbon content of the collected ash were achieved in gas turbine-type can combustors with residence times of less than 20 ms with up to 25 percent (Btu basis) supplemental fuel oil assist. Ash deposition rates on a first-stage turbine nozzle sector were measured and were found to be much lower than would have been predicted from residual petroleum fuel experience because of differences in ash chemistry, and thus, deposition mechanism.

Introduction

The direct firing of coal in gas turbines is by no means a new thrust. Gas turbines were operated on pulverized coal in the 1950s and 1960s [1, 2]. Severe wear and deposition were experienced, largely as a result of the high ash contents and large coal particles. Corrosion, on the other hand, was not a major issue because of the low firing temperatures, which were typically 1300 to 1500°F.

Advances in coal-cleaning technology have reduced reasonably attainable ash levels to less than a tenth of the levels of the parent coal. Ash loadings of 0.1 to 1 percent are technically and economically feasible. However, even at these levels, ash loadings are considerably higher than specified for gas turbine fuels. Thus, contaminant effects – corrosion, erosion, and deposition – continue to be key factors in the development of a coal-fired turbine. Work performed at General Electric has shown that alkali metals, which are implicated in hot corrosion and in deposition enhancement, are in the form of aluminosilicate clays [3] in coal, rather than as soluble species as in contaminated petroleum fuels. Thus, it can be theorized that corrosion and deposition behavior for coal fuels will be considerably different than for petroleum fuels.

Comminution of coal to fine particle sizes and the development of slurry technology greatly enhance the possibility of using coal as a direct replacement for petroleum fuels. The slurry can be handled using nearly conventional pumping, metering, and atomizing systems. Fine coal particles enhance combustion and reduce the erosive effects of the ash, and the high water content will reduce thermal NO_x emissions. However, the presence of water will increase the difficulty of combustion. Combustion delay resulting from the evaporation of water will increase residence time requirements. Additional energy must be added to the evaporation and devolatilization zones through enhanced recirculation of hot combustion gases to the head end of the combustor.

An important element in the development of CWM combustion systems is the fuel atomizer, which must be able to form small droplets to enable rapid combustion. Since intradroplet agglomeration of coal occurs during the combustion process [4], the size of the resultant char particle and, therefore, the time required for char burnout, is dependent on the size of the slurry droplet and not on the coal particle size itself. The size of ash agglomerates and their erosive potential is also dependent on droplet size.

Experiments have been performed at General Electric Corporate Research and Development to study the combustion and deposition behavior of CWM fuels in gas turbine environments. Combustion and deposition rate measurements were performed using turbine components, with the combustor modified for CWM combustion. Combustion and airfoil cooling conditions were representative of current operating regimes on petroleum fuels.

Test Facility

Combustion and deposition experimentation was performed on the so-called "Turbine Simulator" shown in Fig. 1. Its principal components are a modified J-79 aircraft combustor, a LM-500 aircraft derivative gas turbine first-stage turbine airfoil sector, and a connecting transition piece. The modified J-79 can combustor (Fig. 2) was 16.5 cm in diameter and 45 cm in length. The plug-flow residence time was approximately 20 ms. The nozzle cascade consisted (Fig. 3) of a 45-deg sector of the LM-500 first-stage turbine nozzle. The LM-500 is an aircraft derivative turbine with an output of approximately 5000 hp. It is the gas turbine of choice for the coal-fired gas turbine locomotive. A Hastelloy-X transition piece connected the cylindrical combustor with the turbine nozzle sector.

Turbine simulators have been used extensively in our laboratory to study deposition characteristics of heavy petroleum fuels, coal-derived liquids, and coal gas. Results for

Contributed by the Gas Turbine Division of THE AMERICAN SOCIETY OF MECHANICAL ENGINEERS and presented at the 32nd International Gas Turbine Conference and Exhibit, Anaheim, California, May 31-June 4, 1987. Manuscript received at ASME Headquarters February 27, 1987. Paper No. 87-GT-266.

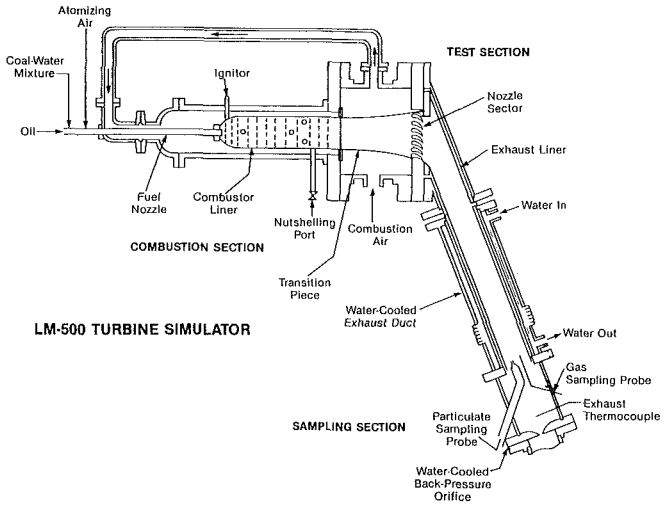

Fig. 1 Schematic diagram of the turbine simulator combustion/deposition test facility

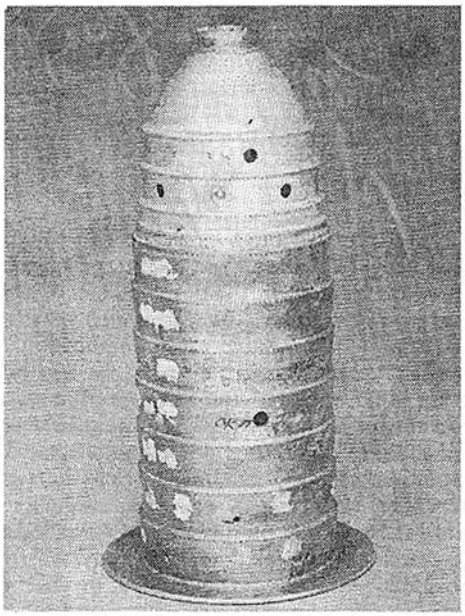

Fig. 2 CWM combustor

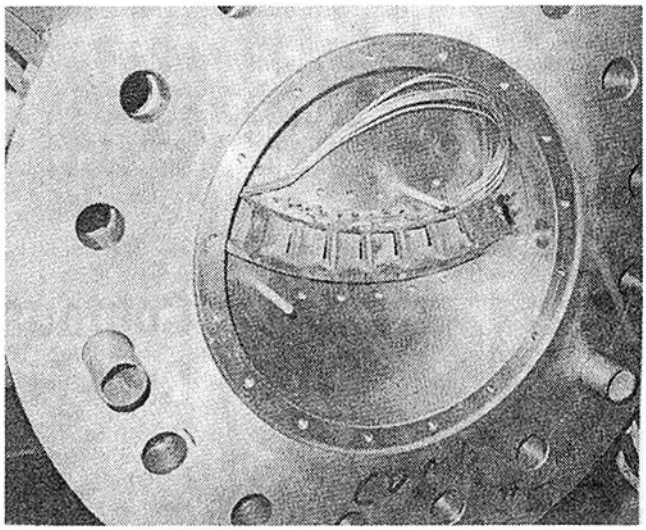

Fig. 3 First-stage turbine nozzle cascade

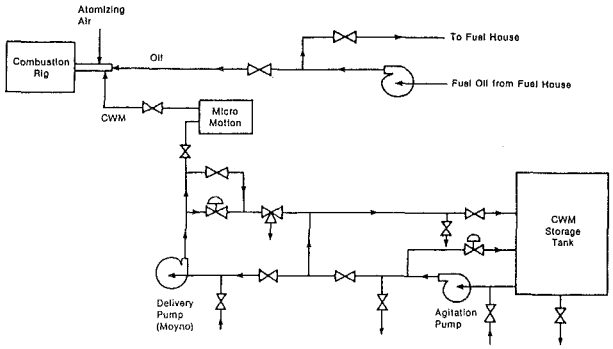

Fig. 4 Fuel delivery system

petroleum fuels have been found to correlate well with field experience.

The fuel delivery and handling system is shown schematically in Fig. 4. The CWM holding tank is a 1.86 m^3 (500 gal) stainless steel tank, which was loaded from 55-gal drums in which the CWM is supplied. A recirculation pump was used to agitate the slurry. A Moyno progressive cavity pump pressurizes and delivers the slurry to the fuel nozzle. The CWM flow rate was controlled with a Paradjust motor speed controller, and the flow rate was monitored with a Micro Motion mass flow meter.

Two fuel nozzles were used for CWM atomization. For Test 1, CWM was atomized by a Parker-Hannefin (PH) nozzle, Drawing No. EDL6840623. It was an air-assist nozzle with atomizing air streams on both sides of the slurry film. This nozzle was designed to deliver up to 409 kg/hr (1.5 gal × min) of slurry. Supplemental fuel oil, used to enhance coal combustion efficiency, was introduced through a side-mounted plain-orifice nozzle. Other tests were performed with a GE-designed dual fuel nozzle with similar flow capacities. This nozzle accommodated both CWM and fuel oil, and atomized them with Mach 1 air flow. No premixing of these two fuels was performed prior to entering the combustor.

Particles in the combustor exhaust were collected using a near-isokinetic gas-quenched probe, in which the sample was rapidly cooled by mixing with nitrogen near the probe entrance. The particles were then collected on a porous stainless steel filter rated at 99.99 percent retention for particles greater than 0.1 μm. Combustion gases were also monitored continuously for NO_x, SO_2, CO, CO_2, O_2, and unburned hydrocarbon content.

During testing, on-line measurement and calculation of key parameters were performed using the TMGR [5] data collection and analysis system. These key parameters include pressures and temperatures in key locations in the combustion, deposition, fuel feed, and sampling systems; on-line calculations of combustion efficiency based on exhaust gas analyses; and nozzle area index number (NAIN), which is a direct measurement of blockage of the turbine nozzle throat due to deposition. NAIN is defined as:

$$\text{NAIN} = \dot{m}\sqrt{T}/P$$

where $\dot{m}$ is the total mass flow of gas through the turbine nozzle; P is the combustion chamber pressure; and T is the firing temperature.

This equation is a simplified form of the throat area for a sonic isentropic nozzle. During deposition testing, monitoring of changes in NAIN gives a quantitative indication of the amount of deposits that have formed in the nozzle throat.

Test Description

Three combustion/deposition tests with CWM and one with

Table 1 Nominal test conditions for CWMM combustion/deposition tests

Chamber pressure, MPa	1.01
Combustor exit temperature, °C	1093
Preheat, °C	404
Air, kg/s	1.0
Atomizing air, kg/s	0.09
CWM, kg/s	0.05
Fuel oil, kg/s	0.005
Nozzle cooling air, kg/s	0.17
Total nozzle flow, kg/s	1.32

Table 2 Otisca coal-water mixture properties

Ash, percent	0.76–0.87
Solids, percent	49.6–50.4
Volatiles, percent dry	38–39
Sulfur, percent dry	0.71–0.89
Particle size, μm	4.0 mean
	95 percent <15

residual fuel were performed and are discussed in this paper. Nominal test conditions are shown in Table 1. Test conditions were selected such that critical operating parameters would be similar to those expected in coal-fueled gas turbines. These operating parameters that were considered critical to ash deposition behavior included firing temperature, combustor residence time, gas velocity, and vane cooling. Another important factor was felt to be combustion efficiency, as large amounts of carbon in the particulates exiting the combustor may significantly affect deposition. To achieve high-combustion efficiencies without undertaking a major combustor development program, supplemental fuel oil in quantities of approximately 25 percent on a Btu basis was used. The effect of the fuel oil was to reduce combustion delay because of slurry water vaporization and to enhance devolatilization. However, it was felt that char burnout, and thus ash behavior, would be little affected by the fuel oil.

The CWM fuel used for all tests was supplied by Otisca Industries. Properties of the CWM are shown in Table 2. This fuel, which was prepared by micronization and physical separation of ash selective agglomeration, was selected based on its availability and likelihood that it would be most representative of a future gas turbine coal fuel.

CWM combustion/deposition tests were performed as follows: CWM was agitated in drums for at least one hour and loaded into the storage tank. During operation, the storage tank was replenished as necessary. Combustion was initiated with fuel oil alone. As the specified test conditions were approached, CWM flow and combustion air flow were gradually increased and fuel oil flow decreased until the test point was reached.

The first combustion/deposition test was performed using the Parker-Hannefin fuel nozzle for the CWM. A side-mounted nozzle was used for fuel oil. At the specified test point, 90 percent combustion efficiency based on residual carbon in the captured ash was obtained when using 28 percent fuel oil. This relatively poor combustion efficiency was attributed to the location of the fuel oil nozzle, resulting in poor mixing of the CWM and fuel oil droplets and disturbance of the flow symmetry in the primary zone. After approximately 5 hours of operation, combustion instabilities were noted. During the following 5 hr the frequency and magnitude of the combustion instabilities increased, and the efficiency of combustion was reduced to less than 40 percent. During the period of the test it was noted that plugging of the CWM fuel nozzle was occurring as indicated by an increase in the CWM feed line pressure. Upon examination, it was found that severe plugging of the fuel nozzle had occurred.

The turbine nozzle cascade was visually examined after the test and was found to be free of deposits. It is probable that

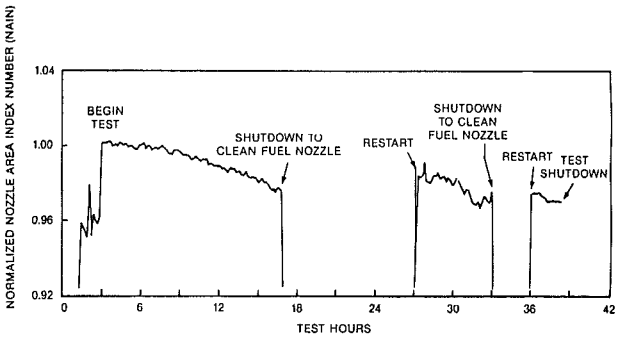

Fig. 5 CWM deposition rate—second run

the large quantities of residual carbon in the particulates played an important role in deposition behavior, although the general applicability of this result is uncertain. Unburned carbon has no inherent tendency to stick on hot metal surfaces, and it may actually erode away existing deposits.

Because of the relatively poor combustion efficiency obtained in the first test, the fuel nozzles were replaced with a single dual-fuel nozzle of General Electric design. This design enabled improved comixing of the CWM and fuel oil. Additionally, it was determined in a nozzle characterization study [6] that considerably finer CWM droplets were obtained with the GE design. A second modification to improve combustion stability was to use coswirl of the atomizing and combustion air rather than counterswirl as had been used in the first test.

In the second CWM test, stable and efficient combustion was achieved. A combustion efficiency of greater than 99 percent, as indicated by a residual carbon content in the captured ash of less than 15 percent, was obtained. Significant deposition was noted after a few hours of operation. Figure 5 shows the deposition rate as indicated by NAIN, normalized to 100 percent at the beginning of the run. Over the next 10 hr, the deposition rate accelerated somewhat as expected. Slow plugging of the fuel nozzle necessitated a shutdown at the 14th hour. The fuel nozzle was then cleaned and the test was restarted. It should be noted that interruptions in deposition tests may have significant effects on deposition rates. However, on restarting the test, the NAIN level was identical to that at the time of the shutdown. After another 6 hours of operation, it was again necessary to clean the fuel nozzle. The deposition test was terminated after a total of 23 hr, with a total NAIN reduction of 3 percent, which was an order of magnitude lower than that predicted from residual fuel oil experience on heavy-duty gas turbine airfoils.

Visual inspection showed that a rusty, scaly deposit had formed on the pressure side and leading edge of the nozzle vanes (Fig. 6). The deposit thickness varied considerably, but was of the order of 200 to 1000 μm. The deposit was quite hard and adherent. The suction side deposit looked completely different, with a powdery appearance. Its thickness was approximately 100 μm (Fig. 7). All film cooling holes appeared to be free of blockage. Although the pressure side deposits were thicker, the suction side deposit was the cause of the measured NAIN reduction because the suction side deposition occurred in the critical throat area.

Although the CWM deposition rate was low relative to residual oil, it was apparent that its use would necessitate intermittent cleaning procedures, perhaps similer to the abrasive cleaning and water washing methods used for residual fuel machines. It was also apparent that the CWM deposits were much tougher and adherent than residual oil deposits. Thus, a deposition/cleanability test was performed. Combustion conditions were nominally the same as in the previous test. A slight modification was made to the fuel nozzle in an attempt to eliminate the plugging problem.

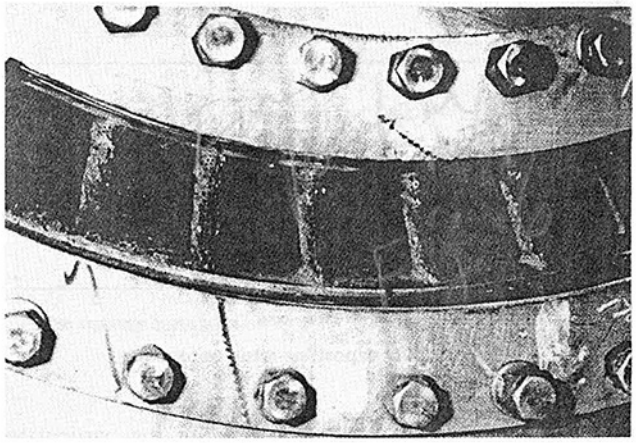

Fig. 6 Photograph of turbine cascade with coal ash deposit—pressure side

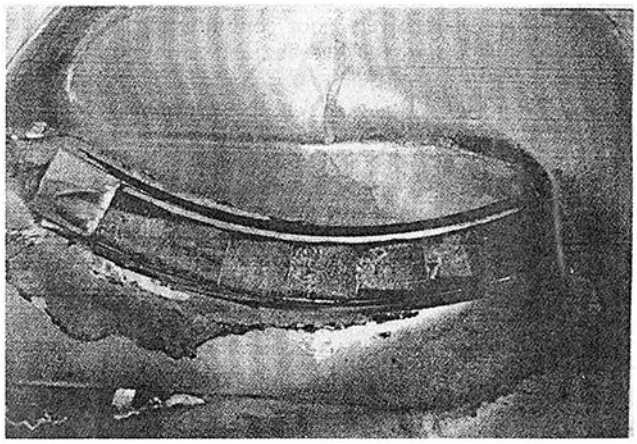

Fig. 7 Photograph of turbine cascade with coal ash deposit—suction side

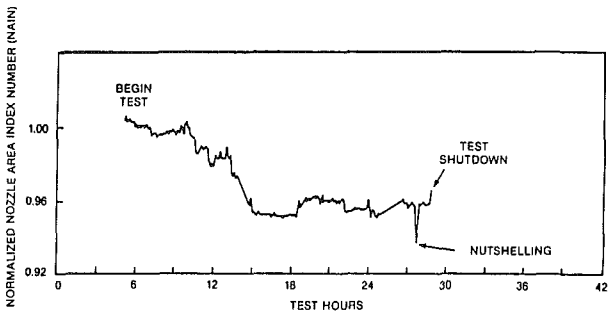

Fig. 8 CWM deposition rate—third run

The deposition rate for the deposition/cleanability test is shown in Fig. 8. The NAIN reduction rate is similar to that for the second CWM run, with the exception of a period between the 13th and 19th hours, where a large apparent decline in NAIN was experienced. Subsequent examination of the data indicated that the cause of this was a drop in combustion air flow rather than in deposition. The run was stopped after 23 hr, at which point NAIN had declined by 4 percent as compared with 3 percent for the previous run, which is excellent agreement.

Combustion efficiencies in excess of 99.5 percent were maintained over the course of the run. However, gradual plugging of the CWM delivery line resulted in loss of CWM flow. This required a gradual increase in the fuel oil flow to maintain constant total combustor exhaust velocity. Thus, at the end of the run the fuel oil flow was 40 percent of the total fuel flow on a Btu basis. Examination of the nozzle showed that the fuel nozzle plugging problem had greatly diminished.

Table 3 Simulated residual oil contaminant levels

Vanadium	200 ppm
Magnesium	600 ppm
Sodium	2 ppm
Sulfur	1 percent

The effectiveness of on-line abrasive cleaning, the standard procedure for removing deposits from residual oil-fired gas turbines, was then assessed. Two charges of 4.5 kg each of crushed nutshells (Carboblast) were injected into the aft end of the combustor while maintaining full firing conditions. No recovery of nozzle throat area was obtained. However, visual inspection showed that a large fraction of the leading edge and pressure side deposits had been removed. None of the suction side deposit, which was much less fused and less adherent, was removed by abrasive cleaning as the large nutshell particles apparently did not impact the suction side.

A second cleaning technique, which is generally used in residual oil-fired gas turbines after multiple nutshellings, is water washing. The object of water washing is to saturate the deposit with water so that refiring will cause rapid volatilization of the water resulting in spalling of the deposits. Water was sprayed into the combustor through the fuel nozzle at low air flow for a period of 30 min. The combustor was then refired on oil for 3 min. Minimal pressure side deposit removal occurred as a result of the water-washing procedure. However it appeared that significant loosening of the deposits occurred. The suction side deposit was almost completely removed. Subsequent refiring and nutshelling removed a large fraction of the remaining pressure side and leading edge deposits.

Thus, it has been shown that the standard gas turbine cleaning procedures of water washing and abrasive cleaning will remove the bulk of the CWM deposits, and therefore will prolong the life of the gas turbine between teardowns. However, deposits are removed only with considerable difficulty and removal is incomplete.

The final run performed in this deposition study was for the purpose of establishing a residual oil deposition rate baseline so that comparisons between coal fuels and dirty petroleum fuels could be made. Although a large data base exists for heavy-duty gas turbines operating on residual oil, no experience exists for the highly film-cooled aircraft derivative airfoils used in this study. For ease of experimentation, simulated residual oil prepared by doping No. 2 fuel oil was used. Previous experimentation has shown that simulated residual oil gives deposition rate results that are in excellent agreement with real residual oil.

The composition of the simulated residual oil is shown in Table 3. Vanadyl sulfate, magnesium sulfate, and sodium chloride were dissolved in water and the solution was emulsified in the fuel oil. Carbon disulfide was added to oil to provide a large source of sulfur.

A deposition test was made under firing conditions identical to the CWM runs. The deposition rate is shown in Fig. 9. After 23 hr of operation, the nozzle area reduction was 12 percent as compared with 3 to 4 percent for the CWM even though the ash loading for the residual oil was much lower. It should be noted that the deposition rate was also much lower than that which would be obtained for heavy-duty gas turbine nozzles. The deposits had an appearance totally unlike the coal deposits. They were quite fragile and evenly distributed over the pressure and suction sides. Deposit buildup was quite irregular, indicating that periodic spalling occurred.

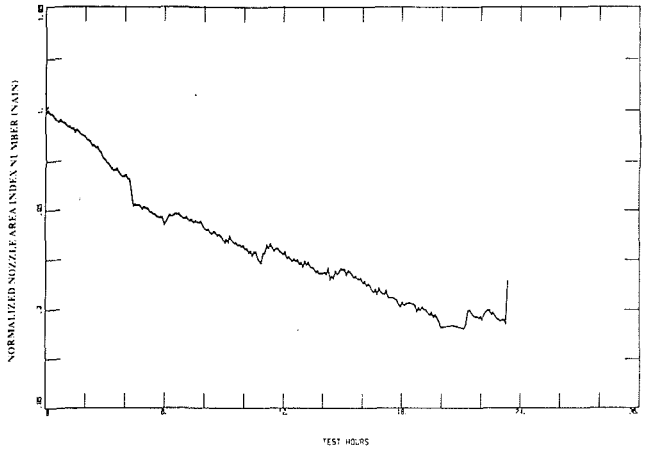

Fig. 9 Residual oil deposition rate

Discussion

The three CWM deposition tests were performed under the same nominal conditions. The initial test differed substantially in both combustion efficiency and deposition rate from the other two tests, indicating an important effect of fuel nozzle atomization characteristics and flow geometry. In the initial test, a Parker-Hannefin single fuel nozzle was used in conjunction with a supplemental fuel oil nozzle, which was mounted on the periphery of the combustor, with its spray axis radial to the combustor. The relatively poor combustion efficiency in this configuration is a result of three factors. The Parker-Hannefin spray nozzle produced spray droplets with a Rosin-Rammler mean size of 25 μm as compared with 20 μm for the GE nozzle [6]. The Parker-Hannefin nozzle also produced a larger fraction of large droplets in excess of 30 μm. The side-mounted oil assist nozzle caused asymmetry in the flow pattern and affected recirculation. Mixing between the oil and the CWM was also poor. Thus the desired affect of reducing combustion delay was not achieved. In the second two CWM experiments, the dual-fuel GE nozzle, with its improved atomization and even distribution of oil and CWM, achieved greater than 99 percent combustion efficiency based on exhaust gas composition and residual carbon in the ash, which was as low as 14 percent.

The plug-flow combustor residence time, without taking account of recirculation, was 20 ms. The effect of the supplemental fuel oil is to reduce combustion delay because of water evaporation and to enhance volatilization. Combustion delay has been estimated to be approximately 5 ms. Thus, it is felt that with improved atomization and enhanced recirculation, CWM combustion without supplemental fuel can be accomplished in current gas turbine-type combustion systems, without the necessity for large offbase combustors. Ash chemistry is an important factor in combustor design. Minimizing combustor residence times should reduce ash fusion and volatilization and, in particular, alkali release, which will reduce impurity effects on the turbine.

In the first CWM deposition run with coal combustion efficiency, which is based on residual carbon in the ash, was approximately 90 percent. No significant deposits were obtained on the nozzle vanes. Although duration of the run was relatively short, subsequent experiments indicate that with good combustion some deposits would be obtained. Since on the average, particulates impinging on the nozzle vanes were 90 percent carbon, we can surmise that this carbon reduced the sticking coefficient of the ash particles. Nonetheless, it would be expected that some of the smaller particles would have been well burned and would have contained little carbon, and thus form deposits. Perhaps the larger carbon-containing particles acted as abrasive cleaners.

For the runs with high-combustion efficiency, deposition on the nozzle vanes resulted in a nozzle area blockage rate of 12 to 16 percent per 100 hr. This nozzle area blockage was caused by a relatively thin suction side deposit, which occurred in the critical throat area. Although the pressure side deposits were thicker and probably were more harmful in the long run, they did not cause substantial nozzle area blockage. It would be expected, however, that the prolonged operation would result in the pressure side deposit becoming the dominant flow resistance.

The large differences in deposition rate and physical characteristics of the deposits indicate a major difference in the mechanism of deposition for petroleum and coal fuels. The formation of deposits for petroleum fuels is enhanced by the presence of "glues," which are liquid at deposition temperatures and which cause adhesion of the refractory components of the ash [7]. These glues are generally considered to be alkali sulfates, which additionally are the key species implicated in hot corrosion. X-ray absorption spectroscopic analysis of the CWM deposits shows that alkali metals were present only as alkali aluminosilicates [8], which are more refractory than are alkali sulfates. Additionally, extreme physical and chemical differences between the CWM pressure and suction side deposits were found [8].

The mechanisms for coal ash deposition, based on the characteristics of the deposits, can be described as follows. The pressure side and leading edge deposits were found to be formed of weakly sintered slag droplets. These slag droplets were formed during combustion, with the larger particles resulting from agglomeration of the coal within a single CWM droplet. The larger slag droplets exiting the combustor deviated from the gas flow streamlines and impacted the pressure side and leading edge of the airfoils. Partial freezing of the droplets occurred as they entered the cool boundary layer. In this partially fused condition, some adhesion to the cooled surface and sintering of the particles took place. However, as evidenced by their spherical morphology, the particles were nearly solid when impaction took place. It was also noted that where film cooling air velocities were high, less deposition took place and the deposits were more easily removed. This was probably both an aerodynamic and thermal effect. Conversely, it was found that the deposits occurring in the region between the leading edge air holes and the first row of pressure side film cooling holes where film cooling effectiveness is relatively poor, were the most difficult to remove.

One conclusion from this observation is that high cooling effectiveness reduces deposition rate, and that as deposits build up and thereby reduce cooling effectiveness, deposition will accelerate.

The suction side deposits reflect the composition of the aerosols found in the probe samples. The apparent primary mechanism for deposition was the diffusion of aerosols to the surface with some adhesion resulting from their partially molten condition. There is no analytical evidence that alkali sulfate glues participate in suction pressure side deposition with coal fuels [8].

Abrasive cleaning was expected to have little effect on the removal of deposits because of their fused nature. The extent of deposit removal with nutshell injection was unexpectedly high. Clearly, however, adequate deposit removal was not accomplished. Because of the insoluble nature of the deposits on the pressure and suction sides, water washing was also expected to be relatively ineffective. However, water washing and refiring almost completely removed the suction side deposit and loosened much of the leading edge and pressure side deposit so that subsequent abrasive cleaning effectiveness was improved. Microscopic examination of the deposits

showed fissures into which the water probably penetrated, thus causing spalling of the deposits during refiring and accompanying vaporization of the water. Removal of the suction side deposit appears to have been by a different route. Little penetration of water into the suction side appears to have been likely due to its lack of cracks and fissures. It is possible that the major component of the suction side deposit, anyhdrite ($CaSO_4$), hydrated to form gypsum ($CaSO_4 \cdot 2 H_2O$). Refiring may then have caused rapid dehydration and evolution of steam, resulting in deposit removal.

Although throat area recovery was not determined after water washing, it is expected that more complete recovery would be achieved because of the effectiveness of suction side deposit removal. However, since complete pressure side deposit removal was not achieved, it is possible that subsequent deposition rates will be greater in the areas where residual, well-adhered deposits are present.

Conclusions

Highly cleaned coal–water mixture (CWM) combustion and deposition experiments have been performed using a modified gas turbine combustor and gas turbine nozzle sector. Several important conclusions can be drawn from the results of these experiments.

It is highly probable that efficient combustion of CWM can be performed in gas turbine-type can or annular combustors. Residence times in the range of 10 to 20 ms are feasible, thus enabling the use of combustors similar to those currently used for gas- and oil-fired gas turbines. In order to achieve rapid combustion, combustion delay and char burnout time must be minimized through effective fuel atomization. Combustors must be designed to achieve a high degree of recirculation to provide heat for rapid evaporation of slurry water and devolatilization.

Because of the differences in deposition mechanism and rate, residual oil experience does not provide a meaningful basis for the prediction of the deposition of coal-based fuels. Alkali sulfates do not play a substantial role in coal ash deposition. Deposition on the pressure side and leading edge are a result of direct impaction of partially fused ash particles. Vane cooling effectiveness thus will have an important effect on the rate and properties of these deposits. The suction side deposits are principally a result of diffusion of aerosols. Increased surface cooling can, in fact, increase suction side deposition rates because of the increased thermal driving force.

An important consequence of the deposition mechanisms for coal ash is that the nozzle area plugging rate may have different implications than for petroleum fuels. The pressure side CWM deposits appear to have been the more important in terms of turbine operability and life than the suction side deposits. However, the nozzle area plugging rate, at least in the early stages of deposition, is dominated by the suction side deposit. Thus, it is desirable to identify methods for determining pressure side deposition rates on-line. Perhaps monitoring of vane temperatures will be an approach. The development of methods for direct visual observation would be extremely useful in the study of coal ash deposition.

For any dirty fuel applications, where deposition will occur in the turbine, cleaning and maintenance procedures must be developed. Based on these experiments, it is clear that deposit removal methods for coal-fired gas turbines will be required. Conventional cleaning by abrasive injection and water washing was found to be unexpectedly effective in the removal of coal ash deposits. However, improvements in cleaning method or in improving deposit cleanabilty characteristics will be required to achieve acceptable cleaning levels.

Acknowledgments

Much of the work described in this paper was performed under funding from the Department of Energy, Morgantown Energy Technology Center.

References

1 *Proceedings of the Conference on Coal Burning Turbines*, McGill University, Department of Mines and Technical Surveys, Ottawa, Nov. 22–23, 1956.

2 *Coal Burning Gas Turbine Project*, Report of the Interdepartmental Steering Committee, Dept. of Minerals and Energy, Dept. of Supply of Australia, Australian Government Publishing Service, 1973.

3 Spiro, C. L., Chen, C. C., Kimura, S. G., Wong, J., and Greegor, R. B., "Characterization of Products from a Direct Coal-Water Mixture Fired Gas Turbine," *Fuel*, Vol. 66, 1987, pp. 563–567.

4 Monroe, L. S., Famayan, F. W., Srinivasachar, W., Beer, J. M., and Sarofim, A. F., "Mineral Matter Transformations in Coal Slurry Flames," *Proc. Third Engineering Foundation Conference on Slagging and Fouling Due to Impurities in Combustion Gases*, Copper Mountain, CO, 1984.

5 Smith, D. P., "TMGR, A Computer-Aided Test System," General Electric publication, 1985.

6 Staub, F. W., *Spray Characterization and CW Slurry Atomization*, General Electric Corporate Research and Development Report 85CRD217, Dec. 1985.

7 Urbas, T. A., and Tomlinson, L. H., "Formation and Removal of Residual Fuel Ash Deposits in Gas Turbines," in: *Ash Deposits and Corrosion Due to Impurities in Combustion Gases*, R. W. Bryers, ed., Hemisphere Publishing Corp., 1977.

8 Spiro, C. L., Kimura, S. G., and Chen, C. C., "Ash Behavior During Combustion and Deposition in Coal-Fueled Gas Turbines," ASME JOURNAL OF ENGINEERING FOR GAS TURBINES AND POWER, this issue.

Ash Behavior During Combustion and Deposition in Coal-Fueled Gas Turbines

C. L. Spiro
S. G. Kimura
C. C. Chen
General Electric Corporate Research and Development, Schenectady, NY 12301

Chemical and physical transformations of coal ash during combustion and deposition in gas turbine environments have been studied. Extensive characterization of the coal–water mixture fuel and deposits obtained on deposition pins and turbine nozzle vanes has been performed. The behavior of alkali metals has been found to be much different from that for petroleum fuels, resulting in lower than expected deposition and probable reduced corrosion rates.

Introduction

The study of coal as an alternative fuel for gas turbine engines represents a significant technical activity by a broad coalition of academic, industrial, and government concerns [1–3]. The issues include fuel preparation, storage, handling, injection, ignition, burnout, corrosion, erosion, deposition, gaseous and aerosol emissions, and economics.

The technology associated with firing a gas turbine on contaminated petroleum fuels is well established. It is possible that much of the wisdom developed through the years of laboratory and in-field studies can be transferred to the coal-fired alternative. However, coal ash constituents are, in general, unlike petroleum ash constituents in both quantity and composition, thus, possibly, having distinctly different corrosion, erosion, and deposition behavior. Deposits may have different sticking coefficients [4], may or may not be affected by deposition "glues" [5], may be more or less corrosive and erosive [6–8].

The objective of this study was to explore the physical and chemical transformations of coal ash during the combustion/deposition processes in gas turbine environments in order to identify the major factors which affect their corrosion, erosion, and deposition behavior. In order to obtain this information, coal–water mixture (CWM) fuels were burned in gas turbine-type can combustors, and deposits and products of combustion were collected and analyzed.

Extensive physical and chemical analyses of the deposits and probe samples were performed. Analytical methods included electron microscopy, X-ray diffraction analysis, energy dispersive X-ray analysis, metallography, wet chemistry, and X-ray absorption spectroscopy using a synchrotron light source.

Fuel Character

Fuels were obtained in the form of aqueous slurries containing approximately 50 weight percent solids and were prepared by physical and chemical de-ashing of high-volatile Eastern bituminous coals. Physical beneficiation of a high-volatile A Kentucky Blue Gem coal was performed by Otisca Industries, Ltd., using the method of selective agglomeration [9]. Properties of the fuel appear in Table 1. A detailed analysis [10, 11] of the Otisca product low-temperature ash revealed quartz, kaolinite, anhydrite, calcite, pyrite, ferric sulfate, and illite.

Germane to alkali speciation in the Otisca CWM was the presence of potassium exclusively as illite as determined by extended X-ray absorption fine structure (EXAFS) spectroscopy [12]. Illite is a layered aluminosilicate clay with gaps between the sheets filled by potassium ions in twelvefold coordination [13]. Spacing between the layers is 10.0 Å. The significance of this structure is that, in order for potassium to be released to the atmosphere, at least 12 chemical bonds must be broken, and alkali must diffuse through a considerable aluminosilicate matrix.

Table 1 Coal-water mixture fuel specifications

Coal-Water-Mixture	AMAX	Otisca
Coal Content, % by wt.	53.0	53.7
Particle size, micron	98.35% < 15	95.1% < 11.5
Viscosity, c.p.	180 at 100/sec	275 at 112/sec
Heating value (dry), Btu/#	15,054	14,880
Proximate analysis (dry),%		
Fixed carbon	64.71	60.29
Volatiles	34.88	38.83
Ash	0.41	0.88
Ultimate analysis (dry), %		
Carbon	84.86	82.95
Hydrogen	5.48	5.34
Nitrogen	1.68	2.08
Sulfur	0.89	0.93
Chlorine	0.25	0.18
Oxygen (by difference)	6.43	7.64
Ash composition, %		
Silica	17.90	16.04
Alumina	11.50	23.21
Ferric oxide	37.60	28.15
Lime	3.24	11.60
Magnesia	0.88	2.88
Sodium oxide	6.70	0.47
Potassium oxide	5.80	0.47
Titania	2.85	1.10
Others	13.53	16.07

Contributed by the Gas Turbine Division of THE AMERICAN SOCIETY OF MECHANICAL ENGINEERS and presented at the 32nd International Gas Turbine Conference and Exhibit, Anaheim, California, May 31–June 4, 1987. Manuscript received at ASME Headquarters February 27, 1987. Paper No. 87-GT-267.

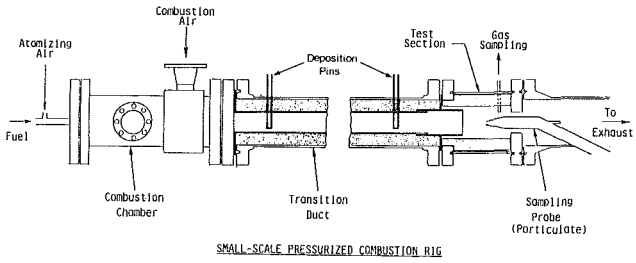

Fig. 1 Schematic of so-called "minirig" combustion system

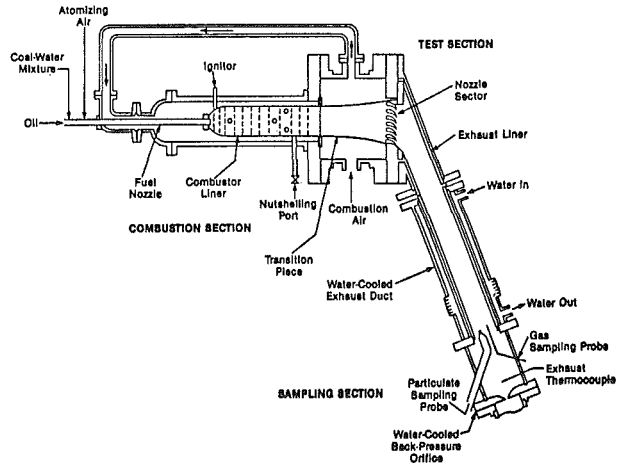

Fig. 2 Schematic of so-called "LM-500 turbine simulator" combustion/deposition test system

The second fuel was prepared by chemical beneficiation, performed by AMAX Extractive Research and Development, Inc., using hot aqueous pressurized caustic as described in detail elsewhere [14]. Noteworthy to this study is that the chemical leaching left a residue of soluble alkali metals (Table 1) considerably in excess of the 1 ppm currently specified for gas turbine fuels. In addition, the leachant was subsequently neutralized with HCl, leaving considerable chloride ion in solution. Finally, because the fuel was milled after chemical leaching, products of comminution resulted in increased iron content.

A detailed X-ray diffraction analysis of the AMAX product low-temperature ash prepared by oxygen plasma treatment at 100°C for several days revealed quartz, hematite, spinel, and a large number of unassigned peaks and a broad amorphous envelope. Recent research by Markuzewski et al. characterizing hot aqueous alkaline [15] and caustic/microwave [16] beneficiated coals revealed the presence of a variety of feldspathoids.

Test Facility

Alkali/ash transformation tests were performed on a small-scale combustion test rig, referred to as the "minirig." The "LM-500 Turbine Simulator" was used for deposition testing. Both test rigs used the same air suppy, CWM delivery, sampling, and data acquistion systems.

The minirig (Fig. 1) consists of a reverse flow combustion liner 4 in. in diameter and 15.5 in. long, housed in an 8-in. pressure vessel with two 3.5-in. viewing windows. A co-swirl configuration, with swirling air, atomizing air, and fuel rotation in the same direction, was employed for flame stability. The products of combustion travel through a backpressure nozzle and an adiabatic duct to the test section where the particulates and gases are sampled. The hot stream is then quenched with water and flows to exhaust.

Table 2 Minirig tests with CWM

	Test 1, AMAX CWM	Test 2, AMAX CWM	Test 3, Otisca CWM	Test 4, Otisca CWM
Pressure, psig	100	103	102	98
Preheat, F	670	660		
Firing temp, F	1675	1950	650	625
Flows, #/s			1700	1990
Air	1.38	1.0	1.0	0.94
Atomizing air	0.08	0.08	0.12	0.12
AMAX CWM	0.042	0.05	0.047	0.053
Oil	0.008	0.0065	0.009	0.009
Oil Btu, %	31	23	31	23
Combustion eff., %	95	99	96	99

Table 3 Test conditions for LM-500 deposition tests 1 and 2

Test #	1	2
Pressure, psig	130-138	130-138
Preheat, F	760	760
Firing temp., F	1950-2050	1850-2000
Flows, #/s		
Air	2.2	2.2
Atomizing air	0.19	0.17-0.2
CWM	0.09-0.10	0.066-0.084
Oil	0.012	0.015-0.025
Vane cooling	0.38-0.40	0.43-0.46
Total	2.8	2.8
Oil Btu, %	15-30	25-45
Combustion Eff., %	99+	99+

Deposits were collected on cylindrical pins made of 0.5-in. Inconel-600 tubing, and were located along the adiabatic duct. The pins were internally air-cooled to maintain desired temperatures.

For the LM-500 Turbine Simulator, an aircraft engine combustor was modified to burn CWM. Deposits were obtained on an LM-500 first-stage turbine airfoil cascade. The LM-500 is an aircraft derivative gas turbine with an output at full load of approximately 5000 hp.

Products of combustion were sampled with a highly quenched probe in which the POC sample entering the probe is quickly cooled by mixing with nitrogen. The particles in the POC sample are collected on a sintered stainless steel filter element rated 99.99 percent for 0.1-μm particles. Gases were analyzed for CO, carbon dioxide, oxygen, hydrocarbons, SO_2, and NO_x.

Test Description

Combustion tests were initiated on fuel oil to achieve design test pressure and temperature. CWM was then gradually introduced into the combustor, and the oil was decreased accordingly. High priority was placed on achieving near-complete carbon burnout so that realistic deposit character could be ensured. In order to accomplish 99+ percent coal combustion efficiency, a small amount of fuel oil was maintained throughout each CWM test. The fuel oil reduced combustion delay due to evaporation of water from the CWM and enhanced devolatilization, thus reducing residence time required for high carbon utilization.

Four minirig combustion/deposition tests were performed with AMAX and Otisca CWM (two each) at nominal firing temperatures of 1700 and 2000°F. Test duration was approximately 4 hr for each test. Table 2 summarizes the testing conditions.

Two CWM combustion/deposition tests were performed employing the LM-500 turbine simulator. Table 3 summarizes the test conditions. A detailed description of these tests and baseline residual oil testing is presented in an accompanying paper [17].

Analytical Results and Discussion

Products of minirig combustion were obtained as rapidly quenched probe samples and deposits on pins, airfoils, and throughout the hot gas pathway. These were studied by a battery of conventional and advanced analytical techniques in-

Fig. 3 Scanning transmission electron micrograph of probe samples obtained by rapidly quenching combustion of AMAX CWM in the minirig; hollow carbonaceous cenospheres, solid slag droplets, and aerosol constituted the products of combustion

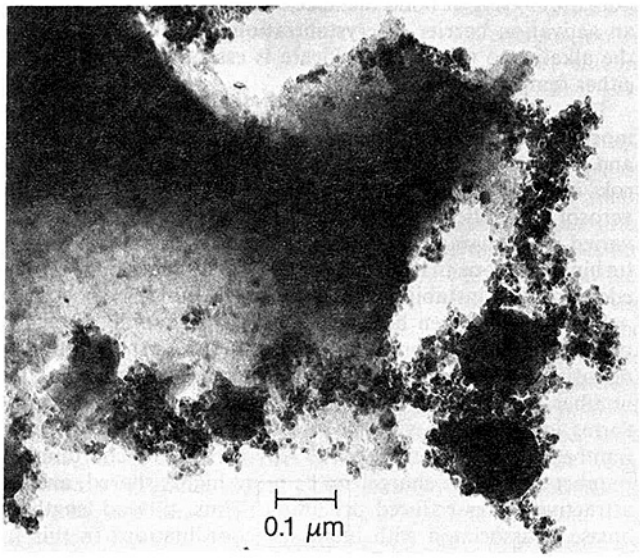

Fig. 4 Scanning transmission micrograph of aerosol product of AMAX CWM combustion in the minirig

cluding electron microscopy, energy dispersive X-ray analysis, X-ray diffraction, and high resolution X-ray absorption spectroscopy employing synchrotron radiation.

Figure 3 is a scanning transmission electron micrograph taken of a probe sample obtained during the 1700°F combustion of AMAX CWM. The salient features include carbonaceous, hollow cenospheres with circular pits along the surface. Along the char surface are smaller spheres which appear black in the micrograph, corresponding to rapidly frozen solid slag droplets. In addition, aerosol from nucleation of vaporized products of combustion can be seen, though aerosol roughly 0.01 μm in diameter is best viewed at higher magnification (Fig. 4).

The cenospheres result from agglomeration of the coal particles within a slurry droplet and rapid devolatilization of the organic matter during its plastic phase [17], which immediately follows evaporation of slurry water. Upon completion of devolatilization, the organic matter becomes rigid and cokelike. Based on the observation of cenospheres greater than 20 μm in diameter, and fragments of what appear to be even larger cenospheres, interparticle agglomeration of organic matter likely takes place to a limited extent during this stage. At this point, limited inorganic transformations are expected to have occurred: mainly pyrite decomposition, clay dehydration, and incipient calcining of carbonate minerals.

Based on the small size of the cenospheres, and their apparent buoyancy, it appears that erosion of the turbine blades, the single most critical barrier problem in the Bureau of Mines/Locomotive Development Committee program [19] in the 1960s, will not be severe provided micronization and good atomization are ensured. Dense particles greater than 10 μm are necessary in order actually to impinge on blade surfaces and erode [20, 21].

The cenospheres are completely destroyed by low-temperature oxygen plasma ashing, demonstrating their carbonaceous framework, and the lack of slag wetting. Neither the slag droplets nor the aerosol were appreciably affected by low-temperature ashing.

Burnout of the cenospheres from AMAX CWM fuel appears to occur by propagation of holes along the char surface. These pits are frequently observed in carbon combustion and gasification involving catalytic mechanisms. In particular, we suggest that the AMAX beneficiation process leaves alkali residues which are catalytic, generating a defect or pit in the char surface and resulting in highly reactive edge carbons. The carbon, presenting a spherical surface, is consumed by propagation of a circular burn front emanating from the catalytic center. The catalytic efficiency of alkali species has been well documented with respect to gasification [22] and combustion [23] with the concomitant appearance of pits and channels [24]. For graphite, the pits are hexagonal [25] or circular [26] depending on the condition of pretreatment, while for coal [24], erratic channels and pits result. The mechanism of alkali catalysis is believed to involve the following mechanism [27]:

$$Na_2O + 1/2\,O_2 = Na_2O_2$$
$$Na_2O_2 + C = Na_2O + CO$$
$$CO + 1/2\,O_2 = CO_2$$

Similar mechanisms for potassium can be written. Iron is also catalytic under reducing conditions [28], as are alkaline earth metals.

One possible consequence of the catalysis is that neither catalytic alkali moiety is appreciably volatile. Indeed, energy dispersive X-ray analysis of the 100 Å aerosol reveals no alkali metals. The appearance of iron in the vapor indicates that the actual char surface temperature in the vicinity of the iron may have reached upward of 2500°C.

The spherical frozen droplets of slag in the quenched probe samples were generally on the order of 0.5 μm in size, and ranged from less than 0.1 μm up to 3 μm in diameter. These formed from melting of ash in the char. The droplets poorly wet the cenosphere surface while molten, and probably progress with the burn front. Neville et al. [29] have observed that, for 100-μm coal particles burned under boiler conditions, some mineral inclusions are fused into single large slag droplets, while others remain isolated. Similar results probably are occurring here, suggesting that as the burn front proceeds, if two droplets intercept one another fusion will generally occur, but that once the carbon is consumed, insufficient heat from the ambient is available to sustain fusion, and solid spheres form. In general, short residence time combustion will favor finer slag droplets and a reduced tendency to erode.

A second set of products from AMAX CWM combustion was deposits on the trailing edge of the air-cooled pins. The deposits were orange red and fluffy, easily removed by scraping with a spatula. When these pin deposits were examined

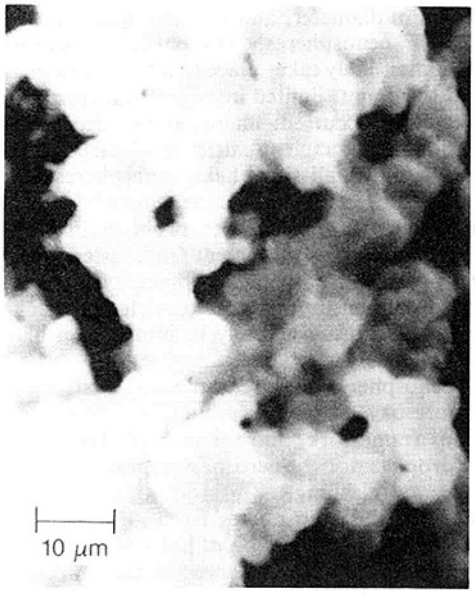

Fig. 5 Pin deposits from AMAX CWM combustion

Fig. 6 Cenospheres from combustion of Otisca CWM appear isotropic

microscopically, clusters of poorly sintered spheres of slag were found, typically below 10 μm in diameter. An example of this appears in Fig. 5. The spheres are reminiscent of the solid spheres which adhere to the edges of the quenched carbonaceous cenospheres taken from the probe, suggesting a common origin. In particular, it appears that the cenospheres impinged on the pins and occasionally stuck. Burnout proceeded to completion after depositing on the pins. Once carbon was consumed, insufficient heat from the ambient was available to fuse the slag droplets, and they retained the frozen spherical morphology, weakly adhering to other pin deposits through occasional sintering and bridging. This view is consistent with their morphology, ease of removal, and the fact that deposits obtained on the two pins were similar in character though the pins had different internal temperatures, while deposits obtained at different firing temperatures were different.

X-ray diffraction analysis was performed by slow scanning with a Rigaku diffractometer. The phases were identified with the JCPDS Inorganic Powder Diffraction File. In the 2000°F deposits hematite (Fe_2O_3), alpha ferric oxide, was a major phase. Feldspathoids constituted another major phase. Feldspathoids have a network aluminosilicate structure that is more open than the feldspars, usually resulting from alkali-rich melts. Common minerals of this class include sodalite, hauynite, and lazurite. A range of solid solutions exists with cationic sites consisting of sodium, calcium and potassium, with anionic sites including sulfate, chloride, and sulfide. Nepheline was found in trace proportions, with a composition (Na, Ca, K) (Al, Fe) (Si, Al)O_4.

Deposits obtained at 1700°F also contain hematite as the major X-ray diffracting phase, but the aluminosilicates remained in a glassy state, with only a minor amount of feldspathoid found on one pin.

X-ray absorption spectroscopy was also applied to these samples, using synchrotron radiation obtained at the wiggler side station IV-1 during a dedicated run of the Stanford Positron-Electron Annihilation Ring (SPEAR) at the Stanford Synchrotron Radiation Laboratory, Stanford, CA. An electron energy of 3.0 GeV at ring currents of ~75 mA was employed. The use of synchrotron radiation to obtain X-ray absorption fine structure [EXAFS] and X-ray absorption near edge [XANES] spectral features on coal and coal ash has been described elsewhere [30, 31]. X-ray analysis of potassium in AMAX products of combustion reveals that the local environment is characteristic of aluminosilicate coordination. Synthetic feldspathoids were prepared and match very well with the observed features in the ash. Although the 2000°F pin deposits crystallized in a feldspathoid lattice, while the 1700°F pin deposits were amorphous, the XANES and EXAFS features revealed identical local environments, and identical potassium–oxygen bond distances. This indicates that there is an activation barrier to crystallization, but that gettering of the alkali into the aluminosilicate is essentially completed at either temperature.

This highlights an important feature of ash thermochemistry—that differences in combustion temperature and deposition surface temperature may play an important role in the ash chemistry, degree of crystallization, fusion, aerosol generation, and gettering. The temperature can be varied by changing fuel–air stoichiometry, by film cooling of turbine vanes, or inadvertently by hot spot generation around eddies or flow instabilities associated with buildup of deposits.

Potassium–oxygen bond distances in the rapidly quenched probe sample were somewhat lower (~ 0.2Å) than in the pin deposits. This suggests that an increase in coordination number takes place during burnout. Potassium primarily forms ionic bonds, with the bond lengths dependent on the number of nearest neighbors. An increase in coordination number means the charge can be more highly shared, and the attractive forces reduced per anion. Thus, a bond-length increase is associated with increased coordination. In this instance, we suggest that the increase in coordination number is associated with gettering of "free" alkali involved in catalytic combustion into a more constrained, less active aluminosilicate moeity. Similar effects were previously observed in our laboratories, with loss of alkali gasification catalysis by gettering into a feldspathoid matrix (kalsilite) [32].

For the physically beneficiated coal obtained by selective agglomeration through the Otisca process, products of combustion shared many of the physical and chemical properties with that of the chemically leached coal, but distinct differences were also obtained.

Both fuels underwent plastic phases accompanied by swelling and carbonaceous cenosphere formation. However, the AMAX caustic-leached coal appeared to burn through a catalytic process, while the Otisca physically beneficiated coal appeared to burn isotropically. A scanning transmission electron micrograph of the Otisca cenospheres appears in Fig. 6. The particle sizes of the fuel and the cenospheres are comparable, suggesting that, to first order, the organic chemistry of micronized CWM associated with rapid pyrolysis, swelling, and char formation, is to first order independent of beneficiation and dependent only on slurry droplet size. On the other

hand, the isotropic burnout suggests that combustion is dependent on the fuel character. As is apparent from analysis of ash (vide infra), the inorganic thermochemistry of CWM combustion is quite dependent on the beneficiation character.

Analysis of quenched products of combustion from Otisca CWM from the probe revealed that its ash thermochemistry reflects initial mineral speciation. A large X-ray amorphous diffraction envelope was observed corresponding to unburned carbon and glass. Peaks due to spinel and anhydrite were also found. The coexistence of glass and spinel is predicted from simple illite thermochemistry [33], independent of other coal constituents.

The presence of calcium sulfate in the probe sample indicates that in situ gettering of sulfur dioxide by indigenous calcined calcite occurs in the millisecond time frame. Whether added calcium in highly dispersed forms can accomplish significant in-bed sulfur capture without having a deleterious effect on ash fusion, deposition, and turbine performance is a subject worthy of further study. The significance of calcium chemistry with respect to Otisca CWM, and the lack thereof for AMAX CWM, is another indication of the important role of beneficiation on performance. AMAX leaches the coal with caustic, and follows with an acid neutralization. The acid leach also removes a major portion of calcium carbonate/hydroxide; in this study 73 ppm calcium oxide was found in AMAX CWM, while the Otisca CWM showed 1020 ppm of CaO on a fuel basis.

In contrast to the pure-iron aerosol from AMAX CWM combustion, the Otisca aerosol showed a rich compostion including iron but also significant levels of sulfur, silicon, potassium, and calcium. Particle sizes in the 100 Å range were also observed with Otisca CWM.

Pin deposits from Otisca CWM combustion were also collected. At 1700°F, the orange, fluffy deposit consisted of hematite, anhydrite, and graphite as major phases, with minor amounts of spinel and traces of glass. At 2000°F, anhydrite was no longer present, suggesting that sulfation of calcium was no longer favored, and calcium entered a feldspar lattice.

The 2000°F pins included a 10–40-μm slag layer on the leading edge, along with the spherical, fluffy grains on the trailing edge. The leading edge deposits consisted of graphite and hematite, with lesser amounts of spinel and plagioclase feldspar showing the calcium component. Massive crystals of single-crystal graphite, up to 300 μm across, were found, with ubiquitous smaller flakes of graphite throughout. The presence of graphite suggests that locally reducing conditions occurred, and unburned carbon dissolved into the melt. The presence of graphite on the pins reveals that air permeability through the slag is low; otherwise the carbon should burn. The inability of oxygen to diffuse through the slag suggests that hot corrosion by oxidation of the base metal is less likely under these conditions. In other words, coal ash may act as a protective scale to inhibit corrosion. On the other hand, work in our laboratories [34, 35] has indicated that the presence of carbon may exacerbate corrosion, or even lead to alternate mechanisms for corrosion involving sulfidation rather than oxidation. Clearly more work is needed in this area.

The trailing edge poorly sintered 1–10 μm spheres of red/orange ash, very similar in appearance to that found in AMAX POC's, showed hematite and plagioclase feldspar, along with an aluminum-rich spinel. The presence of feldspar, as opposed to feldspathoids in AMAX POC's, is likely a consequence of much lower concentrations of alkali in the former. Feldspars are the thermodynamically favored product, and further alkali chemistry is not expected in limited residence times or at reduced temperatures.

Airfoil deposits had both similarities and differences to deposits on pins. This includes both morphology and chemistry. Turbine simulator deposition rates when run on CWM fuels were found to be about 1/3 of that observed with residual oil equivalent fuel [7]. As described below, the absence of sticky alkali sulfate glues in the deposit may be responsible for this.

Fig. 7 Scanning electron micrograph of leading edge deposit on LM-500 turbine simulator

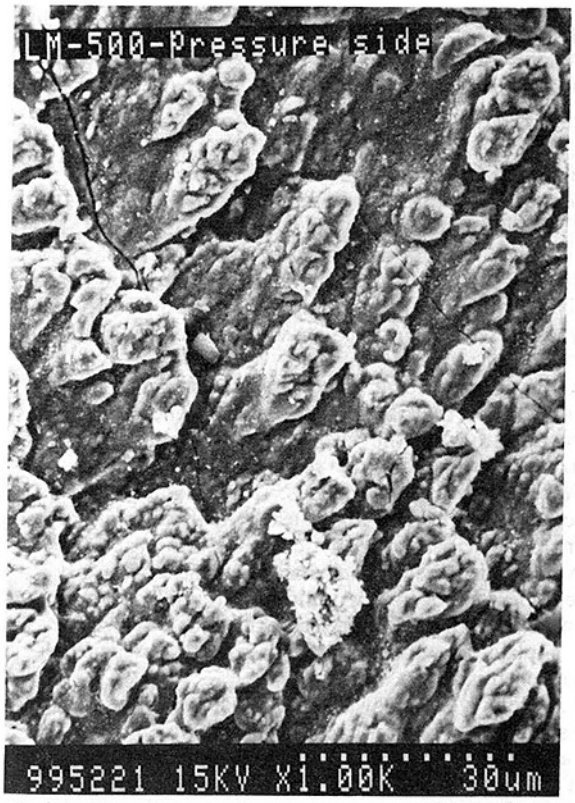

Fig. 8 Scanning electron micrograph of pressure side deposit on LM-500 turbine simulator

Figure 7 is a scanning electon micrograph of the deposit on the leading edge of the stationary cascade. The herringbone pattern consists of small spheres of individually fused, but weakly sintered slag droplets reminiscent of pin deposits from the minirig scaled combustor. A common origin is suspected, in which spherical slag droplets resulted from ash melting, and stuck by inertial impaction to the leading edge. Here final burnout was completed and partial sintering without fusion took place. This is consistent with the observation that the deposits were reasonably easy to mechanically remove both in sampling and nutshelling [7]. The herringbone pattern is associated with the direction of cooling airflow from holes along the leading edge of the vanes. Along the leading edge a combination of plagioclase feldspar, hematite, and spinel was observed.

Figure 8 is a scanning electron micrograph of the pressure side deposit. The morphology suggests a fused underlayer in which a large spherical particle stuck by inertial impaction and was subsequently altered by erosion. The fused layer probably results from less efficient film cooling than on the leading edge where there is a much higher density of cooling holes. It is possible that the pressure side deposits were initially solid, but eventually fused as insulating deposit built up. The large, partly eroded grain in Fig. 8 may well have been present prior to fusion. The pressure side mainly consisted of anhydrite with lesser amounts of hematite, spinel, and glass.

A much more fine-grained deposit appeared on the suction side, apparently formed by thermophoresis, particle diffusion, Brownian motion, and for larger particles, eddy turbulence. The relative importance of these mechanisms is a subject worthy of further study in CWM fired gas turbine combustion. Suction side deposits consisted of hematite, anhydrite, spinel, and plagioclase feldspar.

Conclusions

Based on this limited test matrix of coal–water mixture combustion under gas turbine conditions, no insurmountable technical barriers to commercialization were encountered. Preparation, storage, handling, atomization, and combustion of CWM proceeded smoothly with only minor problems. Due to fine sizes and good atomization, erosion is expected to be limited. Deposits formed at a lower rate than residual oil equivalent fuel, and were removable with difficulty. Deposits may represent a protective scale which will inhibit hot corrosion.

Another significant result of this research was the demonstration that the method of coal beneficiation plays an important role in the entire handling/combustion/deposition/ash thermochemistry sequence when CWM is burned under gas turbine conditions. For example, the AMAX process leaves residual alkali leachant in solution, which appears to participate in catalytic combustion processes. AMAX also neutralizes caustic leachant with acid whose conjugate base appears to occupy anionic sites in a feldspathoid matrix. In addition, the leachant removes most available calcium which plays an otherwise major role in unleached (Otisca) CWM chemistry.

Another key finding was the absence of simple alkali sulfate glues which play a major role in petroleum-fired gas turbines. Alkali sulfates from petroleum fuels are implicated in deposition and hot corrosion. The observed reduced deposition rates compared to resid may be a consequence of the different ash and alkali chemistry of coal, in which aluminosilicate rather than sulfate chemistry dominates.

References

1 *Proceedings of the First Annual Heat Engines Conference Contractors Meeting*, Morgantown, WV, DOE/METC, May 1984.

2 *Proceedings of the Second Annual Heat Engines Conference Contractors Meeting*, Morgantown, WV, DOE/METC-85/6023, May 1985.

3 *Proceedings of the Third Annual Heat Engines Conference Contractors Meeting*, Morgantown, WV, DOE/METC-85/6023, May 1986.

4 Anderson, R. J., Romanski, C. J., and France, J. E., DOE Report DOE/METC-85/2007, Oct. 1984.

5 *Proceedings of High Temperature Corrosion in Energy Systems Symposium*, M. Rothman, ed., Detroit, MI, Sept. 1984, Metallurgical Society of AIME/Materials Science Division.

6 Raask, "Mineral Impurities in Coal Combustion—Behavior, Problems, and Remedial Measure," Hemisphere Publishing, Washington, DC, 1985.

7 Kimura, S. G., Spiro, C. L., and Chen, C. C., "Alkali Species in Coal-Fired Gas Turbines," DE-AC21-85MC22164, Final Report, DOE/MC/22164-2188, 1987.

8 Bryers, R. W., ed., "Corrosion and Deposits Due to Impurities in Combustion Gases," Hemisphere Publishing Co., Washington, DC, 1977.

9 Keller, D. V., Jr., *Fifth Symp. on Coal Slurry for Combustion Tech.*, Tampa, FL, Apr. 1983, U.S. DOE, Pittsburgh, PA, p. 269.

10 Streeter, R., C., "Evaluation of the Effect of Coal Cleaning on Fugitive Elements . . . ," Quarterly Progress Report No. 7, DE-AC22-83PC662690, Apr. 4, 1985.

11 Streeter, R. C., "Evaluation of the Effect of Coal Cleaning on Fugitive Elements . . . ," Monthly Progress Report No. 15, DE-AC22-83PC662690, Apr. 20, 1985.

12 Spiro, C. L., Chen, C. C., Kimura, S. G., Wong, S., and Greegor, R. B., "Characterization of Products From a Direct Coal-Water-Mixture Fired Gas Turbine," *Fuel*, Vol. 66, 1987, pp. 563–567.

13 Bragg, L., Claringbull, G. F., and Taylor, W. H., "Crystal Structures of Minerals," Cornell University Press, Ithaca, NY, p. 254.

14 Bhasin, A. K., Smit, F. J., Anast, K. R., and Doane, R. E., DOE Report DOE/MC/2700-1635, Aug. 1984.

15 Fan, C. W., Markuszewski, R., and Wheelock, T. D., in: "Mineral Matter and Ash in Coal," ACS Symposium 301, K. Vorres, ed., American Chemical Society Press, 1986, p. 462.

16 Richardson, C. K., Markuszewski, R., Durham, K. S., and Bluhm, D. D., in: "Mineral Matter and Ash in Coal," ACS Symposium 301, K. Vorres, ed., American Chemical Society Press, 1983, p. 513.

17 Kimura, S. G., Spiro, C. L., and Chen, C. C., "Combustion and Deposition in Coal-Fired Turbine," ASME JOURNAL OF ENGINEERING FOR GAS TURBINES AND POWER, this isssue.

18 Monroe, L. S., Farmayan, W. F., Srinivasachar, S., Beer, J. M., and Sarofim, A. F., "Slagging and Fouling Due to Impurities in Combustion Gases," *Proceedings of the Engineering Foundation Conference*, Copper Mountain, CO, 1984.

19 *Proceedings of the Conference on Coal Burning Turbines*, Department of Mines and Technical Surveys, McGill University, Ottawa, Nov. 22–23, 1956.

20 Fraas, A. P., "Survery of Turbine Bucket Erosion, Deposits and Corrosion," *Proceedings of the Gas Turbine Division of the ASME Gas Turbine Conference and Products Show*, Houston, TX, Mar. 2–6, 1975.

21 Buckland, B., Carlstrom, L., Junge, R., "Bucket Erosion by Fly Ash," General Electric Report DF-62-GTD -10, July 13, 1962.

22 Spiro, C. L., McKee, D. W., Kosky, P. G., Lamby, E. J., and Maylotte, D. H., "Significant Parameters for the Catalyzed Gasification of Coal Chars," *Fuel*, Vol. 62, 1983, pp. 323–330.

23 Fox, D. A., and White, A. H., *Ind. Eng. Chem.*, Vol. 23, 1931, p. 259.

24 Spiro, C. L., McKee, D. W., Kosky, P. G., and Lamby, E. J., "The Observation of Alkali Catalyst Particles During the Gasification of Carbonaceus Materials in CO_2 and Steam," *Fuel*, Vol. 63, 1984, pp. 686–691.

25 Lang, F. M., Magnier, P., Sella, C., and Trillat, J. J., 1962, *Comptes Rendus*, Vol. 255, 1962, p. 4114.

26 McKee, D. W., and Spiro, C. L., "The Effects of Chlorine Pretreatment on the Reactivity of Graphite," *Carbon*, Vol. 23, 1985, pp. 437–444.

27 McKee, D. W., and Chatterji, C., *Carbon*, Vol. 13, 1975, pp. 381–390.

28 Walker, P. L., Jr., Shelef, M., and Anderson, R. A., *Chemistry and Physics of Carbon*, Vol. 4, Marcel Dekker, 1968, p. 287.

29 Neville, M., McCarthy, J. F., and Sarofim, A. F., *Atmospheric Environment*, Vol. 17, 1983, pp. 2599–2604.

30 Spiro, C. L., Wong, J., Lytle, F. W., Greegor, R. B., Maylotte, D. H., and Lamson, S. H., "Forms of Potassium in Coal and Its Combustion Products," *Fuel*, Vol. 65, 1986, pp. 327–336.

31 Spiro, C. L., Wong, J., Lytle, F., Greegor, R. B., Maylotte, D. H., and Lamson, S. H., "X-Ray Absorption Spectroscopic Investigation of Sulfur Sites in Coal: Organic Sulfur Identification," *Science*, Vol. 226, 1984, pp. 48–50.

32 McKee, D. W., Spiro, C. L., Kosky, P. G., and Lamby, E. J., "The Catalysis of Coal Gasification," *Chemtech*, Vol. 13, 1983, pp. 624–629.

33 Bohor, B. F., *Clays and Clay Minerals*, Vol. 19, 1964, p. 233.

34 McKee, D. W., and Romeo, G., *Metal., Trans.*, Vol. 66A, 1975, p. 101.

35 McKee, D. W., and Romeo, G., "Corrosion Problems in Energy Conversion and Generation," *Electrochem. Soc. Symp.*, 1974, p. 118.

Acoustical Resonance Measurement of Particle Loading in Gas-Solids Flow

A. A. Vetter
Humbug Mountain Research Laboratories,
Duarte, CA 91010

F. E. C. Culick
California Institute of Technology,
Pasadena, CA 91125

The measurement of the frequency of transverse acoustical resonances of a duct can determine the mass loading and size of particles fluidized by a gas phase. A first-order perturbation-iteration acoustical analysis is applied to this two-phase flow measurement, termed the Acoustical Resonance Measurement, in a circular duct. A sample application of pulverized coal fluidized by air in power plant coal piping is examined. The particle loading is determined by measuring the frequency of a single transverse resonance, and the particle size is determined by simultaneously measuring the frequencies of two transverse resonances. The Acoustical Resonance Measurement provides a nonintrusive and real-time measurement of the mass loading and sizing of particles fluidized by a gas phase.

Introduction

Metering dispensed particles fluidized by a gas phase is important in many industrial processes where particles are pneumatically conveyed. There are currently a number of devices which provide information from which the flowrates of particles suspended in a gas can be inferred [1-3]. However, there is not a reliable, nonintrusive, real-time measurement technique for these two-phase flows, particularly for measurements of hot or corrosive gases.

A new technique, termed the Acoustical Resonance Measurement, for determination of the ratio of mass density of solid particles to the mass density of the gas phase by measurement of the frequency of acoustical resonances in a two-phase flow is presented. When particles are added to a gas to form a dispersed two-phase flow, the sound speed in the mixture is lower than the sound speed in the gas phase alone. Acoustical resonances occur in fixed geometries, with the frequencies of the resonances being directly proportional to the sound speed. Determination of the mass loading of pulverized coal in fluidizing air is used as a sample application of the Acoustical Resonance Measurement.

Acoustical Resonance Measurement

There are two fundamental influences of particles on acoustical waves in the two-phase flow: They act to attenuate the waves, and they reduce the speed of sound. The second is a substantial effect which has been measured [4]. The speed of sound propagation through a fluid depends upon the mass density and the elasticity of the fluid. For two-phase flow of solid particles in air, the solid particles mainly affect the sound speed by modifying the mass density of the fluid.

The speed of sound in a pipe could be measured by determining the time for an acoustical wave to traverse the pipe diameter. Because of background noise, that is not a practical method. A better method is to measure the frequency at which the transverse acoustical modes resonate. This method has the advantages of working with a resonance and being conducive to the experimental techniques of signal conditioning by filtering and heterodyne detection.

For a homogeneous, uniform medium, the frequencies of the acoustic modes depend only upon the sound speed and the geometry. A circular pipe exhibits both longitudinal, i.e., along the axial direction, and transverse, i.e., across a cross section, resonances. The solution to the homogeneous wave equation in a uniform medium for the transverse direction involves combinations of Bessel functions in the radial direction and sinusoids in the azimuthal direction [5]. As a consequence of the eigenvalues defining the normal modes being found as zeros of Bessel functions [5, 6], the frequencies of the resonances are not integral multiples of each other. Thus, each of the resonances can be measured independently.

The designation (k, j) for a transverse resonance indicates that the mode has k azimuthal nodal lines and j radial nodal lines. The resonant frequencies of the transverse modes of a circularly cylindrical medium are given by [6]

$$f_{kj} = e_{kj}(a/D) \tag{1}$$

As the particle loading increases, the speed of sound decreases and the frequency of the resonances will decrease proportionally. Given the particle size distribution and values for other physical and thermodynamic parameters of the solid particles and gas, the sound speed in the mixture can be used to calculate the particle loading.

The conditions in each part of the cross section contribute to the determination of the resonant frequencies [7]. To first order, the Acoustical Resonance Measurement determines the average particulate loading for the entire cross section. It is not a line-of-sight or a point measurement.

Contributed by the Power Division for publication in the JOURNAL OF ENGINEERING FOR GAS TURBINES AND POWER. Manuscript received by the Power Division August 1986.

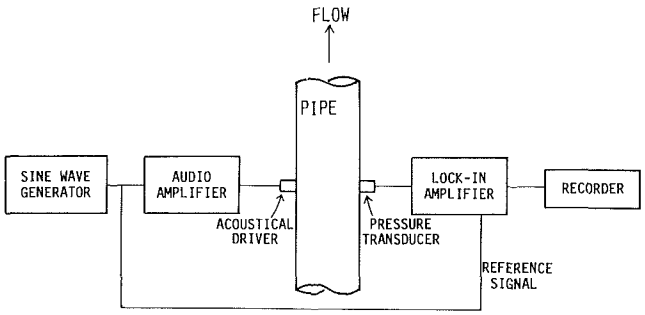

Fig. 1 Schematic diagram of apparatus to determine the coal/air mass density ratio with the acoustical resonance measurement

The acoustical waves disturb the particles so little that the Acoustical Resonance Measurement must be considered a nonintrusive technique. The transmitter and the receiver can be mounted flush to the inside diameter of the pipe so that no probe protrudes into the flow.

The Acoustical Resonance Measurement determines the ratio of mass densities of solid particles to gas phase. To determine the flowrates of each component, an additional independent measurement is required. For applications such as pneumatic transport, a measurement of the flowrate of the fluidized air before particle entrainment would suffice.

An example of the apparatus which can determine the particle loading with the Acoustical Resonance Measurement is schematically represented in Fig. 1. The transmitted signal is obtained from a variable-frequency sine wave generator. This signal is amplified before being fed to an acoustical driver mounted on one wall of the pipe. A pressure transducer is mounted on the pipe wall diagonally opposite the driver. The amplitude and phase of the signal from the pressure transducer are measured with a lock-in amplifier. To measure the particle mass loading, the frequency of the sine wave generator is swept past one of the resonant frequencies. At the resonant condition, the acoustical pressure in the pipe is larger than it is at adjacent frequencies.

Theory

The equations of motion for a two-phase mixture are used as the basis of the present analysis, but are solved in a perturbation-iteration approximation rather than in differential form as chosen by others [8, 9]. Thus, while there are somewhat tighter restrictions on the range of validity (Reynolds number and mass loading), it is considerably easier to treat global problems of waves in chambers.

In particular, the linear results are valid only if the Reynolds number based on relative speed is less than unity. However, it is possible, in a straightforward fashion, to extend the results to higher Reynolds numbers where the drag law is nonlinear [10, 11]. It is also necessary that the mass loading be relatively small, to be rigorous, but the results are likely to be good approximations up to C_m of about 0.4, with errors less than 10 percent. The trends should be qualitatively correct, but errors will increase with larger particle mass loadings.

The particles need not be spherical; deviations may be accommodated in the drag law. Serious quantitative errors may arise if the relaxation time is much greater than the period of the acoustic waves, but corrections will accompany use of a nonlinear drag law. Interactions between the particles are neglected.

The formalism of the acoustical analysis is developed in three steps. Details of the mathematics of these steps can be found in [10, 11]. The specific results for the geometry of the infinitely long circular pipe under consideration here are found in [7].

The conservation equations are first manipulated to produce a nonlinear nonhomogeneous wave equation for the pressure disturbances, with a nonhomogeneous boundary condition. The physical properties of these equations are those for a two-phase mixture. This is a consequence of combining the original conservation equations to give a description of the flow as that for a single average fluid. Nonlinear terms from the gas dynamics are carried to the order of the perturbation Mach number squared.

The second step is based on the expansion of the unsteady pressure and velocity fields in normal modes of the chamber with time-varying amplitudes. After manipulation, nonhomogeneous, second-order, ordinary differential equations are deduced for the time-varying amplitudes of each mode.

In the third step, the method of time averaging [12] is applied to reduce these equations to first order. The solution is then determined as a function of the summation of the contributions from the time varying amplitudes of the modes.

For the limiting case where the particles exactly follow the air movement due to the acoustical waves (called the no-slip condition), the decrease in the sound speed is determined solely by the mass fraction of particles [13] and is independent of particle size

$$a_N^2 = a_0^2/(1+C_m) \tag{2}$$

The particles do not exactly follow the movement of the air in response to acoustical waves, but lag behind, with the larger particles lagging (or slipping) the most. The drag on a particle increases roughly as the cross-sectional area, i.e., as the square of the diameter, while the inertia increases as the mass, i.e., as the cube of the diameter. Hence, as the particle size increases, the inertia force dominates, and the particle responds less to the passing acoustical wave.

The phase shift for a homogeneous, uniform medium is then

$$\theta_n = -\frac{C_m}{2(1+C_m)} \sum_i Y_i \left(\frac{\omega_n W_{d,i}^2}{1+W_{d,i}^2} + (\gamma-1)\frac{C_s}{C_p}\frac{\omega_n W_{t,i}^2}{1+W_{t,i}^2} \right) \tag{3}$$

Nomenclature

a = sound speed
C = heat capacity
C_m = ratio of particle to gas phase mass densities
D = pipe diameter
d = particle diameter
e = eigenvalue
f = resonance frequency
N = Rosin–Rammler dispersion parameter
Pr = Prandtl number
Y = mass fraction
W = dimensionless frequency
γ = gas isentropic exponent = C_p/C_v
θ = phase perturbation
μ = viscosity
ρ = density
ω = angular frequency of acoustic wave

Subscripts

d = momentum
i = counter over particle diameters
N = no-slip condition
n = normal mode
p = constant pressure
s = solid particle property
t = thermal
v = constant volume
0 = zero particle loading

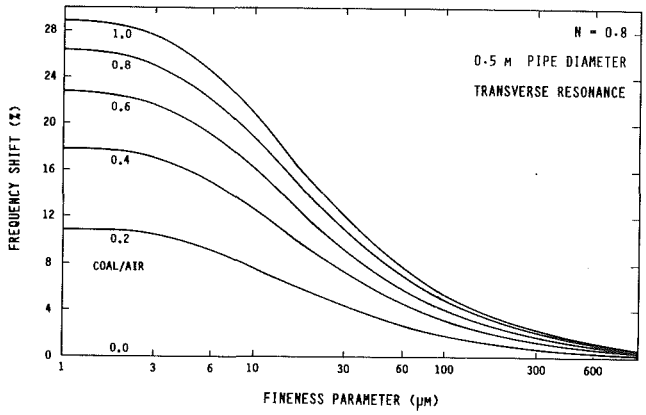

Fig. 2 Frequency shift of the (1, 0) transverse resonance as a function of particle fineness parameter with parametric variation of the coal/air mass density ratio for a 0.5-m-dia pipe and a particle dispersion parameter of 0.8

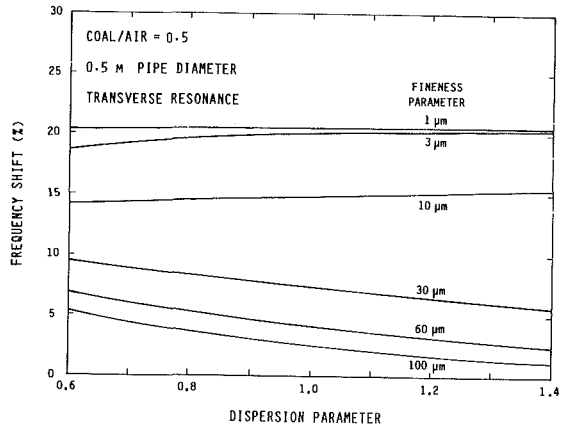

Fig. 4 Frequency shift of the (1, 0) resonance as a function of particle dispersion parameter with range of fineness parameters for a 0.5-m-dia pipe and a coal/air mass density ratio of 0.5

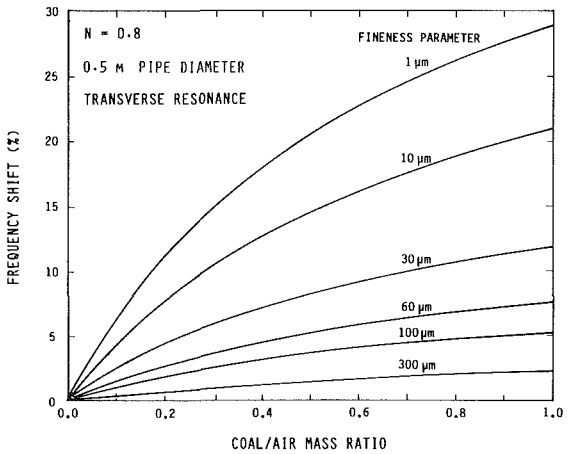

Fig. 3 Frequency shift of the (1, 0) resonance as a function of coal/air mass density ratio with a range of fineness parameters for a 0.5-m-dia pipe and a particle dispersion parameter of 0.8

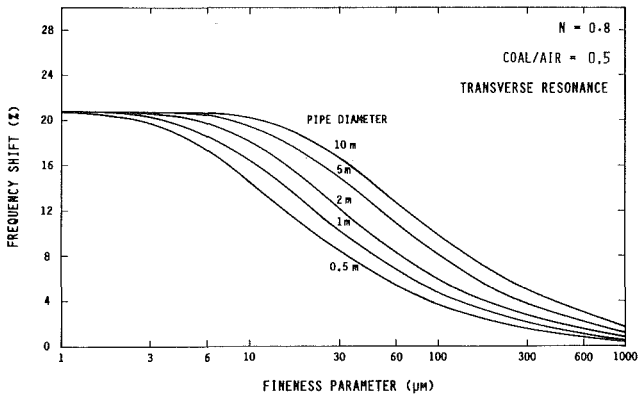

Fig. 5 Frequency shift of the (1, 0) resonance as a function of fineness parameter with a range of pipe diameters for a coal/air mass density ratio of 0.5 and a particle dispersion parameter of 0.8

where the nondimensional frequencies for momentum and thermal exchange are approximated by

$$W_{d,i} = \omega_n (\rho_s d_i^2)/(18\mu)$$

$$W_{t,i} = (3/2)(C_s/C_p)\Pr W_{d,i} \tag{4}$$

Since the sound speed is dependent upon the frequency of the acoustical wave, the resonance frequency for a fixed geometry cannot be determined explicitly. The frequency shifts and sound speeds were determined numerically as functions of the solid/gas mass ratio and the frequency of the propagating wave.

Flow Conditions

The physical conditions which will be used as a sample application are those which are typically found in the coal-conveying piping of a pulverized coal-fired power plant. The fully dispersed regime of interest has high pipe Reynolds number (500,000), low Mach number (0.05), intermediate Froude number (10), near atmospheric pressures, slightly higher than ambient temperatures (340 K), no significant chemical reactions, very fine particles compared to the pipe diameter (ratio of 15,000), and particle mass loadings of the order of, but less than, the fluidizing gas (C_m between 0.2 and 0.8).

The water which is removed from the coal in the pulverizing process enters the air as water vapor. This water vapor changes the molecular weight and the heat capacity of the conveying gas. For the calculations presented here, the absolute humidity in the conveying air was held constant at 4.5 percent.

A two-parameter Rosin–Rammler fit is used for the size distribution of the particles [14, 15]. A dispersion parameter of 0.8, corresponding to pulverized coal downstream of cyclone separators [16, 17], was used. With a dispersion parameter of 0.8, the mass mean particle size is approximately two-thirds the fineness parameter.

Due to irregular shape, a coal particle has a higher drag per mass than would a sphere with the same density and mass. The shape factor for the particles was taken to be 0.75 [18]. The value of specific heat for the dried coal particles used here is an average value of 1.255 kJ/kg [19]. A gas temperature of 335 K was used. The sound speed is independent of pressure in the range found in pneumatic conveying applications.

Results

The resonance frequencies of the lowest order transverse resonance, (1, 0), are shown as a function of Rosin–Rammler fineness parameter with a dispersion parameter of 0.8 for a 0.5-m-dia pipe in Fig. 2. The resonance frequencies are plotted as a function of frequency shift, defined as the difference between the resonance frequency with and without particles divided by resonance frequency without particles $(f_0 - f)/f_0$. The resonance frequency shifts are shown with the particle/gas mass ratio as a parameter. On the right side of Fig. 2, the large particle limit is approached. In this limit, the particles are so large that they can not follow the acoustical wave at the frequency of this resonance; hence, there is no change in

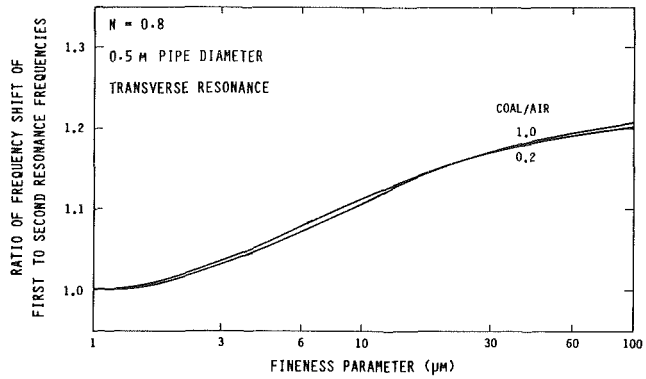

Fig. 6 Ratio of the frequency shift of the (1, 0) resonance to the frequency shift of the (2, 0) resonance as a function of fineness parameter with the coal/air mass density ratio as a parameter for a 0.5-m-dia pipe and a particle dispersion parameter of 0.8

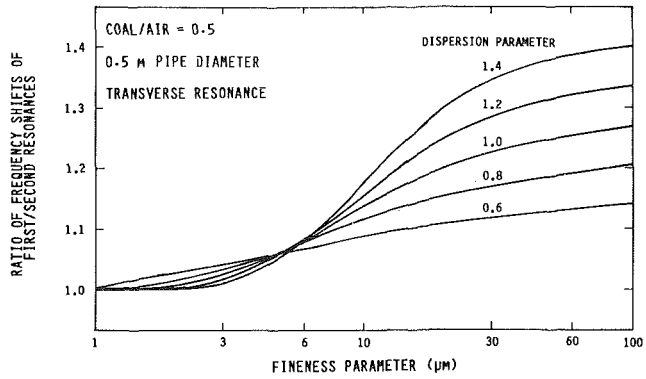

Fig. 7 Ratio of the frequency shift of the (1, 0) resonance to the frequency shift of the (2, 0) resonance as a function of fineness parameter with particle dispersion parameters from 0.6 to 1.4 for a 0.5-m-dia pipe and a coal/air mass density ratio of 0.5

resonance frequency as the coal/air ratio changes. On the left-hand side of Fig. 2, the small particle limit is approached. At this limit, the drag dominates and the no-slip condition is reached where the particles fully follow the acoustical waves.

The frequency shifts are plotted as a function of coal/air mass ratio with parametric variation of fineness parameter in Fig. 3. The clean air limit, i.e., gas phase only, is reached toward the left-hand side of Fig. 3. The bottom curve approaches the large particle limit of no shift. The top curve approaches the small particle limit.

The frequency shift of the lowest order transverse mode is given as a function of dispersion parameter with parametric variations of the fineness parameter for coal/air mass loading of 0.5 in Fig. 4. Higher values of the dispersion parameter indicate less dispersed distributions. As shown by the 1-μm curve in Fig. 4, the small particle limit is independent of the dispersion parameter.

As the pipe diameter increases, the resonance frequency decreases. With no particles in the gas phase, the resonance frequency decreases in proportion to the inverse of the pipe diameter. With particles, the resonance frequency shift is frequency dependent. The effect of increasing pipe diameter, or equivalently decreasing frequency, with a fixed particle distribution can be assessed from Fig. 5. The frequency shift is displayed as a function of fineness parameter for pipe diameters from 0.5 to 10 m at a coal/air mass ratio of 0.5 and a dispersion parameter of 0.8. As the pipe diameter increases, the frequency shift increases until the low frequency limit is reached. This limit is the same no-slip limit applicable to small particles.

The sensitivity of the frequency shift to the particle size is indicated by the slope of the curves in Fig. 5. At the no-slip limit, the slope is horizontal and the frequency shift is independent of particle size. The frequency shift is the most sensitive to the particle size at the point of maximum slope. For the pipe diameters presented in Fig. 5, this occurs for fineness parameters from 20 to 50 μm.

Determination of Particle Size

Since the resonance frequency shift is dependent upon both the frequency of the resonance and the particle size, additional measurements of the shifts of higher order resonances provide information on the particle size. For a given particle size, as the frequency increases, the shift decreases. The ratio of the frequency shift of the (1, 0) resonance to the frequency shift of the (2, 0) resonance is shown as a function of fineness parameter in Fig. 6. These data are for a pipe diameter of 0.5 m and a dispersion parameter of 0.8. The ratio of the two shifts is almost independent of coal/air ratio, with curves for coal/air mass ratio of 0.2 and 1.0 nearly overlapping. Toward the left-hand side of Fig. 6, the no-slip condition is reached for both resonance frequencies, so that the ratio of the shift approaches 1. On the right-hand side, the values of both shifts approach zero, but the ratio approaches a finite value.

The ratio of frequency shifts is plotted as a function of fineness parameter for values of the dispersion parameter from 0.6 to 1.4 in Fig. 7. The ratio of frequency shifts is not independent of the value of the dispersion parameter. However, the dispersion parameter for coal remains nearly constant while the fineness changes [15, 16]. The ratio of the shifts of the first resonance to the shift of the third resonance could provide a means of determining the dispersion parameter.

Conclusions

The propagation of acoustic waves through a gas–solids mixture in a circular pipe has been evaluated with a first-order perturbation-iteration acoustical analysis. This analysis was applied to determine the particulate mass loading of pneumatically conveyed pulverized coal with the Acoustical Resonance Measurement using transverse resonances.

For particles of the order of 1 μm, the shift in the resonance frequency is 29 percent at a coal/air mass ratio of 1.0. Larger particles exhibit a smaller frequency shift. For a particle distribution with a fineness parameter of 30 μm and a dispersion parameter of 0.8 in a 0.5-m-dia pipe, the frequency shift is about 8 percent for a coal/air mass ratio of 0.5.

By measuring the frequency shifts of different resonances, the particle size can be determined. The ratio of shifts of the (1, 0) to the (2, 0) resonances is nearly independent of the coal/air mass ratio.

Acknowledgments

This research was supported by the U.S. Department of Energy Small Business Innovation Research Program.

References

1 Siegel, J. M., "The Measurement of Flow of Hot Dirty Gas," *Proc. 1980 Symposium Instrumentation and Control for Fossil Energy Processes*, Virginia Beach, VA, June 1980; available as Argonne National Laboratory Report ANL-80-62 and Department of Energy Report CONF-800602.

2 Cooper, B. R., et al., "Report to the American Physical Society by the Study Group on Research Planning for Coal Utilization and Synthetic Fuel Production," *Rev. Mod. Phys.*, Vol. 53, No. 4, Part II, Oct. 1981.

3 Carlson, H. M., Frazier, P. M., and Engdahl, R. B., "Meter for Flowing Mixtures of Air and Pulverized Coal," *Trans. ASME*, Vol. 70, 1948, pp. 65–79.

4 Temkin, S., and Dobbins, R. A., "Measurements of Attenuation and Dispersion of Sound by an Aerosol," *Journal of the Acoustical Society of America*, Vol. 40, 1966, pp. 1016–1024.

5 Temkin, S., *Elements of Acoustics*, Wiley, 1981, Chap. 6.

6 Morse, P. M., *Vibration and Sound*, 2nd ed., McGraw-Hill, 1948, Sec. VII.

7 Vetter, A. A., and Culick, F. E. C., "Evaluation of the Acoustical Resonance Measurement of Particle Loading in Two-Phase Flow," U.S. Department of Energy Report DOE/ER/80193-1, Mar. 31, 1985.

8 Epstein, P. M., and Carhart, R. R., "The Absorption of Sound in Suspensions and Emulsions," *Journal of the Acoustical Society of America*, Vol. 25, No. 3, May 1953, pp. 553–565.

9 Temkin, S., and Dobbins, R. A., "Attenuation and Dispersion of Sound by Particulate Relaxation Processes," *Journal of the Acoustical Society of America*, Vol. 40, 1966, pp. 317–324.

10 Culick, F. E. C., "Nonlinear Behavior of Acoustical Waves in Combustion Chamber – I," *Acta Astronautica*, Vol. 3, 1976, pp. 715–734.

11 Culick, F. E. C., "Nonlinear Behavior of Acoustical Waves in Combustion Chamber – II," *Acta Astronautica*, Vol. 3, 1976, pp. 735–757.

12 Bogoliubov, N. N., and Mitropolsky, Yu. A., *Asymptotic Methods in the Theory of Nonlinear Oscillations*, Hindustan Publishing, Delhi, India, 1961.

13 Marble, F. E., "The Dynamics of Dusty Gases," *Annual Review of Fluid Mechanics*, Vol. 2, 1970, pp. 397–446.

14 Field, M. A., et al., *Combustion of Pulverised Coal*, British Coal Utilisation Research Association, 1967, Appendix A.

15 Shotts, R. Q., "Screening," *Coal Preparation*, 3rd ed., American Institute of Mining, Metallurgical, and Petroleum Engineers, 1968, Chap. 8.

16 Vetter, A. A., "Theoretical Calculations for Balancing the Two-Phase Fuel Flows in the Coal Transport Piping of the Coronado Generating Station," Humbug Mountain Research Laboratories, Report HMRL-R-32A:1, Apr. 1982.

17 Vetter, A. A., "Balancing the Pneumatically Conveyed Pulverized Coal Flows of Indian River Station Unit 4," Humbug Mountain Research Laboratories Report HMRL-R-53:1, Mar. 1985.

18 Laitone, J. A., "A Numerical Solution for Gas-Particle Flows at High Reynolds Numbers," ASME Paper No. 81-WA/APM-10, 1981.

19 McCabe, L. C., and Boley, C. C., "Physical Properties of Coals," *Chemistry of Coal Utilization*, Vol. 1, Wiley; Chapman & Hall, 1945.

Performance Deterioration of a Turbofan and a Turbojet Engine Upon Exposure to a Dust Environment

M. G. Dunn

C. Padova

J. E. Moller

Calspan Corporation,
Buffalo, NY 14225

R. M. Adams

Hq. Defense Nuclear Agency,
Alexandria, VA 22310

Results are reported for a measurement program designed to investigate the performance deterioration of a TF33 turbofan and a J57 turbojet engine upon exposure to a dust-laden environment. Engine parameters were measured in order to facilitate the recognition of incipient engine difficulties. In addition, a successful effort was made to operate the engines satisfactorily when they were severely damaged. Two TF33 engines have been operated in the same dust mixture but under different operating conditions and a J57 engine was operated at the same conditions as one of the TF33 engines. The J57 is the core engine of the TF33 with some differences that will be described in the paper. A description of the experimental technique, the operating experiences, photographs of the components taken from the J57 engine in a post-test teardown, and a discussion of the results are presented.

Introduction

Measurement programs designed to ascertain the vulnerability and survivability of gas turbine engines in airborne weapon systems are currently producing operational results which apply to a broad range of combat scenarios. Battlefield situations have been postulated in triservice studies [1, 2]. However, the reported work does not consider the response of the engine to ingestion of dust-laden air. Survivability studies for airborne command aircraft must consider potential engine degradation caused by the ingestion of atmospheric dust in the operational theater. The reality of this engine degradation mechanism has been dramatically emphasized by recent incidents in which gas-turbine-powered air transports have attempted to traverse volcanic ash clouds. Motivated by the disastrous nature of these encounters on engine performance, the measurement program described in this paper was initiated.

Gas turbine engines are routinely tested for the effect of ingestion of solid particles according to the procedures of Military Specification MIL-E-5007D, the commonly known Arizona road-dust test. Within the last several years the material used in the road-dust test was changed from an earthlike material to a crushed quartz material. Encounters with volcanic clouds and clouds of earthlike soils are felt to be much different than the MIL-E-5007D test in material chemical composition, particle size distribution, and cloud concentration [3]. Since the volcanic cloud encounters, many other instances of engine failure as a result of ingesting earth material, sand, or cement dust have come to light.

During the initial portion of this program, it was recognized that several different mechanisms could be active in altering engine performance during or after exposure to the dust-laden environment and that the potential of each should be recognized. Encountering a particle-laden environment of the type of interest here falls into the category of an unanticipated degradation and may be manifested in one or more of the following ways: (*a*) glassification on hot-section components, (*b*) erosion in compressor blading and rotor path, (*c*) partial or total blockage of cooling passages, and (*d*) oil system or bleed air supply contamination. Each of these was experienced in the ash cloud encounters [3–5]. Compressor erosion has been the subject of research conducted by Tabakoff et al. [6–10] for many years and is known to result in the loss of surge margin even if glassification does not occur.

Several of the potential adverse effects of dust-laden air on engine performance have been noted above. The intent of the research described in this paper was to ascertain how the cloud could be recognized if natural light or cloud conditions preclude direct visual observation, what form of damage the engine sustains, which of the engine diagnostics available to the crew provide an indication of engine degradation, and how one manipulates the controls so as to generate significant thrust after the engines have been severely damaged. In this regard, the research performed to date has provided answers that will be described in the paper. The paper describes the experimental apparatus; the preparation and analysis of the dust mixture; test procedures, data analysis, and teardown observations; and a set of conclusions regarding engine operations in a dust-laden environment.

Contributed by the Gas Turbine Division of THE AMERICAN SOCIETY OF MECHANICAL ENGINEERS and presented at the 32nd International Gas Turbine Conference and Exhibit, Anaheim, California, May 31–June 4, 1987. Manuscript received at ASME Headquarters February 10, 1987. Paper No. 87-GT-111.

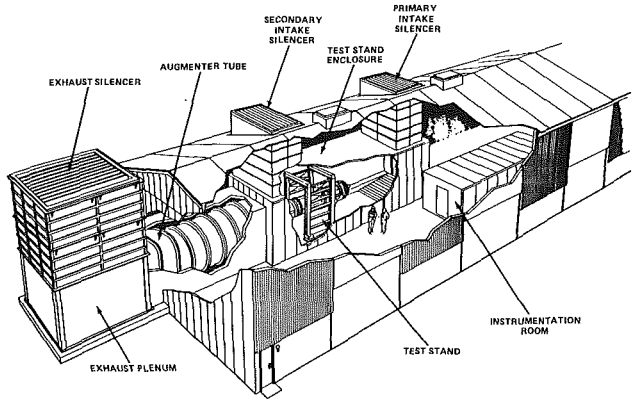

Fig. 1 Large engine research cell

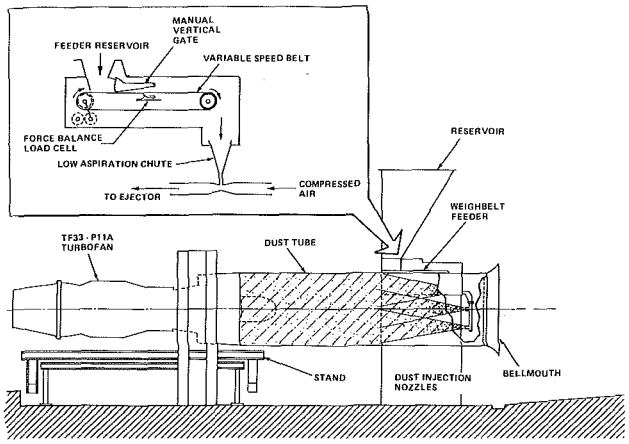

Fig. 2 Schematic of dust injection system

Experimental Apparatus

The research program in the area of propulsion system dust vulnerability and survivability requires a unique facility that allows one to subject operating engines to very adverse environments without endangering either an airplane or a flight crew. This facility can be used to obtain detailed propulsion system tolerance measurements for a full-scale engine under controlled laboratory conditions. The research facility has been built within a larger building, permitting tests unhampered by weather. The test setup includes the engine test stand, operating equipment, and instrumentation. Two major features of the experimental apparatus are a noise suppression system and a dust injection system.

In order to operate large thrust engines in populated areas, it was necessary to provide a noise suppression system. The one used for these measurements is an air-cooled unit (see [13] for more detail) composed of a primary intake silencer, a secondary intake silencer, an engine test stand enclosure, and an exhaust silencer system (consisting of an augmenter tube, an exhaust plenum, and an exhaust silencer). Figure 1 illustrates the complete test setup, including the noise suppression system.

The Dust Injection System (DIS) is the heart of the test apparatus and was built to achieve the objective of the engine measurements: accurate regulation of the dust environment. It was established early in the program that the dust injection system must provide a controlled range of mean particle sizes from 425 to 40 μm and dust concentrations from 30 to 700 mg/m^3, all evenly dispersed in the incoming air. The DIS is schematically shown in Fig. 2. The DIS consists of the dust tube, dust injection nozzles, weigh-belt feeder and dust reservoir, and a bellmouth. The weigh-belt feeder includes process monitoring instrumentation to allow precise control of dust being fed to the test engine. The dust is delivered to the injection nozzles by compressed air. To test both TF33 and J57 engines, the downstream-most section of the dust tube can be changed to match the diameter of the engine.

The 3.65-m (12 ft) long dust pipe provides a conduit to the engine face. The dust pipe contains a cluster of six nozzles through which the dust is introduced at the upstream end. This combination of multiple nozzles and length of dust pipe is used to establish a uniform and equilibrated dust cloud just upstream of the fan face. It is important that the velocity of the dust particles be in equilibrium with the local velocity of the air stream ahead of the engine face in order to correctly simulate the encounter with a stabilized cloud. From this initial state of dispersion, the air and the dust particles are accelerated and turned by the bullet nose to the engine fan similar to what occurs in flight.

The dust is delivered to each of the six nozzles as a high-loading air-particle dispersoid transported by compressed air from a two-stage centrifugal compressor in a MA-1A engine start cart. Both the particulate material and the carrier airflow are carefully metered. The carrier airflow is constant at all feed rates and engine thrust settings. The lines are sized to limit the airflow to 2 percent of inlet air and deliver the particles into the inlet air at a release velocity which is closely matched to the local value. The plenum is maintained at 310 kPa (45 psi) by the compressor and in each line the air weight flow is controlled by a 4.8 mm (3/16-in.) metering orifice. Downstream of the orifices, the air passes through a venturi which is loaded with the dust. The dust is metered by the belt feeder above the venturi and enters the carrier air by the combined action of gravity and moderate aspiration (1- to 15-in. water range) from the venturi. The latter is provided to capture the fine particles that tend to recirculate in the chute of the feeder. The actual configuration of the pneumatic lines of the DIS was carefully laid out so that adverse effects on the dust particle characteristics due to rough mechanical handling were minimized. A gravimetric weigh-belt feeder was selected for the DIS because of its ability to provide continuous, accurate feeding of dry materials over the broad range from 45 g/min to 10 kg/min (0.1 to 22 lb/min). The feeder employs the variable-speed belt operating principle.

The TF33 is the turbofan derivative of the J57 turbojet. Therefore, the J57 flow path and compressor and turbine construction were similar to those of the TF33. The particular TF33 used for the measurements described here was a P11A model which used titanium for the LP and HP compressor blade construction. However, the J57 HP compressor blades (P19W model used here) are constructed of steel. There was a lot of speculation, but few data [12], suggesting that steel blades would wear much better than titanium. Thus, the J57-P19W became an ideal engine with which to answer several important questions regarding erosion.

Dust Preparation and Analysis

The two turbofan engines and the one turbojet engine were all operated in air laden with particulate material from a mixture of two types of soils (Hollywood sand and Corona clay), volcanic ash from a Mt. St. Helens eruption, and small amounts of a clayey additive (Wyoming bentonite). The sand soil is decomposed granite that was obtained from the northwestern Santa Monica Mountains (Hollywood Hills area). The clay soil is weathered material from surrounding rock outcrop units and was obtained from the high ground of the Ternescal Canyon area near Corona, CA. These soils were found by separate DNA studies to be representative of the dust environments of interest. The volcanic ash provides a point of possible comparison with the aircraft ash cloud en-

Table 1 Blending proportions of the four materials composing the input dust

Hollywood Sand	
Premix Recipe:	14.82%of < 106 μm size bin 35.98% of < 180 μm size bin 49.20% of 106-250 μm size bin 100.0
Mt. St. Helens Ash	
Premix Recipe:	32.84% of < 106 μm size bin 67.16% of 106-180 μm size bin 100.0
Corona Clay	
Premix Recipe:	74.53% of < 106 μm size bin 25.47% of 106-250 μm size bin 100.0
Bentonite	
As available	100% of < 106 μm size bin
Mixing Recipe of Premixed Materials Above:	
1/3 H. sand + 1/3 Ash + $\frac{2.5}{9}$ C. Clay + $\frac{0.5}{9}$ Bentonite	

counters, and lends a glassy material content to the mixture. The particle size distribution of each constituent was precisely controlled by pulverizing the raw clay, sand, and ash and grading each material in four size bins. Drying of the Corona clay and Hollywood sand soils was also required. The final moisture contents were 5.1 and 2 percent, respectively, for Corona clay and Hollywood sand. From the graded materials the dust blend was prepared by mixing one part ash, one part sandy soil, and one part clay soil plus bentonite, each portion containing particle sizes below 250 μm as shown in Table 1.

For ingestion by the engine, the dust must be uniformly dispersed in air. The important physical properties of dust particles in air are size, shape, and weight. The individual constituents were evaluated for these properties. Scanning electron microscope (SEM) micrographs, composition spectra, and particle size distribution plots of the dust blend used for these measurements are presented in Figs. 3–5. The SEM micrographs of Fig. 3 indicate that the processing of the base soils did not alter significantly the particle shape and surface texture characteristics or the amount of natural fines in the dust. In the elemental composition spectrum of Fig. 3 it is particularly important to note the absence of titanium. Titanium alloy is used extensively in the compressor of the TF33 engine. Metal removal upon particle impact was expected to result in the detection of elemental Ti in samples of the dust which have passed through the compressor and were collected in the ECS bleed air.

Figure 4 presents particle size distribution data which were obtained with three different measurement techniques. Dry size analysis data were obtained by using U.S. Standard sieves and a sieve shaker, and by using the Alpine Air Jet Sieve ® separator. Dry size analysis data can only be obtained for particle sizes larger than 38 μm. Wet size analysis data were obtained with the L&N Microtrac™ equipment. The Microtrac™ data could only be obtained for particle sizes smaller than 176 μm and larger than 1.9 μm. There is little difference between the results which were obtained with the two dry sieve analysis techniques. Accordingly, a single solid line was faired through the data in Fig. 5 to represent the particle size distribution

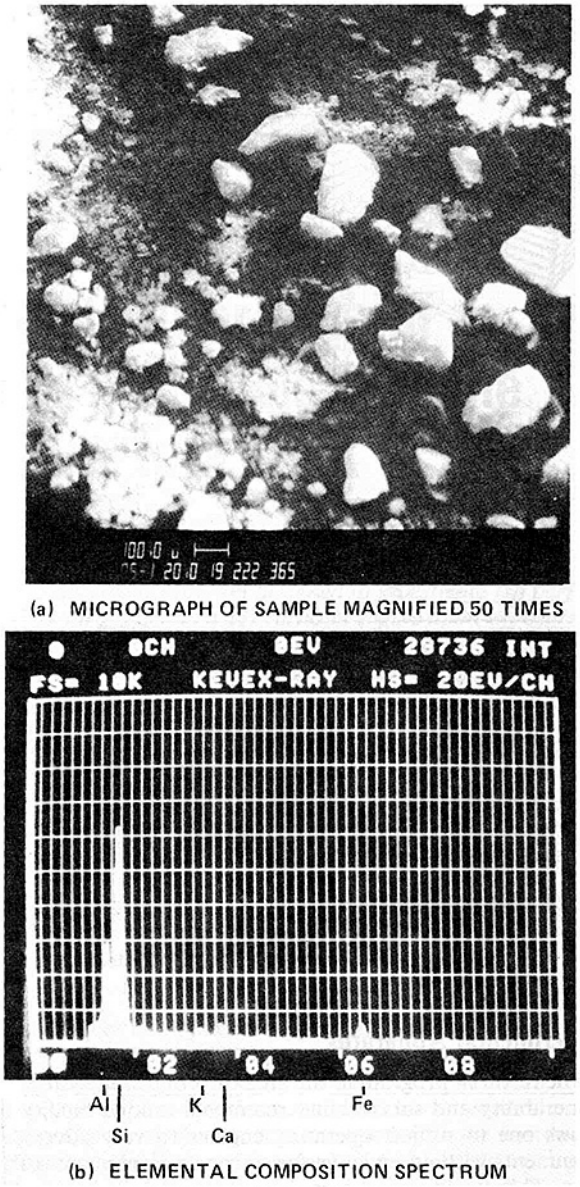

Fig. 3 Scanning electron micrograph and composition spectrum of dust blend

(PSD) from dry sieve analysis. An average mean particle diameter of 58 μm is indicated from this PSD. For reference, the PSDs of three commonly used dust mixtures are indicated in Fig. 5 by dot-dash lines and appropriate labels.

Test Procedures, Data Analysis, and Teardown Observations

Test Procedures. During the course of this measurement program, two TF33 turbofan engines and one J57 turbojet were subjected to a dust-laden environment. The dust composition and particle size distribution were the same for all engines, but the dust concentration and the engine thrust settings were different. The first TF33 engine was exposed to dust concentrations of 120 mg/m^3 at a cruise thrust setting for several different exposure times. The second TF33 engine was exposed to substantially greater dust concentrations, in the range of 120 mg/m^3 to 480 mg/m^3, at engine thrust settings of either military rated thrust (MRT) or cruise thrust for several different exposure times. The J57 engine was exposed to conditions equivalent to the second TF33. The total dust loading

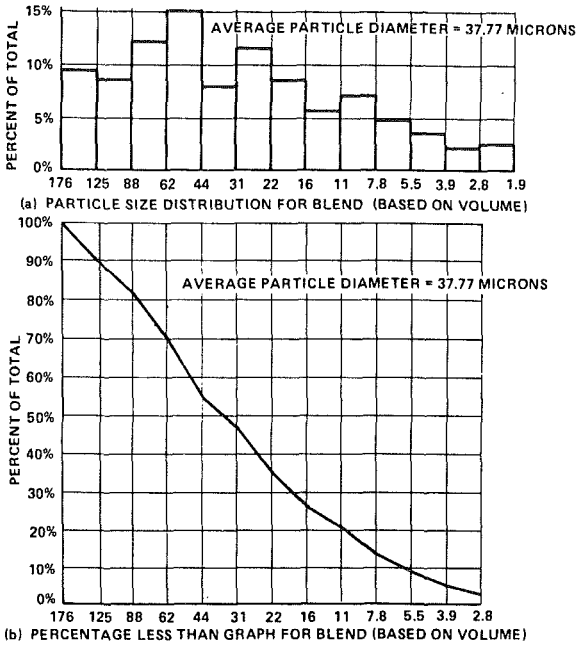

Fig. 4 Wet particle size analysis results

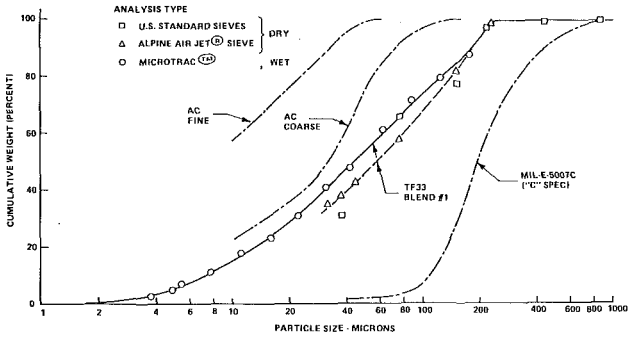

Fig. 5 Particle size distribution for dust specimens

Table 2 Conditions at which engines were operated

First TF33 Turbofan

Run (#)	Actual Load (Kg)	Conc. (mg/m^3)	Exposure Time		Power	TIT °C	EGT °C
			This runs, hrs	Cum., hrs			
46	40	120	1.45	1.45	descent	600	299
47	40	120	0.73	2.18	cruise	672	336
48	80	120	1.35	3.53	cruise	680	341
49	140	120	2.28	5.82	cruise	680	341
50	183	120	2.97	8.78	cruise	680	341
51	189	120	3.08	11.87	cruise	680	341
Total = 672				11.87			

Second TF33 Turbofan

Run (#)	Actual Load (Kg)	Conc. (mg/m^3)	Exposure Time		Power	TIT °C	EGT °C
			This run, hrs	Cum., hrs.			
61	26	120	0.38	0.38	MRT	918	477
62	34	240	0.25	0.63	MRT	875	463
63	33	480	0.125	0.76	MRT	873	461
64	80	240	0.75	1.51	cruise	679	340
65	140	240	1.40	2.91	cruise	677	338
66	200	480	1.0	3.91	cruise	682	343
70	27	120	0.52	4.43	crusie	715	363
71	26	--	0.30	4.73	idle	530	265
Total = 566				4.73			

J57 Turbojet

Run (#)	Actual Load (Kg)	Conc. (mg/m^3)	Exposure		Thrust Setting	TIT °C	EGT °C
			This Run, hrs.	Cum., hrs.			
80	9.3	120	0.38	0.38	MRT	892	577
81	12.1	240	0.25	0.63	MRT	895	579
82	11.8	480	0.125	0.76	MRT	881	569
83	32.3	240	0.75	1.51	cruise	739	466
84	60.5	240	1.40	2.91	cruise	743	468
85	86.2	480	1.00	3.9	cruise	739	466
86	2.4	240	0.05	3.9	cruise	743	468
87	45.5	480	0.50	4.4	cruise	743	468
89	7.7	240	0.175	4.59	cruise	743	468
91	15.9	970	0.083	4.67	MRT	880	568
92	62.7	970/1385	0.283	4.95	MRT/cruise	880/743	568/468
Total = 346.4				4.95			

for the J57 was different than the TF33 at the same matrix point because the air weight flow is significantly different. The TF33 is a 1.1:1 bypass ratio turbofan. At takeoff rated thrust, the TF33 consumes 460 lb/s of air compared to 185 lb/s for the J57. Thus the J57 measurements were made by equating total loading instead of exposure times. The test conditions for each engine are listed in Table 2.

The general experimental procedure was to bring the engine to the exhaust gas temperature (EGT) set point, allow it to stabilize thermally, perform 6 s accelerations and decelerations, obtain a set of baseline readings at the EGT set point, and then initiate dust injection into the airstream. For the duration of the measurement, the engine pressure ratio (EPR) corresponding to the initial EGT set point was maintained. For an engine that is undergoing deterioration, this means that power level angle (PLA) adjustments may be necessary during the experiment. At the completion of each data point, the hot section was borescoped to look for glassified deposits in the combustor or the turbine, and the compressor and the fan were borescoped to look for tip or flow path erosion. The borescope was equipped with a camera so that photographs of the components could be obtained.

In all the test runs, immediately upon initiation of the dust, a striking glow was observed at the fan face for the TF33 and at the compressor face for the J57. The glow is a well-known phenomenon called St. Elmo's glow or fire that results from a buildup of electrostatic charge on the dust particles and on the moving metallic surfaces. St. Elmo's glow was observed by the British Airways crew during their encounter with the Galunggung volcanic cloud [4]. During the course of the measurement program, the glow was photographed and typical pictures are given in Figs. 6 and 7. Figure 6 is a wide angle photograph of the dust tube, the dust injection nozzles, and the fan face glow. Figure 7 is a close-up photograph of the fan face. The first fan stage rotor fence and the first stage inlet guide vane are not obscured by the glow because the momentum exchange between these surfaces and the dust particles is too low to cause charge accumulation. The second stage inlet guide vane appears as a shadow in the illumination field of the first and second rotors. Three silhouettes appearing on Fig. 7 are the result of the dust injection nozzles. The location of these nozzles can be more clearly seen on Fig. 6. A very bright ring of light appears at the first and second rotor tip/shroud regions. The illumination in this region may be brighter for several reasons, e.g., (*a*) higher dust particle concentrations due to centrifuging, (*b*) greater optical depth and unobstructed view of the illumination, and (*c*) scintillation at the rotor tip. Also visible in this photograph is the bullet nose and a total pressure probe.

After the engines had been operated at conditions described in Table 2, they all began to surge violently and upon further exposure could not be accelerated beyond the idle thrust condition. At this point in time, the first TF33 and the J57 were disassembled for inspection.

Data Analysis. For the purposes of this paper, attention

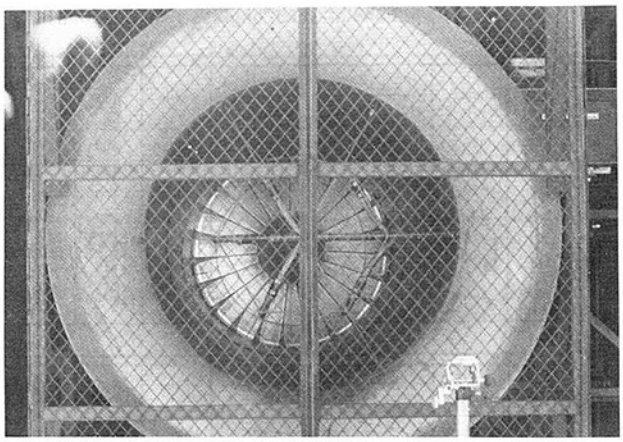

Fig. 6 Photograph of St. Elmo's glow at fan face

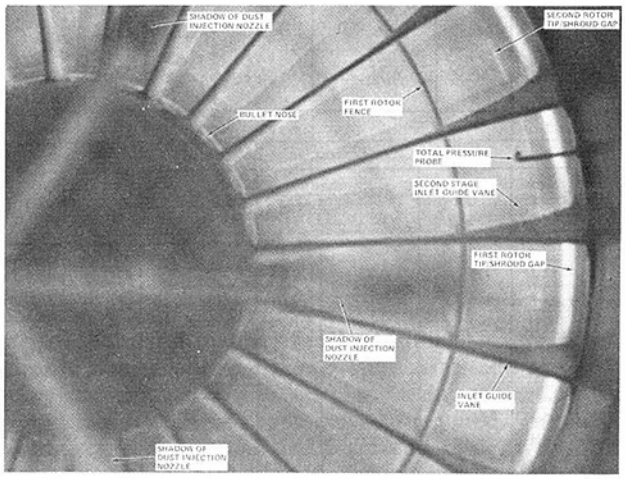

Fig. 7 Close-up photograph of St. Elmo's glow at fan face

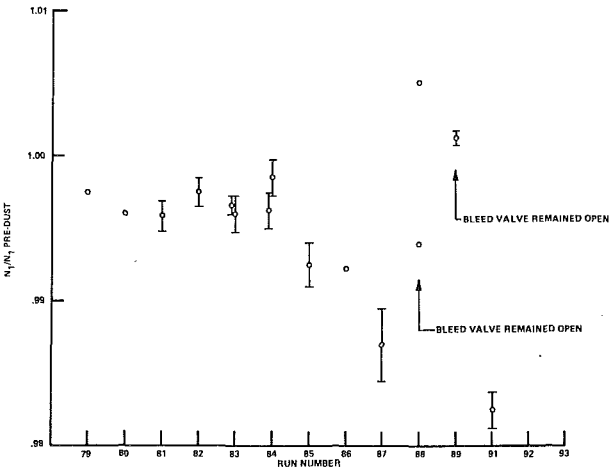

Fig. 8 Ratio of J57 LP compressor speed to corresponding value prior to dust ingestion

will be confined to the analytic results and teardown of the J57 engine. A much more detailed discussion of both TF33 engines is given in [11] and a much more detailed description of the J57 measurements is given in [13]. Comparison of the second TF33 and the J57 test points given in Table 2 illustrates that Runs #80 to #85 are identical to Runs #61 to #66; Run #87 is the same time duration as Run #70 but at four times the dust concentration. For the J57, additional tests were made. Runs #81, #91, and #92 were added because it was still possible to generate significant thrust with the engine by carefully controlling bleed valves in an unconventional manner as described in [14]. After returning the power lever angle to idle at the completion of Run #92, the engine could not be accelerated through violent surges. It was at this point that the J57 engine was removed from the cell and torn down for inspection. While both a TF33 and the J57 were torn down, the component wear was very similar for the two engines. Thus, attention will be directed to the J57 analytic results and teardown.

During the course of the measurements, it became obvious that several of the measured engine parameters provided indications of performance deterioration long before the initial tailpipe surge was experienced. The specific parameters that will be summarized here are: (*a*) the low-pressure compressor speed N_1, (*b*) the high-pressure compressor speed N_2, (*c*) the air flow rate W_a, and (*d*) the EGT. Each of these parameters was normalized by the corresponding value obtained prior to exposing the engine to the dust environment.

Figure 8 is plot of the actual N_1 divided by the nondeteriorated engine N_1 (predust exposure) at the same EPR value as a function of run number. A post-teardown inspection of the LP compressor indicated that the component did sustain some significant damage suggesting that the LP performance map did change, but it is difficult to know to what extent. Assuming that the LP performance map did not sustain a major change, then a decreasing speed suggests a decreasing air weight flow. A 1 percent decrease in N_1 corresponds to a decrease in air flow rate of approximately 2 lb/s. The result shown on Fig. 8 indicates that, for Runs #79 to #84, the measured LP compressor spool speed ratio was about 0.998 of the predust exposure value. Runs #80, #81, and #82 were performed at MRT setting. Runs #83 to #89 were performed at cruise thrust setting, and #91 and #92 were back to MRT. During Run #84, a lower than anticipated N_1 for the same EPR value was the initial indication of an incipient problem, well before the initial engine surge was detected. Note that the ratio continues to decrease with increased exposure time until Run #88 at which time the ratio trend reversed. However, this reversal is felt to be the result of the bleed valve remaining open well after it should have closed. Two data points are shown for Run #88, the one at 1.04 for which the valve was fully open and the one at 0.993 for which it was close to being, but not completely, closed. On Run #89, we again experienced difficulty with the bleed valve failing to close on the prescribed schedule and the readings were taken with the valve open. For Run #91, the bleed valve operated properly and the data are in line with the decreasing N_1 trend.

Figure 9 is a corresponding plot for the HP compressor spool. The post-test teardown inspection confirmed that the HP compressor had sustained extensive erosion damage during completion of the test matrix. During the initial run, the HP speed indicated that the dust was having an influence. Between Run #82 and #83, we changed from operating at MRT to operating at cruise and the N_2 ratio briefly returned to nearly 1.0. However, with increased dust exposure time, the speed ratio began to climb toward 1.02. Again, note that when the bleed valve fails to close on schedule, as it did for Runs #88 and #89, the impact on the speed ratio is significant. The HP spool speed is an input to the fuel flow controller making it difficult to ascertain whether the result described in Fig. 9 is due to a shift in the compressor operating map or due to a response of the controller. Certainly the behavior is atypical for a normal compression system, decreasing air flow rate and increasing spool speed, which on the steady-state operating line would be considered to be contrary to normal compressor behavior.

Figure 10 presents the ratio of air weight flow rate with ingestion to the corresponding value at the same EPR reading but prior to ingestion. The trend is consistent with that il-

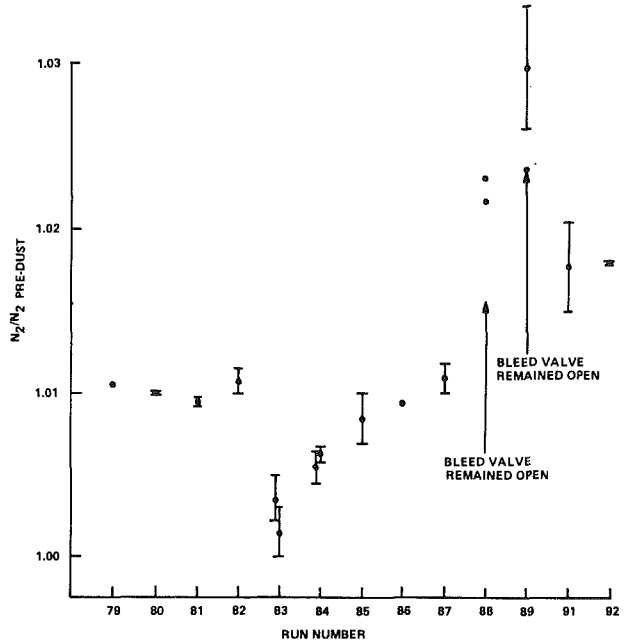

Fig. 9 Ratio of J57 HP compressor speed to corresponding value prior to dust ingestion

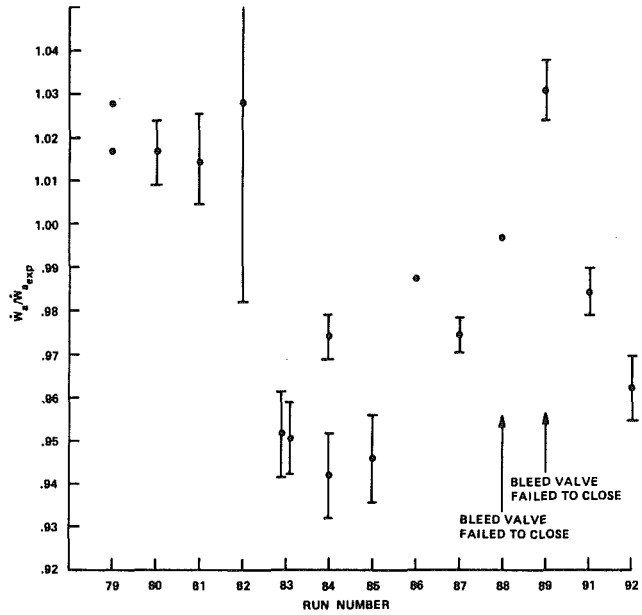

Fig. 10 Ratio of J57 air weight flow rate to corresponding value prior to dust ingestion

lustrated by the LP and HP spool speed results in that the air weight flow rate through the machine is decreasing with increasing compressor erosion. The effect is particularly noticeable after completion of the third MRT run, Run #82. Run #83 was at cruise thrust, but post-Run #82 borescope photographs of the 16th stage compressor blades indicated that the compressor had undergone significant erosion damage. The results for Runs #88 and #89 are out of line with the data from Runs #83 to #87 because the bleed-valve schedule was fouled as a result of LP and HP damage. The final two runs were MRT and the bleed valve finally closed, but not until the N_2 speed was well above the normal valve closing value.

Teardown Observations. The teardown procedure is to place the engine in a vertical position and progress from the tail cone toward the inlet guide vanes. Figure 11 is a photograph of the first stage LP guide vanes. A yellowish-orange discoloration was noted on this vane as shown on the photograph. However, the interesting aspect of this photograph is the obvious erosion of the trailing edges of three or four vanes directly in line with the combustor cans.

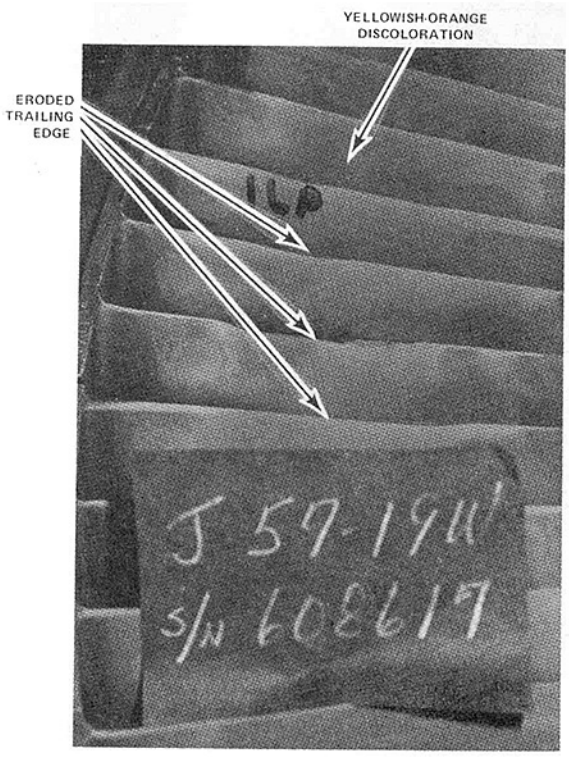

Fig. 11 Phtograph of J57 first-stage LP turbine vane row

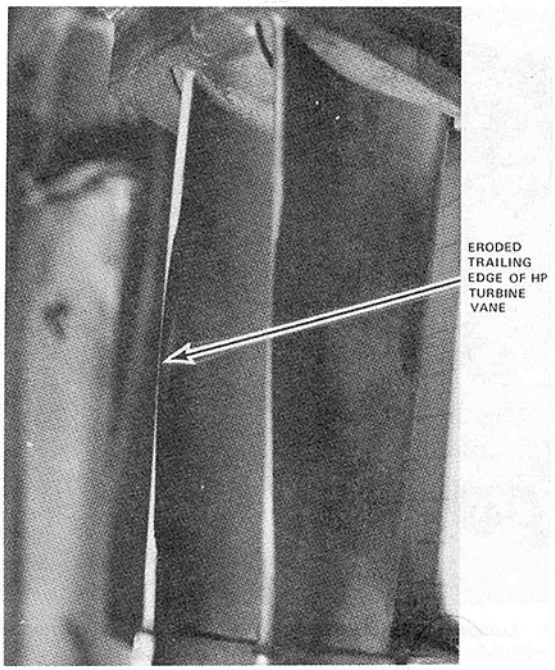

Fig. 12 Photograph of J57 HP turbine vane trailing-edge erosion

Figure 12 is a photograph of the HP turbine vane. Severe erosion was observed in the midspan trailing edge portion of the vanes that were directly in line with the combustor cans as illustrated by the photograph of Fig. 12. The erosion pattern

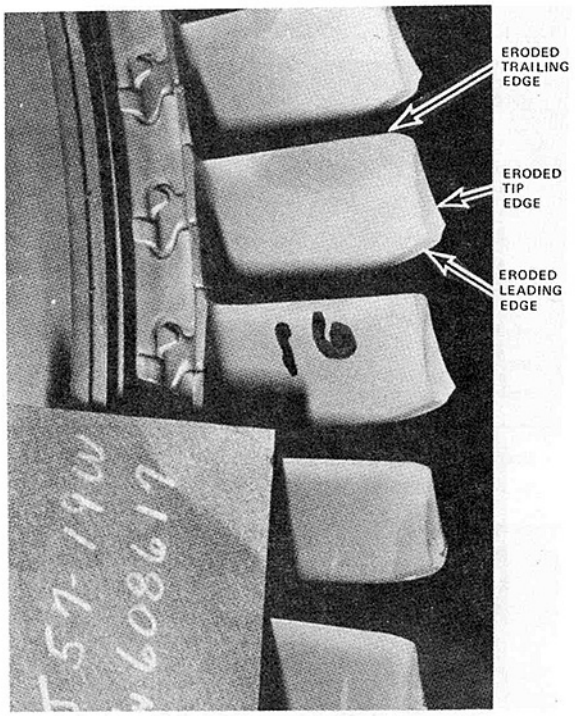

Fig. 13 J57 16 stage HP compressor blade

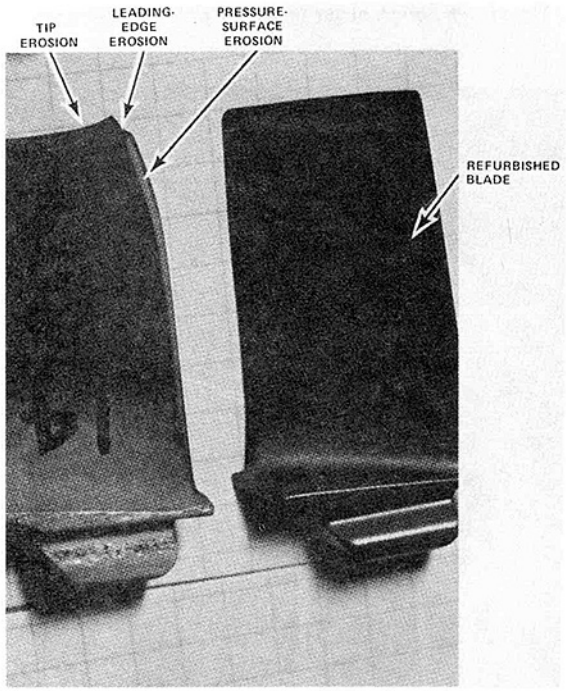

Fig. 14 Comparison of disassembled J57 14th stage HP compressor blade with refurbished blade

suggests a concentrated dust pattern in the combustor exit flow near the two-thirds span location. The vane erosion will result in an adverse influence on the blade incidence angle. However, in the absence of detailed turbine performance measurements, it is difficult to ascertain the importance of the vane erosion on overall engine performance.

The 16th stage blade pressure surface shown in Fig. 13 illustrates the severe leading-edge erosion and tip wear. What cannot be seen from the photograph is that the leading and trailing edges were polished razor sharp from about midspan out to the tip. The cusp formed on the tip was also razor sharp as was the remainder of the tip. The same type of sharp edge

STAGE	ACCEPTABLE CLEARANCE, in.	MEASURED CLEARANCE	
		AT LEADING EDGE CUSP, in.	AT TRAILING EDGE, in.
1	0.005 TO 0.093	0.069	0.090
2		0.049	0.100
3		0.090	0.164
4		0.150	0.150
5		0.054	> 0.054
6		0.027	0.050
7		0.020	0.090
8		0.033	0.090
9		0.044	> 0.044
10	0.025 TO 0.103	NOT AVAILABLE	NOT AVAILABLE
11		0.090	0.180
12		0.085	0.240
13		0.095	0.280
14		0.120	0.240
15		0.110	0.130
16		0.100	>> 0.100

Fig. 15 Measured tip/casing clearances for J57 LP and HP compressor after dust exposure

described above was found on the blades of the other HP compressor stages. The suction surface experienced polishing accompanied by light to moderate abrasion, but without significant material removal. Significant polishing from about midspan to the tip was evident. Upon closer inspection, one finds that little material has been removed from the suction surface and the leading-edge and tip regions are sharp due to pressure surface material removal.

Figure 14 is a pressure surface view of a 14th stage blade which provides a comparison between the disassembled blade and a reworked blade taken from supply. Evidence of significant profile change can be seen in the leading edge outer spanwise and tip regions. In addition, some erosion of the pressure surface material near the leading edge can also be seen. Severe erosion is again evident on these blades, but for this particular stage, the erosion extended over most of the blade span and for a significant portion of the chord. The blade profile has undergone considerable modification as a result of dust erosion.

Figure 15 is a summary of the J57 LP and HP blade tip/compressor casing clearances measured during disassembly at two blade chord positions: (*a*) at the leading edge or cusp, and (*b*) at the trailing edge. Also included on the figure are the acceptable tip/casing values which are 0.005 to 0.093 in. for the LP and 0.025 to 0.103 in. for the HP stages. As has been illustrated by the photographs presented in this paper, the most severe tip-region material removal occurred near the trailing edge of the blade. For some stages of the HP compressor, the tip clearance was on the order of 7 mm (0.280 in.), which exceeded the specifications by a factor of about three. The tip/casing clearances throughout the entire HP compressor were unacceptable and those for the LP were marginal at best.

When the engines were run in their deteriorated states, they were typically capable of operating from idle to slightly above idle and would sometimes operate at points well above idle after carefully coaxing the machine through a zone of hard surges (these surges occur at a frequency in the 1 to 2 Hz range). Up to a point, the anti-ice system and the bleed valve override switch can be used to avoid these surges, even in a badly deteriorated engine. This agrees with typical HP compressor maps; surge margin is largest at very low speeds, then quickly reaches a minimum at higher speeds and then increases somewhat beyond that. The technique developed for performing this task is described in detail in [14].

Conclusions

As a result of information obtained from the measurements performed on two TF33 turbofan engines and one J57 engine, the following conclusions can be drawn:

1 The presence of St. Elmo's glow at the engine face is indicative of dust material in the environment. Upon continued

exposure, EPR (or P_{T7}), EGT, and fuel flow rates will begin to deteriorate. The engine operation time in the dust-laden environment is limited and the engine parameters noted above should be carefully monitored.

2 In the presence of a dust cloud, a decreasing EPR is indicative of loss in compressor efficiency and suggestive of compressor wear. To maintain EPR, the PLA will have to be advanced with associated increases in EGT and fuel flow rate readings. At high altitude, an engine in this state is susceptible to surge and flame out. It may be possible to restart the engine at lower altitudes, but care must be taken whenever advancing the PLA.

3 Prolonged operation in the dust-laden environment will result in permanent engine damage with associated surging and the possible inability to generate adequate thrust.

4 Glassification did not occur in either the TF33 or the J57 hot section when operated at the highest turbine inlet temperature because the TIT was too low to cause significant melting of the material.

5 Glassification did not occur in the J57 at the same MRT setting when the dust concentration was increased from 480 mg/m^3 to a value in excess of 1000 mg/m^3.

6 Steel compressor blades do not wear significantly better than titanium blades when exposed to the same environment.

Acknowledgments

The research reported in this paper was sponsored by the Defense Nuclear Agency under Contract DNA 001-83-C-0182.

References

1 Thorndson, L. W., "Combat Survivability With Advanced Aircraft Propulsion Development," AIAA/SAE/ASME 17th Joint Propulsion Conference, Colorado Springs, CO, July 27–29, 1981, Paper No. AIAA-81-1506.

2 Sullivan, J. D., Thompson, W. S., and Kingery, C. N., "Detonation of a Fuel-Air Cloud by J-52 Turbojet Ingestion," Army Armament Research and Development Command, ARBRL-MR-03304, Aug. 1983.

3 Mitchell, H. J., and Gilmore, F. R., "Dust-Cloud Effects on Aircraft Engines – Emerging Issues and New Damage Mechanisms," RDA-TR-120012-001, Mar. 1982.

4 Chambers, J. C., "The 1982 Encounter of British Airways 747 With the Mt. Galunggung Eruption Cloud," AIAA 23rd Aerospace Sciences Meeting, Reno, NV, Jan. 14–17, 1985, AIAA Paper No. 85-0097.

5 Smith, W. S., "International Efforts to Avoid Volcanic Ash Clouds," AIAA 23rd Aerospace Sciences Meeting, Reno, NV, Jan. 14–17, 1985, AIAA Paper No. 85-0101.

6 Tabakoff, W., and Hussein, M. F., "Effects of Suspended Solid Particles on the Properties in Cascade Flow," *AIAA Journal*, Aug. 1971, pp. 1514–1519.

7 Tabakoff, W., and Hussein, M. F., "Pressure Distribution on Blades in Cascade Nozzle for Particulate Flow," *Journal of Aircraft*, Sept. 1971, pp. 736–738.

8 Hussein, M. F., and Tabakoff, W., "Dynamic Behavior of Solid Particles Suspended by Polluted Flow in a Turbine Stage," *Journal of Aircraft*, July 1973, pp. 434–440.

9 Grant, G., and Tabakoff, W., "Erosion Prediction of Turbomachinery Resulting From Environmental Solid Particles," *Journal of Aircraft*, May 1975, pp. 471–478.

10 Tabakoff, W., and Bahan, C., "Effects of Solid Particles Suspended in Fluid Flow Through an Axial Flow Compressor Stage," presented at the 5th International Symposium on Airbreathing Engines, Bangladore, India, Feb. 16–21, 1981.

11 Dunn, M. G., Padova, C., and Moller, J. C., "Performance Deterioration of an Operational TF-33 Turbofan Engine Upon Exposure to a Simulated Nuclear Dust Environment," DNA-TR-86-62-V1, Jan. 1986.

12 Tabakoff, W., Malak, M. F., and Hamed, A., "Laser Measurements of Solid Particles Rebound Parameters Impacting on 2024 Aluminum and 6A1-4V Titanium Alloys," AIAA 18th Fluid Dynamics and Plasmadynamics and Laser Conference, Cincinnati, OH, July 16–18, 1985, Paper No. AIAA-85-1570.

13 Dunn, M. G., Padova, C., and Moller, J. C., "Performance Deterioration of Turbojet Engine Upon Exposure to a Dust Environment," DNA-TR-86-62-V2, July 1986.

14 Batcho, P. F., Moller, J. C., Padova, C., and Dunn, M. G., "Interpretation of Gas Turbine Response Due to Dust Ingestion," ASME JOURNAL OF ENGINEERING FOR GAS TURBINES AND POWER, this issue.

Interpretation of Gas Turbine Response Due to Dust Ingestion

P. F. Batcho
J. C. Moller
C. Padova
M. G. Dunn
Calspan Corporation,
Buffalo, NY 14225

A measurement program currently underway at Arvin/Calspan Advanced Technology Center has been used in the evaluation of observed engine behavior during dust ingestion. The Pratt and Whitney TF33 turbofan and J57 turbojet were used in the investigation. Solid particle ingestion was found to erode the compressor blades and result in substantial performance deterioration. The engines were found to have increased susceptibility to surge at low power settings. The roles that anti-ice and intercompressor bleed air play in surge avoidance are discussed. A discussion of the fuel controller behavior in a deteriorated engine and its effect during steady-state engine operation is also presented. Experimental data obtained during testing were compared to a predictive capability developed to describe deteriorated engine response. The effects of tip clearance, blade profile, and secondary flows were taken into account. The results show good agreement with experimentally observed engine behavior.

1 Introduction

Potential engine damage caused by the ingestion of dust-laden air is a serious consideration for the operation of gas turbine engines in nuclear or volcanic dust clouds. The reality of this issue has been dramatically emphasized by recent [1, 2] incidents in which gas-turbine-powered air transports have attempted to traverse volcanic clouds.

Several different mechanisms can be active in altering engine performance during or after exposure to a dust-laden environment. Encountering a particle-laden environment of the type of interest here falls into the category of an unanticipated degradation and may be manifested in one or more of the following ways: (*a*) glassification of hot-section components, (*b*) erosion in compressor blading and rotor paths, (*c*) blockage of cooling paths, and (*d*) oil system or bleed air supply contamination. Severe compressor erosion was experienced by all of the engines used in this measurement program and this particular aspect of the result will be described. The problem of component erosion by particulate-laden air flows has been the subject of study for many years [3–9] and is known to result in the loss of surge margin.

The discussion in this paper will be confined to the effort expended in predicting the influence of erosion on the engine performance and in reconciling these predictions with the experimental data obtained from two TF33 turbofans and one J57 turbojet exposed to the same dust environment. One of the TF33 engines and the J57 engine were completely disassembled so that detailed post-test measurements of the components could be obtained. As a result of the detailed measurements performed on the deteriorated engines and the operational experience obtained with them, it is possible to evaluate the predictive ability of a model developed in the following sections of this paper.

2 Review of Experimental Apparatus and Operation

The TF33 turbofan and the J57 turbojet measurements discussed in this paper were performed in Calspan's Large Engine Research Cell (LERC). The LERC is described in detail in [10].

Following preliminary baseline runs, the engines were exposed to dust at concentrations, power settings, and exposure times given by their respective test matrices. The test matrices were based on knowledge of previous engine behavior and environments the engines were postulated to experience. The individual runs were chosen to give a qualitative indication of the influence of concentration and power setting on damage rate and damage mechanism. For a detailed discussion on experimental procedures, see [10]. All readings were taken just before dust ingestion and several times during ingestion.

Results obtained from two engines, the P/W TF33-P11A and the P/W J57-19W, will be described in this paper. The J57 is a twin spool turbojet engine. At Takeoff Rated Thrust (TRT), it generates approximately 12,000 lb of thrust while pumping 185 lb/s of air at a turbine inlet temperature of 1640°F. The TF33 is the turbofan derivative of the J57. The TF33 generates 18,000 lb of thrust at TRT, pumps 460 lb/s of air, and has a turbine inlet temperature of 1660°F. It is appropriate to run these engines as an erosion comparison pair because the two have very similar internal flow geometries and the HP compressor rotor blades are constructed from different materials: The HP compressor blades of the J57-19W are steel and those of the TF33-11A are titanium.

Four engines have been run in this measurement program: three TF33-P11As and one J57-19W. Dust mixture, time at

Contributed by the Gas Turbine Division of THE AMERICAN SOCIETY OF MECHANICAL ENGINEERS and presented at the 32nd International Gas Turbine Conference and Exhibit, Anaheim, California, May 31–June 4, 1987. Manuscript received at ASME Headquarters February 10, 1987. Paper No. 87-GT-112.

assigned power settings, and concentration have varied among engines. A detailed description of the individual engine behavior is given in [10–12]. The discussion in this paper will be confined to the second and third TF33 and the J57. Severe compressor erosion accompanied by hard engine surges describes the behaviors of these engines. All three were brought into states of substantial deterioration at higher power settings and while attempting to accelerate from idle surge occurred. In states of relatively mild deterioration, acceleration rate had to be limited and after heavy deterioration, the engines could not be accelerated at all. It also became apparent that over the course of exposure, the erosion caused a readjustment of operating parameters, especially rotor speeds and fuel and air flows.

3 Brief Review of Erosion Theory Fundamentals

Engine components which are exposed to dust-laden air sustain damage by continuous pitting and cutting of the metal surfaces. Impact velocities of the particles are influenced by inlet air velocity and rotational speed of the rotor blades. Typically, the impact velocity at the first engine rotor is 600 ft/s or less.

At the microscopic level, a statistical approach must be used in describing the erosion process because the simple conceptual case of a single particle impacting at a given velocity and angle is in practice "randomized" by several complicating factors. For example, the particles themselves are nonhomogeneous in hardness and irregular in shape with several sharp corners. As they approach the metal surface with no preferential orientation, they do a random amount of work on it. A substantial fraction of the particle momentum will go into deformation of target material or shear and impulse of target fragments. In addition, the effective angle of impact is randomized by the fact that, after an initial incubation period, the target material becomes pitted with craters and the local impact angle between the small particle and the eroded surface may deviate considerably from the approach angle before the impact. All these effects have been discussed previously in the literature [13–17].

A methodology to predict erosion of gas turbine components must separately define the particulate environment from front to rear of the engine, the shape of the target area and the associated flowfield, and the erosion rate for the special target materials. The flowfield for the uneroded engine is also complex, but known, since the effect of the presence of the particles on the aerodynamics of the engine can be ignored (to a first approximation for all the low-concentration applications of interest here). On the other hand, local changes in geometry may have an important influence on the local erosion rate as the engine components are eroded.

Among the fundamental parameters for modeling erosion, the erosion rate is conceptually well defined and may be obtained experimentally [18]. For a target immersed in a gas particle stream a capture ratio must be determined. The difficulty in determining appropriate values of the capture ratio at specific engine locations for stator vanes, rotor blades, and housing surfaces will become apparent from the later discussion of gas-particle dynamics in multistage turbomachines.

Limiting considerations to well-defined erosion rate data, one finds that some major trends are well established and bear significantly on gas turbine erosion. Experimental observations [16, 18–22] indicate that dust angle of attack and velocity strongly influence the erosion rate for a given combination of dust and target material. Other parameters such as particle size and shape and dust concentration may have a lesser effect, if any, on the results. The influence of angle of attack on the removal rate of material is one of the most distinct features of the erosion of ductile materials such as engine metals. In the velocity range from 250 to 600 ft/s, the erosion rate increases rapidly with angle of attack from zero at 0 deg to a maximum value which occurs at an angle of approximately 20 deg. As the angle of attack increases further from this value, the erosion rate decreases gradually to a residual value of 90 deg. There is a lack of agreement among the results of the theories based on kinetic energy exchange and the experimental results. A more detailed description of the material presented in this paper is given in [23].

Erosion in multistage turbomachines is significantly more complex than the erosion of simple targets such as flat or cylindrical specimens. This is due primarily to the changes which the erodent particles incur from the inlet to the exit of the engine as well as the difficulties in tracing the particle trajectories through the engine gas path. The cumulative influence of particle dynamics and changes in the dust environment makes erosion of both stationary and moving machine components very dependent on their stage location and on the specific engine design. The motion of the particles that are convected through the compressor and the turbine should be analyzed to derive bounds on the location and severity of component erosion. Considerations related to the trajectories for particles having different sizes are necessary to estimate the erodent weight and characteristics at each stage location.

From the brief status review given above, it is clear that a number of fundamental erosion issues must be resolved before

Nomenclature

A = flow area
c = chord
c_l = blade lift coefficient
C_L = cascade lift coefficient
C_D = cascade drag coefficient
C_x = axial velocity
$N2$ = percent of HPC rotational speed
N = number of stages
P = static pressure
P_t = total pressure
$\bar{r}$ = hub-tip mean radius
r_t = tip radius
s = cascade blade spacing
U = rotational speed
W = relative velocity at camber line
w = weight flow
α = airfoil angle of attack
β = relative fluid angle
γ = ratio of specific heats
δ = ratio of total pressure to NASA standard sea-level pressure at 2116 psi
θ = ratio of total temperature to NASA standard sea level temperature of 518.7 R
λ = tip clearance/blade height
ξ = total pressure loss coefficient
ρ = density
ρ_r = reduced density
σ = $1-0.3\,\lambda$
ϕ = flow coefficient
ψ = total pressure coefficient
ω_e = fraction of blade height influenced

Subscripts

1 = stage inlet
2 = stage outlet
3 = compressor inlet
4 = compressor outlet
i = cascade inlet
ii = cascade outlet
is = isentropic
A = air
L = loss
m = cascade mean fluid value
t = tip

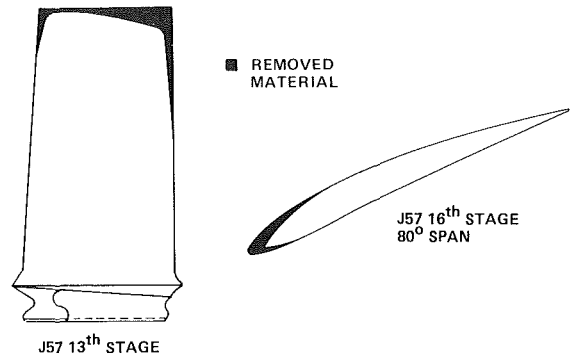

Fig. 1 Typical blade erosion

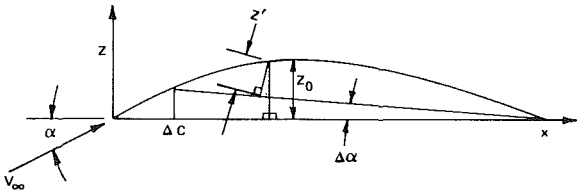

Fig. 2 Formulating changes of the mean camber line

a priori predictions of erosion in realistic turbomachine configurations can be made. At present, two important areas for which additional basic information would be helpful are: (*a*) particle breakup models and data, and (*b*) erosion rates at elevated temperatures [24]. Having recognized this situation, the remainder of this study followed the approach of a semiempirical analysis in which experimental observations relative to the level and pattern of erosion in the TF33 and J57 engines were utilized to interpret the operation of the deteriorated engines. These observations could also be used to guide in the prediction of deteriorated engine behavior.

4 Formulation of Performance Deterioration

Ingestion of dust-laden air has the effect of deteriorating the performance of a gas turbine engine as a result of gas path component erosion. The eroded blades are known to lose the ability to increase the total pressure of the stage efficiently. In an effort to quantify the loss in performance of the engine, a compressor stage will be discussed and then extrapolated into a complete compressor map. First a suitable stage performance map will be calculated from the pre-ingestion compressor map. Then, a deteriorated stage performance will be determined from loss correlations and measured blade erosion. The deteriorated stage performance maps are finally stacked to arrive at an overall deteriorated compressor map.

To estimate the change in stage performance with respect to erosion, the primary sources of total pressure loss affected by the blade aerodynamic efficiency were considered. Attention was given to three distinct origins of total pressure loss: (*a*) losses associated with increasing tip clearance; (*b*) profile losses due to the blade boundary layer; and (*c*) secondary flow losses produced at the hub end wall and casing boundary layer regions. Of considerable interest is the presence of total pressure losses in the tip region which are large in comparison with the other regions. Within the compressor, the impact of dust-laden air will cause considerably greater blade leading edge erosion at the larger span locations as well as tip region erosion. This blade profile modification is illustrated in Fig. 1 which illustrates a J57 HP compressor blade that has been subjected to a dusty environment [11]. This machine uses both an LP and an HP compressor and the erosion of both components is described in [11]. It suffices here to note that the severity of erosion increases from the front to back stages of both compressors, being most severe in the seven-stage HP compressor.

4.1 Tip Clearance Total Pressure Losses. Several authors [25–31] have presented techniques for estimating losses due to tip clearance leakage. Experimental results [26] show a linear decrease in efficiency with increased tip clearance to blade height ratio. Theoretical models have shown fair agreement [28] with experimental results in certain regions of clearance ratio.

Recently, a model presented in [26] was found to agree well with the experimental result of seven different axial flow compressors. The model accounts for leakage loss and pressure gradient losses associated with the flow interaction of the leakage vortex. The expression given in [26] for changes in efficiency in an axial flow compressor blade row can be combined with the definition of cascade lift coefficient based on mean velocity and the definition of efficiency to obtain an expression for the total pressure loss coefficient due to tip clearance effects. As shown in [23], equation (1) can be used to estimate the total pressure loss induced by increased tip clearance and by changes in the lift coefficient resulting from blade profile changes at the tip

$$\xi_{\mathrm{TIP}} = \left[\frac{0.759}{\bar{r}/r_t}\sqrt{\frac{\phi^2\sigma C_L}{\sin^3\beta_m\cos\beta_m}} + \frac{1.17\phi}{\sigma^2\bar{r}/r_t\tan\beta_m}\right]\psi_{is}\lambda \quad (1)$$

As illustrated earlier, the principal effects of erosion on the airfoil are removal of material in the pressure surface leading edge region, thinning of the trailing edge, and reduced leading edge radius. Reference [7] shows a significant increase in two-dimensional profile losses as a result of blade erosion. Due to the high loading at the leading edge of an airfoil, it is expected that any change in this region will be significant. The effect of thickness distribution along the airfoil was assumed to have a minor effect on the overall dynamic performance of the airfoil. The effect of leading edge erosion will be modeled by a change in the mean camber line of the airfoil (see Fig. 2). This change will result in an increase in the angle of zero lift and thus a decrease in blade lift coefficient at fixed inlet flow angle. A reasonable estimate of the contribution to the lift coefficient from the mean camber line is accomplished using thin airfoil theory. It is demonstrated in [23], with the use of classical thin airfoil theory, that for any given eroded state

$$\Delta c_l = 1.5\pi E(\Delta c) \quad (2)$$

where

$$E(\Delta c) = [Z_0/c]_{\Delta c}/(1-\Delta c/c)$$

$$\Delta c/c << 1$$

$$\cos(\Delta\alpha) \approx 1$$

Equation (2) approximates the change in two-dimensional blade lift coefficient due to leading edge erosion and is dependent on the height of the uneroded camber line at the eroded leading edge. Note that the change in blade lift coefficient from equation (2) should be subtracted from the uneroded blade lift coefficient when used to estimate profile losses. For the purpose of this paper, the uneroded blade lift coefficient is obtained by a method outlined in the following paragraph.

It is not recommended that classical thin airfoil theory be used to find the uneroded blade lift coefficient since turbomachinery blades are typically highly cambered. Rather, an improved potential flow solution was obtained by using a modification of classical airfoil theory which removes the assumptions of small angle of attack and small camber angle.

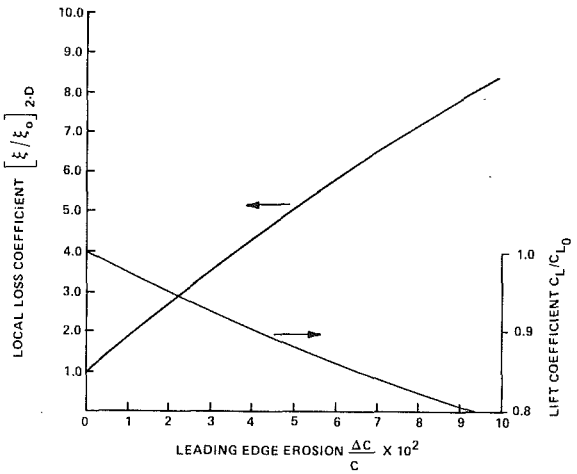

Fig. 3 Effect of leading edge erosion on cascade lift and two-dimensional loss coefficients

For purposes of evaluation of the perturbation velocity (u, w) the sheet vortex is taken to lie on the x axis, in the range $0 \leq X \leq C$, rather than on the line $Z = Z(X)$. Details of the method used in this development are given in [23].

4.2 Modeling Blade Profile Losses. Thus far the development has concentrated on the tip region. The considerations made in deriving the local c_l apply also to any other spanwise location. In order to relate the blade lift coefficient to the cascade lift coefficient, a modifying coefficient K (described in [32, 33]) must be used to account for the effects of channel flow in the cascade. Although the use of a cascade coefficient may seem to oversimplify the formulation of the cascade lift coefficient, it has been found to be reasonable in subsonic flow [32, 33]. Typical values of K are approximately 0.5 for axial flow compressors. For small changes in chord, K can be assumed to remain constant.

Now that a means of tracing changes in cascade lift coefficient with respect to leading edge erosion exits, a method of relating lift coefficient to cascade profile losses must be developed. From a two-dimensional control volume analysis on a cascade, expressions for lift and drag coefficients have been formulated [34] and are given below.

$$C_D = \frac{(\Delta P_t)_L}{\frac{1}{2}\rho W_m^2} \frac{s}{c} \cos \beta_m \tag{3}$$

$$C_L = 2 \frac{s}{c} \cos \beta_m (\tan \beta_i - \tan \beta_{ii}) - C_D \tan \beta_m \tag{4}$$

The loss coefficient based on mean velocity is given by the total pressure loss across the blade divided by the dynamic pressure. Equation (4) was developed from a two-dimensional analysis and may be solved for drag coefficient to arrive at a two-dimensional profile loss coefficient. To express loss coefficient with respect to tip rotational speed, an assumption of constant axial velocity through the blade row is made to yield

$$\xi_m \phi^2 \cos \beta_m = \xi \tag{5}$$

$$\xi_{\text{PROFILE}} = \phi^2 \cos^2 \beta_m \left[\frac{2(\tan \beta_i - \tan \beta_{ii})}{\tan \beta_m} - \frac{c}{s} \frac{C_L}{\sin \beta_m} \right] \tag{6}$$

There are numerous detailed accounts of two-dimensional cascade tests which will give a good estimate of the profile losses [35]. With the stage performance map given and the blade lift coefficient computed the modifying coefficient may be obtained using the definition of cascade lift coefficient.

In addition, from knowledge of uneroded lift coefficient, profile loss coefficient, and blade row geometry, the $\tan \beta_i - \tan \beta_{ii}$ term may be computed. The blade profile of a J57 16th stage compressor blade was used to obtain changes in lift and total pressure loss coefficient with respect to leading edge erosion (see Fig. 3). Since erosion is concentrated in the tip region, the spanwise averaged profile loss increase is not represented by Fig. 3. Equation (7) accounts for the uneroded portion of the blade near the hub and provides the averaged total pressure loss coefficient due to leading edge erosion in the tip region.

$$\xi_{\text{PROFILE}} = \xi_0 [\omega_e (\xi/\xi_0 - 1) + 1] \tag{7}$$

4.3 Secondary Flow Losses. The losses due to secondary flows must also be examined due to their strong dependence on lift coefficient. The literature contains correlations (e.g., [34]) of losses due to secondary flows given by $C_D = 0.018\, C_L^2$ or referring to equations (3) and (5) a loss coefficient given by equation (6)

$$\xi_{\text{SEC}} = 0.018\, \phi^2 C_L^2 c/s \cos \beta_m \tag{8}$$

Since the secondary flow is the result of the hub endwall and casing boundary layers and their respective local lift coefficient, equation (8) will be separated into two parts. The correlation will be assumed to have equal contributions from endwall and casing boundary layers for the uneroded condition. As the tip region is eroded the local two-dimensional lift coefficient will decrease and thus secondary flow losses in the tip region decrease. The contribution due to the hub endwall region will be assumed constant due to relatively little erosion in this region.

5 Stage Performance Deterioration

In order to study the effect of erosion on overall compressor deterioration, a loss in stage performance will be modeled. Experimental studies presented in [25] shows the effect of tip leakage flow on a stage performance map. The study indicates that a change in slope does not occur, but rather an overall shift of the pressure coefficient and efficiency versus flow coefficient curves produces the observed result. This behavior will allow the changes in performance to be modeled at the design point and then used to produce an entire eroded performance map. This assumption is of particular importance since the modeling results are not expected to yield accurate predictions at off-design operating points. To estimate efficiency and performance, the previous total pressure loss formulations will be used with the knowledge of the stage characteristics. Compressor stages are typically designed to have approximately a 50 percent stage reaction for peak efficiency. The flow coefficient may be related to the relative mean fluid angle by

$$\phi = \tfrac{1}{2} \cot \beta_m \tag{9}$$

The design point is taken to be at a constant flow coefficient as the stage deteriorates. On this basis, the mean fluid angle and difference in tangents of inlet and exit fluid angles will be assumed constant at the design point. The assumption of 50 percent stage reaction also gives an equal amount of losses through rotors and stators. The computed and measured stage characteristics are given in Table 1 for the 13th stage of the J57 HP compressor. The measured blade erosion and calculated changes in pressure coefficient and efficiency at the design point are given in Table 2 for the 13th stage.

Table 1 Thirteenth stage characteristics

Mean to tip radius	r/r_t	0.92
Solidity	c/s	1.0
Design flow coefficient	ϕ	0.685
Design pressure coefficient	ψ	0.543
Tip clearance	τ	0.05″
Blade height	h	2″
Mean fluid angle	β_m	36 deg
	$\tan\beta_i - \tan\beta_{ii}$	0.464
Stagger angle	ν	30 deg
Polytropic efficiency	η_{pc}	0.86
Profile loss coefficient	ξ_{profile}	0.012
Cascade modifying coefficient	K	0.20
Cascade lift coefficient	C_l	0.64
Total loss coefficient	ξ	0.050

Table 2 Performance change due to erosion, 13th stage

Chord change at tip	$\Delta C_{l/c}$	0.06
Average chord change	$\Delta c/c$	0.03
Leading edge influence	ω_e	0.3
Decrease in efficiency	$\Delta\eta_{st}$	0.084
Decrease in pressure coefficient	$\Delta\psi$	0.050
Tip clearance increase	$\Delta\tau$	0.063
Increase in loss coefficient	ξ/ξ_0	1.51

Table 3 Computed performance loss in stages

Stage	$\Delta\psi$	$\Delta\eta_{st}$	$\xi/\xi_{0,\text{ total}}$
10	0.010	0.18	1.10
11	0.036	0.062	1.47
12	0.047	0.079	1.51
13	0.051	0.084	1.51
14	0.113	0.190	2.13
15	0.120	0.200	2.14
16	0.139	0.232	2.23

The above calculations were made assuming no increases in losses through the stator. Formulation of loss in performance was carried out for all seven stages of the high-pressure compressor and are presented in Table 3. These loss estimates were computed with the use of the stage performance formulated from a 69.9 percent speed line, which will be discussed later.

6 Modeling Compressor Response

The procedure described in the previous section can be used to determine stage performance deterioration when the actual stage performance characteristics are given. This was not the case for the TF33 and J57 engines which were used in these measurements. Therefore, a method was developed to obtain the stage performance map from the overall compressor map. It is important to incorporate a compression efficiency in the method so that off-design performance can be computed. The only available input parameters are assumed to be the compressor map with corresponding overall adiabatic efficiencies. The method outlined below is based on the relationship between a constant rotational speed line and the stage total pressure coefficient curve. The compressor map provides the relationship among mass flow, total pressure rise, and overall efficiencies along constant rotational speed lines. The inlet total pressure was assumed to be atmospheric pressure and the density was chosen to be that at standard conditions. The exit velocity was calculated knowing the inlet conditions, compressor flow areas, and the efficiency. The total pressure increase can be averaged by the number of stages and a pressure coefficient for inlet and exit stages can be averaged. A suitable averaged stage map can then be used in a stage stackup procedure. Each stage was assumed to have the same performance map but different operating points. The exit conditions can then be calculated from the continuity equation and the definition of total pressure. In order to obtain a third equation and thus allow the calculation of density, velocity, and pressure at the exit, the second law of thermodynamics and the definition of polytropic compression efficiency were used [23].

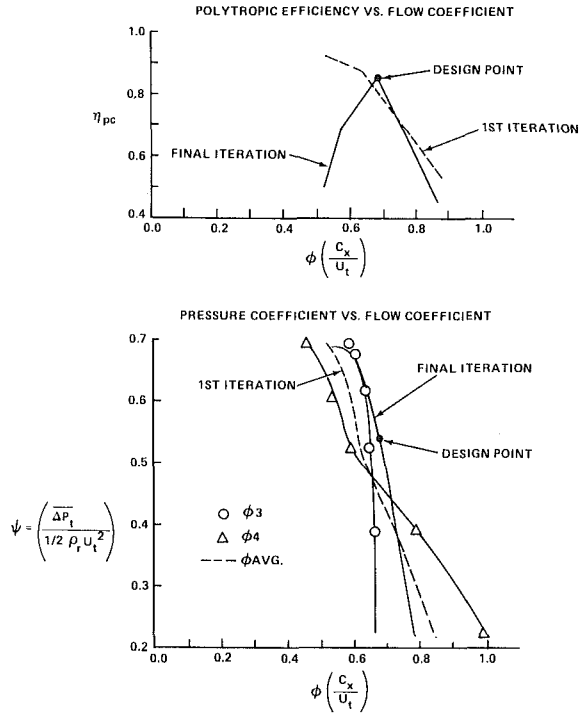

Fig. 4 Estimated stage performance map from the 69.9 percent *N2* line

The average flow coefficient is computed from the average of inlet and exit velocity divided by tip rotational speed. The average pressure coefficient is computed from the averaged total pressure rise per stage divided by the reduced density

$$\bar{\psi} = \frac{(P_{T4} - P_{T3})}{\tfrac{1}{2} N \rho_r U_t^2} \tag{10}$$

where

$$\rho_r = \frac{2\rho_3\rho_4}{\rho_3 + \rho_4}$$

N = number of stages

By using the reduced density, the method essentially averages the input mechanical energy per stage. Figure 4 shows the computed averaged stage performance map for a 69.9 percent rotational speed line. This map was used to reconstruct the constant-speed line of the compressor map by a stage stacking technique described later. A slight adjustment was needed to reproduce the compressor map line. This was due to the lack of available compressor efficiency data which required that estimates of local values be made. From the previous calculations of changes in stage performance an eroded performance map for several stages is given in Fig. 5. If stage performance data were available, they would be preferable to an averaged stage map. Also, the above averaged performance map will only yield accurate results for the constant-speed line used.

6.1 Generating an Eroded Compressor Map From Stage Stacking. From the computed averaged stage performance map, the stage stacking technique was used to duplicate the constant-speed line of the compressor map. The following procedure of stacking the stages to arrive at an overall total pressure rise was followed. From the knowledge of inlet conditions and mass flow, the inlet flow coefficient may be calculated. The total pressure rise and polytropic efficiency may then be found from the stage performance map. It was assumed that the drop in polytropic efficiency is closely approximated by the loss in stage efficiency. From the stage exit total pressure and an assumed constant mean axial velocity, the static pressure rise is estimated from the definition of total

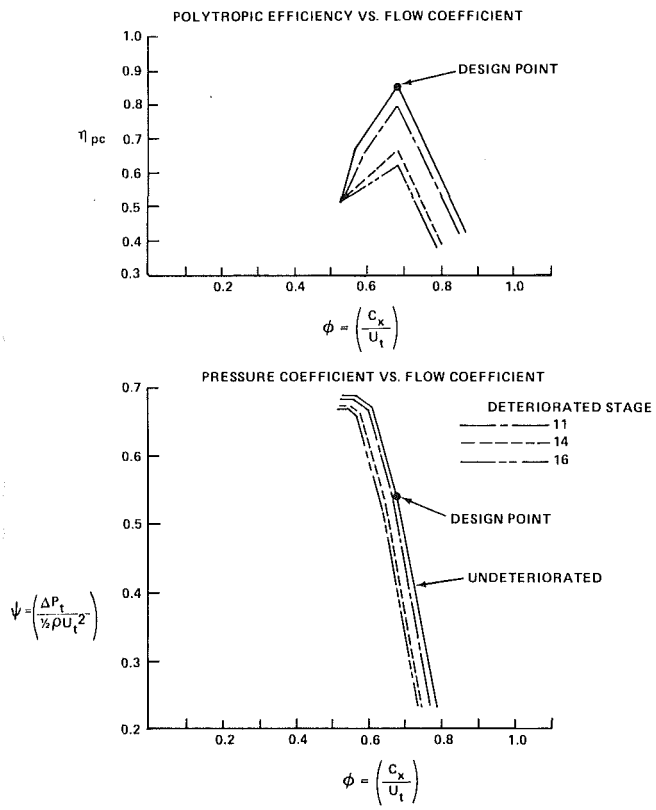

Fig. 5 Estimated stage performance deterioration from measured erosions

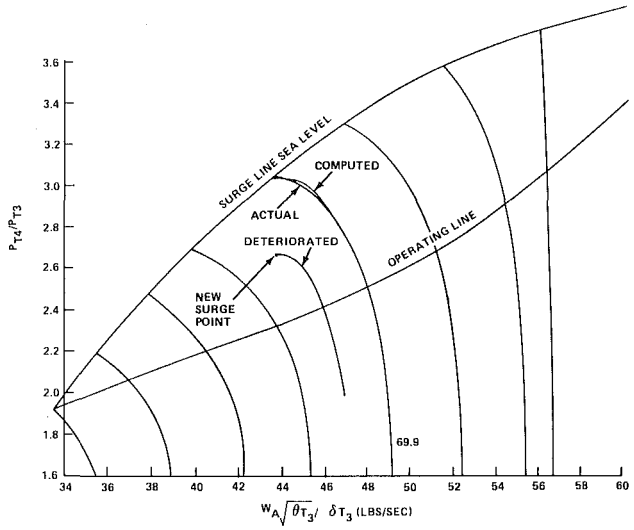

Fig. 6 Computed change in compressor performance

Table 4 Loss in compressor stability

	Uneroded	Eroded	Percent decrease
Surge margin	0.305	0.148	51
Surge pressure ratio	0.234	0.129	45

pressure. The static exit density rise is then computed from the total pressure rise and polytropic efficiency [23]

$$\left(\frac{P_{T2}}{P_{T1}}\right)^{\gamma^*/\gamma} = \left(\frac{P_2}{P_1}\right)^{1/\gamma}\left(\frac{\rho_1}{\rho_2}\right)$$

where

$$\gamma^* = \frac{(\gamma-1)(1-\eta_{pc})}{\eta_{pc}} \tag{11}$$

The axial velocity entering the next stage is computed from continuity equation (12). The entrance density is assumed to equal the previous exit stage's density

$$C_{x_2} = \frac{\rho_i}{\rho_2}\frac{A_i}{A_2}C_{x_i} \tag{12}$$

Figure 6 shows the clean 69.9 percent constant-speed line and a corresponding eroded line computed using this stage stacking technique. It is assumed that the operating line of the compressor does not shift due to the relatively unchanged fuel controller, combustor, and turbine. The shift in speed lines does illustrate a decrease in corrected weight flow and total pressure rise at a constant rotational speed. The loss in corrected weight flow at the constant speed line of 69.9 percent was computed to be 4.4 percent of the expected weight flow of the undeteriorated engine at the operating line.

To examine the change in surge line with respect to erosion, a comparison of compressor stability will be made between an undeteriorated and a deteriorated low-speed line. For constant properties, the inlet axial velocity is given by the weight flow through the compressor. Therefore, the inlet flow coefficient will be the same for both the deteriorated and undeteriorated speed line at the weight flow corresponding to the undeteriorated compressor surge line. In the case of a low-speed surge, the front stages are at high incidence, due to lower flow coefficient, and the back stages are approaching a choking condition. With increasing stage deterioration, the back stages (at the same speed) are experiencing a lower density relative to their uneroded operation. This will cause the exit velocity to be elevated even higher than the uneroded operating value. The deteriorated engine then moves closer to choking the rear stages with the same inlet flow coefficient. With the flow coefficient corresponding to stage stall unchanged for the deteriorated stage, the front stages remain at their unstable high incidence values. It is reasonable to assume then that compressor surge will occur at the same corrected weight flow as that of the undeteriorated compressor at low-speed operation. The losses in available surge margin and surge pressure ratio at the 69.9 percent speed surge point were estimated and are presented in Table 4 [36].

7 Deteriorated Engine Response

Given the J57-P19W and TF33-P11A engines, there are two ways the engine operator can alter the compressor inlet and exit conditions to make them less prone to surge. They are the intercompressor bleed and the anti-icing air systems.

As the engine is accelerated through a scheduled LPC pressure ratio, the intercompressor bleed valve closes and the spools rematch. Pressure ratio across the LPC rapidly rises and the HPC pressure ratio first falls and then rises with increasing thrust. By being presented with air at lower density and velocity than if the valve were closed, the HPC is less likely to experience the low-speed front-stage surge generated by high angle of attack from rear stage choking. When the valve does close in normal operation, density and velocity at the high compressor rapidly increase but at this rotor speed the compressor can sufficiently compress the air so as to not choke the rear stages.

The anti-ice air system serves to raise the temperature of the metal surface at the face of the engine in order to avoid potentially dangerous ice buildup. The system routes hot air from the cowling downstream of the HPC through a thermally adjusted valve, inside the first fan stator, and to the engine inlet. By bleeding air from the exit end of the HPC, the anti-ice air system effectively reduces the flow restriction felt by the HPC

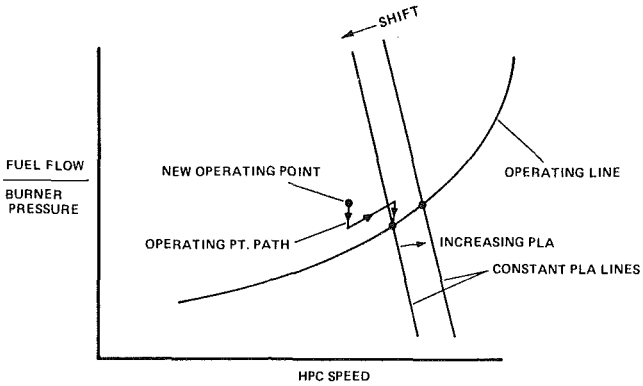

Fig. 7 Fuel controller map

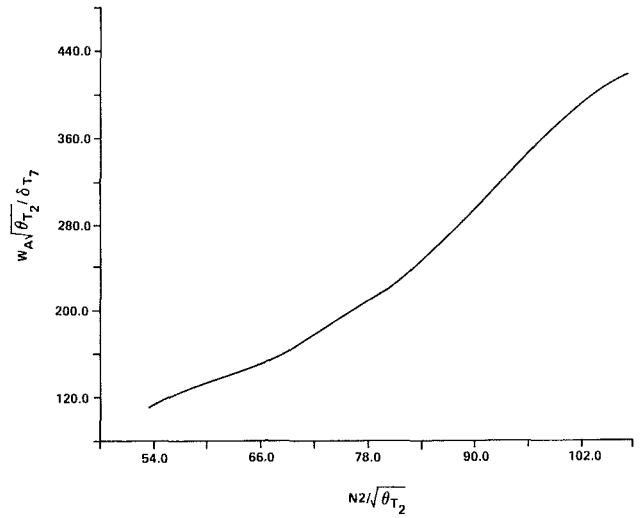

Fig. 8 Fourth-order polynomial fit to the pre-exposure calibration data

and moves it away from surge at all speeds, particularly the front stages at low speed.

Both of the systems described above were used during the measurement program to make acceleration to higher power settings possible. They were found to become effective at different deterioration and power levels than each other. One of the TF33s eroded to a point at which it could not be accelerated through a power setting just above idle unless the anti-ice air system was operating. The power setting involved was low enough for the bleed door to be in the open position and any surge in this regime would be in the high-pressure compressor front stages. The amount of air bled for anti-icing is scheduled based on ambient inlet air temperature with larger amounts bled at lower temperatures. This method of surge avoidance, then, may not be effective at high ambient temperatures unless the thermally controlled valve were overridden (which is not a feature of these engines). Anti-ice air did not have a noticeable influence on surge margin other than at the low power settings previously mentioned.

After further exposure, the TF33 experienced surges at steady state just above the bleed door closing point and a single surge each time it was accelerated through closing. The HPC is operating at nearly its design optimum speed at the time of bleed door closing and is relatively difficult to send into surge. The LPC is at the same time rotating at low speed with relatively little margin and is likely to go to front stage surge. As erosion progressed, the engine spools rematched to reflect the change in work distribution between them. Typically, the air weight flow for a given engine speed and the low

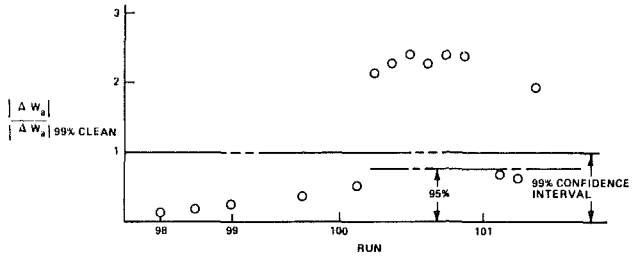

Fig. 9 Deviation from baseline weight flow versus rotational speed curve

compressor speed for a given EPR decreased. High compressor speed for a given EPR increased. That both low compressor speed and air flow decreased is to be expected in an undamaged compressor and indeed the low spools from the engines were relatively undamaged.

The fuel controller sets fuel flow based on a preset schedule of HPC speed, burner pressure, and power lever angle (PLA). A sketch of a fuel controller map is shown in Fig. 7. For a given PLA, the controller maintains a fixed fuel flow-to-burner pressure ratio and a fixed compressor speed by metering fuel to the combustor. Whenever the power setting is above cruise, burner pressure is constant and the controller adjusts fuel flow to maintain control speed. For power settings below cruise, fuel flow, burner pressure, and speed all increase with increasing power. Fuel flow increases faster than burner pressure with increasing speed.

It is felt that the fuel controller contributed to the quasi-steady-state surge described earlier. During hour preceding surge, the PLA was increased several times to compensate for decreasing EPR. HPC speed had remained constant and both fuel flow and burner pressure had been falling. Each time the PLA was adjusted, burner pressure increased to its "prefall" value and fuel flow exceeded its value. On the fuel control map this is represented by a leftward shift on the constant PLA lines and a new operating point above the operating line. The fuel controller response can be either to cut fuel flow (which it did several times initially) or to search for a new one-line operating point at a higher speed (which it did before going into surge). This would mean the instantaneous operating point would move to the left and the fuel flow would begin to increase to return to the line. If this increased burner pressure was sufficient to overpower the exit pressure of the HPC then surge would occur.

7.1 Deterioration in Weight Flow. The experimental data taken during testing of the third TF33 will be evaluated for comparison with clean air baseline data. A fourth-order polynomial fit (Fig. 8) was performed on the baseline data with a 99 percent confidence interval of $\Delta | W_A \sqrt{\theta_{T_2}}/\delta_2 | = 4.38$ lb/s. The deviation from the baseline curve was then evaluated as dust ingestion progresses. It is expected that as ingestion of dust progresses the weight flow of air through the engine will decrease with respect to rotational speed. The deviation of experimental data from the baseline curve is normalized by the Z statistic corresponding to a 99 percent confidence interval for an assumed standard normal distribution. Figure 9 illustrates the normalized distribution of weight flow in order of increasing cumulative dust ingested. A significant number of data points fall outside the undeteriorated 99 percent confidence interval indicating a change in engine performance outside the computed fluctuations of the undeteriorated data.

The predicted decrease in corrected weight flow at $N_2/\sqrt{\theta_T}$ of 69.9 percent speed is at a normalized deviation of 1.71. This value represents the average expected for a sample of data at 69.9 percent rotational speed. By assuming that the standard

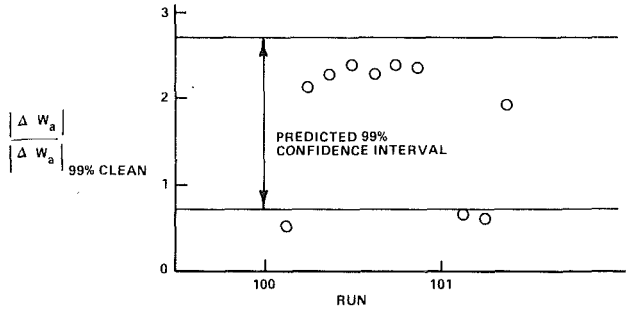

Fig. 10 Comparison of predicted deterioration with experimental data

deviation of the data for the deteriorated engine is equal to the standard deviation of the undeteriorated engine, we may compute the 99 percent confidence interval of the deteriorated performance. Note that the predicted value corresponds to the last run since the measured erosions were taken from the blades of a torn-down engine. Figure 10 shows the predicted deteriorated 99 percent confidence interval and associated sampled data points for the last few runs. The majority of the sampled data do fall within the 99 percent confidence interval predicted and indicate good agreement with predicted results. Some of the dispersion of the data may be due to the fact that the majority of the data were sampled at the design speed and the calculations were performed for the 69.9 percent speed value. It is not possible to determine the functional dependence of deviation from the baseline curve on rotational speed due to the limited range of power settings sampled.

8 Conclusions

A measurement program currently underway at Calspan has been used in the evaluation of observed engine behavior during dust ingestion. The major effect of solid particle ingestion was the erosion and subsequent performance deterioration of the HPC. The most noticeable feature of blade removal was increased tip clearance and blade leading edge erosion. The increase in proportionate blade loss through the compressor will result in substantial performance deterioration in both the LPC and HPC stages.

The observations obtained from the analysis and data described in this paper indicate that a deteriorated engine will be increasingly likely to surge when low-speed acceleration is initiated. Indications of deterioration were found to be reduced burner pressure and air weight flow for a given HPC speed. In an eroded engine before the final stage of deterioration, the intercompressor bleed and anti-ice air served to decrease the susceptibility to surge at low power settings. Specifically, use of anti-ice air can serve to decrease the likelihood of off-idle surges; use of intercompressor override can serve to avoid surge at bleed door closing. Off-idle surges emanate from the HPC and intercompressor bleed door closing surge emanates from the LPC. The influence of erosion is to make the front stages of the HPC and LPC more prone to surge. It was also observed that near cruise power the fuel controller can send a deteriorated engine, while operating at steady state and having a narrow surge margin, into autoacceleration and surge.

To quantify the performance deterioration a predictive capability was developed based on a semiempirical method. The individual stages were modeled to evaluate the effects of increased tip clearance and leading edge effects. The change in total pressure rise and efficiency for the undivided stages were calculated and used to develop new performance maps. The stages were then stacked to arrive at a deteriorated compressor map. The qualitative effect of shifting the constant speed lines toward reduced mass flow and lower pressure ratio is in agreement with experimental observations. The quantitative results of reduction in corrected weight flow gave good agreement with experimental data. The reduction in surge margin at the 69.9 percent $N2$ surge line was predicted to be on the order of 50 percent. Although quantitative measurements of surge margin are not available, the observed engine behavior does agree with the expected results of such a loss.

Acknowledgments

The research reported in this paper was sponsored by the Defense Nuclear Agency under Contract DNA 001-83-C-0182.

References

1 Mitchell, H. J., and Gilmore, F. R., "Dust-Cloud Effects on Aircraft Engines—Emerging Issues and New Damage Mechanisms," RDA-TR-120012-001, Mar. 1982.

2 Chambers, J. C., "The 1982 Encounter of British Airways 747 With the Mt. Galuggung Eruption Cloud," AIAA 23rd Aerospace Sciences Meeting, Jan. 14-17, 1985, Reno, NV, AIAA Paper No. 85-0097.

3 Tabakoff, W., and Hussein, M. F., "Effects of Suspended Solid Particles on the Properties in Cascade Flow," *AIAA Journal*, 1971, pp. 1514-1519.

4 Tabakoff, W., and Hussein, M. F., "Pressure Distribution on Blades in Cascade Nozzle for Particulate Flow," *Journal of Aircraft*, 1971, pp. 736-738.

5 Hussein, M. F., and Tabakoff, W., "Dynamic Behavior of Solid Particles Suspended by Polluted Flow in a Turbine Stage," *Journal of Aircraft*, 1973, pp. 434-440.

6 Grant, G., and Tabakoff, W., "Erosion Prediction of Turbomachinery Resulting From Environmental Solid Particles," *Journal of Aircraft*, 1975, pp. 471-478.

7 Tabakoff, W., and Bahan, C., "Effects of Solid Particles Suspended in Fluid Flow Through an Axial Flow Compressor Stage," presented at the 5th International Symposium on Airbreathing Engines, Feb. 16-21, 1981, Bangalore, India.

8 Tabakoff, W., "Compressor Erosion and Performance Deterioration," AIAA/ASME 4th Joint Fluid Mechanics, Plasma Dynamics, and Lasers Conference, Atlanta, GA, May 12-14, 1986.

9 Hamed, A., "Effect of Particle Characteristics on Trajectories and Blade Impact Patterns," AIAA/ASME 4th Joint Fluid Mechanics, Plasma Dynamics, and Laser Conference, Atlanta, GA, May 12-14, 1986.

10 Dunn, M. G., Padova, C., and Moller, J. C., "Performance Deterioration of an Operational TF33 Turbofan Engine Upon Exposure to a Simulated Nuclear Dust Environment," DNA-TR-86-62-VI, Jan. 1986.

11 Dunn, M. G., Padova, C., and Moller, J. C., "Performance Deterioration of Turbojet Engine Upon Exposure to a Dust Environment," DNA TR-86-62-V2, July 1986.

12 Dunn, M. G., Padova, C., and Moller, J. C., "Deterioration of a TF33 Turbofan When Exposed to a Scoria-Laden Dust Environment," DNA-86-62-V23, Aug. 1986.

13 Finnie, I., "The Mechanism of Erosion of Ductile Metals," ASME *Journal of Applied Mechanics*, Vol. 25, 1958, pp. 527-532.

14 Finnie, I., Wolak, J., and Kabil, Y., "Erosion of Metals by Solid Particles," *Journal of Materials*, Vol. 2, 1967, pp. 692-700.

15 Goodwin, J. E., Sage, W., and Tilly, G. P., "Study of Erosion by Solid Particles," *Proceedings of the Institute of Mechanical Engineers*, Vol. 184, Pt. 1, 1969-70, pp. 279-292.

16 Tilly, G. P., and Sage, W., "The Interaction of Particle and Material Behavior in Erosion Processes," Wear, Vol. 16, 1970, pp. 447-465.

17 Rao, P. V., and Buckley, D. H., "Characterization of Solid Particle Erosion Resistance of Ductile Metals Based on Their Properties," ASME JOURNAL OF ENGINEERING FOR GAS TURBINES AND POWER, Vol. 107, 1985, pp. 669-678.

18 Rao, P. V., and Buckley, D. H., "Effect of Surface Configuration During Solid Particle Impingement Erosion," ASME JOURNAL OF ENGINEERING FOR GAS TURBINES AND POWER, Vol. 107, 1985, pp. 661-667.

19 Sheldon, G. L., and Kanhere, A., "An Investigation of Impingement Erosion Using Single Particles," *Wear*, Vol. 21, 1972, pp. 195-209.

20 Sheldon, G. L., and Finnie, I., "On the Ductile Behavior of Nominally Brittle Materials During Erosive Cutting," *Journal of Engineering Industry*, 1966, pp. 387-392.

21 Tabakoff, W., Malak, M. F., and Hamed, A., "Laser Measurements of Solid Particles Rebound Parameters Impacting on 2024 Aluminum and 6A1-4V Titanium Alloys," presented at the 18th Fluid Dynamics Conference, Cincinnati, OH, July 1985, Paper No. MAA-85-1570.

22 Hamed, A., Tabakoff, W., and Mansour, M. L., "Turbine Erosion Exposed to Particulate Flow," ASME Paper No. 86-GT-258, 1986.

23 Batcho, P. F., Moller, J. C., Padova, C., and Dunn, M. G., "Interpretation of Gas Turbine Response Due to Dust Ingestion," DNA TR-86-306, Sept. 1986.

24 Tabakoff, W., Hamed, A., and Ramachandran, J., "Study of Metals Erosion in High Temperature Coal Gas Streams," ASME JOURNAL OF ENGINEERING OF POWER, Vol. 102, 1980, pp. 148-152.

25 Inoue, M., Kuroumaru, M., and Fukuhara, M., "Behavior of Tip Leakage Flow Behind an Axial Compressor Rotor," ASME JOURNAL OF ENGINEERING FOR GAS TURBINES AND POWER, Vol, 108, 1986, pp. 7–37.

26 Senoo, Y., and Ishida, M., "Pressure Loss Due to the Tip Clearance of Impeller Blades in Centrifugal and Axial Blowers," ASME JOURNAL OF ENGINEERING FOR GAS TURBINES AND POWER, Vol. 108, 1986, pp. 32–37.

27 Lakshminarayana, B., Sitaram, N., and Zhang, J., "End-Wall and Profile Losses in a Low-Speed Axial Flow Compressor Rotor," ASME JOURNAL OF ENGINEERING FOR GAS TURBINES AND POWER, Vol. 108, 1986, pp. 22–31.

28 Lakshminarayana, B., "Methods of Predicting the Tip Clearance Effects in Axial Flow Turbomachinery," ASME *Journal of Basic Engineering*, Vol. 92, No. 9, 1970, pp. 467–482.

29 Hah, C., "A Numerical Modeling of Endwall and Tip-Clearance Flow of an Isolated Compressor Rotor," ASME JOURNAL OF ENGINEERING FOR GAS TURBINES AND POWER, Vol. 108, 1986, pp. 15–21.

30 Khabba, G., and Senoo, Y., "The Influence of Tip Clearance on Stall Limits of a Rectilinear Cascade of Compressor Blades," ASME *Journal of Basic Engineering*, 1961, pp. 371–378.

31 McNair, R. E., "Tip Clearance Effects on Stalling Pressure Rise in Axial Flow Compressors," *ASME Symposium on Compressor Stall, Surge, and System Response*, Mar. 1960, pp. 47–50.

32 Horlock, J. H., *Axial Flow Compressors, Fluid Mechanics and Thermodynamics*, Kreiger, 1973, pp. 29–45.

33 Hawthorne, W. R., *Aerodynamics of Turbines and Compressors*, Princeton University Press, 1964, Section B.

34 Hill, P., and Peterson, C., *Mechanics and Thermodynamics of Propulsion*, Addison-Wesley, New York, 1965, pp. 238–312.

35 Howell, A. R., "NACA Members of Compressor and Turbine Research Division Aerodynamic Design of Axial-Flow Compressors," NACA RME 56B03b, 1956; revised NASA S.R. 36, 1965.

36 Oates, G. C., *The Aerothermodynamics of Aircraft Gas Turbine Engines*, AFAPL-TR-78-52, Chap. 23.

Journal of Engineering for Gas Turbines and Power

Discussion

Effect of Control Algorithms on Magnetic Journal Bearing Properties[1]

C. R. Burrows.[2] Magnetic bearings are now commercially available and offer an attractive solution to the problem of controlling the vibration of a rotor. However, experience reported in the literature [20, 21] supports the authors' contention that "the most difficult part of the design of magnetic bearings is the control algorithms." I uphold this view, while recognizing that it is only due to the excellent work by Schweitzer [1, 2] and others in overcoming the problems associated with magnetic bearing design that we have reached this stage.

It is the challenge to design control algorithms for multimode rotor-bearing systems which has occupied the attention of my research group for a number of years.

We have concentrated on the use of a magnetic bearing as a control element for a flexible rotor supported in oil-film bearings. These bearings add to the difficulty of the design problem, not least because with these elements it is unrealistic to study an uncoupled model. Some progress has been made [4, 22–24], but the general problem of designing a closed-loop controller for a multimode rotor-bearing system still requires much research effort.

In our current work we are experimenting with a magnetic bearing to control a 100-mm-dia shaft supported on oil-film bearings. Our control strategy developed in [24] has been complemented. This both estimates the system matrix and calculates the optimum control force on-line. The work will be discussed in a forthcoming ASME paper [25].

References

20 Cataford, G. F., and Lancee, R. P., "Oil-Free Compression on a Natural Gas Pipe Line," ASME Paper No. 86-GT-293.

21 Foster, E. G., Kulle, P., and Peterson, R. A., "The Application of Active Magnetic Bearings to a Natural Gas Pipeline," ASME Paper No. 86-GT-61.

22 Burrows, C. R., and Sahinkaya, M. N., "Control of Oil-Whirl by Pole Assignment," presented at ACC, San Diego, CA, June 1984.

23 Sahinkaya, M. N., and Burrows, C. R., "Control of Stability and the Synchronous Vibration of a Flexible Rotor Supported on Oil-Film Bearings," ASME *Journal of Dynamic Systems, Measurement and Control*, Vol. 107, 1985, pp. 139–144.

24 Burrows, C. R., and Sahinkaya, M. N., "Vibration Control of Multimode Rotor Bearing Systems," *Proc. Royal Soc. Lond.*, Vol. A386, 1983, pp. 77–94.

25 Burrows, C. R., Sahinkaya, M. N., and Clements, S., "Electromagnetic Control of Oil-Film Supported Rotors Using Sparse Measurements," submitted for presentation at the ASME Vibration and Noise Meeting, Boston, MA, Sept. 1987.

[1] By R. R. Humphris, R. D. Kelm, D. W. Lewis, and P. E. Allaire, published in the October 1986 issue of the JOURNAL OF ENGINEERING FOR GAS TURBINES AND POWER, Vol. 108, No. 4, pp. 624–632.

[2] Professor, Head of the Division of Dynamics and Control, University of Strathclyde, Glasgow, United Kingdom.